

Three-phase CO₂ methanation

-

Methanation reaction kinetics and transient behavior of a slurry bubble column reactor

zur Erlangung des akademischen Grades eines
DOKTORS DER INGENIEURWISSENSCHAFTEN (Dr.-Ing.)

der Fakultät für Chemieingenieurwesen und Verfahrenstechnik des
Karlsruher Instituts für Technologie (KIT)

genehmigte
DISSERTATION

von

Dipl.-Ing. Jonathan Lefebvre
aus Liancourt Saint Pierre in Frankreich

Referent:	Prof. Dr.-Ing. Thomas Kolb
Korreferent:	Prof. Dr.-Ing. Jörg Sauer
Tag der mündliche Prüfung:	25 Januar 2019

à ma famille

Table of Contents

Table of Contents	I
Notation	V
Symbols (Latin)	V
Symbols (Greek)	VIII
Dimensionless numbers	IX
Abbreviations	X
Indices	XI
1 Introduction	1
2 Literature review	3
2.1 Catalytic methanation	3
2.1.1 Fundamentals and thermodynamics	3
2.1.2 Methanation catalyst	3
2.1.3 Deactivation of methanation catalyst	5
2.1.4 CO ₂ methanation mechanism on Ni catalyst	6
2.1.5 CO ₂ methanation kinetic rate equations for Ni catalysts	8
2.1.6 Methanation reactor concepts	10
2.2 Slurry bubble column reactors	11
2.2.1 Hydrodynamics of slurry bubble column reactors	11
2.2.1.1 Flow regimes	12
2.2.1.2 Minimum suspension conditions for solid catalysts	13
2.2.1.3 Backmixing	14
2.2.1.4 Gas holdup	15
2.2.2 Mass transfer in slurry bubble column reactors	16
2.2.3 Heat transfer in slurry bubble column reactors	18
3 Objective and approach	19
4 Gas solubilities of CO₂ methanation products in dibenzyltoluene	21
4.1 Experimental setup	22
4.2 Materials	23
4.2.1 Gases	23
4.2.2 Suspension liquid	23
4.3 Experimental method	23
4.3.1 Experimental procedure	23
4.3.2 Data analysis and calculations	24

4.4	Results and discussion	26
4.4.1	CH ₄ solubility in dibenzyltoluene	26
4.4.2	H ₂ O solubility in dibenzyltoluene	27
4.4.3	Henry's law constant temperature dependency	28
4.4.4	Comparison with literature data	30
4.4.5	Consequence of gas solubility on three-phase CO ₂ methanation reaction	31
4.5	Summary	32
5	Three-phase CO₂ methanation reaction kinetics	33
5.1	Experimental setup	34
5.1.1	Gas supply system	34
5.1.2	Reactor	35
5.1.3	Gas analysis	36
5.2	Materials	36
5.2.1	Gases	36
5.2.2	Catalysts	36
5.2.3	Suspension liquids	37
5.3	Experimental method	37
5.3.1	Experimental procedure	37
5.3.1.1	Catalyst activation	37
5.3.1.2	CO ₂ methanation experiments	38
5.3.2	Data analysis and calculations	39
5.3.3	Development of a reaction rate equation	40
5.4	Results and discussion	41
5.4.1	Catalyst test	41
5.4.2	Influence of the liquid phase on reaction kinetics	44
5.4.3	Development of a reaction rate equation	46
5.4.3.1	Educt influence on the CO ₂ reaction rate	46
5.4.3.2	Product influence on the CO ₂ reaction rate	48
5.4.3.3	Reaction rate equation	49
5.4.3.4	Sensitivity analysis	50
5.5	Summary	51
6	Comparison between two-phase and three-phase CO₂ methanation reaction kinetics	53
6.1	Experimental setup	54
6.2	Materials	55
6.3	Experimental method	56
6.3.1	Experimental procedure	56
6.3.2	Data analysis and calculations	57
6.3.3	Development of a reaction rate equation	58
6.4	Results and Discussion	59
6.4.1	Influence of temperature and gas partial pressure on the CO ₂ reaction rate	59
6.4.2	Reaction rate equation	64

6.4.3	Comparison of two-phase and three-phase methanation kinetics	66
6.5	Summary	67
7	Performance of a slurry bubble column reactor for transient CO₂ methana- tion	69
7.1	Literature review on reactor modeling	70
7.1.1	Slurry bubble column reactor	70
7.1.2	Tube bundle reactor	71
7.2	Reactor modeling	72
7.2.1	Slurry bubble column reactor model	73
7.2.2	Tube bundle reactor model	79
7.3	Results and discussion	82
7.3.1	Determination of methanation reactor design	82
7.3.1.1	Slurry bubble column reactor design	82
7.3.1.2	Tube bundle reactor design	86
7.3.1.3	Reactor control strategy	89
7.3.2	Transient Power-to-Gas operation	90
7.3.2.1	Effect of gas load increase on methanation reactor performance	90
7.3.2.2	Transient slurry bubble column reactor	91
7.3.2.3	Transient tube bundle reactor	92
7.3.3	Reactor improvement considerations	94
7.4	Summary	96
8	Summary	99
9	Zusammenfassung	103
10	Outlook	107
	Verification of the contribution from the co-authors	109
	Publication list	113
	Curriculum vitae	115
	Appendix	117
A	Material properties	117
A.1	Gas purity	117
A.2	Dibenzyltoluene properties	117
B	Calculation of physical properties	118
B.1	Gas properties	118
B.1.1	Gas density, ρ_G	118
B.1.2	Dynamic viscosity, μ_G	118
B.1.3	Specific heat capacity, $c_{p,G}$	119
B.1.4	Thermal conductivity, λ_G	119
B.1.5	Binary molecular diffusion coefficient, D_{12}	119
B.1.6	Parameters for Peng Robinson equation of state	119

B.2	Slurry properties	120
B.2.1	Slurry density, ρ_{SL}	120
B.2.2	Slurry dynamic viscosity, μ_{SL}	120
B.2.3	Slurry heat capacity, $c_{p,\text{SL}}$	120
B.2.4	Slurry heat conductivity, λ_{SL}	120
B.2.5	Gas diffusion coefficient in liquid phase, $D_{i,\text{L}}$	121
B.3	Fixed-bed properties	121
B.3.1	Thermal conductivity of the catalyst bed, λ_{bed}	121
B.3.2	Effective radial thermal conductivity of the catalyst bed, $\lambda_{\text{eff},r}$	121
B.3.3	Heat transfer coefficient at the internal reactor wall, α_{wall}	122
C	Mass transfer in and around catalyst particles	122
C.1	Mass transfer coefficient gas-catalyst particle, k_{G}	122
C.2	Effective pore diffusion coefficient in a catalyst particle, $D_{i,\text{eff}}$	122
C.3	Catalyst efficiency, η_{cat}	123
D	Criterion for plug flow reactor behavior	123
E	Criteria for estimation of absence of mass and heat transfer limitation	124
F	Evaluation of minimum gas velocity for complete solid suspension in a slurry bubble column reactor	125
G	Supporting materials for gas holdup correlations	125
H	Supporting materials for volumetric mass transfer correlations	126
I	Evaluation of mass-transfer resistance in a slurry bubble column reactor	127
J	Supporting results: gas solubility experiments	129
J.1	Exemplary gas solubility experiment	129
J.2	Validation of the experimental procedure	129
J.3	Ar solubility in dibenzyltoluene	130
K	Chemical equilibrium of three-phase CO_2 methanation	132
L	Supporting results: three-phase methanation kinetic experiments	134
M	Supporting results: modeling of CO_2 methanation reactors	135
M.1	Model assumptions	135
M.2	Influence of cell number on CO_2 conversion using the slurry bubble column reactor model	136
M.3	Influence of inlet gas temperature on the performance of the tube bundle reactor	137
M.4	Effect of gas load on slurry bubble column reactor reactor	137
M.5	Effect of gas load on tube bundle reactor	138
M.6	Effect of gas load step change on slurry bubble column reactor	139
M.7	Effect of gas load step change on tube bundle reactor	142
M.8	Design algorithm	144
N	Evaluation of data accuracy	146
O	Technical drawings	148
References		151

Notation

Symbols (Latin)

Symbol	Description	Unit
a_j	volumetric surface area	1/m
A	surface	m ²
A_H	parameter describing the temperature dependency of Henry's law constants	-
A_R	reactor cross sectional area	m ²
b	Parameter for Peng Robinson equation of state	m ³ /mol
B_H	parameter describing the temperature dependency of Henry's law constants	K
c_i	concentration	mol/m ³
c_i^*	concentration at gas/liquid equilibrium	mol/m ³
c_p	specific heat capacity at constant pressure	J/(kg·K)
C_H	parameter describing the temperature dependency of Henry's law constants	K ²
d	diameter	m
$D_{i,j}$	diffusion coefficient	m ² /s
E_A	activation energy of reaction	J/mol
g	gravitational constant on Earth	m/s ²
G	Gibbs free energy	J
$GHSV$	gas hourly space velocity	1/h
h_R	reactor height	m
$H_{i,px}$	molar fraction-based Henry law's constant	bar

$H_{i,pc}$	concentration-based Henry law's constant	bar·m ³ /mol
$H_{i,cc}$	dimensionless Henry law's constant	-
H ₂ /CO ₂	ratio between H ₂ and CO ₂ molar fraction	-
Δh_r^θ	specific reaction enthalpy at standard conditions	J/mol
$\Delta h_{i,ad}$	specific adsorption enthalpy	J/mol
k	reaction rate constant	mol/(kg·s·mol ^{0.5} ·m ^{-1.5})
$k_{i,j}$	mass-transfer coefficient	m/s
k_0	pre-exponential factor	mol/(kg·s·mol ^{0.5} ·m ^{-1.5})
$k_j a_i$	volumetric mass-transfer coefficient	1/s
K	Parameter to express the reaction rate limitation due to chemical equilibrium closeness	-
K_{eq}	equilibrium constant	-
K_i	Adsorption constant	m ³ /mol
L	length	m
m	mass	kg
M	molecular mass	kg/mol
n	amount of substance	mol
\dot{n}	molar flow	mol/s
N	number	-
p	absolute pressure	bar
p_{crit}	critical pressure	bar
p_i	partial pressure	bar
p_r	reduced pressure	-
p_v	vapor pressure of a liquid at gas/liquid equilibrium	bar
p_0	absolute pressure at standard conditions	bar
r	radius	m

r_i	catalyst mass-specific reaction rate	mol/(kg·s)
R	universal gas constant	J/(mol·K)
S_i	selectivity	-
s	specific entropy	J/(mol·K)
t	time	s
T	absolute temperature	K or °C
T_{crit}	critical temperature	K or °C
T_r	reduced temperature	-
\bar{T}_{SL}	mean slurry temperature	K or °C
u	superficial velocity	m/s
v	molar volume	m ³ /mol
V	volume	m ³
\dot{V}	volume flow	m ³ /s
w_j	mass fraction	-
x, y, z	space coordinates	m
x_i	liquid molar fraction	-
X_{CO_2}	CO ₂ conversion	-
y_i	gas molar fraction	-
Y_1	Effect of solids on gas holdup	-
Z	compressibility factor	-

Symbols (Greek)

Symbol	Description	Unit
α	heat transfer coefficient	W/(m ² ·K)
δ	relative error	-
δ_j	film thickness	m
Δv_i	diffusion volume	-
η_{cat}	catalyst efficiency	-
Γ	gas sparger influence on gas holdup	-
λ	thermal conductivity	W/(m·K)
ε	porosity or void fraction	-
μ	dynamic viscosity	Pa·s
ν_i	stoichiometric coefficient	-
ρ	density	kg/m ³
σ	surface tension	N/m
$\tau_{\text{mod,CO}_2}$	modified CO ₂ residence time	kg·s/mol
$\theta(T, \omega)$	acentric function for Peng Robinson equation of state	m ³ /mol
φ_S	volumetric solid fraction	-
ω	acentric factor for Peng Robinson equation of state	-

Dimensionless numbers

Symbol	Description	Definition	Meaning
Ar	Archimedes number	$\frac{(\rho - \rho_L) \cdot \rho_L \cdot g \cdot L^3}{\mu_L^2}$	$\frac{\text{Buoyancy force}}{\text{Viscous force}}$
Bo	Bodenstein number	$Pe'_{ax} \cdot \frac{L_R}{d_P}$	$\frac{\text{Convective mass transfer}}{\text{Axial diffusive mass transfer}}$
Da_I	Damköhler number I	$\frac{\rho_P \cdot r_i \cdot L}{u \cdot c_i}$	$\frac{\text{Reaction rate}}{\text{Advective mass transfer}}$
Da_{II}	Damköhler number II	$\frac{\rho_P \cdot r_i}{k_j a_i \cdot c_i}$ or $\frac{\rho_P \cdot r \cdot L^2}{D_{i,eff} \cdot c_i}$	$\frac{\text{Reaction rate}}{\text{Mass transfer}}$
Da_{III}	Damköhler number III (steady state)	$\frac{\rho_P \cdot r_i \cdot \Delta h_r \cdot L}{\rho \cdot c_p \cdot u \cdot T}$	$\frac{\text{Reaction heat release rate}}{\text{Advective heat transfer}}$
Da'_{III}	Damköhler number III (transient)	$\frac{\rho_P \cdot r_i \cdot \Delta h_r }{\rho \cdot c_p \cdot \frac{\Delta T}{\Delta t}}$	$\frac{\text{Reaction heat release rate}}{\text{Heat accumulation}}$
Fr	Froude number	$\frac{u}{\sqrt{g \cdot L}}$	$\frac{\text{Inertia force}}{\text{Gravity force}}$
Nu	Nusselt number	$\frac{\alpha \cdot L}{\lambda}$	$\frac{\text{Convective heat transfer}}{\text{Conductive heat transfer}}$
Pe	Peclet number (heat)	$\frac{\rho \cdot c_p \cdot u \cdot L}{\lambda} = Re \cdot Pr$	$\frac{\text{Advective heat transfer}}{\text{Conductive heat transfer}}$
Pe'	Peclet number (mass)	$\frac{u \cdot L}{D_{i,j}} = Re \cdot Sc$	$\frac{\text{Advective mass transfer}}{\text{Diffusive mass transfer}}$
Pr	Prandtl number	$\frac{\mu \cdot c_p}{\lambda}$	$\frac{\text{Diffusive momentum transfer}}{\text{Conductive heat transfer}}$
Re	Reynolds number	$\frac{\rho \cdot u \cdot L}{\mu}$	$\frac{\text{Inertia force}}{\text{Viscous force}}$
Re_P	Reynolds number (particle)	$\frac{\rho \cdot u_{P,set} \cdot d_P}{\mu}$	$\frac{\text{Particle inertia force}}{\text{Viscous force}}$
Sc	Schmidt number	$\frac{\mu}{D_{i,j} \cdot \rho}$	$\frac{\text{Diffusive momentum transfer}}{\text{Diffusive mass transfer}}$
Sh	Sherwood number	$\frac{k_{i,j} \cdot L}{D_{i,j}}$	$\frac{\text{Convective mass transfer}}{\text{Diffusive mass transfer}}$
St	Stanton number (steady state)	$\frac{\alpha}{\rho \cdot c_p \cdot u} = \frac{Nu}{Re \cdot Pr}$	$\frac{\text{Convective heat transfer}}{\text{Advective heat transfer}}$
St'	Stanton number (tran- sient)	$\frac{\alpha \cdot a_{cool} \cdot \Delta T_{cool}}{\rho \cdot c_p \cdot \frac{\Delta T}{\Delta t}}$	$\frac{\text{Convective heat transfer}}{\text{Heat accumulation}}$
Φ	Thiele modulus	$\frac{d_P}{2} \cdot \sqrt{\frac{r_i \cdot \rho_P}{D_{i,eff} \cdot c_i}}$	$\frac{\text{Reaction rate}}{\text{Diffusive mass transfer}}$

Abbreviations

Symbol	Description
ADM	axial dispersion model
CAPEX	capital expenditure
CFD	computational fluid dynamics
CNG	compressed natural gas
CSTR	continuous stirred-tank reactor
DBT	dibenzyltoluene
DFT	density functional theory
EU	European Union
FTS	Fischer-Tropsch synthesis
GC	gas chromatograph
LHHV	Langmuir-Hinshelwood-Hougen-Watson
LNG	liquefied natural gas
MASI	most abundant surface intermediates
MFC	mass flow controller
NIST	National Institute of Standards and Technology
ODE	ordinary differential equation
PDE	partial differential equation
PEM	polymer electrolyte membrane
PFR	plug flow reactor
PtG	Power-to-Gas
RDS	rate determining step
RWGS	reverse water-gas shift
SBCR	slurry bubble column reactor
SNG	synthetic natural gas
STP	standard Temperature and Pressure ($T = 273.15$ K, $p = 1.01315$ bar)
TBR	tube bundle reactor
TCD	thermal conductivity detector
TGA	thermogravimetric analysis
2PM	two-phase methanation
3PM	three-phase methanation
*	catalyst active site

Indices

Symbol	Description
ad	adsorption
ax	axial
bed	bed of catalyst
B	bubble
cal	calculated
cat	catalyst
cool	cooling
crit	critical
dry	dry gas
eff	effective
exp	experimental
G	gas
het	heterogeneous regime
hole	hole
<i>i</i>	index for gas species
in	inlet
<i>j</i>	index for phase
Kn	Knudsen
large	large bubbles
L	liquid
lit	literature
m	mass
max	maximum value
meth	CO ₂ methanation
mod	modified
molecule	molecule
n	molar
out	outlet
pore	pore
P	catalyst particle
r	reaction
R	reactor
set	settling
small	small bubbles
S	solid
SL	slurry
tube	reactor tube
tot	total
Tank	Tank
v	vapor
wall	reactor or tube wall
*	phase equilibrium

1 Introduction

With the COP21 Paris Agreement, the parties of the United Nations Framework Convention on Climate Change agreed on reducing greenhouse gas emissions in order to keep the increase in global average temperature well below 2 K compared to pre-industrial era [1]. One way to achieve this goal is to reduce the CO₂ emissions through a drastic increase of the share of renewable and environmentally friendly energy sources like wind and sunlight in our energy systems. Electrical energy can be easily used to power many applications in the mobility and heat sector. Nevertheless, wind and sunlight are intermittent and fluctuating contrary to fossil energy sources. Consequently, the increase of renewables in the electrical energy share may lead to mismatch between the demand and the production resulting in power grid instability. To assure a safety energy supply while increasing the share in renewable energies in the final energy consumption several measures must be applied: extension of the current power grid, development of smart grids and smart energy users, and coupling of the different energy sectors (power/heat/chemical energy carriers).

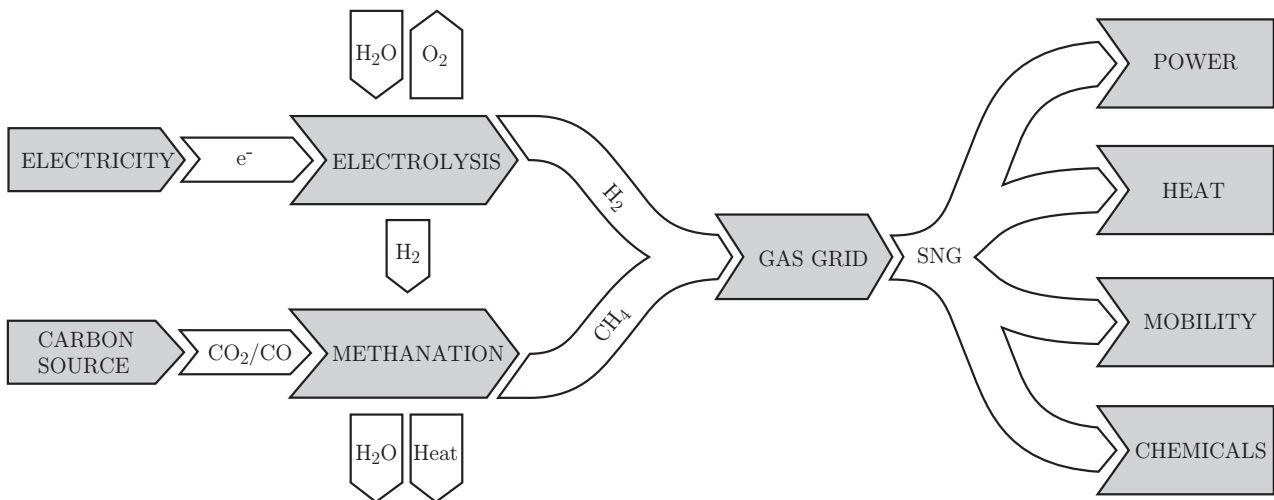


Figure 1.1: Flow diagram of the Power-to-Gas process.

The Power-to-Gas (PtG) process pictured in Figure 1.1 aims at transforming renewable electrical energy into chemical energy carriers with high energy density [2]. These chemical energy carriers can be stored over long periods of time and be transported over large distances coupled with low losses. The first PtG process step consists in transforming excess electricity into H₂ via water electrolysis. The resulting H₂ can be injected to some extent into the existing natural gas grid or be used as fuel for mobility. Nevertheless, H₂ storage capacity is rather limited and would not cover the European energy needs in case of absence or lack of wind and sunlight for several weeks. Instead of storing H₂, this energy carrier can react with CO or CO₂ into CH₄ via a catalytic methanation step. CH₄ is the main component of synthetic

natural gas (SNG), which can be injected into the natural gas grid and used for numerous applications [2–5]. The carbon source for CO and CO₂ can be biomass, an industrial process or even air.

As renewable energy sources are intermittent and fluctuating, the electrolysis step within the PtG process must be able to work under transient operating conditions. To minimize the size of a H₂ buffer between the electrolysis and methanation steps, the methanation reactor should be also operated under transient operating conditions. State-of-the-art catalytic methanation reactors are adiabatic fixed-bed reactors for CO methanation and tube bundle reactors (TBR) for CO₂ methanation [6]. Both reactor concepts have been developed for steady-state operation and can suffer from significant and undesired temperature changes during transient operation [7], e.g. formation of hot spots.

Recent investigations carried out during the PhD thesis of Manuel Götz [8] at Engler-Bunte-Institut, Fuel Technology of Karlsruhe Institute of Technology, showed promising results for transient catalytic CO and CO₂ methanation with a slurry bubble column reactor operated at pressures up to 20 bar and temperatures up to 320 °C. In this reactor, a Ni/Al₂O₃ catalyst was suspended in dibenzyltoluene and fluidized by the ascending gas phase. Though this reactor suffered from mass-transfer limitations, the high heat capacity of the slurry phase as well as the good reactor mixing allowed for very efficient heat removal and almost isothermal operating conditions.

In this work, further experimental investigations were carried out to get a better understanding of slurry bubble column reactors for transient CO₂ methanation. Based on own experimental data and data from the literature, a simulation tool for slurry bubble column reactor was developed. This tool was applied to simulate steady-state as well as transient CO₂ methanation slurry bubble column reactor operation. These simulation results were compared with simulations of a state-of-the-art fixed-bed methanation reactor to evaluate the potential of slurry bubble column reactor technology against current and mature CO₂ methanation reactor technology.

2 Literature review

This chapter reviews the available literature on catalytic CO₂ methanation, from fundamentals to CO₂ methanation reaction mechanism and methanation reactor concepts. This chapter deals also with slurry bubble column reactors addressing the topics of hydrodynamics as well as mass and heat transfers.

2.1 Catalytic methanation

Catalytic methanation has been extensively reviewed in literature. Kopyscinski et al. [9] focused on the historical and technical development of catalytic methanation reactors, while Gao et al. [10] focused on methanation catalyst development. An overall review on catalytic methanation has been recently carried out by Rönsch et al. [6] which addresses the abovementioned topics as well as modeling of catalytic methanation reactors.

2.1.1 Fundamentals and thermodynamics

The methanation of carbon dioxide is an exothermic reaction as defined in Eq. 2.1.



Thermodynamically low temperatures and high pressures favor methane production (see Figure 2.1). However, for technical systems, temperatures higher than 200 °C and catalysts promoting the reaction are required [6, 9].

2.1.2 Methanation catalyst

Typical heterogeneous catalysts used for methanation are metals of group VIII [6, 10, 11]. Mills and Steffgen classified the turnover frequency and methane selectivity of several active components as following [12]:

- Turnover frequency: Ru > Fe > Ni > Co > Mo;
- Selectivity to methane: Ni > Co > Fe > Ru.

Due to its good methanation activity, high methane selectivity and comparatively low price, nickel is the most commonly applied active metal for methanation applications [6, 10, 13]. The main drawbacks of Ni catalysts as compared to other metals of group VIII are the high

sensibility to sulfur components which deactivate Ni catalysts, as well as possible vapor/solid reactions which lead to nickel leaching out of the methanation reactor (see section 2.1.3).

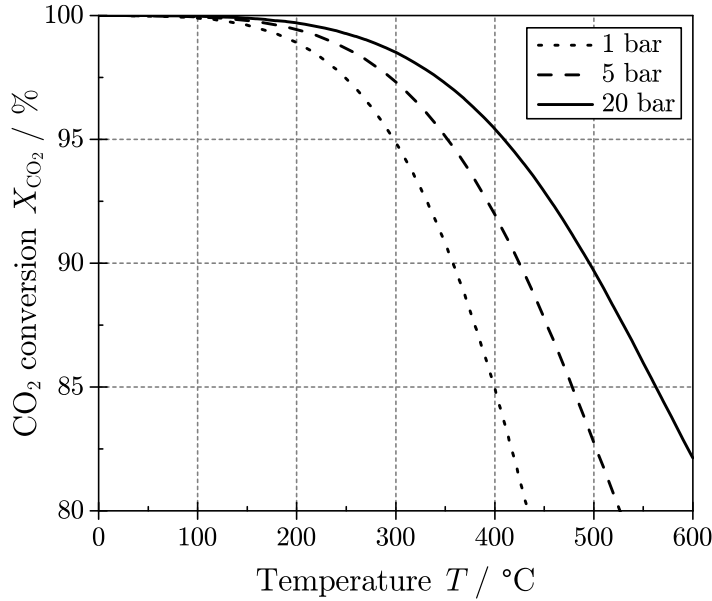


Figure 2.1: Influence of absolute pressure on the equilibrium conversion of CO₂ for a stoichiometric feed gas composition. The equilibrium constant K_{eq} is taken from

$$[14]: K_{\text{eq}} = \frac{p_{\text{H}_2\text{O}}^2 \cdot p_{\text{CH}_4}}{p_{\text{H}_2}^4 \cdot p_{\text{CO}_2}} \cdot p_0^2 = 135 \cdot T^{-3.998} \cdot \exp\left(\frac{158700}{RT}\right). \text{ Units are SI.}$$

Supports play an important role for heterogeneous catalysts. Indeed, they affect the metal-support interaction as well as the metal dispersion, influencing the catalyst activity, selectivity and stability [10]. Common supports for nickel catalysts are metal oxides showing large surface area, e.g. Al₂O₃ [15–31], SiO₂ [17–19, 25, 32–44], TiO₂ [18, 19, 25, 31, 45], ZrO₂ [15, 29, 31, 46–53] and CeO₂ [29, 54–60]. The effects of support nature (Al₂O₃, SiO₂ or TiO₂) on Ni-based catalysts were investigated under CO methanation conditions [18, 19]. It was found that catalyst activity is influenced by support nature. Reaction rates were ordered as following: Ni/TiO₂ > Ni/Al₂O₃ > Ni/SiO₂. The better activity of the Ni/TiO₂ catalyst was attributed to enhanced CO dissociation and carbon hydrogenation [19]. Next to supported catalysts, unsupported catalysts like Raney[®] nickel, which also show high surface area, can be used for methanation application [15, 61].

Promoters can also alter significantly the catalyst activity, selectivity and stability by changing the electron mobility on the catalyst surface or structure (pore geometry, metal dispersion, mechanical strength...) [6, 10]. For instance, at the right concentrations, MgO can mitigate carbon deposition and particle sintering of Ni/Al₂O₃ catalysts [20, 62–65], while an optimal La₂O₃ doping on Ni/Al₂O₃ was shown to increase the catalyst activity by increasing Ni dispersion and H₂ uptake [66]. A certain concentration of V₂O₃ was found to enhance the activity, the coke resistance and the thermal stability of a Ni/Al₂O₃ catalyst [67] and an optimal CeO₂ doping could improve the reducibility and the long-term stability of a Ni/Al₂O₃ catalyst [68]. For the above-mentioned experiments, improved catalyst activity, selectivity and stability were obtained for an optimal promoter concentration. At lower or higher promoter concentrations, these catalyst properties were less enhanced or even negatively impacted.

2.1.3 Deactivation of methanation catalyst

Catalyst deactivation is defined as the decrease in catalyst activity and/or selectivity over time [69]. The deactivation mechanisms of a nickel-based methanation catalyst can be classified into three different types: chemical, thermal and mechanical [69]. In Table 2.1 these mechanisms are listed and described shortly.

Table 2.1: Mechanisms of methanation catalyst deactivation [69].

Type	Mechanism	Reversible	Description
Chemical	Poisoning	At times	Strong chemisorption of species on catalytic active sites, thereby blocking sites for catalytic reaction.
	Vapor/solid reaction	At times	Reaction of fluid, support, or promoter with catalytic active sites producing inactive sites.
Thermal	Sintering	No	Thermal induced loss of catalytic surface area / active phase-support reactions reducing the number of active sites.
Mechanical	Fouling	Mostly	Physical deposition of gas or liquid species onto the catalyst surface and pores reducing the catalytic active sites.
	Attrition/crushing	No	Loss of catalytic active sites due to abrasion or loss of internal surface area due to mechanical-induced crushing of the catalyst particle.

Poisoning of nickel catalysts used in methanation mostly happens due to impurities in the synthesis gas, e.g. sulfur components like hydrogen sulfide. H_2S adsorbs and dissociates on the metal surface; the bond between adsorbed sulfur and catalyst surface is very stable which makes the reversible reaction difficult. Nickel catalysts are extremely sensitive towards sulfur poisoning: 1 - 100 ppb of H_2S at 400 °C and 1 bar may reduce catalytic activity by three to four orders of magnitude [69]. This phenomenon makes an efficient sulfur removal from the inlet gas stream inevitable. Other electronegative atoms like chlorine or phosphorus are also harmful for nickel catalyst, because they change the electron density on the catalyst surface. This lowers the adsorption rate, adsorption energy and saturation amount of CO and H_2 on Ni and decreases the catalyst activity [70].

Vapor/solid reactions can also deactivate Ni catalysts. Under methanation operating conditions nickel can react with carbon monoxide to form highly volatile nickel carbonyls $\text{Ni}(\text{CO})_4$. These carbonyls can be formed at low temperatures and high partial pressures of carbon monoxide. However, the formation of nickel carbonyl does not occur under CO_2 methanation conditions. Gaseous nickel carbonyls can be carried out of the reactor with the outlet gas stream resulting in nickel loss on the catalyst surface. Nickel carbonyls can also diffuse

on the catalyst surface and later decompose, which results in an increase in nickel particle size [71, 72]. Thereby the catalyst activity is also decreased. The movement of nickel atoms coupled with nickel carbonyl diffusion is similar to the sintering process but occurs at low temperatures.

Sintering is a thermal degradation process which is defined as the decrease in active catalyst surface area caused by crystallite growth. When exposed to high temperatures, atoms move and coalesce, which leads to formation of larger particles. This process leads to a decrease or even loss of catalyst active surface area [73]. Sintering is a strongly temperature dependent process and does not occur below the so-called Tamman temperature. The Tamman temperature of nickel is 590 °C, therefore no sintering is expected under three-phase methanation conditions ($T < 350$ °C).

Fouling is defined as the physical coverage of a surface with a deposit. Different carbon species can be responsible for the fouling of methanation catalysts. While carbon forms through disproportionation of carbon monoxide, coke is a product of decomposition and/or condensation of higher hydrocarbons [69]. Under CO methanation conditions, carbon monoxide irreversibly dissociates and adsorbs on the catalyst surface [69]. The adsorbed carbon can block the catalyst pores, encapsulate particles or even form carbon filaments with a nickel atom on top [73]. Carbon formation is a very common phenomenon for CO methanation. Nevertheless, it does not occur under CO₂ methanation operating conditions.

Attrition of catalyst due to abrasion (particle/particle or particle/reactor wall) is a common problem for fluidized-bed reactors and less importantly for slurry-bed reactors [69]. This phenomenon leads to catalyst mass loss.

Crushing of catalyst particle can result from thermal stress (fast catalyst heating or cooling) [69]. Under steady-state operations these situations do not appear. However, these situations can take place for PtG application which implies numerous startup and shutdown procedures as well as gas load variations [6].

2.1.4 CO₂ methanation mechanism on Ni catalyst

CO₂ methanation can be seen as the combination of reverse water-gas shift (RWGS) reaction (Eq. 2.2) followed by CO methanation (Eq. 2.3) [33, 35, 74–81].



Besides CH₄, higher hydrocarbons can be produced under methanation conditions via the Fischer-Tropsch reaction (Eq. 2.4).



During methanation of carbon monoxide, formation of elemental carbon is also possible. The dissociation of carbon monoxide leading to carbon formation is described by the Boudouard reaction (Eq. 2.5).



Although the catalytic CO_2 methanation seems to be a quite simple reaction, its mechanism is still unclear and under investigation. Two main mechanisms have been postulated so far.

The first mechanism implies a CO intermediate pathway where CO_2 is converted to CO via the RWGS. The subsequent reaction mechanism is identical to CO methanation. Hereby, the dissociation of adsorbed CO_2^* to CO^* is the rate determining step (RDS) of the reaction: $\text{CO}_2^* \xrightarrow{\text{RDS}} \text{CO}^* \rightarrow \text{CH}_4$ [33, 35, 74–82]. This mechanism (1) is represented in Figure 2.2. The second mechanism implies a direct methanation pathway without a CO intermediate but with formation of surface formate (COOH^*), this step being the RDS: $\text{CO}_2^* \xrightarrow{\text{RDS}} \text{COOH}^* \rightarrow \text{COH}^* \rightarrow \text{CH}_4$, see also (2) in Figure 2.2 [46, 56, 83–86].

The CO methanation mechanism is also unclear and often discussed in the literature. Again, two pathways were suggested. The first mechanism implies a carbon pathway where adsorbed CO^* dissociates to adsorbed carbon, whereby this dissociation is the RDS: $\text{CO}^* \xrightarrow{\text{RDS}} \text{C}^* \rightarrow \text{CH}_4$, see (3) in Figure 2.2 [87–93]. The second CO mechanism implies a hydrogen-assisted pathway without CO dissociation but with carbon hydroxyl (COH^*) formation. The formation of COH is the RDS: $\text{CO}^* \xrightarrow{\text{RDS}} \text{COH}^* \rightarrow \text{CH}_4$, see (4) in Figure 2.2 [94–98].

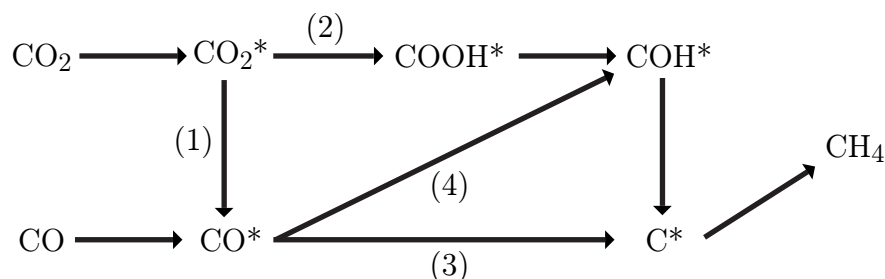


Figure 2.2: Scheme of the possible CO_2 and CO methanation reaction mechanisms.

In section 2.1.2, it was shown that catalyst composition (active metal content, support, promoter) can strongly influence the activity and selectivity of methanation catalysts. Hence, the methanation reaction mechanism probably differs from catalyst to catalyst. Further density functional theory (DFT) studies coupled with in-situ spectroscopy experiments should help in identifying a comprehensive methanation reaction mechanism [99–101]. However, this is out of the scope of this work. In this work, attention will be paid on the development of a kinetic rate equation for three-phase CO_2 methanation. The knowledge of the CO_2 methanation mechanism is helpful but not necessary to carry out this task.

2.1.5 CO₂ methanation kinetic rate equations for Ni catalysts

Since the discovery of the catalytic CO₂ methanation reaction on nickel, several kinetic rate equations were developed for nickel catalysts. These kinetic rate equations are listed in Table 2.2 and sorted by publication year.

The kinetic reaction rate equation derived by Xu and Froment [102] is often cited and used in the literature. Indeed, it is one of the few kinetic rate equations derived on a commercial Ni catalyst. In addition, it covers a wide and relevant range of CO₂ methanation operating conditions and predicts selectivity to CH₄ and CO. Nevertheless, this rate equation was primarily developed for steam reforming and not for CO₂ methanation purpose. The recent rate equation developed by Koschany et al. [27] covers a broader range of operating conditions and is especially designed for CO₂ methanation. However, it was developed on a self-made catalyst, which is less relevant for industrial CO₂ methanation applications.

The kinetic rate equations summarized in Table 2.2 can be classified into two groups: power law rate equations with [32, 37, 103–106] or without [107–109] adsorption term and Langmuir-Hinshelwood-Hougen-Watson (LHHV) rate equations based on "microkinetics" models [27, 35, 102, 110].

Power law rate expressions are often used for industrial applications, since they are quite simple and valid for the operating conditions at which they were measured (see Eq. 2.6):

$$r_{2\text{PM}} = \frac{1}{m_{\text{cat}}} \cdot \frac{dn_{\text{CO}_2}}{dt} \Big|_{\text{reaction}} = k \prod_i^i c_i^{\alpha_i}. \quad (2.6)$$

The reaction rate constant k is given by the Arrhenius equation, with E_A the activation energy of the reaction (Eq. 2.7). The activation energy of the CO₂ methanation is in the range of 60 to 100 kJ/mol.

$$k = k_0 \cdot \exp\left(-\frac{E_A}{RT}\right). \quad (2.7)$$

More complexed kinetic rate equations are the so-called Langmuir-Hinshelwood-Hougen-Watson (LHHV) kinetic rate equations, considering Langmuir adsorption isotherms. Typical LHHV kinetic rate equations are represented by Eq. 2.8:

$$r_{2\text{PM}} = \frac{k \prod_i^i c_i^{\alpha_i}}{\left(1 + \sum_i K_i c_i\right)^{\alpha_i}}. \quad (2.8)$$

In Eq. 2.8 K_i represents the equilibrium constant for the adsorption of the species i on the catalyst active sites and is described by Eq. 2.9.

$$K_i = K_{i,0} \cdot \exp\left(-\frac{\Delta h_{i,\text{ad}}}{RT}\right) \quad (2.9)$$

Table 2.2: Available CO₂ methanation kinetic rate equations over Ni catalysts sorted by publication year.

T °C	p_R bar	E_A kJ/mol	Rate equation	Ref.
260 - 400	1	n.a.	$r_{2PM} = \frac{k(p_{CO_2}p_{H_2}^2 - p_{CH_4}p_{H_2O}^2/K_{eq}p_{H_2}^2)}{(1+K_{H_2}p_{H_2}^{0.5}+K_{CO_2}p_{CO_2})^5}$	[103]
280 - 400	2 - 30	55 - 58	$r_{2PM} = \frac{kp_{CO_2}p_{H_2}^4}{(1+K_{H_2}p_{H_2}+K_{CO_2}p_{CO_2})^5}$	[32]
160 - 180	1	86	$r_{2PM} = kp_{CO_2}^{0.5}$	[107]
200 - 230	1	106	$r_{2PM} = \frac{kp_{CO_2}}{1+K_{CO_2}p_{CO_2}}$	[104]
227 - 327	0.04 - 0.16	94	$r_{2PM} = \frac{kp_{CO_2}^{0.5}p_{H_2}^{0.5}}{(1+K_1p_{CO_2}^{0.5}/p_{H_2}^{0.5}+K_2p_{CO_2}^{0.5}p_{H_2}^{0.5}+K_3p_{CO_2})^2}$	[35]
277 - 318	11 - 18	61	$r_{2PM} = \frac{kp_{CO_2}^{0.66}p_{H_2}^{0.21}}{1+K_{H_2}p_{H_2}+K_{CO_2}p_{CO_2}}$	[37]
250 - 350	1	n.a.	$r_{2PM} = \frac{kp_{H_2}p_{CO_2}^{0.33}}{1+K_{H_2}p_{H_2}+K_{CO_2}p_{CO_2}+K_{H_2O}p_{H_2O}}$	[105]
250	0.35 - 0.5	72.5	$r_{2PM} = \frac{kp_{H_2}^{0.5}p_{CO_2}^{0.33}}{(1+K_{H_2}p_{H_2}^{0.5}+K_{CO_2}p_{CO_2}^{0.5}+K_{H_2O}p_{H_2O})^2}$	[106]
360 - 520	1 - 65	90	$r_{2PM} = kp_{CO_2}^{0.7}$	[108]
300 - 400	3 - 10	240.1 (r_1) 243.9 (r_2)	$r_{2PM} = -\frac{r_1+r_2}{(1+K_{CO}p_{CO}+K_{H_2}p_{H_2}+K_{CH_4}p_{CH_4}+K_{H_2O}p_{H_2O}/p_{H_2})^2}$ with $r_1 = k_1/p_{H_2}^{2.5} (p_{CH_4}p_{H_2O} - p_{H_2}^3p_{CO}/K_1)$ and $r_2 = k_2/p_{H_2}^{3.5} (p_{CH_4}p_{H_2O}^2 - p_{H_2}^4p_{CO_2}/K_2)$	[102]
225 - 270	1	78.7	$r_{2PM} = \frac{kp_{CO_2}p_{H_2}^{0.5}}{p_{H_2}^{0.5}+K_{CO_2}p_{CO_2}}$	[111]
220 - 300	8	84	$r_{2PM} = kp_{CO_2}^{0.47}p_{H_2}^{0.54} \left(1 - \frac{p_{CH_4}p_{H_2O}^2}{p_{H_2}^4p_{CO_2}K_{eq}}\right)$	[109]
180 - 340	1 - 15	77.5	$r_{2PM} = \frac{kp_{H_2}^{0.5}p_{CO_2}^{0.5} \left(1 - \frac{p_{CH_4}p_{H_2O}^2}{p_{H_2}^4p_{CO_2}K_{eq}}\right)}{(1+K_{OH}p_{H_2O}/p_{H_2}^{0.5}+K_{H_2}p_{H_2}^{0.5}+K_{mix}p_{CO_2}^{0.5})^2}$	[27]
180 - 210	10 - 20	95	$r_{2PM} = \frac{kp_{H_2}^{0.5}p_{CO_2}^{0.5}}{(1+K_1p_{CO_2}^{0.5}/p_{H_2}^{0.5}+K_2p_{CO_2}^{0.5}p_{H_2}^{0.5}+K_3p_{H_2O})^2}$	[110, 112]

2.1.6 Methanation reactor concepts

As methanation is a highly exothermic reaction, the main issue related to the design of a methanation reactor is temperature management. The various reactor concepts that were developed for technical methanation applications, namely adiabatic or cooled fixed-bed reactor, structured reactor, fluidized-bed reactor, and slurry bubble column reactor, offer different solutions to tackle this issue. An overview of these concepts is given below. A detailed review dealing with the historical development of technical methanation reactors can be found elsewhere [6, 9, 113].

In **fixed-bed reactors**, catalyst pellets ($2 < d_p < 7$ mm) are disposed in an empty tube forming a catalytic bed material. Methanation fixed-bed reactors are either employed as adiabatic or cooled fixed-bed reactors. For **adiabatic fixed-bed reactors**, the temperature control is achieved by using a series of adiabatic reactors, typically 2 to 5, with intercooling [114–118] and sometimes gas recirculation [114–117]. Due to the adiabatic mode of operation, the catalyst must be able to withstand a broad temperature range (250 - 700 °C). Hence, the main challenges related to the methanation catalyst are cracking and sintering (see section 2.1.3). Alternatively, **cooled fixed-bed reactors** can be applied for methanation [4, 119, 120]. Due to the cooling, the methanation plant is simpler and contains less reactors. However, cooled fixed-bed reactors have a more complex design and therefore show higher capital expenditure than adiabatic systems. The main drawback of fixed-bed reactors is related to poor heat transfer which leads to formation of temperature hot spot. In addition, high pressure drop related to packed-bed density and gas velocity characterizes fixed-bed reactors.

Structured reactors such as monolithic reactors were developed to tackle the drawbacks of fixed-bed reactors. These reactors consist of well-defined interconnected or separated channels. The catalytic material ($d_p < 100$ μm) is deposited on the channel wall or the channel wall itself is a porous catalytic material. When the channels are made of metal, e.g. steel or aluminum, structured reactors can feature better heat transport capacities and lower pressure drop than fixed-bed reactors [121, 122]. Depending on the metallic material, the radial heat transport can be improved by two to three orders of magnitude [123]. Micro-structured reactors represent a further development of structured reactors and are characterized by a high surface-to-volume ratio resulting in more efficient heat transfer [124–127]. Drawbacks of structured reactors are the more complicated catalyst deposition on the channel structure, as well as the difficulty of replacing the deactivated catalyst: once the catalyst has been deactivated, the whole reactor has to be equipped with a new catalytic channel structure. Another development of structured reactors is the sorption enhanced methanation reactor concept. The water produced by the methanation reaction is removed from the gas phase by the catalyst carrier showing adsorbent functionality, thereby, thermodynamic limitation is reduced. For the subsequent water removal, temperature and/or pressure swing can be applied [128, 129].

In **fluidized-bed reactors**, catalyst particles ($50 < d_p < 200$ μm) are fluidized by the gas stream introduced at the bottom of the reactor [9]. The intensive solids mixing within a fluidized-bed reactor combined with the high heat capacity of solid materials as compared to gas phase result in almost isothermal conditions and high heat transfer between bed material and immersed cooling surfaces [130]. Offering more efficient heat removal is the major advan-

tage of this reactor concept, which allows for using one single reactor with a rather simplified design [131, 132]. Nevertheless, attrition processes take place between catalyst particles as well as between catalyst particles and reactor wall. Eventually, very fine catalyst particles are elutriated from the reactor resulting in catalytic mass loss [69].

Other methanation reactor concepts are based on **slurry bubble column reactors** [8, 133–135]. The slurry bubble column reactor developed during the PhD thesis of Manuel Götz [8] carried out at Engler-Bunte-Institut, Fuel Technology, of the Karlsruhe Institute of Technology, implies a commercial Ni/Al₂O₃ catalyst suspended in dibenzyltoluene (trade name MARLOTHERM[®] SH from *Sasol*). A detailed description of slurry bubble column reactors is given in the next section.

2.2 Slurry bubble column reactors

Slurry bubble column reactors (SBCR) are very adaptable gas/liquid/solid contacting devices [136]. The first and simplest form of SBCR is illustrated in Figure 2.3. It consists in a vertical tube with no internals. The gas is fed at the bottom through a gas sparger and the reactor is filled with a mixture of pulverized solid catalysts ($d_p < 500 \mu\text{m}$) and liquid called slurry. The slurry phase can be led to the reactor co-currently or counter-currently or even operated as a batch (no external circulation) [136, 137]. However, this simple SBCR form is rarely used in practice. Instead, a great number of modifications, e.g. internals like sieve trays, packings, shafts or static mixers are implemented to influence the hydrodynamics of SBCR [136].

Due to the high heat capacity of the liquid phase and the good mixing of the slurry phase, excellent reactor heat management can be achieved in SBCR. Consequently, SBCR are usually implemented to control the temperature of highly exothermic reactions like Fischer-Tropsch synthesis, methanol synthesis as well as other hydrogenation and oxidation reactions [137, 139–143]. Furthermore, de Swart et al. [144] showed that transient SBCR operations are possible for Fischer-Tropsch synthesis, as the excellent SBCR heat management prevent thermal runaway even under transient conditions. Heat removal from SBCR can be achieved e.g. with tube bundles placed within the slurry phase. Up to 30 m²/m³ of specific heat-transfer area can be installed in a SBCR [136].

The main drawback of SBCR as compared to two-phase reactors is related to the additional gas/liquid mass transfer limiting the effective reaction rate [136, 137]. Besides, though the construction of SBCR itself is relatively simple, the design of SBCR is highly complex and requires detailed knowledge of reactor hydrodynamics as well as mass and heat transfer. These topics are discussed in the following sections.

2.2.1 Hydrodynamics of slurry bubble column reactors

Hydrodynamics of SBCR can be characterized by flow regimes, minimum suspension conditions for solid particles, backmixing, and gas holdup.

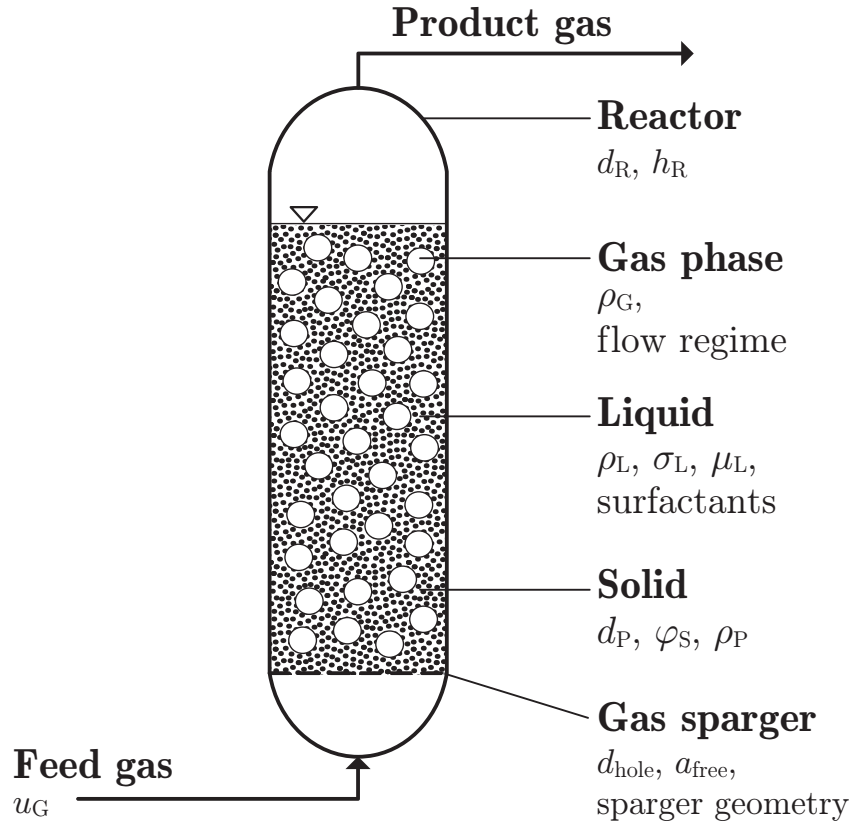


Figure 2.3: Parameters influencing the design of slurry bubble column reactor, adapted from [138] (liquid phase as batch; wettable particles).

2.2.1.1 Flow regimes

Three flow regimes can be distinguished in SBCR as illustrated in Figure 2.4. At low superficial gas velocities u_G (see Eq. 2.10) - later referred to as gas velocity - the **homogeneous regime** can be observed. This regime is characterized by a narrow bubble size distribution and a gas holdup which increases linearly with increasing u_G (no bubble coalescence). In the pseudo-homogeneous regime, the gas holdup increases linearly with increasing u_G , but a broader bubble size distribution is observed [137, 139].

$$u_G = \frac{\dot{V}_G}{A_R} \quad (2.10)$$

By increasing the gas velocity over the transition gas velocity $u_{G,\text{trans}}$, the system changes from the homogeneous to the **heterogeneous regime** where small and large bubbles coexist. The broader bubble size distribution results from bubble coalescence and breakup processes. In the heterogeneous regime, large bubbles rise in the center of the column with high velocities. The rising of large bubbles leads to a circulating flow of the liquid phase: the liquid ascends in the center of the column and descends between the column center and wall. This circulating flow is so vigorous that small bubbles follow the movement of the liquid phase [136]. Furthermore, the gas holdup no longer increases linearly with increasing u_G but with an exponent comprised between 0.4 and 0.7 depending on the reacting gas/liquid/solid system [136].

For SBCR with small reactor diameter, the **slug flow regime** takes place at elevated gas

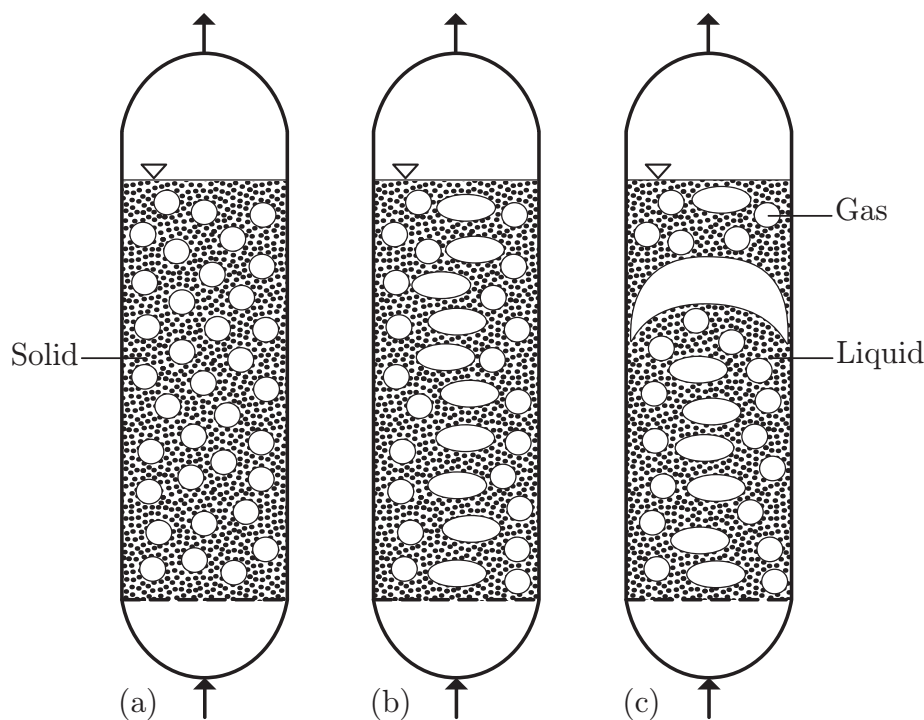


Figure 2.4: Flow regimes which can be observed in a slurry bubble column reactor: homogeneous (a), heterogeneous (b) and slug flow (c) regimes.

velocities: large bubbles are formed and rise with a plug flow behavior. These large bubbles can be almost as large as the reactor diameter and have a characteristic slug shape [136]. In this regime, the liquid ascends with the large bubbles and descends along the reactor wall in the cross section area which is not occupied by the gas bubbles.

SBCR are usually operated in the homogeneous or the heterogeneous regime. The slug flow regime is undesired, as a poor mass transfer between gas and liquid phase is achieved. The homogeneous regime is characterized by low gas velocity ($u_G < 0.05$ m/s) and consequently low backmixing as well as low gas holdup and mass transfer (details related to these parameters are given in the next sections). On the contrary, the heterogeneous regime is characterized by higher gas velocity and therefore higher backmixing as well as higher gas holdup and mass transfer as compared to the homogeneous regime. Heterogeneous regime conditions are relevant for three-phase CO_2 methanation performed in a SBCR, if the enhanced mass transfer can make up for the decrease in effective gas concentration as a result of the increased backmixing.

2.2.1.2 Minimum suspension conditions for solid catalysts

For an optimal utilization of the solid catalyst present in a SBCR, solid particles must be completely suspended in the liquid phase [137]. For complete solid suspension the drag force applied by the liquid phase on the solid particles must be high enough to compensate for the solid settling force. This is illustrated in Eq. 2.11, which describes the minimum gas velocity for complete solid suspension in the liquid phase $u_{G,\min}$. In Eq. 2.11 it is assumed that the gas is evenly sparged through a flat plate that extends over the whole column bottom [145].

$$u_{G,\min} = 0.8 \cdot u_{P,\text{set}} \cdot \left(\frac{\rho_P - \rho_L}{\rho_L} \right)^{0.6} \cdot \varphi_S^{0.146} \cdot \left(\frac{\sqrt{g \cdot d_R}}{u_{P,\text{set}}} \right)^{0.24} \cdot \left(1 + 807 \cdot \left(\frac{g \cdot \mu_L^4}{\rho_L \cdot \sigma_L} \right)^{0.578} \right) \quad (2.11)$$

With φ_S the volumetric solid fraction in a SBCR (see Eq. 2.12).

$$\varphi_S = \frac{V_S}{V_L + V_S} \quad (2.12)$$

Eq. 2.11 requires the knowledge of the terminal velocity of a single catalyst particle $u_{P,\text{set}}$. $u_{P,\text{set}}$ can be calculated with the particle Reynolds number Re_P . Under three-phase methanation conditions, the drag force is not described by Stoke's drag (dilute suspension) or by Newtonian drag (high fluid velocity) but with the transitional drag ($0.2 < Re_P < 1000$). For transitional drag, Re_P can be estimated with the correlation described in Eq. 2.13 [146].

$$Re_P = 18 \left[\sqrt{1 + \frac{1}{9} \sqrt{Ar}} - 1 \right]^2 \quad (2.13)$$

Considering the properties of the three-phase methanation system investigated in this work, the minimum gas velocity for complete catalyst suspension calculated with Eq. 2.11 is in the range 0.0006 - 0.0021 m/s (see calculation in the Appendix F).

2.2.1.3 Backmixing

Backmixing in SBCR has usually a negative influence on the effective reaction rate, as the effective gas concentration in the slurry phase is reduced [147]. The extent of backmixing in each phase (gas, liquid, and solid) is generally different and must be considered separately [137]. Backmixing in the liquid phase is a function of reactor diameter d_R as well as gas velocity u_G : in bubble columns with a small diameter, the liquid phase shows almost no backmixing, while large units behave more like stirred tanks [136, 142].

Gas phase backmixing depends on the formation of large and small bubbles [136]. In the homogeneous regime (only small bubbles), the gas phase flow is usually assumed as a plug flow. In the heterogeneous regime, the large gas bubbles rise in the center of the column, while the small gas bubbles follow the liquid phase, which ascends in the center of the reactor and descends along the reactor wall. Consequently, the large gas bubble flow is usually modeled as plug flow, while the backmixing of small gas bubbles is assumed to be identical to the liquid phase [136, 137].

Axial dispersion models characterize backmixing with an integral parameter called axial dispersion coefficient. Numerous authors [148–155] studied the axial dispersion of the liquid phase within a bubble column reactor and proposed correlations to describe the axial dispersion coefficient of the liquid phase $D_{L,\text{ax}}$. Unfortunately, these correlations were developed for two-phase systems (no solid) and mostly with air-water systems. Despite the absence of a relevant correlation for $D_{L,\text{ax}}$ in SBCR, the correlation developed by Deckwer et al. [155] (see Eq.

2.14) is usually applied to describe axial liquid dispersion in SBCR, e.g. for Fischer-Tropsch synthesis [144, 156].

$$D_{L,ax} = 0.678 \cdot d_R^{1.4} \cdot u_G^{0.3} \quad (2.14)$$

2.2.1.4 Gas holdup

Gas holdup ε_G in a SBCR is defined as the ratio between the volume of the gas phase and the volume of the three phases as expressed in Eq. 2.15.

$$\varepsilon_G = \frac{V_G}{V_G + V_L + V_S} \quad (2.15)$$

Knowledge of the gas holdup is very important for the design of a SBCR, as it represents the gas inventory within the reactor. In addition, gas holdup knowledge is usually required for the prediction of gas/liquid mass transfer within SBCR (see section 2.2.2). Unfortunately, the prediction of gas holdup is highly complex because ε_G depends on many parameters like reactor geometry (d_R, h_R), gas sparger geometry, gas phase properties (ρ_G, u_G), liquid phase properties (ρ_L, σ_L, μ_L , surfactants), solid phase properties (d_P, ρ_P, φ_S) as well as flow regime.

Gas holdup increases with increasing gas density and velocity, while gas holdup decreases with increasing liquid viscosity, surface tension, and velocity as well as with increasing solid density, concentration, and diameter (when wettable particles are considered). The column diameter d_R and the reactor height to diameter ratio h_R/d_R have no effect on ε_G for $d_R > 0.15$ m and $h_R/d_R > 6$, respectively [142].

At lot of correlations were developed to predict the gas holdup in bubble columns [157–175]. However, only few correlations were derived for slurry bubble column reactors (i.e. with solids) operated at high temperatures and pressures relevant for three-phase methanation [160, 168, 171, 174, 175]. In the following, attention is paid to the correlation developed by Morsi's research group [171], as it is the only available correlation that covers the operating conditions of the three-phase methanation (see Table G.1 in the Appendix).

Behkish et al. [171] developed a gas holdup correlation (see Eq. 2.16, parameter units are SI) which takes into account material properties, reactor dimensions as well as sparger geometry. They did not make a distinction between regimes: the correlation is meant to be valid for both homogeneous and heterogeneous regimes.

$$\varepsilon'_G = 4.94 \cdot 10^{-3} \cdot \left(\frac{\rho_L^{0.415} \cdot \rho_G^{0.177}}{\mu_L^{0.174} \cdot \sigma_L^{0.27}} \right) \cdot u_G^{0.553} \cdot \left(\frac{p}{p - p_v} \right)^{0.203} \cdot \Gamma^{0.053} \left(\frac{d_R}{1 + d_R} \right)^{-0.117} \cdot e^{Y_1} \quad (2.16)$$

Behkish et al. [171] used a different definition for the gas holdup ε'_G described as ratio between the volume of the gas phase divided by the volume of both liquid and solid phases (see Eq. 2.17). Eq. 2.18 can be applied to express the usual gas holdup ε_G as function of ε'_G .

$$\varepsilon'_G = \frac{V_G}{V_L + V_S} \quad (2.17)$$

$$\varepsilon_G = \frac{V_G}{V_G + V_L + V_S} = \frac{\varepsilon'_G}{1 + \varepsilon'_G} \quad (2.18)$$

The term Γ in Eq. 2.16 describes the influence of the gas sparger on ε'_G , while the exponent Y_1 takes into account the effect of solids on ε'_G . For heterogeneous regime conditions, the correlation can differentiate between the gas holdup of large bubbles (Eq. 2.19) and small bubbles (Eq. 2.20) using the factor F_{het} . The definitions of Γ , Y_1 , and F_{het} are given in the Appendix G.

$$\varepsilon'_{G,\text{large}} = \varepsilon_G'^{0.84} \cdot F_{\text{het}} \quad (2.19)$$

$$\varepsilon'_{G,\text{small}} = \varepsilon'_G - \varepsilon'_{G,\text{large}} \quad (2.20)$$

2.2.2 Mass transfer in slurry bubble column reactors

The film model is often used to provide a graphic description of mass transfer within SBCR. In this model, a phase is divided between a bulk and a film of thickness δ_j at the interphase. Mass transfer limitation is only located in the film. Figure 2.5 shows the evolution of educt gas concentration along the three phases of a SBCR.

The profile pictured in Figure 2.5 is described by the following steps:

1. Mass transfer from the gas bulk to the gas/liquid interphase: $\frac{1}{V} \frac{\partial n_i}{\partial t} = k_G a_i \cdot (c_{i,G} - c_{i,G}^*)$
2. Gas dissolution in the liquid film assumed at equilibrium: $c_{i,G}^* = H_{i,cc} \cdot c_{i,L}^*$
3. Mass transfer from the gas/liquid interphase to the liquid bulk:
 $\frac{1}{V} \frac{\partial n_i}{\partial t} = k_L a_i \cdot (c_{i,L}^* - c_{i,L})$
4. Mass transfer within the liquid bulk
5. Mass transfer from the liquid bulk to the liquid/solid interphase:
 $\frac{1}{V} \frac{\partial n_i}{\partial t} = k_S a_i \cdot (c_{i,L} - c_{i,S}^*)$
6. Mass transfer within the catalyst pores $\frac{1}{V} \frac{\partial n_i}{\partial t} = D_{i,\text{eff}} \cdot \left(\frac{2}{r} \cdot \frac{\partial c_{i,S}^*}{\partial r} + \frac{\partial^2 c_{i,S}^*}{\partial r^2} \right)$
7. Adsorption and chemical reaction: $\frac{1}{V} \frac{\partial n_i}{\partial t} = k \cdot \eta_{\text{cat}} \prod c_{i,S}^{\alpha_i}$

For gas products the mass transfer is reversed: it begins in the catalyst pores and goes through the same aforementioned processes to the gas phase.

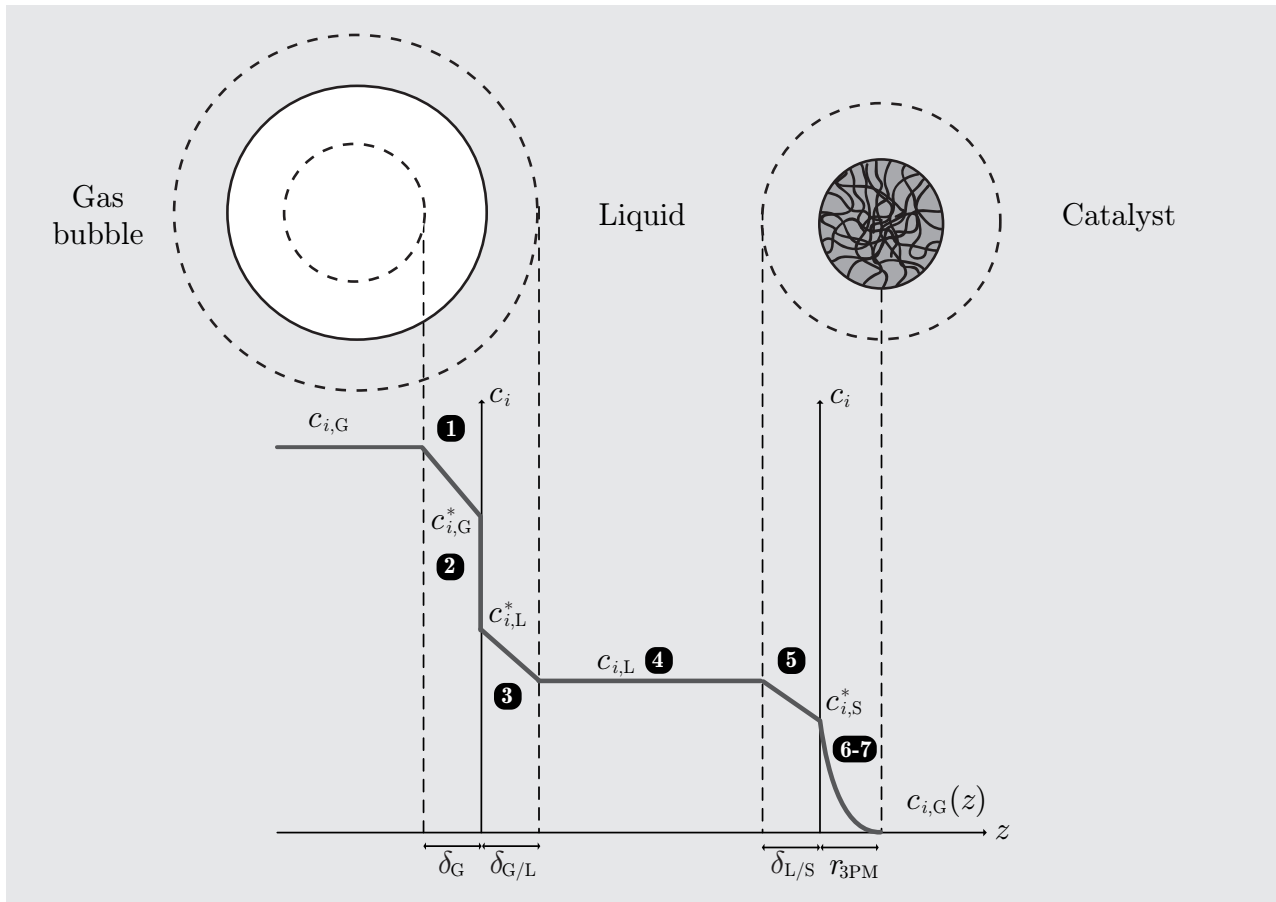


Figure 2.5: Concentration profile of an educt gas species along the three phases of a slurry bubble column reactor (film model).

Not all of these steps are relevant to describe the effective reaction rate within a SBCR (see calculation in Appendix I). The mass transfer from the gas bulk to the gas/liquid interphase (step 1) is not a limiting step, as long as educt gases are not too diluted with another gas species (gas product or liquid phase vapor). The gas/liquid equilibrium (step 2) is also not limiting, as the gas/liquid film thickness is very small. Due to bubble rising, effective mixing in the liquid phase is obtained. As a consequence, mass transfer within the liquid bulk (step 4) is fast and not limiting the effective reaction rate. Additionally, the mass transfer from the liquid bulk to the liquid-solid interphase (step 5) can be neglected; as the catalyst diameter used in a SBCR for three-phase methanation is small ($d_p \leq 100 \mu\text{m}$), the volumetric interphase area between liquid and solid $a_{L/S}$ and the corresponding mass transfer are high. Furthermore, gas diffusion within catalyst pores (step 6) is faster than the chemical reaction rate.

Thus, the two remaining steps relevant for the description of the effective reaction rate are the mass transfer from the gas/liquid interphase to the liquid bulk (step 3) and the chemical reaction (step 7). In the following paragraphs, more details are given on the volumetric liquid-side mass-transfer coefficient, $k_L a_i$. The description of the chemical reaction kinetics of the three-phase CO_2 methanation is one of the main topics of this thesis and is treated in chapters 5 and 6.

The volumetric liquid-side mass-transfer coefficient $k_L a_i$ is the product of the liquid-phase mass-transfer coefficient $k_{L,i}$ and the volumetric gas/liquid interphase area $a_{G/L}$, see Eq 2.21.

Like gas holdup, $k_L a_i$ is a function of the gas velocity, gas sparger geometry and gas/liquid/-solid system [136, 176]. A great number of $k_L a_i$ correlations are available in the literature [160, 165, 166, 169, 171, 174, 177–187]. Most of them consider the validity of the penetration theory for mass transfer, i.e. a proportionality $k_L a_i \sim D_{i,L}^{0.5}$. In addition, $k_L a_i$ correlations are usually proportional to the gas holdup ε_G .

$$a_{G/L} = \frac{A_{G/L}}{V_R} \quad (2.21)$$

In this work the correlation developed by Lemoine et al. [186] was used (see Eq. 2.22, parameter units are SI), as it is the only available correlation that covers the three-phase methanation operating conditions (see Table H.1 in the Appendix). This correlation requires the knowledge of gas holdup ε_G , bubble diameter d_B (see Eq. H.1 and H.3 in the Appendix) as well as gas sparger influence represented by Γ (Eq. G.1 in the Appendix).

$$k_L a_i = 6.14 \cdot 10^4 \cdot \frac{\rho_L^{0.26} \cdot \mu_L^{0.12} \cdot \varepsilon_G^{1.21} \cdot D_{i,L}^{0.5}}{\sigma_L^{0.12} \cdot \rho_G^{0.06} \cdot u_G^{0.12} \cdot d_B^{0.05} \cdot T^{0.68}} \cdot \Gamma^{0.11} \cdot \left(\frac{d_R}{1 + d_R} \right)^{0.4} \quad (2.22)$$

2.2.3 Heat transfer in slurry bubble column reactors

One of the main advantages of SBCR is the effective heat removal and the resulting isothermal reactor temperature profile. Heat transfer within SBCR depends on slurry phase properties but also on gas velocity (see Eq. 2.24). Very similar correlations were developed for the estimation of heat transfer coefficient α within SBCR [188–203]. In this work the correlation proposed by Deckwer [189] and described in Eq. 2.23 was used, as the correlation validity range covers the three-phase methanation operating conditions. This correlation is also often applied in the literature [144, 156].

$$St = 0.1 \cdot (Re \cdot Fr \cdot Pr^2)^{-1/4} \quad (2.23)$$

After simplification Eq. 2.23 can be rewritten to obtain the heat transfer coefficient between slurry phase and internal heat transfer area α (see Eq. 2.24, units are SI).

$$\alpha = 0.1 \cdot \left[c_{p,SL} \cdot \rho_{SL}^{3/2} \cdot \lambda_{SL} \left(\frac{u_G \cdot g}{\mu_{SL}} \right)^{1/2} \right]^{1/2} \quad (2.24)$$

Slurry heat capacity (Eq. B.15), density (Eq. B.13), thermal conductivity (Eq. B.16), and viscosity (Eq. B.14) correlations can be found in the Appendix B.2.

3 Objective and approach

The objective of this PhD thesis was to understand and predict the behavior of a SBCR operated under transient CO₂ methanation condition. For this purpose, a SBCR simulation tool based on detailed experimental and literature data was developed. It was used to design a SBCR for PtG application using a biogas as carbon source and H₂ from a PEM electrolyzer. Based on the literature review performed in chapter 2, following information had to be known to build a SBCR simulation tool: reactor hydrodynamics, gas/liquid mass transfer, heat transfer, and chemical reaction rate.

Hydrodynamic parameters of special interest were the gas holdup ε_G , which represents the gas inventory in a SBCR, and the axial dispersion coefficients in the gas phase and liquid phase, $D_{G,ax}$ and $D_{L,ax}$, respectively. Axial dispersion coefficients are integral parameters describing the backmixing of their respective phase inside the reactor. Furthermore, two parameters were required for the description of gas/liquid mass transfer within a SBCR: the volumetric gas/liquid mass-transfer coefficient $k_L a_i$, and the Henry's law constant $H_{i,cc}$ for each of the gas species involved in CO₂ methanation. $k_L a_i$ characterizes mass-transfer rate, while $H_{i,cc}$ describes gas solubility in the slurry phase. Heat transfer between the slurry phase and the heat-transfer area was described by the heat transfer coefficient α . Finally, the chemical reaction rate was characterized by a kinetic rate equation r_{3PM} .

In the PhD thesis of Götzt [8] carried out at Engler-Bunte-Institut Fuel Technology, a total of five liquid phases were tested as solvent for three-phase CO₂ methanation. The liquid dibenzyltoluene (DBT), trade name MARLOTHERM[®] SH from *Sasol*, was found to be the most adequate solvent, as this liquid showed high temperature stability up to 350 °C and acceptable hydrodynamic properties. Furthermore, Götzt et al. had already investigated the solubility of CO₂, CO and H₂ in DBT at temperatures involved in CO₂ methanation [204] and developed a gas holdup correlation for a SBCR operated in the homogeneous regime, and at elevated pressures and temperatures relevant for methanation [175]. However, the rest of the above-mentioned key design parameters were missing.

The approach of this PhD thesis is shown in Figure 3.1. In this work, the experimental work focused on the determination of the CO₂ methanation product solubilities in dibenzyltoluene (chapter 4), as well as on the determination of a kinetic rate equation describing the three-phase CO₂ methanation reaction kinetics (chapter 5 and 6). Hereby, special attention was paid on the understanding of the liquid phase influence on the catalytic CO₂ methanation. First, a commercial catalyst was chosen after testing several commercially available catalysts for three-phase CO₂ methanation (chapter 5). Then, the CO₂ methanation reaction rate was investigated with several suspension liquids (chapter 5), as well as in absence of liquid (chapter 6). Based on these experiments, the impact of a liquid phase on the CO₂ methanation reaction kinetics was clarified. Furthermore, a kinetic rate equation describing the kinetics of

the three-phase and two-phase CO₂ methanation was derived from these experiments.

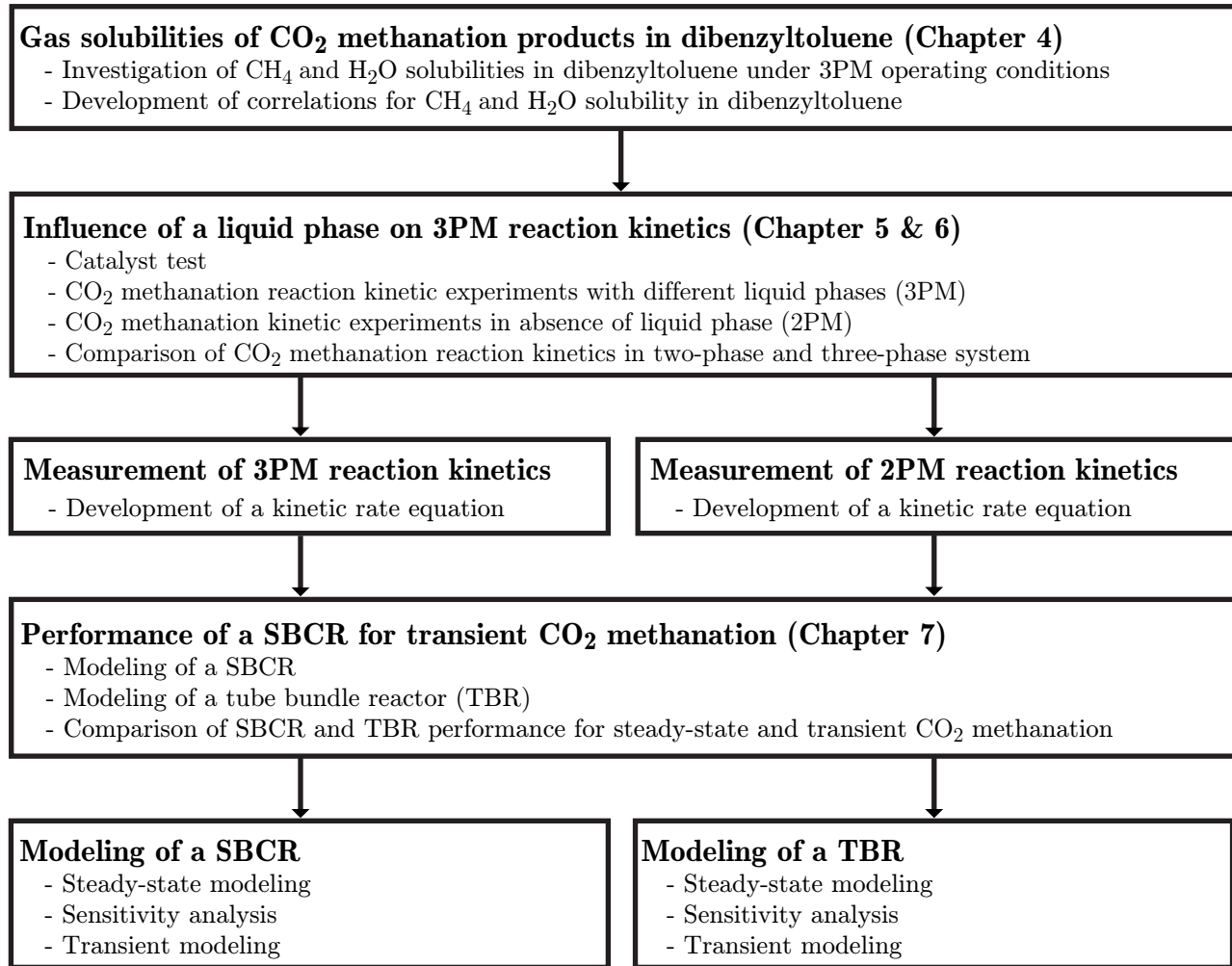


Figure 3.1: Scheme of the PhD thesis approach and its division in chapters.

Finally, a transient modeling of a catalytic CO₂ methanation SBCR was carried out based on experimental data gathered in chapters 4 and 5, as well as on literature data related to hydrodynamics and mass and heat transfer within SBCR. Next to this simulation, a transient modeling of a tube bundle reactor (TBR), i.e. the type of CO₂ methanation reactor installed in the benchmark PtG facility in Werlte (Germany) [205], was performed. To conclude, results from steady-state and transient SBCR and TBR simulations were compared to assess the performance of a SBCR for catalytic CO₂ methanation (chapter 7).

4 Gas solubilities of CO₂ methanation products in dibenzyltoluene

In the PhD thesis of Götzt [8], a total of five liquid phases were tested as solvent for three-phase CO₂ methanation. The liquid dibenzyltoluene (DBT), was found to be the most adequate solvent. Indeed, this liquid showed high temperature stability up to 350 °C and acceptable hydrodynamic properties (see section A.2 in the Appendix) [204].

In chapter 2 it was shown that gas components involved in a SBCR for CO₂ methanation, i.e. CO₂, H₂, H₂O, and CH₄, must dissolve into the liquid phase in order to react at the surface of the catalyst. Next to methanation gas species, Ar and N₂ were used as inert gases in three-phase methanation experiments to calculate mass balance as well as CO₂ conversion (see chapter 5). Accordingly it was necessary to understand the mechanisms determining the solubility of these gas species in DBT before starting three-phase CO₂ methanation kinetic experiments.

Götzt et al. [204] investigated the solubility of CO₂, CO and H₂ in DBT at temperatures relevant for CO₂ methanation, i.e. 200 to 300 °C. However, experimental solubility data for CH₄ and H₂O in DBT were missing. That is the reason why this chapter deals with the determination of these gas solubilities at temperatures relevant for CO₂ methanation. Next to CH₄ and H₂O, the solubility of Ar in DBT was also investigated. However, the corresponding experimental results are shown in the Appendix J.3, as these data are not directly relevant to understand the CO₂ methanation reaction kinetics in a three-phase system.

Gas dissolution is achieved when the chemical potential of the gas phase equals the chemical potential of the gas species dissolved in a solvent as shown in Eq. 4.1.

$$\left(\frac{\partial G_{i,G}}{\partial n_{i,G}}\right)_{p,T} = \left(\frac{\partial G_{i,L}}{\partial n_{i,L}}\right)_{p,T} \quad (4.1)$$

The chemical potential of a gas species dissolved in the liquid phase can be also expressed as combination of specific enthalpy and entropy according to Eq. 4.2. The lower the chemical potential, the higher the gas solubility is.

$$\left(\frac{\partial G_{i,L}}{\partial n_{i,L}}\right)_{p,T} = h_{i,L} - T \cdot s_{i,L} \quad (4.2)$$

Gas solubility in solvents is usually quantified by the Henry's law constant $H_{i,px}$ defined in Eq. 4.3. Gas solubility is the inverse of $H_{i,px}$.

$$H_{i,px} = \lim_{x_i \rightarrow 0} \frac{p_i}{x_i} \quad (4.3)$$

The Henry's law states that Henry's law constant is directly proportional to the partial pressure of the gas over the liquid phase, when the molar fraction of dissolved gas in the solvent x_i is small (see Eq. 4.4).

$$x_i = \frac{n_{i,L}}{n_{i,L} + n_L} \quad (4.4)$$

Part of the following solubility investigations were carried out during the master thesis of Simone Nagel [206] and part of these results were published in [207].

4.1 Experimental setup

The setup pictured in Figure 4.1 was used for the solubility experiments and is similar to the one used by Götz et al. [204]. It was mainly composed of a gas supply system, a feed tank, an autoclave reactor and a vacuum pump.

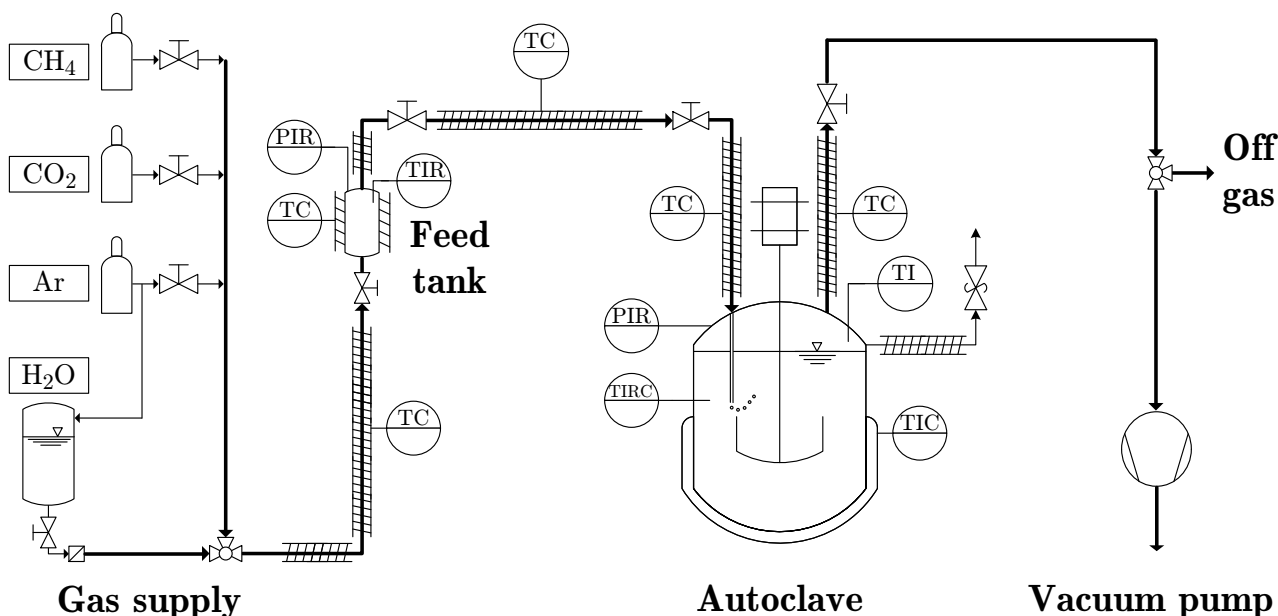


Figure 4.1: Flow chart of the experimental setup used for gas solubility measurement

The gas supply system delivered compressed CH_4 , CO_2 and Ar, while a distilled water tank pressurized with Ar was used for H_2O supply. The gases were fed via the gas supply system into the feed tank which could be isolated from the rest of facility with two shut-off valves. The feed tank pressure and temperature were monitored with an electronic sensor type D-10 provided by *WIKA* (precision ± 0.01 bar) and a thermocouple type K from *Electronic Sensor GmbH* (precision ± 1.5 °C), respectively. Furthermore, heating wires from *Horst GmbH*, a thermocouple type K from *Electronic Sensor GmbH* (precision ± 1.5 °C) as well as a temperature controller of *LCS Isotherm GmbH* were used to regulate the feed tank temperature.

After the feed tank, gases flowed towards an autoclave reactor manufactured by *Büchi Glas Uster AG* (type versoclave). This reactor was made of stainless steel (type 1.4571) with a usable volume of 1 l and could stand temperatures and pressures up to 400 °C and 60 bar, respectively. The temperature of the liquid phase inside the reactor was monitored by a Pt-100 thermocouple (precision ± 0.8 °C) and this temperature was used as control parameter for the heating/cooling system incorporated in the reactor jacket. An electronic pressure sensor type D-10 provided by *WIKA* (precision ± 0.01 bar) and a thermocouple provided by *Electronic Sensor GmbH* (type K, precision ± 1.5 °C) placed on the reactor cover plate were used to measure the reactor gas phase pressure and temperature, respectively. A rotary stainless steel turbine stirrer and a stainless steel baffle from *Büchi Glas Uster AG* placed inside the reactor allowed for a good mixing of the liquid phase with the gas phase. The stirrer could be operated at up to 3000 rotations per min. As for the feed tank, the autoclave reactor could be isolated from the rest of the facility using two shut-off valves. Downstream of the autoclave reactor the gases could be blown off into an extractor hood. To fully void the facility, a vacuum pump type Alcatel T12365 provided by *Franklin Electric* was used.

4.2 Materials

4.2.1 Gases

The gases used in these experiments were CH₄, CO₂ and Ar. The purity and the supplier of these gases are given in Table A.1. Steam was generated through vaporization of distilled water as explained in section 4.3.1.

4.2.2 Suspension liquid

The suspension liquid used for the solubility investigation was dibenzyltoluene (DBT) provided by *Sasol* with the trade name MARLOTHERM[®] SH. An overview of the physical properties of DBT is given in Appendix A.2.

4.3 Experimental method

4.3.1 Experimental procedure

The evacuation method was applied for the experimental determination of Henry's law constants. First, a well-defined mass of DBT was filled into the autoclave reactor. Then, the whole facility described in Figure 4.1 was voided with the vacuum pump until an absolute pressure of 10 mbar was reached. This voidage procedure aimed for extracting air from the facility, while keeping the liquid phase inside the autoclave. The feed tank and its corresponding pipes with a known volume V_{Tank} were thereafter pressurized with the gas to be investigated and the whole facility was then heated up to the desired temperature. Once the experimental

temperature was reached, the feed tank pressure p_{Tank} and temperature T_{Tank} as well as the autoclave pressure p_{R} and temperature T_{R} were recorded. Thereafter, the gas contained in the feed tank was stepwise fed into the autoclave reactor and its corresponding pipes. The volume of the autoclave reactor and its pipes V_{R} was previously measured and was well-defined. After each step, the feed tank and autoclave pressure and temperature were recorded, once they were stabilized. This procedure was repeated until the same pressure was reached in the feed tank and in the autoclave. An exemplary experiment is shown in Figure J.1.

For H₂O solubility experiments, the feed tank was first filled with a well-defined amount of pressurized water. Then, the feed tank temperature was increased till the desired experimental conditions were reached.

In order to validate the aforementioned experimental procedure, solubility experiments were carried out with the well-defined CO₂/H₂O system. The solubility of CO₂ in distilled H₂O were investigated at several temperatures and compared with literature data. The results of these experiments are shown in Appendix J.2.

Once the experimental procedure was validated, solubility experiments with CH₄ and H₂O in DBT were conducted at the temperatures summarized in Table 4.1. For each temperature, one solubility experiment was carried out. In addition, these solubility experiments were performed at pressures between 2 and 12 bar, which are relevant for three-phase CO₂ methanation.

Table 4.1: Investigated temperatures for the determination of CH₄ and H₂O solubilities in DBT

Gases	Temperature
-	°C
CH ₄	240; 260; 280; 300; 320
H ₂ O	250; 270; 290

In this work, no interaction between dissolved gas species was taken into account, as gas solubility was measured with pure gases. For a gas mixing relevant for CO₂ methanation, intermolecular interactions may be expected and discrepancies with the gas solubilities measured in this work may take place.

4.3.2 Data analysis and calculations

For simplification, the situation before feed tank discharge is numbered 1, while the situation after discharge is numbered 2. In the experiment the tank and reactor pressure as well as temperature in situation 1 and 2 were recorded (see an example in Figure J.1 in the Appendix).

The number of moles in the gas phase $n_{i,G}$ (feed tank with pipes, and reactor with pipes) was calculated using Eq. 4.5.

$$n_{i,G} = \frac{pV}{ZRT} \quad (4.5)$$

The necessary compressibility factor Z was evaluated with the Peng Robinson equation of state described with Eq. 4.6 [208].

$$p = \frac{RT}{v-b} - \frac{\theta(T, \omega)}{v(v+b) + b(v-b)} \quad (4.6)$$

The function $\theta(T, \omega)$ describes the volume deviation of a gas molecule from a perfect sphere using the acentric factor ω (see Eq. 4.7) [209]. The species dependent parameters p_{crit} , T_{crit} and ω are summarized in Table B.1, while $\theta(T, \omega)$ is defined in Eq. B.11.

$$\omega = -\log p_r(T_r = 0.7) - 1 \quad (4.7)$$

The calculation of the molar fraction of dissolved gas x_i required the knowledge of the number of moles dissolved in the liquid phase $n_{i,R,L,2}$ and the solvent number of moles n_L . The first calculation step for the evaluation of $n_{i,R,L,2}$ was to determine the number of moles discharged from the feed tank $\Delta n_{i,G,\text{Tank}}$ with Eq. 4.8, as $\Delta n_{i,G,\text{Tank}}$ corresponds to the number of moles discharged into the reactor $\Delta n_{i,R}$.

$$\Delta n_{i,G,\text{Tank}} = n_{i,G,\text{Tank},2} - n_{i,G,\text{Tank},1} = \Delta n_{i,R} \quad (4.8)$$

Then, the number of moles in the reactor gas phase $n_{i,G,R,2}$ was calculated with Eq. 4.5. In this equation, the volume V corresponds to the difference $V_R - V_L$ and the partial pressure p_i corresponds to the difference between the experimental pressure p_R and the saturation pressure of the liquid phase p_v . Finally, the number of moles dissolved in the liquid phase $n_{i,R,L,2}$ was calculated with Eq. 4.9 and x_i was evaluated using Eq. 4.4.

$$n_{i,R,L,2} = \Delta n_{i,R} - n_{i,R,G,2} \quad (4.9)$$

Afterwards, the Henry law's constant $H_{i,px}$ was evaluated by plotting the gas partial pressure in the reactor as a function of x_i . The slope of the obtained curve represents $H_{i,px}$. Special attention was paid to the quality of the linear fit p_i over x_i . If the fit deviated from $R^2 = 0.95$, the Henry law was not valid or the experiments were not properly carried out. Measurement uncertainty was evaluated with the differential method. Details about measurement uncertainty evaluation are given in Appendix N.

4.4 Results and discussion

4.4.1 CH₄ solubility in dibenzyltoluene

Results of CH₄ solubility experiments carried out between 240 and 320 °C in DBT are pictured in Figure 4.2. Henry's law is respected in these experiments, as the worst fit shows a R² of 0.9554. CH₄ solubility shows almost no temperature dependency. Chappelow and Prausnitz [210] investigated the solubility of CH₄ in squalane and found a small positive temperature influence on $H_{\text{CH}_4,px}$ (see also section 4.4.3).

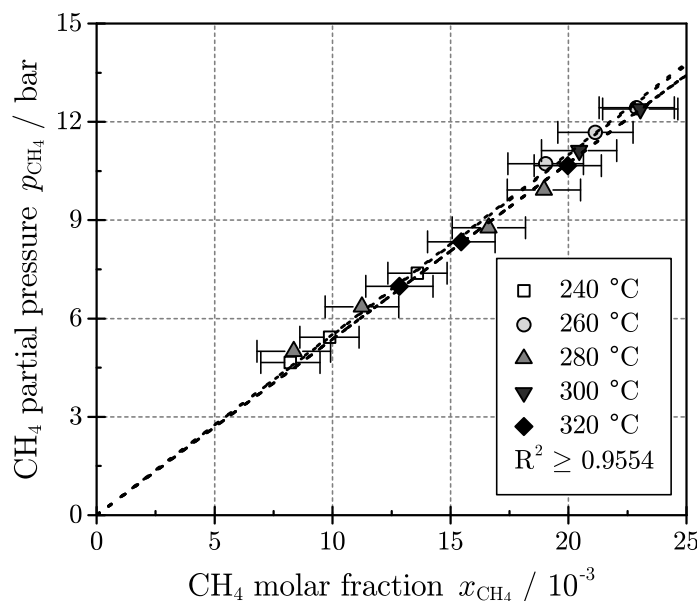


Figure 4.2: CH₄ solubility in DBT for temperatures between 240 and 320 °C. Dashed lines corresponds to the fit $p_{\text{CH}_4} = H_{\text{CH}_4,px} \cdot x_{\text{CH}_4}$.

Table 4.2 summarizes the Henry's law constants $H_{\text{CH}_4,px}$ derived from Figure 4.2. $H_{\text{CH}_4,px}$ decreases by ca. 2 % between 240 and 320 °C. Measurement uncertainty is satisfactory with ca. ± 2 %. This is due to the high instrumental accuracy as well as the relatively low Henry's law constant, i.e. relatively high CH₄ solubility in DBT.

Table 4.2: Experimental Henry's law constant of CH₄ in DBT for temperatures between 240 and 320 °C.

T °C	$H_{\text{CH}_4,px}$ bar
240	549.6 ± 15.8
260	551.9 ± 5.1
280	537.5 ± 14.6
300	537 ± 5.1
320	537.6 ± 9.5

4.4.2 H₂O solubility in dibenzyltoluene

Figure 4.3 shows the results of H₂O solubility experiments carried out between 250 and 290 °C in DBT. Henry's law is valid for these experiments, as the worst fit exhibits a R² of 0.9928. In Figure 4.3, it can be clearly observed that the slope of each fit, i.e. $H_{\text{H}_2\text{O},px}$, increases with increasing temperature. This observation was also reported for H₂O solubility in squalane [211] (see also section 4.4.3).

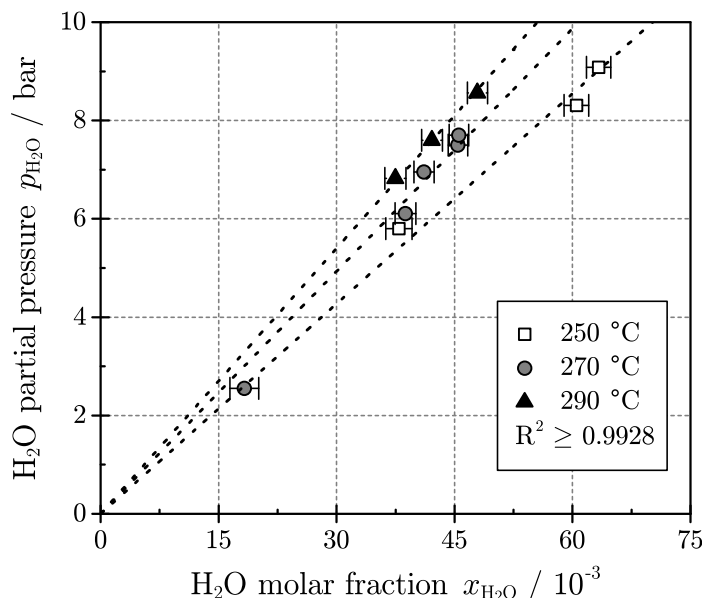


Figure 4.3: H₂O solubility in DBT for temperatures between 250 and 290 °C. Dashed lines corresponds to the fit $p_{\text{H}_2\text{O}} = H_{\text{H}_2\text{O},px} \cdot x_{\text{H}_2\text{O}}$.

In Table 4.3 the Henry's law constants $H_{\text{H}_2\text{O},px}$ derived from Figure 4.3 are summarized. From 250 to 290 °C $H_{\text{H}_2\text{O},px}$ increases by ca. 26 %. Measurement uncertainty is excellent for H₂O with ca. ± 0.4 % variance, because H₂O solubility in DBT is high, i.e. three times higher than CH₄ solubility in DBT.

Table 4.3: Experimental Henry's law constant of H₂O in DBT for temperatures between 250 and 290 °C.

T °C	$H_{\text{H}_2\text{O},px}$ bar
250	142.5 ± 0.6
270	164.5 ± 0.4
290	180.1 ± 0.4

Only three valid solubility experiments for H₂O in DBT were obtained in this PhD thesis, as it was particularly challenging to assure a constant temperature in the experimental setup. Often, a less isolated part of the facility resulted in cold spots leading to water condensation and invalid measurements. In term of further experiments, it is recommended to carry out gas solubility measurements in a facility which is perfectly tempered, e.g. by placing the experimental setup in an oven.

4.4.3 Henry's law constant temperature dependency

The temperature dependency of Henry's law constants $H_{i,px}$ for CO_2 , H_2 , CH_4 , H_2O in DBT is shown in Figure 4.4. Experimental data for CO_2 and H_2 solubilities in DBT were taken from [204]. The Henry's law constants in DBT range in descending order as follows: H_2 , CH_4 , CO_2 , and H_2O . For all gases, except H_2 , $H_{i,px}$ increases with increasing temperature. The highest temperature dependency is observed for H_2 , followed by H_2O , CO_2 and CH_4 .

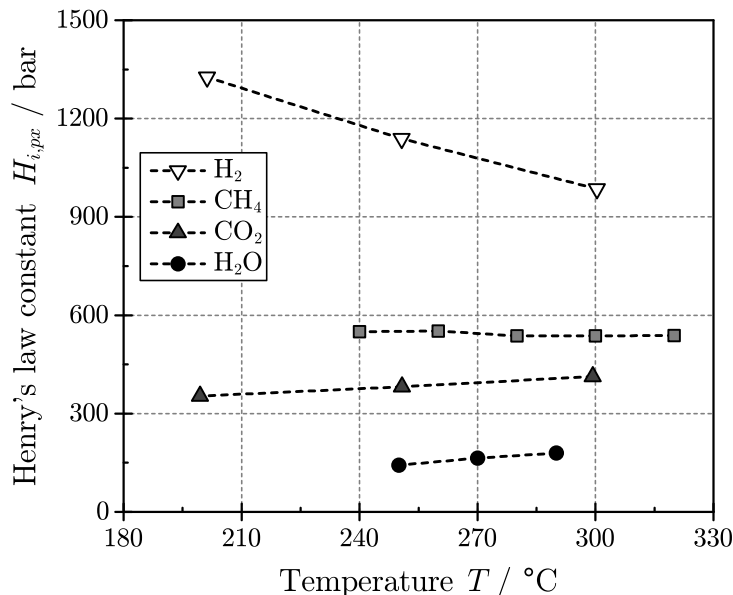


Figure 4.4: Evolution of Henry's law constants $H_{i,px}$ in DBT with temperature. Experimental data for CO_2 and H_2 are taken from [204].

The temperature dependency of Henry's law constants observed in Figure 4.4 can be qualitatively described by the so-called enthalpy-entropy compensation [212]. The Henry's law constant $H_{i,px}$ depends on the chemical potential of the dissolved gas species. As such it is a function of solute enthalpy and entropy (see Eq. 4.2), i.e. $H_{i,px}$ increases when the solute enthalpy increases and decreases when the solute entropy increases. The entropy term describes the degree of vacancy between the solvent molecules, i.e. the number of sites available for gas species [213]. On the other hand, the enthalpy term depends on intermolecular forces and generally increases with increasing temperatures [214]. At high temperatures, H_2 shows little intermolecular interactions with solvents due to its small size and physical symmetry. Hence, the enthalpy term for H_2 is very small and the Henry's law constant of H_2 at high temperatures depends mostly on the entropy term. Consequently, $H_{\text{H}_2,px}$ decreases with increasing temperature as the solute entropy increases (see Figure 4.4). Compared to H_2 , CH_4 , CO_2 and H_2O are more polar and much bigger molecules which offer intermolecular interactions with solvents. As such, the Henry's law constants $H_{i,px}$ of these three gases depend mostly on the dissolved gas enthalpy. As the solute enthalpy of these gases rises with increasing temperature, $H_{i,px}$ for CH_4 , CO_2 and H_2O rises with increasing temperature.

The Henry's law constant $H_{i,px}$ is not a very convenient parameter for chemical reaction engineering and mass-based or mole-based concentrations are usually preferred to x_i to express the amount of dissolved gas in a liquid phase. This is the reason why, the concentration-based

Henry's law constant $H_{i,pc}$ is introduced in Eq. 4.10.

$$H_{i,pc} = \lim_{c_{i,L} \rightarrow 0} \frac{p_i}{c_{i,L}} = H_{i,px} \cdot \frac{M_L}{\rho_L} \quad (4.10)$$

The concentration-based Henry's law constant $H_{i,pc}$ is defined as the ratio between the gas partial pressure and the gas concentration in the liquid phase. Hereby, the concentration of dissolved gas in the liquid phase is defined according to Eq. 4.11.

$$c_{i,L} = \frac{n_{i,L}}{V_L} \quad (4.11)$$

The fit expressed in Eq. 4.12 is proposed to mathematically describe the temperature dependency of Henry's law constants (T in K). This fit was previously used by Götz et al. [204] to express the temperature dependency of Henry's law constants for CO₂ and H₂ in DBT.

$$H_{i,pc} = \exp \left(A_H + \frac{B_H}{T} + \frac{C_H}{T^2} \right) \quad (4.12)$$

By plotting $\ln H_{i,pc}$ as function of the inverse temperature $1/T$ (see Figure J.4 in the Appendix) and fitting the obtained curves with a polynomial equation, it is possible to obtain the parameters A_H , B_H , and C_H for each investigated gas species. These parameters as well as their temperature validity range are summarized in Table 4.4. For CO₂ and H₂ the parameters A_H , B_H , and C_H have been taken from [204].

Table 4.4: Parameter A_H , B_H and C_H for the $H_{i,pc}$ correlation. Data for CO₂ and H₂ taken from [204].

Gases	A_H -	B_H K	C_H K ²	Validity range °C
CO ₂	-2,158	6.09798·10 ²	-3.22499·10 ⁵	25 - 300
H ₂	-2,3838	7.01147·10 ²	0	100 - 300
CH ₄	1.0697	-2.8567·10 ³	7.0853·10 ⁵	240 - 300
H ₂ O	-2.1325·10 ¹	2.1971·10 ⁴	-6.5256·10 ⁶	250 - 290
Ar	9.7404	-1.1352·10 ⁴	2.8542·10 ⁶	240 - 270

In the present PhD thesis, the correlation described in Eq. 4.12 is sometimes extrapolated beyond its validity range. For instance, H₂O solubility experiments do not cover the whole three-phase methanation temperature range of 220 - 320 °C.

4.4.4 Comparison with literature data

The experimental Henry's law constants $H_{i,pc}$ for CO_2 , H_2 , CH_4 , and H_2O in DBT were compared with Henry's law constants measured in other organic oils, namely squalane and octadecane, as these liquids were later used as liquid phase for three-phase CO_2 methanation experiments (see chapter 5). Figure 4.5 compares CO_2 and H_2 solubilities in DBT, squalane and octadecane [211], while Figure 4.6 compares CH_4 and H_2O solubilities in DBT and squalane [210, 211].

Figure 4.5 shows that the temperature dependency of $H_{\text{CO}_2,pc}$ and $H_{\text{H}_2,pc}$ is very similar in each liquid phase. In addition, the same decreasing order in $H_{i,pc}$ takes place for CO_2 and H_2 : DBT, then squalane and finally octadecane. Hence, at same CO_2 and H_2 partial pressures, octadecane offers the highest CO_2 and H_2 concentration in the liquid phase. Besides, H_2 and CO_2 solubility discrepancy between DBT and the other liquids is ca. 20 %.

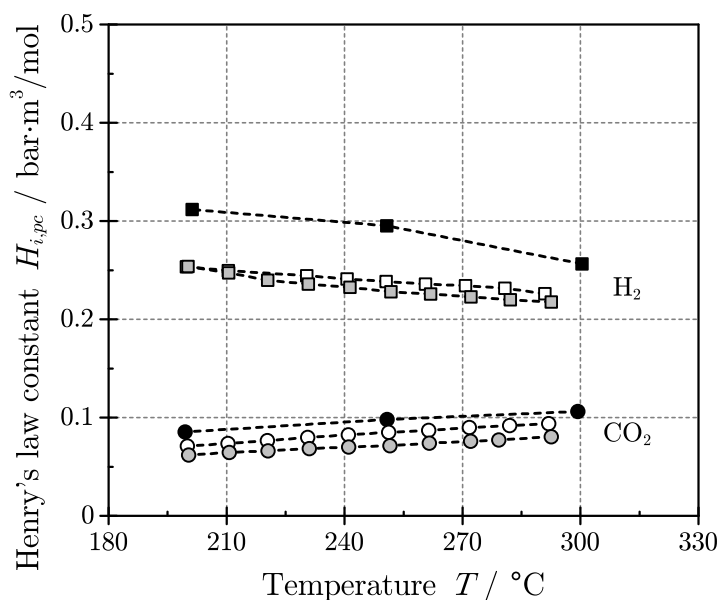


Figure 4.5: Evolution of Henry's law constants $H_{i,pc}$ for CO_2 (\circ) and H_2 (\square) in DBT (black), squalane (white), and octadecane (grey) with temperature. Henry's law constants for DBT taken from [204]. Henry's law constants for squalane and octadecane taken from [211].

Figure 4.6 shows also that the temperature dependency of $H_{\text{CH}_4,pc}$ and $H_{\text{H}_2\text{O},pc}$ is very similar in DBT and squalane. In both liquid phases $H_{\text{CH}_4,pc}$ is higher than $H_{\text{H}_2\text{O},pc}$. However, the solubility discrepancy between DBT and squalane is much higher for CH_4 (ca. 50 %) as compared to H_2O (ca. 17 %). In addition, H_2O solubility is higher in DBT as compared to squalane: H_2O is the only methanation component that shows a better solubility in DBT as compared to squalane.

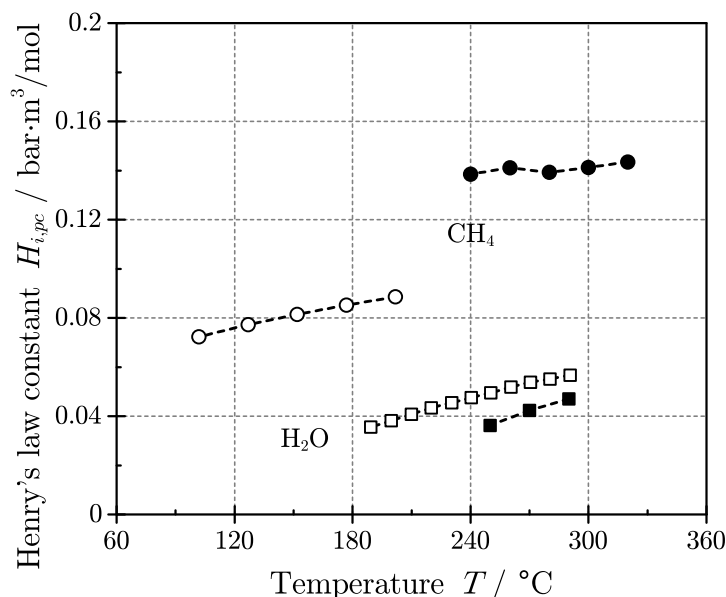


Figure 4.6: Evolution of Henry's law constants $H_{i,pc}$ for CH₄ (○) and H₂O (□) in DBT (black) and squalane (white) with temperature. Henry's law constants for squalane taken from [210, 211].

4.4.5 Consequence of gas solubility on three-phase CO₂ methanation reaction

DBT shows lower solubility for CO₂ and H₂ as well as higher solubility for H₂O as compared to squalane and octadecane. This means that DBT offers lower methanation educt concentrations and higher H₂O concentration as compared to squalane and octadecane. According to the literature, CO₂ methanation reaction kinetics is enhanced by increasing educt concentrations and decreased by increasing H₂O concentrations [27, 110]. Assuming that gas concentrations in the liquid phase are the kinetic relevant parameters for three-phase CO₂ methanation kinetics, CO₂ methanation performed in DBT should lead to lower reaction rates as compared to CO₂ methanation carried out in squalane or octadecane under the same gas partial pressures.

The main advantage of DBT compared to squalane and octadecane is its higher temperature stability (up to 350 °C) and lower vapor pressure. Hence, three-phase methanation can be operated at higher temperatures in DBT as compared to squalane or octadecane. Typical activation energies for CO₂ methanation are in the range of 70 to 90 kJ/mol (see Table 2.2 in chapter 2). Considering the Arrhenius equation (see Eq. 2.7), it means that CO₂ methanation reaction rates are roughly doubled every 20 K between 200 and 350 °C. Squalane and octadecane can be used as solvent for three-phase methanation up to 290 °C, while DBT can be used up to 350 °C. As a consequence, 8 times higher CO₂ methanation reaction rates may be obtained in DBT at 350 °C, which compensates for the worse methanation gas solubilities.

4.5 Summary

The objective of this chapter was to measure the solubilities of CH_4 and H_2O in DBT for temperatures and pressures relevant of three-phase CO_2 methanation. For this purpose, the evacuation method was applied using a new experimental facility. This experimental procedure was validated beforehand with the measurement of well-known CO_2 solubility in H_2O .

CH_4 and H_2O solubility experiments were conducted for temperatures between 240 and 320 °C as well as for pressures between 2 and 12 bar (see Figures 4.2 and 4.3). Based on these experiments, correlations describing gas solubility temperature dependency were developed (see Eq. 4.12 and Table 4.4). It was shown that the different Henry's law constant temperature dependencies (see Figure 4.4) can be explained by the so-called enthalpy-entropy compensation.

The solubilities of CO_2 methanation components in DBT were compared with other liquids (see Figures 4.5 and 4.6), namely squalane and octadecane, which were later used as liquid phase for three-phase CO_2 methanation experiments (see chapter 5). It was shown that DBT offers lower CO_2 and H_2 solubilities as well as higher H_2O solubility as compared to squalane or octadecane. This is a drawback for DBT, because it leads to lower CO_2 methanation reaction rates, considering that gas concentration in the liquid phase is the kinetic relevant parameter to describe three-phase methanation kinetics. This drawback is compensated by the higher temperature stability and lower vapor pressure of DBT compared to squalane and octadecane. Thanks to these properties, CO_2 methanation performed in DBT can be operated at higher temperatures leading to considerably higher reaction rates.

5 Three-phase CO₂ methanation reaction kinetics

In his PhD thesis, Götz [8] tested a total of five liquid phases as solvent for three-phase CO₂ methanation. The liquid dibenzyltoluene (DBT) was found to be the most adequate solvent, as this liquid shows high temperature stability up to 350 °C and acceptable hydrodynamic properties (see section A.2 in the Appendix) [204]. However, Heling [215] showed that the Ni/Al₂O₃ catalyst used in the work of Götz reacts with DBT under methanation conditions, resulting in solvent degradation and catalyst deactivation. This is the reason why a new CO₂ methanation catalyst, which does not react with the liquid phase, had to be found before conducting further kinetic investigations.

DBT belongs to the group of polycyclic aromatic hydrocarbons (PAH). It is known that supported metal catalysts not only catalyze the methanation reaction but also the hydrogenation and cracking of aromatic compounds [216]. While Ni catalyzes the hydrogenation of aromatics components, the acidic catalyst support is responsible for PAH cracking [216, 217]. Al₂O₃ is well-known to be a strong acidic support. On the contrary, SiO₂ is a neutral support and is less prompt to catalyze hydrocracking [218, 219]. Hence, Ni/SiO₂ catalysts represent a good alternative to Ni/Al₂O₃ catalyst for three-phase methanation. Raney[®] nickel is a catalyst derived from nickel-aluminum alloy. By applying NaOH on this catalyst it is possible to dissolve Al from NiAl₃ and Ni₂Al₃ compounds to obtain a porous and methanation active NiAl catalyst with a weaker acidity as compared to the standard Ni/Al₂O₃. Therefore, a Raney[®] nickel catalyst may also be a substitute for the Ni/Al₂O₃ catalyst. Ru catalysts can be used as methanation catalyst and are active at lower temperatures as compared to Ni catalyst (ca. 180 °C) [123]. Operating a three-phase methanation reactor at lower temperatures would bring two advantages. First, the maximum achievable CO₂ conversion would be higher due to a more favorable thermodynamic equilibrium (see Figure 2.1). In addition, PAH cracking would be reduced, since cracking is enhanced by increasing temperature [217, 220]. Thus, Ru catalysts represent a good alternative to the Ni/Al₂O₃ catalyst.

In this chapter, the commercial Ni/Al₂O₃ catalyst from the work of Götz was compared to a commercial Ni/SiO₂ catalyst, a commercial Raney[®] Nickel catalyst, and two different commercial Ru/Al₂O₃ catalysts under three-phase methanation conditions. For these experiments, a slurry reactor operated as a continuous flow stirred-tank reactor (CSTR) was used to evaluate the CO₂ methanation reaction rates as well as the stability of the three-phase system.

Once a suitable catalyst was identified, the influence of a liquid phase on the reaction kinetics of the CO₂ methanation was investigated to clarify whether gas partial pressure or gas concentration in the liquid phase are the relevant parameters to describe the three-phase

CO₂ methanation kinetics. Looking at similar processes in the literature, the influence of solvents on reaction kinetics is neither well-defined nor well understood. For the liquid-phase hydrogenation of cyclohexene on Pd, Madon et al. [221] showed that H₂ concentration in the liquid phase is the relevant parameter to describe the reaction kinetics. However, when Pt was applied for the same reaction, Gonzo and Boudart [222] showed that H₂ partial pressure in the gas phase is the relevant kinetic parameter. In three-phase Fischer-Tropsch synthesis, gas partial pressures - and not gas concentrations in the slurry phase - are usually applied in kinetic rate equations [223, 224]. For three-phase methanol synthesis, Graaf et al. [225, 226] used gas concentration in the liquid phase to describe the reaction kinetics. However, the experimental activation energy of the three-phase CO₂ methanol synthesis was reported to be much lower than the activation energy in a comparable two-phase system.

To clarify the influence of a liquid phase on the reaction kinetics of the CO₂ methanation, three-phase methanation experiments were carried out with three suspension liquids offering different gas solubilities. Experiments were performed at either same gas partial pressures or same gas concentrations in the liquid phase to find out which parameter is relevant for the description of the three-phase CO₂ methanation kinetics.

Once the influence of liquid phase on the CO₂ methanation reaction kinetics was clarified, further three-phase CO₂ methanation kinetic experiments were carried out to derive a kinetic rate equation for a CO₂ partial pressure of 1 bar and temperatures between 220 and 320 °C.

Part of the following experiments were carried out during the master theses of Daniel Safai, Nike Trudel, and Ulli Hammann [227–229]. The major part of the following results was published in [207].

5.1 Experimental setup

The experimental setup can be divided into three main parts: gas supply system, reactor and gas analysis (see Figure 5.1).

5.1.1 Gas supply system

The gas volume flow rates of CO₂, H₂, CH₄, N₂ and Ar were dosed with mass flow controllers (MFC) provided by *Bronkhorst*. Steam could be added to the feed gas stream via a combination of a demineralized water MFC and an evaporator from *Bronkhorst*. Downstream of the MFC the gases were mixed in a feed tank and preheated to the desired reaction temperature via heating wires placed around the pipes and the feed tank. The feed tank temperature was measured with a thermocouple provided by *Electronic Sensor GmbH* (type K, precision ± 1.5 °C), while the feed tank pressure was monitored via an electronic pressure sensor from *Bronkhorst* (precision ± 0.1 bar). The dry feed gas stream could also bypass the reactor and fed directly to the gas analysis unit.

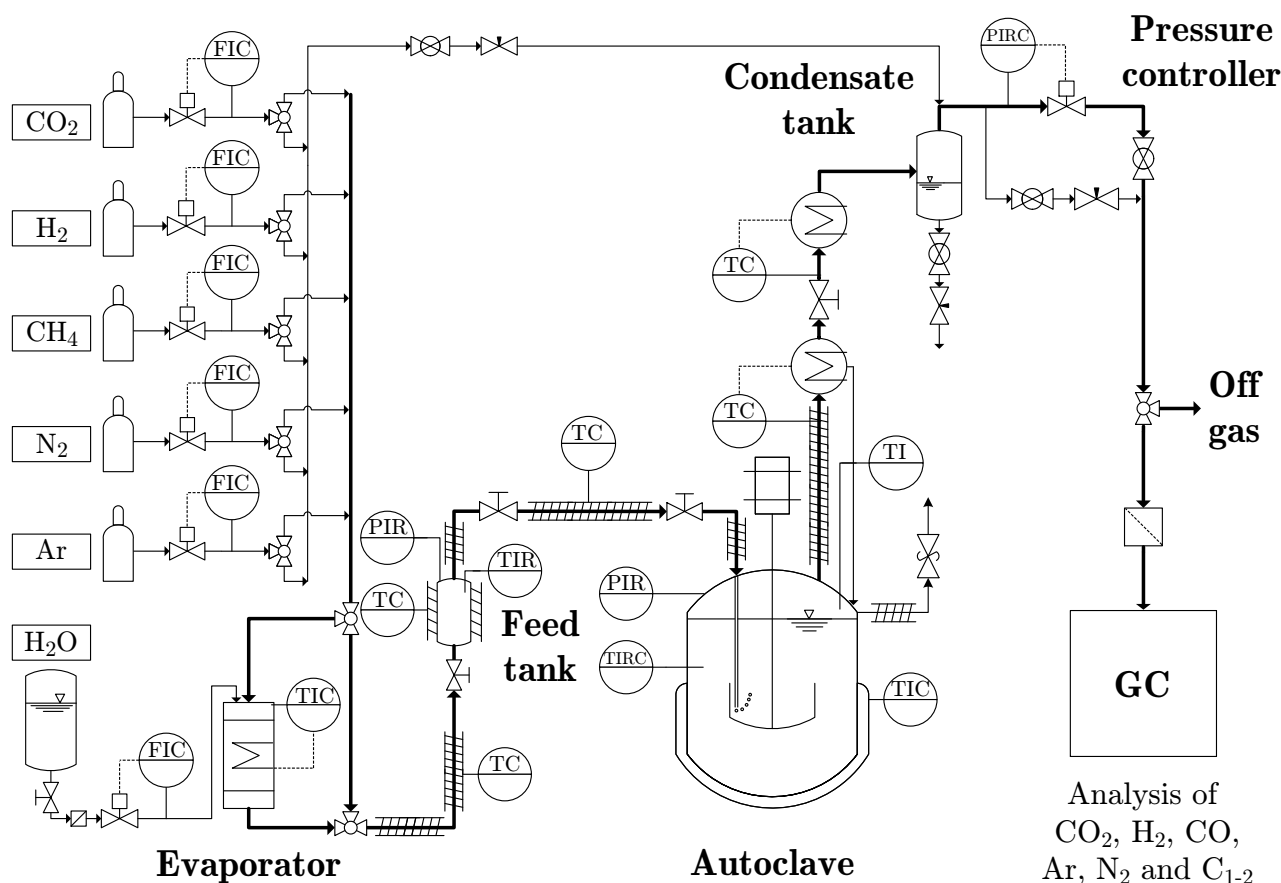


Figure 5.1: Flow chart of the experimental setup used for three-phase methanation kinetic investigation.

5.1.2 Reactor

An autoclave reactor manufactured by *Büchi Glas Uster AG* (type versoclave) was used for the experiments as a CSTR. The reactor was made of stainless steel (type 1.4571) with an effective capacity of 1 l and could stand temperatures and pressures up to 400 °C and 60 bar, respectively. The temperature of the liquid phase inside the reactor was monitored by a Pt-100 thermocouple (precision ± 0.8 °C); this temperature was used as control parameter for the heating/cooling system incorporated in the reactor jacket. An electronic pressure sensor provided by *Bronkhorst* (precision ± 0.1 bar) and a thermocouple provided by *Electronic Sensor GmbH* (type K, precision ± 1.5 °C) placed on the reactor cover plate were used to monitor the reactor gas phase pressure and temperature, respectively. A rotary stainless steel turbine stirrer and a stainless steel baffle from *Büchi Glas Uster AG* placed inside the reactor allowed for a good mixing of the slurry phase with the gas phase. The stirrer could be operated at up to 3000 rotations per min.

Thereafter, the gas stream exiting the reactor was cooled to ca. 200 °C in order to condense most of the entrained solvent, while the produced water stayed in the vapor phase. Then, the almost oil-free gas stream was cooled to 5 °C in order to condense water and the rest of the solvent. For this purpose a condensate tank was installed downstream of the reactor. After the condensate tank, a pressure controller provided by *Bronkhorst* regulated the autoclave

reactor pressure (precision ± 0.15 bar). The dry and cool product gas stream exiting the pressure controller could either be directed to the extractor hood or to the gas chromatograph via a three-way valve.

5.1.3 Gas analysis

The product and feed gas streams were analyzed with gas chromatograph (GC) model G3581A by *Agilent Technologies*. The GC used a thermal conductivity detector (TCD) and was calibrated for H₂, Ar, N₂, CO₂, CH₄, CO, as well as for C₂H₄ and C₂H₆. The cycle time of a GC analysis was about 3 minutes.

5.2 Materials

5.2.1 Gases

The gases used in these experiments were CO₂, H₂, CH₄, N₂ and Ar. The purity and the supplier of these gases are given in Table A.1. Water vapor was produced from demineralized water.

5.2.2 Catalysts

Two commercial nickel-based catalysts with either alumina or silica support (Ni/Al₂O₃ and Ni/SiO₂, respectively) and two commercial ruthenium-based catalysts with alumina support (Ru/Al₂O₃) were employed in this work. These catalysts were delivered as pellets of 5 x 5 mm. In pellet form, the catalyst was not suited for kinetic investigation, as the relatively high catalyst size could lead to undesired intra-particle mass-transfer limitation. To overcome this issue, catalyst pellets were first milled and sieved. Only the particle size fraction of 50 - 100 μm was applied. Besides, Raney[®] nickel catalyst provided by *Merck* in form of powder was used. The catalysts used in the experiments were named according to Table 5.1.

Table 5.1: Name and major components of the catalysts used in the experiments.

Catalyst name	Composition
Nicom1	Ni/Al ₂ O ₃
Nicom2	Ni/SiO ₂
RaneyNi	NiAl
Rucom1	Ru/Al ₂ O ₃
Rucom2	Ru/Al ₂ O ₃

5.2.3 Suspension liquids

The liquids employed in this work were squalane (Purity 99 %, *Sigma Aldrich*), octadecane (Purity 99 %, *VWR International GmbH*), and dibenzyltoluene (DBT, trade name MARLOTHERM[®] SH, *Sasol*). These liquids were chosen because they covered a wide range of gas solubilities and had sufficiently low vapor pressure at relevant reaction temperatures. Solubility data of the methanation relevant gas species in squalane and octadecane were taken from [211], while gas solubilities in DBT were taken from Chapter 4 and [204]. An overview of the physical properties of DBT is given in the Appendix A.2.

5.3 Experimental method

5.3.1 Experimental procedure

5.3.1.1 Catalyst activation

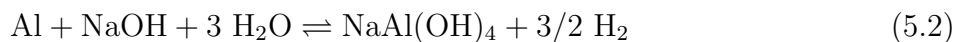
The commercial nickel and ruthenium catalysts were delivered in their oxidized form and had to be reduced before starting the methanation reaction. For this purpose, a two-phase fixed-bed reactor was designed and built, as the required reduction temperature of 400 °C was much higher than the temperature stability of the liquids (< 350 °C), which made catalyst reduction in the suspension impossible. A sketch of the reduction reactor is given in Figure O.1.

Nickel oxide was reduced with hydrogen to pure nickel according to the reaction described in Eq. 5.1. A similar reaction occurred for the reduction of the Ru-based catalysts.



To carry out this reduction reaction, the sieved nickel and ruthenium catalysts were filled into the reduction reactor. This reactor was then heated up to 400 °C at atmospheric pressure with a mixture of Ar/H₂ = 1/1 and a volume flow rate of 44 l/h at standard temperature and pressure (STP). These operating conditions were maintained for 24 h. Then, the heating was switched off and the reactor was cooled down to atmospheric temperature, while prolonging the Ar/H₂ gas stream.

The Raney[®] nickel catalyst was delivered as nickel/aluminum alloy and required another activation method, which did not involve a reaction with H₂ at elevated temperatures. For Raney[®] nickel catalyst, aluminum was removed by suspending the alloy in a sodium hydroxide solution. Sodium hydroxide reacted with aluminum to aluminate and hydrogen according to Eq. 5.2. Aluminate dissolved in the solution and the remaining solid particle exhibited a highly porous structure with a high nickel content.



In both cases, catalyst reoxidation had to be avoided. For this purpose, the activated catalysts were suspended in the suspension liquid under inert Ar atmosphere. In this chapter, it has to be noted that the mass of catalyst, m_{cat} , is the mass of **activated catalyst** used for methanation experiments.

5.3.1.2 CO₂ methanation experiments

Before each methanation experiment, the slurry phase consisting of suspension liquid and activated catalyst was filled into the autoclave reactor and heated up to reaction temperature. At the same time, a 200 ml/min (STP) volume flow rate of Ar/H₂ = 1/1 was sent through the reactor in order to prevent catalyst oxidation.

When the reaction temperature was reached, the reactor inlet volume flow rate as well as composition were changed to CO₂ methanation operating conditions. The autoclave reactor was used as CSTR. Consequently, the inlet volume flow rates of each gas species - except CO₂ to maintain a constant CO₂ residence time - were step by step varied to obtain well-defined outlet gas compositions, especially an outlet CO₂ partial pressure of 1 bar. A constant Ar volume flow rate of 100 ml/min (STP) was for instance maintained constant during the experiment to facilitate the calculation of outlet volume flow rates (see section 5.3.2), while the volume flow rate of N₂ was adjusted to reach a constant total inlet volume flow rate.

Furthermore, for each set of experiments absence of mass-transfer limitation in the liquid phase was verified through variation of the autoclave agitator speed. An example is shown in Figure 5.2 for an experiment performed with the commercial Ni/SiO₂ catalyst suspended in DBT at a reaction temperature of 260 °C. It can be seen that the CO₂ conversion X_{CO_2} does not increase any further for an agitator speed above 800 1/min. Above this threshold, no mass-transfer resistance in the liquid phase has to be considered.

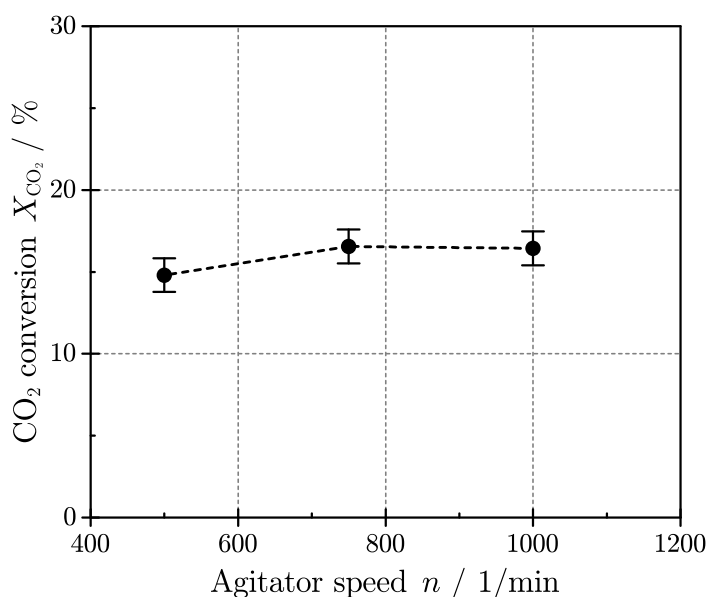


Figure 5.2: Influence of agitator speed on the CO₂ conversion observed with Ni/SiO₂ catalyst suspended in DBT ($T = 260$ °C, $p_{\text{H}_2,\text{out}} = 4$ bar, $p_{\text{CO}_2,\text{out}} = 1$ bar, $\tau_{\text{mod,CO}_2} = 14$ kg · s/mol).

This observation was also confirmed for all other experimental conditions. Thus, an agitator speed of 1000 1/min was selected for all the experiments described in this chapter.

5.3.2 Data analysis and calculations

The total outlet volume flow rate (STP), $\dot{V}_{\text{total,out,STP}}$, was calculated according to Eq. 5.3, as the Ar volume flow rate remained constant during the experiment.

$$\dot{V}_{\text{total,out,STP}} = \dot{V}_{\text{total,in,STP}} \frac{y_{\text{Ar,in}}}{y_{\text{Ar,out}}} \quad (5.3)$$

Knowing $\dot{V}_{\text{total,out,STP}}$ as well as the gas composition at the reactor inlet and outlet via GC measurements, the catalyst performance was evaluated via the calculation of the CO₂ conversion, the methanation reaction rate and the selectivities to methanation products.

The CO₂ conversion X_{CO_2} was determined by the following equation Eq. 5.4.

$$X_{\text{CO}_2} = \frac{\dot{n}_{\text{CO}_2,\text{in}} - \dot{n}_{\text{CO}_2,\text{out}}}{\dot{n}_{\text{CO}_2,\text{in}}} \quad (5.4)$$

The three-phase CO₂ methanation catalyst mass-based reaction rate $r_{3\text{PM}}$, further referred to as CO₂ methanation reaction rate, was expressed as following (Eq. 5.5):

$$r_{3\text{PM}} = -\frac{1}{m_{\text{cat}}} \cdot \frac{dn_{\text{CO}_2}}{dt} \quad (5.5)$$

Introducing the modified CO₂ residence time (Eq. 5.6):

$$\tau_{\text{mod,CO}_2} = \frac{m_{\text{cat}}}{\dot{n}_{\text{CO}_2,\text{in}}} \quad (5.6)$$

the experimental CO₂ methanation reaction rate $r_{3\text{PM,exp}}$ observed in the autoclave reactor used as a CSTR was calculated with Eq. 5.7:

$$r_{3\text{PM,exp}} = \frac{X_{\text{CO}_2}}{\tau_{\text{mod,CO}_2}} \quad (5.7)$$

The selectivity S_i to CH₄, CO, or C₂H₆ was defined as the ratio of produced CH₄, CO, or C₂H₆ to converted CO₂ (Eq. 5.8).

$$S_i = \frac{\dot{n}_{i,\text{out}} - \dot{n}_{i,\text{in}}}{\dot{n}_{\text{CO}_2,\text{in}} - \dot{n}_{\text{CO}_2,\text{out}}} \quad (5.8)$$

During the experiments, attention was paid to the carbon and hydrogen balance. The carbon balance was defined as the ratio of the sum of outlet CO₂, CO, CH₄, C₂H₆, and C₂H₄ molar flow rates to the sum of all inlet molar flow rates containing carbon (Eq. 5.9).

$$\frac{\dot{n}_{\text{C,out}}}{\dot{n}_{\text{C,in}}} = \frac{\dot{n}_{\text{CO}_2,\text{out}} + \dot{n}_{\text{CO},\text{out}} + \dot{n}_{\text{CH}_4,\text{out}} + 2 \dot{n}_{\text{C}_2\text{H}_6,\text{out}} + 2 \dot{n}_{\text{C}_2\text{H}_4,\text{out}}}{\dot{n}_{\text{CO}_2,\text{in}} + \dot{n}_{\text{CH}_4,\text{in}}} \quad (5.9)$$

The GC used in this work could only detect CO, CO₂ and CH₄, C₂H₆ and C₂H₄ as gas components containing carbon. Hence, in the carbon balance in Eq. 5.9 only these components were taken into account when calculating the outlet molar flow rates containing carbon. Despite this limited gas analysis, the carbon balance was higher than 98.5 % for all the experiments.

Equivalent to the carbon balance, the hydrogen balance was defined as ratio of the sum of outlet H₂, CH₄, C₂H₆, C₂H₄, and H₂O molar flow rates to the sum of all inlet molar flow rates containing hydrogen (Eq. 5.10).

$$\frac{\dot{n}_{\text{H},\text{out}}}{\dot{n}_{\text{H},\text{in}}} = \frac{2 \dot{n}_{\text{H}_2,\text{out}} + 4 \dot{n}_{\text{CH}_4,\text{out}} + 6 \dot{n}_{\text{C}_2\text{H}_6,\text{out}} + 4 \dot{n}_{\text{C}_2\text{H}_4,\text{out}} + 2 \dot{n}_{\text{H}_2\text{O},\text{out}}}{2 \dot{n}_{\text{H}_2,\text{in}} + 4 \dot{n}_{\text{CH}_4,\text{in}} + 2 \dot{n}_{\text{H}_2\text{O},\text{in}}} \quad (5.10)$$

The water in the product gas stream, $\dot{n}_{\text{H}_2\text{O},\text{out}}$, was condensed upstream of the GC. Therefore $\dot{n}_{\text{H}_2\text{O},\text{out}}$ could not be estimated based on GC measurements. However, $\dot{n}_{\text{H}_2\text{O},\text{out}}$ could be calculated over the oxygen balance according to Eq. 5.11.

$$\dot{n}_{\text{H}_2\text{O},\text{out}} = \dot{n}_{\text{H}_2\text{O},\text{in}} + 2 \dot{n}_{\text{CO}_2,\text{in}} - 2 \dot{n}_{\text{CO}_2,\text{out}} - \dot{n}_{\text{CO},\text{out}} \quad (5.11)$$

5.3.3 Development of a reaction rate equation

A power law rate equation with product limitation was used to describe the experimental CO₂ reaction rates (see Eq. 5.12). Furthermore, during the experiments, a CH₄ selectivity above 95 % was observed. Hence, side reactions along the main CO₂ methanation reaction were ignored for the development of the kinetic rate equation.

$$r_{3\text{PM},\text{cal}} = k \cdot \frac{c_{\text{H}_2,\text{L}}^\alpha \cdot c_{\text{CO}_2,\text{L}}^\beta}{(1 + K_{\text{H}_2\text{O}} \cdot c_{\text{H}_2\text{O},\text{L}})^\gamma} \cdot K \quad (5.12)$$

k is the reaction rate constant as defined in Eq. 5.13, while $K_{\text{H}_2\text{O}}$ describes the adsorption constant of H₂O on the nickel catalyst (see Eq. 5.14). As the adsorption enthalpy of H₂O, $\Delta h_{\text{H}_2\text{O},\text{ad}}$, was not found in literature, $K_{\text{H}_2\text{O}}$ was set to 1 m³/mol in this work, i.e. the influence of H₂O on the reaction rate does not vary with temperature. Other values were tested for $K_{\text{H}_2\text{O}}$ and delivered similar fits.

$$k = k_0 \cdot \exp\left(\frac{-E_A}{R \cdot T}\right) \quad (5.13)$$

$$K_{\text{H}_2\text{O}} = K_{\text{H}_2\text{O},0} \cdot \exp\left(-\frac{\Delta h_{\text{H}_2\text{O},\text{ad}}}{RT}\right) \quad (5.14)$$

In Eq. 5.12, K describes the limitation of $r_{3\text{PM}}$ when the reaction system approaches the chemical equilibrium described by K_{eq} (see Eq. 5.15). K was expressed as function of gas partial

pressure according to [27, 230] and it was assumed that chemical equilibrium is characterized by the gas phase equilibrium and not by the liquid phase equilibrium, i.e. only the activities of the species in the gas phase were taken into account for the calculation of K . Further details related to chemical equilibrium of three-phase CO₂ methanation are given in the Appendix K.

$$K = 1 - \frac{p_{\text{H}_2\text{O},\text{out}}^2 \cdot p_{\text{CH}_4,\text{out}}}{p_{\text{H}_2,\text{out}}^4 \cdot p_{\text{CO}_2,\text{out}}} \cdot \frac{p_0^2}{K_{\text{eq}}} \quad (5.15)$$

The gas concentrations in the liquid phase $c_{i,\text{L}}$ were estimated with Eq. 5.16 which is valid under the premise of ideal gas behavior.

$$c_{i,\text{L}} = \frac{p_i}{H_{i,\text{pc}}} \quad (5.16)$$

The chemical equilibrium constant K_{eq} was estimated through minimization of the system's Gibb's enthalpy. The Gibb's enthalpies of the gas species were calculated using gas enthalpy and entropy correlations from NIST Chemistry WebBook [231]. The kinetic parameters k , α , β , and γ were determined by least-square minimization of the deviation between calculated CO₂ reaction rates $r_{3\text{PM},\text{cal}}$, (Eq. 5.12), and experimentally observed CO₂ reaction rates $r_{3\text{PM},\text{exp}}$ (Eq. 5.7). In a first step, α , β and γ were guessed and k was determined for each investigated temperature. Then, k_0 and E_A were calculated from linear regression of the Arrhenius equation (see Eq. 5.17). The deviation between $r_{3\text{PM},\text{cal}}$ and $r_{3\text{PM},\text{exp}}$ was determined and α , β , and γ were further varied until the deviation reaches a minimum. This two-step method aimed for verifying the first-step fit through the examination of the Arrhenius plot fit quality. Only Arrhenius fits with $R^2 \geq 0.98$ were considered.

$$\log_{10} k = \log_{10} k_0 - \frac{E_A}{R \cdot \ln 10} \cdot \frac{1}{T} \quad (5.17)$$

5.4 Results and discussion

5.4.1 Catalyst test

Before determining the reaction kinetics of three-phase CO₂ methanation, a catalyst test was performed in DBT with the nickel and ruthenium catalysts listed in Table 5.1 under the operating conditions summarized in Table 5.2. To identify the most adequate CO₂ methanation catalyst, the CO₂ reaction rate as well as the product selectivities were determined after 100 h of operation. In further experiments the long-term catalyst stability in DBT was investigated. To do so, the operating conditions listed in Table 5.2 were applied and the CO₂ reaction rates were monitored over a period of 240 h.

The results of the catalyst test are shown in Figure 5.3. Nicom1 offers the highest CO₂ reaction rates. However, after 100 h of operation Nicom1 lost 70 % of its initial activity. As expected, Nicom1 reacts with DBT and deactivates. This behavior is not observed for the

other catalysts. Hence, the catalyst support does influence the cracking of DBT and catalysts with less acidic support like SiO_2 are less prompt to DBT cracking.

Table 5.2: Process parameters for catalyst test.

Parameters	Variation	units
T	250	$^{\circ}\text{C}$
$p_{\text{CO}_2,\text{out}}$	0.83	bar
$p_{\text{H}_2,\text{out}}$	3.3	bar
p_{R}	5	bar
$\tau_{\text{mod},\text{CO}_2}$	20.5	$\text{kg}\cdot\text{s}/\text{mol}$
m_{cat}	0.9 - 1.0	10^{-3} kg

With decreasing order of CO_2 reaction rates the investigated catalysts range as following: Nicom2 > RaneyNi > Nicom1 > Rucom1 > Rucom2. Aside CO_2 reaction rates, selectivity is a significant criterion for the choice of the right three-phase methanation catalyst. For all catalysts almost no selectivity to C_2H_6 can be observed. However, the investigated catalysts show different selectivities to CH_4 and CO , S_{CH_4} and S_{CO} , respectively. In decreasing order of S_{CH_4} , the catalysts can be classified as following: Rucom1 > Nicom2 > Nicom1 > RaneyNi > Rucom2. Although Rucom1 exhibits the highest S_{CH_4} , the associated reaction rate is about 2.5 times smaller as compared to Nicom2. As such, Nicom2 is the best trade between reaction rate and CH_4 selectivity.

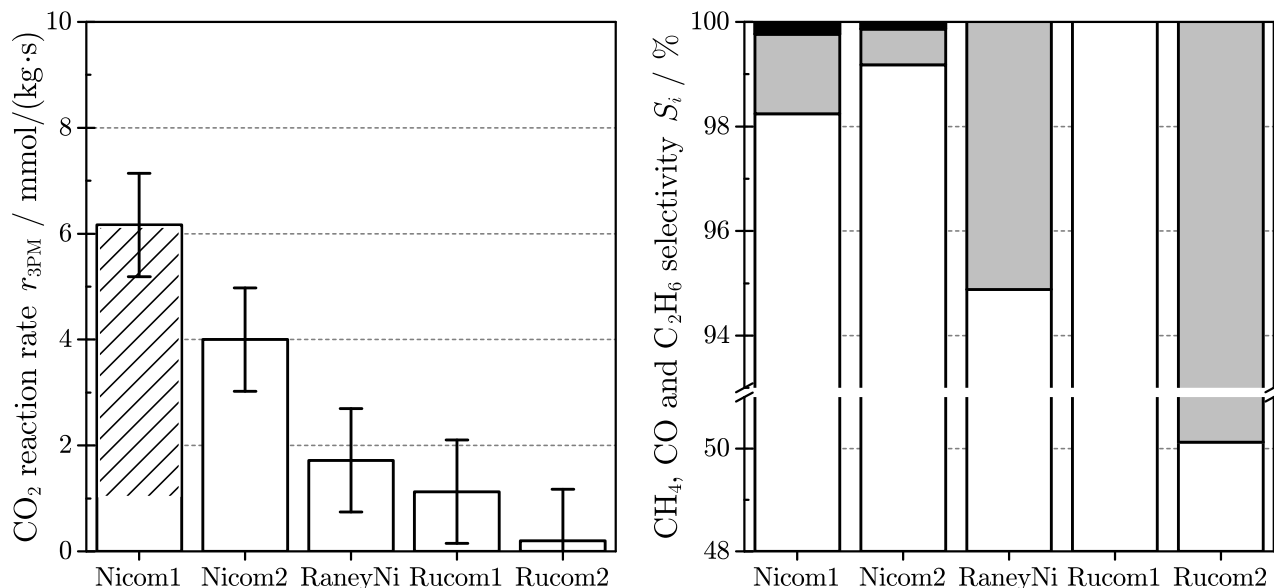


Figure 5.3: CO_2 reaction rates (left) and selectivities to CH_4 , CO , and C_2H_6 , respectively in white, grey, and black (right) for different methanation catalysts ($T = 250 \text{ }^{\circ}\text{C}$, $p_{\text{R}} = 5 \text{ bar}$, $\tau_{\text{mod},\text{CO}_2} = 20.5 \text{ kg}\cdot\text{s}/\text{mol}$, $(\text{H}_2/\text{CO}_2)_{\text{G,out}} = 4.0$, $p_{\text{CO}_2,\text{out}} = 0.83 \text{ bar}$).

Furthermore, Rucom2 shows the lowest S_{CH_4} (ca. 50 %). Combined with the lowest $r_{3\text{PM}}$, Rucom2 is the worst tested catalyst. Ru catalysts are known to have a lower selectivity to CH_4 than Ni catalysts (see section 2.1.2). However, a low selectivity combined with a low

reaction rate is not usual for Ru catalysts. In absence of specific reduction method for Ru catalysts from the suppliers, the same reduction method was applied for each catalyst (see section 5.3.1.1). Reason for unexpected low methanation performance of Ru catalysts may be an unadapted reduction procedure. In addition, considering Ni catalysts only, RaneyNi shows the lowest S_{CH_4} . Therefore, it can be assumed that the absence of support in RaneyNi is detrimental to S_{CH_4} and that Al_2O_3 or SiO_2 help for reaching high S_{CH_4} .

Based on the catalyst test, Nicom2 seems to be the most adequate catalyst for three-phase CO_2 methanation. To confirm this, further experiments were carried out to investigate the long-time activity of Nicom2. The results of these experiments are shown in Figure 5.4. The long-time activity of Nicom1 is shown next to Nicom2 for comparison purpose. As expected, the CO_2 reaction rates observed with Nicom1 rapidly decrease and after 200 h they stabilize at ca. 30 % of the initial activity. On the contrary, $r_{3\text{PM}}$ observed with Nicom2 do not vary over the investigated period of time. As such Nicom2 is a stable catalyst for three-phase CO_2 methanation.

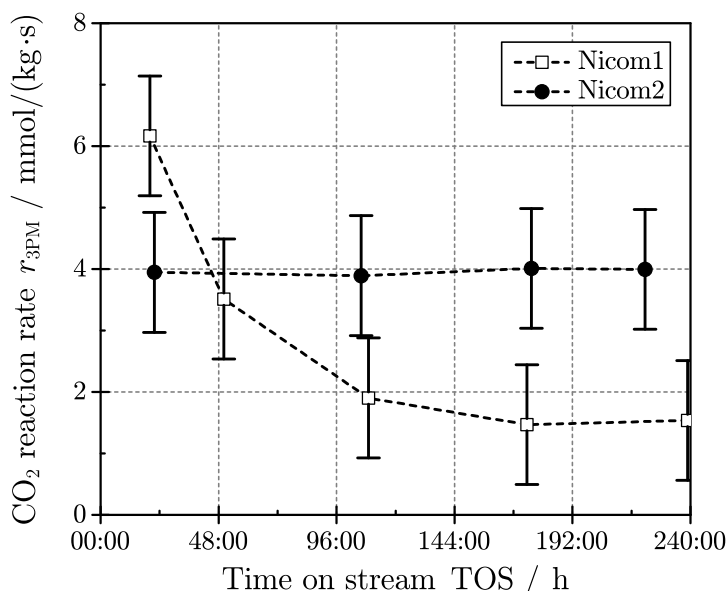


Figure 5.4: Evolution of the CO_2 reaction rates over time for two commercial catalysts ($T_{\text{R}} = 250 \text{ }^\circ\text{C}$, $p_{\text{R}} = 5 \text{ bar}$, $\tau_{\text{mod},\text{CO}_2} = 20.5 \text{ kg}\cdot\text{s}/\text{mol}$, $(\text{H}_2/\text{CO}_2)_{\text{G,out}} = 4.0$, $p_{\text{CO}_2,\text{out}} = 0.83 \text{ bar}$).

To sum up, Nicom2, i.e. a commercial Ni/ SiO_2 catalyst, shows the highest CO_2 reaction rates combined with high selectivity to CH_4 . Furthermore, this catalyst does not deactivate under three-phase methanation operating conditions and does not degrade the liquid phase. As a consequence, this catalyst was seen as a suitable catalyst for three-phase methanation and was used in further CO_2 methanation experiments.

5.4.2 Influence of the liquid phase on reaction kinetics

To investigate whether gas partial pressures or gas concentrations in the liquid phase are the rate-determining parameters for the three-phase CO₂ methanation, three different liquids - squalane, octadecane, and DBT - offering different gas solubilities were used as suspension liquids. For the first experiments, same H₂ and CO₂ partial pressures were applied for all three suspension liquids for temperatures of 220 to 260 °C. Then, H₂ and CO₂ partial pressures were adjusted to obtain the same H₂ and CO₂ concentrations in the different liquid phases for a reaction temperature of 230 °C. For both sets of experiments, the CO₂ reaction rate as defined in Eq. 5.7 was evaluated. CH₄ and H₂O partial pressures or concentrations in the liquid phase were not adjusted for the methanation experiments in octadecane, as $H_{\text{CH}_4,pc}$ and $H_{\text{H}_2\text{O},pc}$ in octadecane were not available in literature.

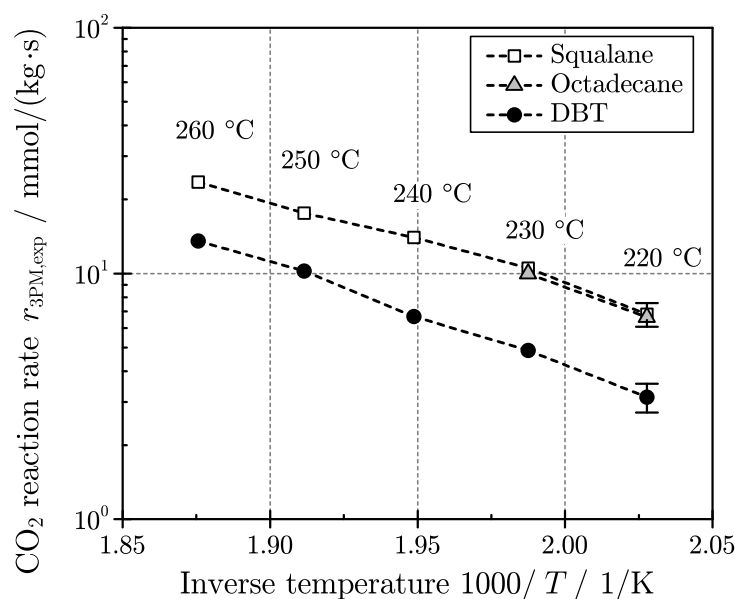


Figure 5.5: Arrhenius plot: influence of temperature on the CO₂ reaction rates observed in squalane, octadecane, or DBT ($p_R = 16$ bar, $p_{\text{H}_2,\text{out}} = 4$ bar, $p_{\text{CO}_2,\text{out}} = 1$ bar).

The temperature influence on the CO₂ reaction rate $r_{3PM,exp}$ observed in squalane, octadecane, and DBT at $p_{\text{H}_2,\text{out}} = 4$ bar and $p_{\text{CO}_2,\text{out}} = 1$ bar is shown in Figure 5.5. Experiments in octadecane could not be performed at temperatures above 230 °C, as octadecane crystallized at the cooled reactor outlet and blocked the outlet gas flow (octadecane is solid under 27 °C). Nevertheless, the results obtained from the unimpeded octadecane experiments were regarded as sufficient to clarify the influence of a liquid phase on the CO₂ methanation reaction kinetics. Consequently, the experimental setup of this work was not adapted to make up for the crystallization issue. In Figure 5.5, similar activation energies ranging from 75 to 84 kJ/mol can be derived from the Arrhenius plots. Hence, temperature has the same influence on the CO₂ reaction rates for all liquid phases. This range of activation energy is typical for CO₂ methanation reaction performed in the gas phase [6, 27, 110] and it confirms that the experiments have been carried out in absence of mass and heat transfer limitations.

In Figure 5.6, CO₂ reaction rates observed in the three different liquids at 230 °C either at same H₂ and CO₂ partial pressures (left) or at same H₂ and CO₂ concentrations in the

liquid phase (right) are compared to each other. At identical H_2 and CO_2 partial pressures different reaction rates are observed depending on the applied liquid phase. In DBT, the CO_2 reaction rate is about two times lower as compared to experiments performed in squalane or octadecane.

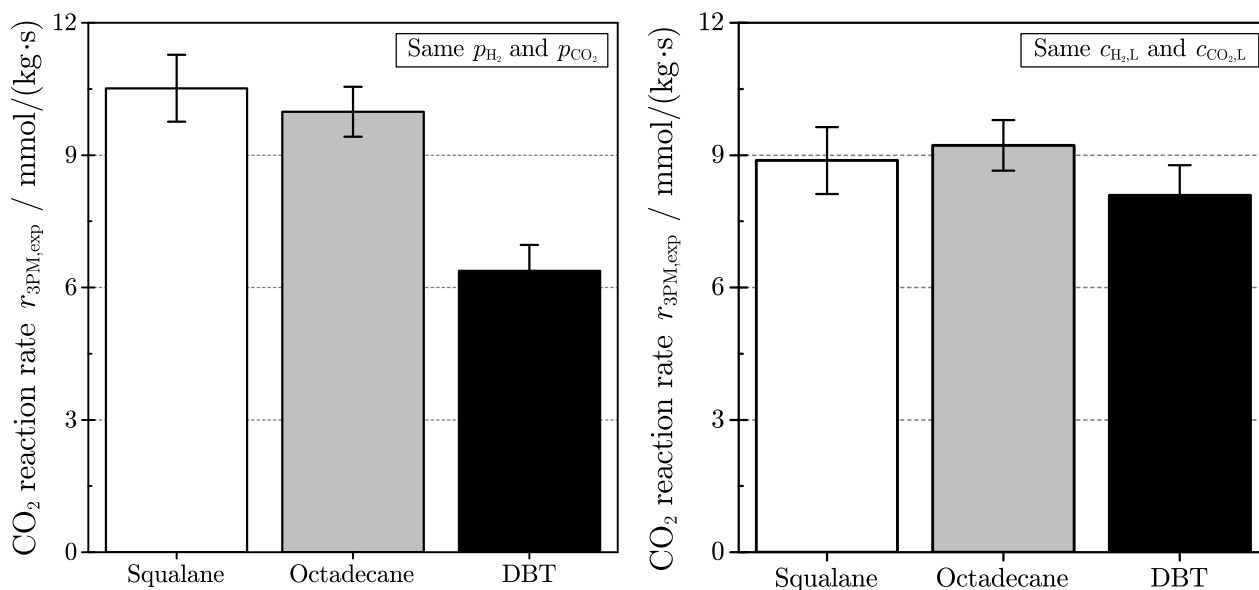


Figure 5.6: Comparison of CO_2 reaction rates at 230 °C, $p_R = 16$ bar, and $\tau_{mod,CO_2} = 17 - 20$ kg·s/mol observed in squalane, octadecane, and DBT at $p_{H_2,out} = 4$ bar and $p_{CO_2,out} = 1$ bar (left), and $c_{H_2,L} = 7.23$ mol/m³ and $c_{CO_2,L} = 5.72$ mol/m³ (right).

These discrepancies can be explained by the different gas solubility offered by the liquids: at identical H_2 and CO_2 concentrations in the liquid phase, all the experimental CO_2 reaction rates are similar to each other. The highest $r_{3PM,exp}$ is obtained in octadecane, while $r_{3PM,exp}$ determined in squalane and DBT are about 4 % to 12 % lower as compared to octadecane experiments. The slightly lower $r_{3PM,exp}$ in DBT as compared to squalane and octadecane can be explained by the higher H_2O solubility in DBT. H_2O has a negative influence on $r_{3PM,exp}$ (see section 5.4.3.2). Hence, the higher H_2O concentration in DBT as compared to squalane results in lower $r_{3PM,exp}$. Other explanation is based on molecular interactions during solvation: the Henry's law constants necessary for the calculation of gas concentrations in the liquid phase were derived from experiments with pure gases and do not account for intermolecular interactions. Hence, real gas concentrations in the liquid phase can differ from the ones derived from pure gas solubility correlations. Further explanation lies in solvent adsorption effect on the catalyst active sites: DBT is an aromatic compound with a higher adsorption as compared to paraffins like octadecane and squalane [217, 221]. Consequently, DBT can block more active sites as compared to octadecane and squalane, which results in lower CO_2 reaction rates. Nevertheless, the difference in CO_2 reaction rates between the investigated three-phase systems remains low and is covered by measurement uncertainty.

Based on these results, it can be concluded that gas concentration in the liquid phase and not gas partial pressure is the relevant parameter to describe the CO_2 methanation reaction kinetics in a three-phase reactor. With this background, a reaction rate equation for the three-phase CO_2 methanation was derived from kinetic experiments performed in DBT.

5.4.3 Development of a reaction rate equation

For the development of a three-phase methanation kinetic rate equation, kinetic experiments were performed in DBT. In a first set of experiments performed at 260 °C, outlet educt and product gas partial pressures were systematically varied to identify their influence on the CO₂ reaction rate. For the remaining experiments, educt and product partial pressures were simultaneously varied between temperatures of 220 °C to 320 °C, as shown in Table 5.3.

Table 5.3: Variation of process parameters for the development of a kinetic rate equation.

Parameters	Variation	Units
T	220 - 320	°C
$p_{\text{CO}_2,\text{out}}$	0.5 - 2.3	bar
$p_{\text{H}_2,\text{out}}$	2.9 - 12.9	bar
$p_{\text{CH}_4,\text{out}}$	0.04 - 1.4	bar
$p_{\text{H}_2\text{O},\text{out}}$	0.08 - 2.8	bar
p_{R}	8 - 18	bar
$\tau_{\text{mod},\text{CO}_2}$	1.7 - 35	kg·s/mol
m_{cat}	0.16 - 0.8	10 ⁻³ ·kg
$(\text{H}_2/\text{CO}_2)_{\text{G},\text{out}}$	1.71 - 12.796	-
$(\text{H}_2/\text{CO}_2)_{\text{L}}$	0.58 - 4.35	-

Each catalyst batch used for the reaction kinetic experiments was operated under three-phase methanation conditions for at least 300 h and no catalyst deactivation was observed during this period of time. With the results of 91 verified experiments, a three-phase methanation kinetic rate equation was developed according to section 5.3.3.

5.4.3.1 Educt influence on the CO₂ reaction rate

The influence of H₂ concentration on the CO₂ reaction rate at 260 °C is shown in Figure 5.7. $r_{3\text{PM},\text{exp}}$ is increased by 52 % when $c_{\text{H}_2,\text{L}}$ rises from 2.8 to 12.9 bar. Consequently, the H₂ reaction order derived from logarithmic linearization of the results shown in Figure 5.7 is about 0.3 at 260 °C. By increasing the reaction temperatures from 220 to 320 °C an increase in H₂ reaction order from ca. 0.25 to 0.45 can be observed (see Figure L.1 in the Appendix). The positive influence of H₂ concentration on the CO₂ reaction rate has been already reported in the literature with H₂ reaction orders ranging from 0.2 to 1 [27, 32, 35, 37, 105, 106, 110].

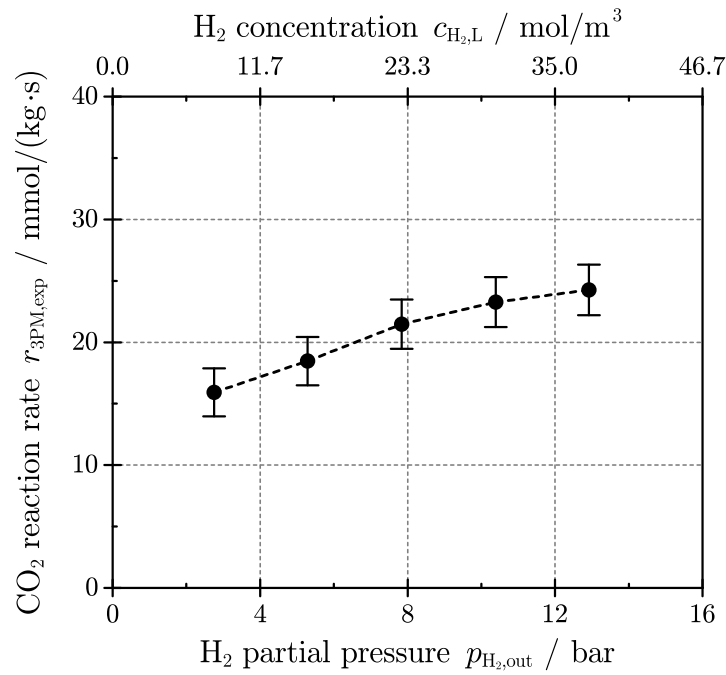


Figure 5.7: Influence of H₂ concentration on the CO₂ reaction rate ($T = 260$ °C, $p_{\text{R}} = 18$ bar, $p_{\text{CO}_2,\text{out}} = 1$ bar, $p_{\text{CH}_4,\text{out}} = 0.27$ bar, $p_{\text{H}_2\text{O},\text{out}} = 0.79$ bar, $\tau_{\text{mod},\text{CO}_2} = 2.7$ kg·s/mol).

The impact of CO₂ concentration on the CO₂ reaction rate at 260 °C is shown in Figure 5.8.

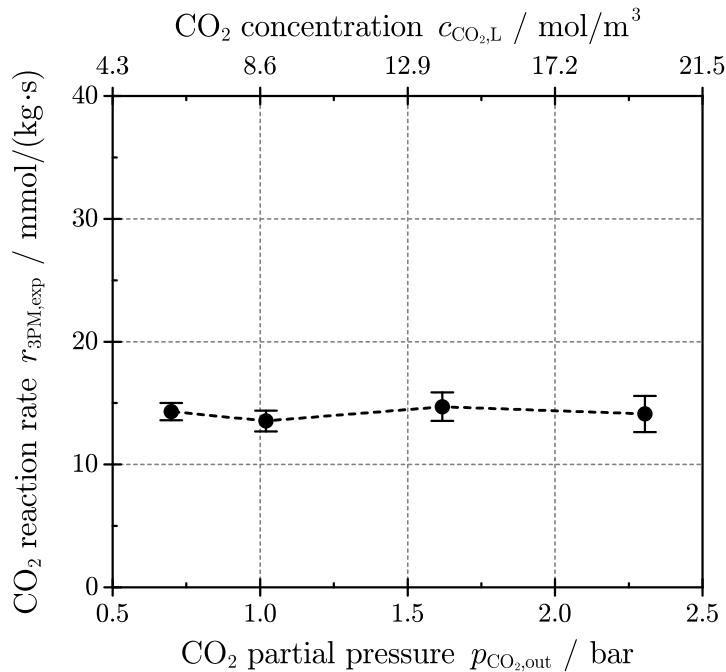


Figure 5.8: Influence of CO₂ concentration on the CO₂ reaction rate ($T = 260$ °C, $p_{\text{R}} = 18$ bar, $p_{\text{H}_2,\text{out}} = 4$ bar, $p_{\text{CH}_4,\text{out}} = 0.27$ bar, $p_{\text{H}_2\text{O},\text{out}} = 0.79$ bar, $\tau_{\text{mod},\text{CO}_2} = 7.6 - 20$ kg·s/mol).

The influence of $c_{\text{CO}_2,\text{L}}$ is significantly smaller as compared to $c_{\text{H}_2,\text{L}}$. The CO_2 reaction rate is only increased by ca. 15 % when $c_{\text{CO}_2,\text{L}}$ is doubled. Considering the other kinetic experiments performed at temperatures from 220 to 320 °C, an increase in CO_2 reaction order from 0.1 to 0.18 is observed by increasing temperatures (see Figure L.2 in the Appendix). The positive influence of CO_2 concentration on $r_{3\text{PM},\text{exp}}$ has been also described in the literature, however, with higher CO_2 reaction orders ranging from 0.33 to 1 [27, 32, 35, 37, 105, 106]. Lim et al. [110] reported a small influence of CO_2 concentration on the CO_2 reaction rate at high CO_2 concentrations and stoichiometric H_2/CO_2 ratios. They reported an influence of CO_2 concentration on $r_{3\text{PM},\text{exp}}$ only at low CO_2 concentrations and over-stoichiometric H_2/CO_2 ratios. In this work, due to the different H_2 and CO_2 gas solubility ($H_{\text{H}_2,px} \gg H_{\text{CO}_2,px}$), the reaction system is characterized by sub-stoichiometric H_2/CO_2 ratios. Hence, under 3PM operating conditions, H_2 and not CO_2 is the limiting reactant. Accordingly, the CO_2 reaction order is low.

5.4.3.2 Product influence on the CO_2 reaction rate

Figure 5.9 shows that an increase in $c_{\text{CH}_4,\text{L}}$ has no impact on $r_{3\text{PM},\text{exp}}$ at 260 °C. This trend can be observed for other reaction temperatures. Therefore, CH_4 reaction order is 0. This finding is also reported for two-phase experiments [27, 32, 35, 37, 105, 106, 110].

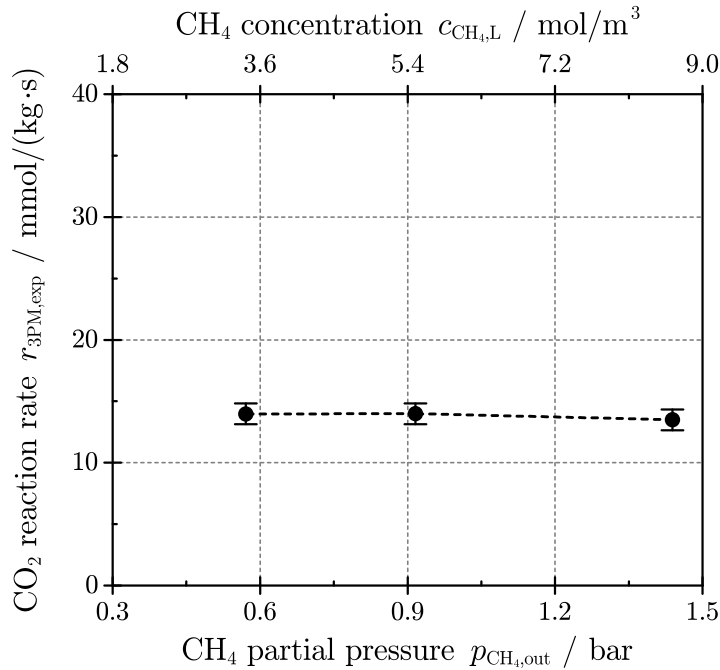


Figure 5.9: Influence of CH_4 concentration on the CO_2 reaction rate ($T = 260$ °C, $p_{\text{R}} = 8$ bar, $p_{\text{CO}_2,\text{out}} = 1$ bar, $p_{\text{H}_2,\text{out}} = 4$ bar, $p_{\text{H}_2\text{O},\text{out}} = 0.53$ bar, $\tau_{\text{mod},\text{CO}_2} = 14.9$ kg·s/mol).

The influence of H_2O concentration on $r_{3\text{PM},\text{exp}}$ at 260 °C is shown in Figure 5.10. A small increase in $c_{\text{H}_2\text{O},\text{L}}$ leads to a reduction of $r_{3\text{PM},\text{exp}}$ by about 10 %. However, a further increase in $c_{\text{H}_2\text{O},\text{L}}$ does not significantly decrease $r_{3\text{PM},\text{exp}}$. In addition, the decrease in $r_{3\text{PM},\text{exp}}$ with increasing $c_{\text{H}_2\text{O},\text{L}}$ is more pronounced with increasing temperatures: the H_2O reaction order

increases from 0.1 to 0.13 in the temperature range of 220 to 320 °C (see Figure L.3 in the Appendix). The inhibiting effect of H₂O on the CO₂ methanation reaction kinetics has been also observed by Lim et al. [110]. According to them, the negative influence of H₂O on the CO₂ methanation rate is explained by the adsorption of H₂O on the catalyst active sites, preventing H₂ or CO₂ to adsorb and further react on the catalyst.

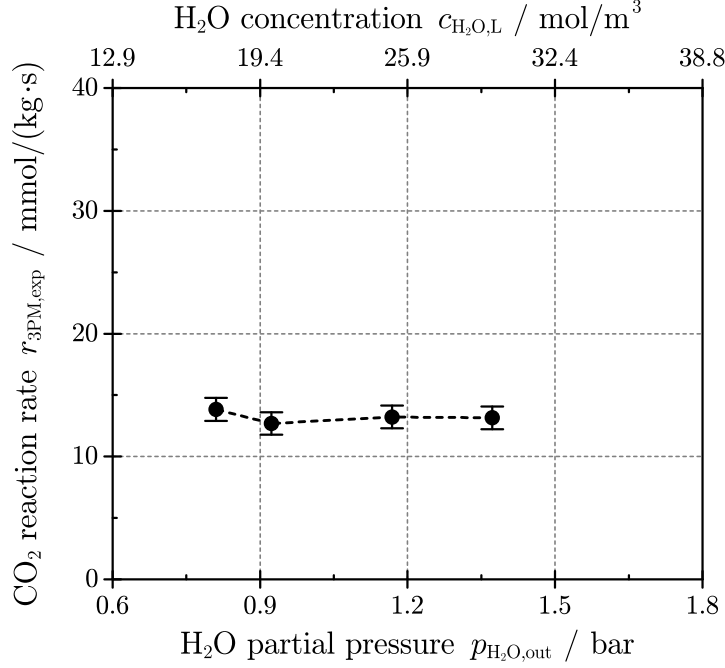


Figure 5.10: Influence of H₂O concentration on the CO₂ reaction rate ($T = 260$ °C, $p_{\text{R}} = 18$ bar, $p_{\text{CO}_2,\text{out}} = 1$ bar, $p_{\text{H}_2,\text{out}} = 4$ bar, $p_{\text{CH}_4,\text{out}} = 0.55$ bar, $\tau_{\text{mod,CO}_2} = 16.7$ kg·s/mol).

5.4.3.3 Reaction rate equation

A kinetic rate equation has been derived from the experiments performed at 260 °C in the previous section, and from the experiments performed at temperatures ranging from 220 to 320 °C which are collected in Appendix L. The kinetic rate equation resulting from the least-square minimization is described in Eq. 5.18.

$$r_{3\text{PM,cal}} = 3.90699 \cdot 10^5 \cdot \exp\left(\frac{-79061}{R \cdot T}\right) \cdot \frac{c_{\text{H}_2,\text{L}}^{0.3} \cdot c_{\text{CO}_2,\text{L}}^{0.1}}{(1 + 1 \cdot c_{\text{H}_2\text{O,L}})^{0.1}} \cdot K \quad (5.18)$$

An activation energy E_A of 79 kJ/mol - typical for CO₂ methanation - is retrieved from the rate equation optimization. The parity plot between experimental CO₂ reaction rate and CO₂ reaction rate derived from Eq. 5.18 is shown in Figure 5.11. A good agreement between the experimental results and the model is obtained. Assessing a normal distribution, a standard deviation between $r_{3\text{PM,exp}}$ and $r_{3\text{PM,cal}}$ of 6.0 % is achieved.

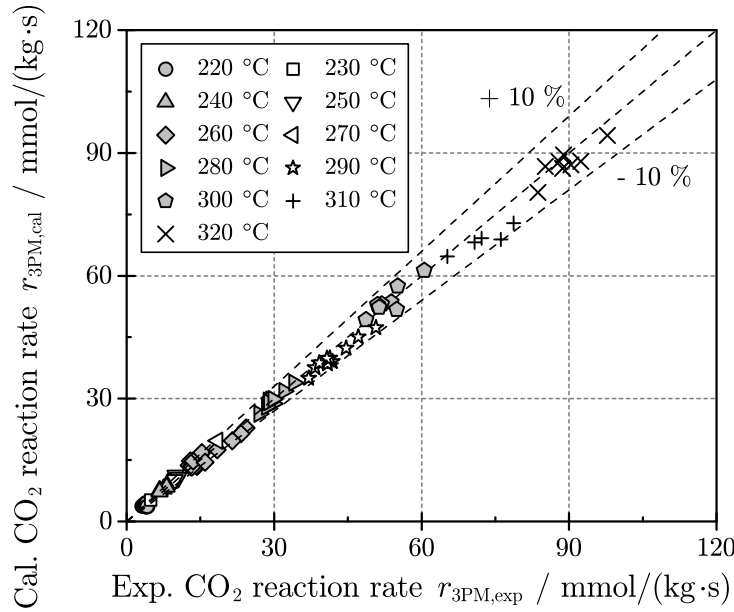


Figure 5.11: Parity plot between experimental and calculated CO₂ reaction rates. Reaction rates are calculated with the kinetic rate equation described in Eq. 5.18.

5.4.3.4 Sensitivity analysis

In order to understand the discrepancy between calculated and experimental CO₂ reaction rates, a sensitivity analysis was carried out on the reaction rate equation given in Eq. 5.18. For this analysis, the reaction temperature as well as CO₂, H₂, and H₂O concentrations were varied according to the uncertainties listed in Table 5.4. An extreme case scenario was obtained by setting simultaneously the uncertainty of the parameters to their maximum or minimum value. These uncertainties were calculated using the differential method described in the Appendix N.

Table 5.4: Measurement uncertainties for the sensitivity analysis.

Parameters	Variation
T	± 1 K
p_i	± 4 %
$H_{H_2,pc}$	± 14 %
$H_{CO_2,pc}$	± 5 %
$H_{H_2O,pc}$	± 5 %

Figure 5.12 shows the influence of measurement uncertainties on the calculated CO₂ reaction rates. $c_{H_2,L}$ has the strongest impact on $r_{3PM,cal}$ followed by temperature, $c_{CO_2,L}$ and $c_{H_2O,L}$. The decreasing influence of gas concentration from H₂ to H₂O is directly related to the gas species reaction order expressed in Eq. 5.18 as well as the uncertainty of each Henry's law constant. On the other hand, the temperature impact on $r_{3PM,cal}$ is related to the reaction activation energy. Considering the extreme case scenario, the measurement uncertainties result in a deviation in $r_{3PM,cal}$ of ca. 8.5 %. These uncertainties can therefore explain the standard deviation between $r_{3PM,exp}$ and $r_{3PM,cal}$ observed in Figure 5.11. To reach a better

match between $r_{3\text{PM,exp}}$ and $r_{3\text{PM,cal}}$ it is mandatory to improve the measurement accuracy, especially the confidence in $H_{\text{H}_2,pc}$ which exerts the strongest influence on the calculated CO_2 reaction rates.

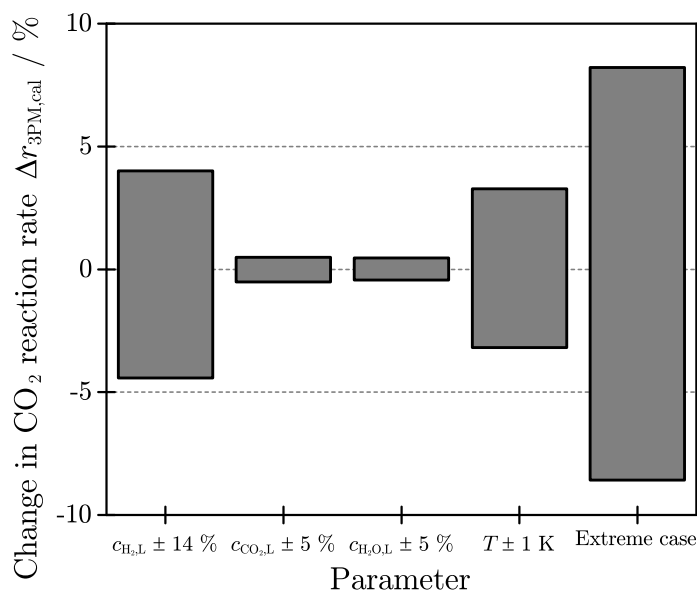


Figure 5.12: Sensitivity analysis on the three-phase CO_2 methanation kinetic rate equation described in Eq. 5.18 ($T = 260 \text{ }^\circ\text{C}$, $c_{\text{H}_2,\text{L}} = 11.71 \text{ mol/m}^3$, $c_{\text{CO}_2,\text{L}} = 8.51 \text{ mol/m}^3$, $c_{\text{CH}_4,\text{L}} = 1.24 \text{ mol/m}^3$, $c_{\text{H}_2\text{O},\text{L}} = 9.68 \text{ mol/m}^3$).

Further source of discrepancy between experimental and calculated data is related to the different catalyst samples that have been used in the experiments. For the development of a kinetic rate equation, only one sample of catalyst is usually applied. However, 9 different catalyst samples were used in the experiments described in this chapter. Even though the catalyst samples were taken from the same catalyst batch, each sample shows slightly different catalytic activities compared to the others. These differences can be related to the uncertainty during catalyst weighing or by catalyst reoxidation during catalyst suspension in the liquid phase.

5.5 Summary

The objectives of this chapter were to identify an optimum methanation catalyst which does not deactivate and crack the liquid phase dibenzyltoluene under CO_2 methanation operating conditions, to clarify the influence of a liquid phase on the CO_2 methanation reaction kinetics, and to develop a kinetic rate equation for three-phase CO_2 methanation. For this purpose, experiments were carried out in a continuous stirred-tank slurry reactor.

A commercial Ni/SiO_2 catalyst suspended in dibenzyltoluene was found to be stable under CO_2 methanation conditions, while delivering satisfying CO_2 conversion as well as high selectivity to CH_4 (see Figures 5.3 and 5.4). The other tested nickel catalysts were either deactivating or showing lower activity and CH_4 selectivity. The good stability of the Ni/SiO_2 catalyst as

compared to the Ni/Al₂O₃ catalyst used previously in the PhD thesis of Götz [8] is probably related to the lower acidity of the catalyst support which is less prompt to catalyze cracking of the suspension liquid dibenzyltoluene. Next to nickel catalysts, commercial ruthenium-based catalysts were tested. They showed almost no CO₂ conversion with almost no selectivity to CH₄. This poor catalyst activity is probably related to an unadapted catalyst reduction method.

Choosing the commercial Ni/SiO₂ catalyst for further experiments, the influence of the liquid phase on the CO₂ methanation reaction kinetics was investigated. To do so, three different liquid phases, namely squalane, octadecane and dibenzyltoluene were used as suspension liquid for three-phase CO₂ methanation experiments performed at same temperature and either at same gas partial pressures or same gas concentrations in the liquid phase (see Figure 5.6). At same gas partial pressures, the three reacting systems showed different CO₂ reaction rates. However, at same gas concentrations in the liquid phase, similar CO₂ reaction rates were observed. Hence, the relevant parameter to describe the three-phase CO₂ methanation reaction kinetics is not gas partial pressure but gas concentration in the liquid phase. Furthermore, a liquid phase does not influence the CO₂ methanation reaction kinetics but impacts the available reactant concentrations around the catalyst resulting from liquid-specific gas solubilities.

Based on these findings, 91 reaction kinetic measurements were performed in dibenzyltoluene at a CO₂ partial pressure of 1 bar and temperatures between 220 °C and 320 °C to derive a kinetic rate equation describing the three-phase CO₂ methanation kinetics. The kinetic rate equation (see Eq. 5.18) is able to predict the experimental reaction rates with a standard deviation of 6.0 % (see Figure 5.11). Besides, a sensitivity analysis (see Figure 5.12) showed that measurement accuracy related to H₂ solubility in DBT must be improved to reach a better fit between experimental and calculated reaction rates.

6 Comparison between two-phase and three-phase CO₂ methanation reaction kinetics

In chapter 5, it was postulated that (i) a liquid phase influences the effective reaction rate but not the intrinsic chemical reaction rate and (ii) gas concentration in the liquid phase, not gas partial pressure, is the relevant parameter to describe the CO₂ methanation reaction kinetics.

For the experiments performed in chapter 5, several catalyst samples from a single catalyst batch were prepared: they were reduced in a fixed-bed reactor (see section 5.3.1.1) and then suspended in different liquids under an inert atmosphere before proceeding to the methanation experiments. As it could not be fully excluded that catalyst reoxidation and deactivation took place during the catalyst suspension procedure, there was a need to confirm statements (i) and (ii) in a reacting system where catalyst reoxidation is excluded. In addition, it was reported in chapter 5 that a significant part of experimental uncertainty is related to the calculation of H₂ concentration in the liquid phase, which depends on the knowledge of Henry's law constants. As the solubility of H₂ in organic oils is usually low, the experimental uncertainty of the corresponding Henry's law constants is quite high (see chapter 4).

This chapter intends to confirm statements (i) and (ii) using a different experimental approach. If the liquid phase only influences the reaction rate in terms of effective gas concentrations at the catalyst surface, operating a two-phase (gas/solid) fixed-bed reactor under three-phase methanation operating conditions should lead to identical reaction rates. Graaf et al. followed the same path to study the influence of a liquid phase on three-phase methanol synthesis kinetics: they measured the methanol synthesis kinetics in a two-phase reactor [226] and then in a three-phase reactor [211, 225, 232]. They showed that the activation energy derived from three-phase methanol synthesis experiments is much lower than the activation energy derived from two-phase methanol synthesis experiments [225]. In contrary to the statement in chapter 5 they concluded that the liquid phase influences significantly the reaction kinetics of the methanol synthesis.

In this chapter, kinetic experiments were carried out in a two-phase fixed-bed reactor under three-phase CO₂ methanation conditions. Hereby, the influence of temperature and reactant as well as product partial pressures on the two-phase methanation (2PM) reaction kinetics was studied. Based on these experiments a kinetic rate equation has been derived and used to reproduce three-phase CO₂ reaction rates obtained from experiments performed in chapter 5.

The following experiments were carried out during the master thesis of Ulli Hammann [229]

and the major part of the following results was published in [233].

6.1 Experimental setup

The experiments were carried out in the experimental setup shown in Figure 6.1, which is similar to the one used by Iglesias et al. [223, 234].

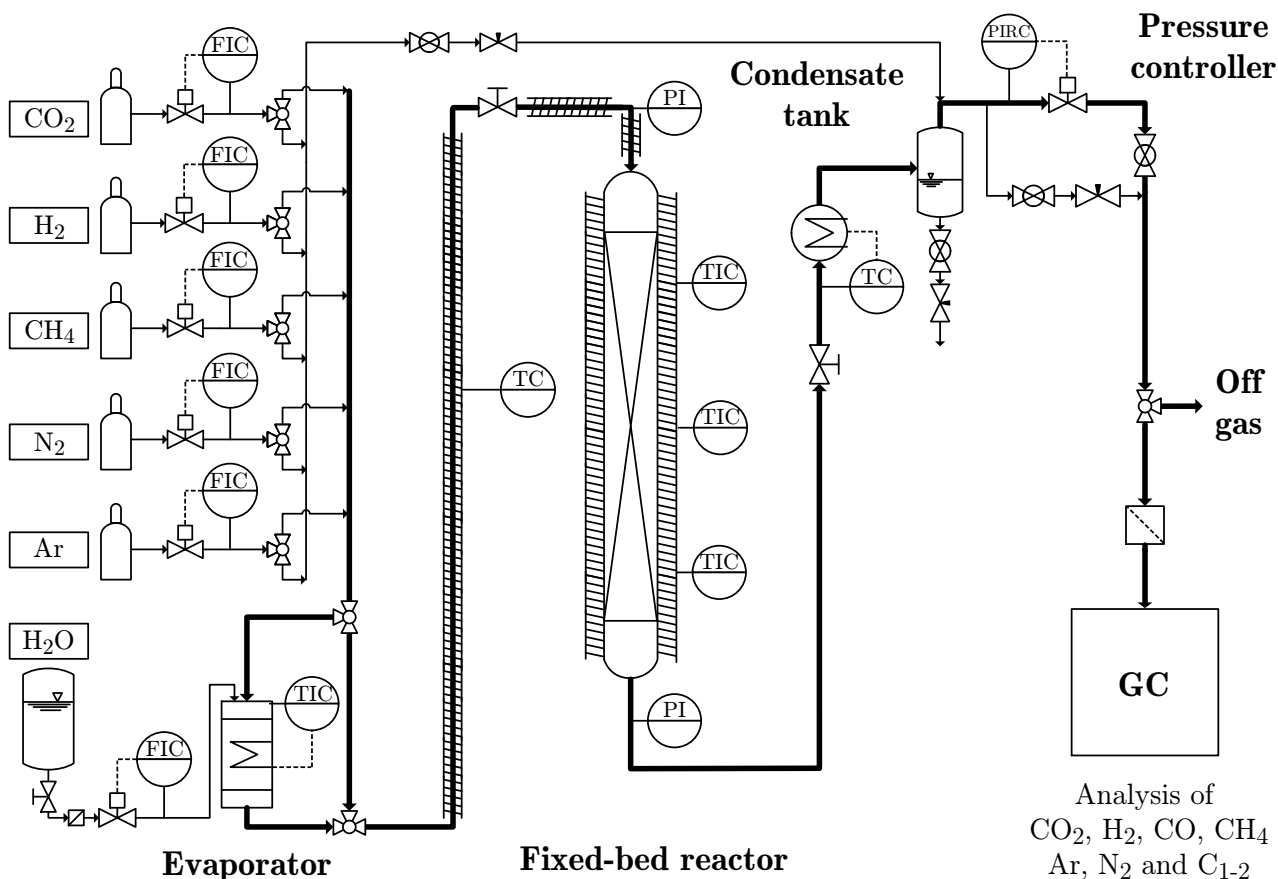


Figure 6.1: Flow scheme of the experimental setup.

The gases CO₂, H₂, CH₄, H₂O, Ar, and N₂ with purities superior to 99.995 % were supplied via a set of mass flow controllers (*Bronkhorst*). The gas mixture was heated up to the desired inlet temperature before entering the reactor.

The reactor was a glass tube ($d_t = 8$ mm and $L_t = 700$ mm) used as plug flow reactor (PFR). The glass tube was filled with catalyst particles ($d_p = 50 - 100$ μm) diluted by inert SiO₂ particles ($d_p = 100 - 160$ μm) in order to mitigate temperature hot spots within the particle bed. The weight ratio of catalyst to SiO₂ is 1 to 8.

The catalyst particle size range was chosen to minimize pressure drop and to rule out inter- or intra-particle mass and heat transfer limitations [235–237]. The absence of intra-particle mass transfer limitation was validated by the Weisz-Prater criterion [235] for each kinetic measurement. The temperature profile along the catalyst bed was measured with a moveable thermocouple placed in a centrally positioned thermowell. A bed of inert particles was placed

in front of the catalyst bed to serve as gas mixing and preheating zone. A second bed of inert particles was positioned after the catalyst bed to adjust the vertical position of the reaction zone to one of the heating blocks. The glass reactor itself was placed in a stainless-steel tube to allow experiments at high pressures. The annular space between the glass and the metal reactor was sealed with an O-ring to prevent gas recirculation and bypass effects. The steel tube was heated via three heating blocks which were insulated with glass wool against the environment. This construction is shown in Figure O.2 in the Appendix.

Isothermal conditions along the fixed bed were systematically verified using the moveable thermocouple, i.e. the axial temperature spread (ΔT_{ax}) was below 1 K for all experiments. Isothermal conditions were reached by application of high gas velocities and fine tuning of the three reactor heating blocks. Two catalyst beds were prepared for the experiments reported in this work: one bed with 0.5 g of catalyst and a second bed with 0.1 g of catalyst. Indeed, isothermal condition could not be achieved with the first catalyst bed at temperatures higher than 260 °C. With the second catalyst bed, isothermal conditions were reached even for the highest investigated reactor temperature of 300 °C.

At the reactor outlet, the product gas was cooled to 15 °C to condense most of the produced water. After passing a pressure controller (*Bronkhorst*), the dry product gas was analyzed in a gas chromatograph (GC 7890A, *Agilent*) for CH₄, CO₂, CO, Ar, N₂, H₂, C₂H₄, and C₂H₆.

6.2 Materials

The catalyst used in this chapter was a commercially available Ni/SiO₂ catalyst for methanation applications. It was from the same catalyst batch as used in the previous three-phase methanation experiments. Prior to each experiment, the catalyst was reduced for 24 hours at 400 °C in an Ar/H₂ = 1/1 atmosphere flowing at 40 l/h (STP) in the experimental setup shown in Figure 6.1. After the reduction procedure, the reactor was cooled under the same Ar/H₂ = 1/1 atmosphere to reaction temperature and the desired gas atmosphere was applied. The same reduction method was applied for the catalyst used in three-phase methanation experiments (see chapter 5), i.e. the catalyst was reduced in a fixed-bed reactor under the above-mentioned conditions before being suspended in the liquid phase under an inert atmosphere.

Previous three-phase methanation kinetic investigations were conducted with a pre-reduced catalyst and catalyst mass-specific reaction rates were determined with the reduced and not the oxidized catalyst mass. In this work, oxidized catalyst particles were placed inside the fixed-bed reactor. Hence, knowledge of the catalyst mass loss after the reduction procedure was required to compare two-phase and three-phase CO₂ methanation reaction rates. To gain such knowledge, thermogravimetric analyses (TGA) were performed in a TGA device, model 209 F1 provided by *Netzsch*: three oxidized catalyst samples from 16 to 20 mg were first heated to 400 °C with a ramp of 8 K/min and then reduced for 24 h. For both heating and reduction programs, a volume flow rate of 50 ml/min (STP) with a composition N₂/H₂ = 1/1 was sent through the TGA device. The average catalyst mass loss after reduction was 22.88 %. Using this mass loss, the mass of oxidized catalysts applied to the fixed-bed reactor could

be converted to the reduced catalyst mass.

6.3 Experimental method

6.3.1 Experimental procedure

For the development of a kinetic rate equation, a total of 213 experiments were conducted under systematic variation of the parameters listed in Table 6.1 in order to obtain broad range of operating conditions and CO₂ conversion ($0.02 \leq X_{\text{CO}_2} \leq 0.75$).

Table 6.1: Investigated experimental conditions for the development of a kinetic rate equation.

T °C	$p_{\text{H}_2,\text{in}}$ bar	$p_{\text{CH}_4,\text{in}}$ bar	$p_{\text{H}_2\text{O},\text{in}}$ bar	$\tau_{\text{mod,CO}_2}$ kg·s/mol
200; 220; 240; 260; 280; 300	1; 2; 3; 4; 5	0; 0.4; 0.8	0; 0.4; 0.8; 1.2; 1.6	1.6; 2; 2.7; 8; 10; 13

All experiments were conducted with an inlet CO₂ partial pressure of 1 bar and a reactor pressure of 9.2 bar. N₂ was fed at a constant volume flow rate of 50 ml/min: it was used as reference gas for closing the system mass balance. Ar was used as inert buffer gas: the volume flow rate was adjusted in order to maintain a constant overall volume flow rate of 620 ml/min (STP) at the reactor inlet. A broad range of H₂/CO₂ ratio from 1 to 5 was chosen to cover three-phase methanation sub-stoichiometric conditions with typical H₂/CO₂ ratios of 1 to 2, and to also cover the H₂/CO₂ ratios of conventional two-phase methanation. In addition to the experiments shown in Table 6.1, experiments were performed to investigate the influence of inlet CO₂ partial pressure on the CO₂ reaction rates. For these experiments, $p_{\text{CO}_2,\text{in}}$ was varied from 0.75 to 1.25 bar resulting in H₂/CO₂ ratio ranging from 0.8 to 6.6. For both investigated catalyst beds, no deactivation was observed during the experiments (time on stream higher than 700 h for each catalyst bed).

To check the applicability of PFR behavior on the fixed-bed reactor, the Bodenstein number Bo , which compares advective and diffusive mass transfer, was calculated for each experimental condition according to Eq. 6.1. The calculation of the axial Peclet number Pe'_{ax} is described in the Appendix D.

$$Bo = Pe'_{\text{ax}} \cdot \frac{L_{\text{R}}}{d_{\text{P}}} \quad (6.1)$$

The Bodenstein number range was 541 - 1201. Therefore, the PFR assumption ($Bo > 100$) was verified for all applied experimental conditions [238].

6.3.2 Data analysis and calculations

N_2 was used as reference gas to determine the reactor outlet molar flow rate for each gas component. Knowing the reactor inlet molar flow rate \dot{n}_{in} as well as the N_2 molar fraction at the reactor inlet and outlet from gas chromatographic (GC) analysis, the outlet molar flow rate of each gas component was calculated from the measured gas molar fraction $y_{i,out}$ according to Eq. 6.2.

$$\dot{n}_{i,out} = \dot{n}_{out} \cdot y_{i,out} = \dot{n}_{in} \cdot \frac{y_{N_2, in}}{y_{N_2, out}} \cdot y_{i,out} \quad (6.2)$$

During each experiment, attention was paid to the atomic balance over the reactor; measurements with a carbon and hydrogen balance error higher than $\pm 1\%$ were rejected. H_2O could not be detected by the applied GC; the outlet H_2O molar flow rate was calculated from the oxygen balance over the reactor. The CO_2 conversion X_{CO_2} was expressed with Eq. 6.3:

$$X_{CO_2} = \frac{\dot{n}_{CO_2,in} - \dot{n}_{CO_2,out}}{\dot{n}_{CO_2,in}} \quad (6.3)$$

With the modified CO_2 residence time τ_{mod,CO_2} , see Eq. 6.4,

$$\tau_{mod,CO_2} = \frac{m_{cat}}{\dot{n}_{CO_2,in}} \quad (6.4)$$

the integral CO_2 reaction rate \bar{r}_{2PM} was calculated according to Eq. 6.5.

$$\bar{r}_{2PM} = \frac{X_{CO_2}}{\tau_{mod,CO_2}} \quad (6.5)$$

The true CO_2 reaction rate r_{2PM} was calculated solving the PFR design equation Eq. 6.6:

$$\tau_{mod,CO_2} = \int_0^{X_{CO_2}} \frac{dX_{CO_2}}{r_{2PM}} \quad (6.6)$$

To solve Eq. 6.6, a kinetic rate equation r_{2PM} had to be derived beforehand.

In the following diagrams, the integral reaction rate \bar{r}_{2PM} which was directly derived from the experiments was used to describe the experimental results. The integral CO_2 reaction rate was used rather than the CO_2 conversion, as it takes into account the CO_2 residence time within the reactor (τ_{mod,CO_2}). This was particularly important when the influence of CO_2 partial pressure on the methanation reaction kinetics was investigated (see Figure 6.4 and Figure 6.5). Indeed, for these experiments the CO_2 partial pressure and the CO_2 residence time had to be varied simultaneously through variation of the inlet volume flow rate of CO_2 , while keeping the other relevant operating parameters (except N_2 volume flow rate) constant.

For each measurement, data accuracy was evaluated with the method of partial derivatives. The resulting error bars are given in each of the following diagrams.

6.3.3 Development of a reaction rate equation

A power law rate equation with product limitation (see Eq. 6.7) as reported in chapter 5 was used to describe the CO₂ reaction rates observed in this work. Side CO₂ reactions to product other than CH₄ (e.g. CO) were not considered as the selectivity to CH₄ was higher than 90 % for all the experiments.

$$r_{2\text{PM}} = k \cdot \frac{c_{\text{H}_2}^\alpha \cdot c_{\text{CO}_2}^\beta}{(1 + K_{\text{H}_2\text{O}} \cdot c_{\text{H}_2\text{O}})^\gamma} \cdot K \quad (6.7)$$

k is the reaction rate constant as defined in Eq. 6.8, while $K_{\text{H}_2\text{O}}$ describes the adsorption constant of H₂O on the nickel catalyst (see Eq. 6.9). As the adsorption enthalpy of H₂O was not found in literature, $K_{\text{H}_2\text{O}}$ was set to 1 m³/mol in this work, i.e. the influence of H₂O on the reaction rate does not vary with temperature (see section 6.4.1). Other values were tested for $K_{\text{H}_2\text{O}}$ and delivered similar fits.

$$k = k_0 \cdot \exp\left(\frac{-E_A}{R \cdot T}\right) \quad (6.8)$$

$$K_{\text{H}_2\text{O}} = K_{\text{H}_2\text{O},0} \cdot \exp\left(-\frac{\Delta h_{\text{H}_2\text{O},\text{ad}}}{RT}\right) \quad (6.9)$$

K describes the limitation of $r_{2\text{PM}}$ when the reaction system approaches the chemical equilibrium described by K_{eq} (see Eq. 6.10). Usually, gas partial pressures are used to derive kinetic rate equation for CO₂ methanation [27, 32, 35, 37, 102–108, 110–112]. However, gas concentrations were used here to investigate the principles of three-phase methanation. Gas concentrations c_i were estimated with Eq. 6.11 which is valid under the premise of ideal gas behavior.

$$K = 1 - \frac{p_{\text{H}_2\text{O},\text{out}}^2 \cdot p_{\text{CH}_4,\text{out}}}{p_{\text{H}_2,\text{out}}^4 \cdot p_{\text{CO}_2,\text{out}}} \cdot \frac{p_0^2}{K_{\text{eq}}} \quad (6.10)$$

$$c_i = \frac{p_i}{R \cdot T} \quad (6.11)$$

The chemical equilibrium constant K_{eq} was estimated through minimization of the system's Gibb's enthalpy. The species' Gibb's enthalpies were calculated based on the species' enthalpies and entropies taken from NIST Chemistry WebBook [231]. The reaction kinetic parameters k , α , β , and γ were determined by a least-square minimization of the deviation between calculated CO₂ conversion $X_{\text{CO}_2,\text{cal}}$, (derived from Eq. 6.7) and experimentally observed CO₂ conversion $X_{\text{CO}_2,\text{exp}}$ (Eq. 6.3). As a first step α , β , and γ were guessed and k was determined for each investigated temperature. Then, k_0 and E_A were calculated from linear regression in an Arrhenius plot (see Eq. 6.12). The deviation between $X_{\text{CO}_2,\text{cal}}$ and $X_{\text{CO}_2,\text{exp}}$ was determined and α , β , γ , and $K_{\text{H}_2\text{O}}$ were further varied until the deviation reached a minimum.

$$\log_{10} k = \log_{10} k_0 - \frac{E_A}{R \cdot \ln 10} \cdot \frac{1}{T} \quad (6.12)$$

6.4 Results and Discussion

6.4.1 Influence of temperature and gas partial pressure on the CO₂ reaction rate

The temperature influence on the integral CO₂ reaction rate $\bar{r}_{2\text{PM}}$ is shown in Figure 6.2 for H₂/CO₂ ratios ranging from 1 to 5 and temperatures ranging from 200 to 300 °C.

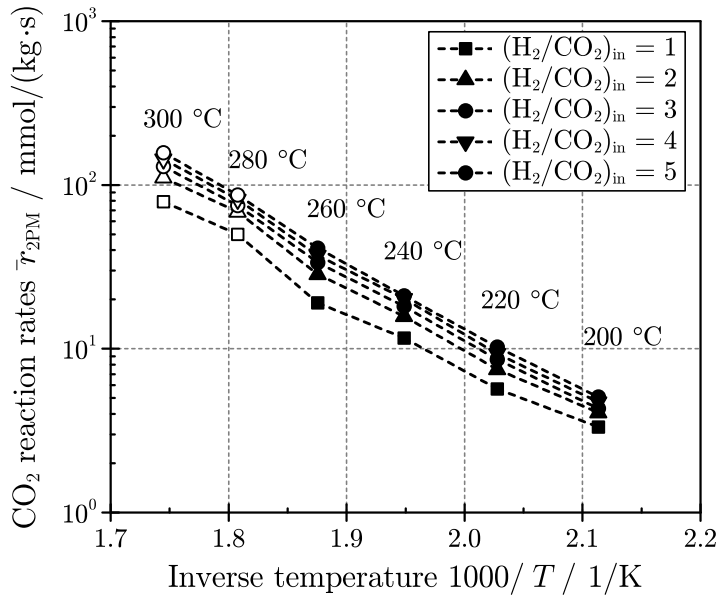


Figure 6.2: Arrhenius plot: influence of temperature and inlet H₂/CO₂ ratio on the CO₂ reaction rates ($p_R = 9.2$ bar, $p_{\text{CO}_2,\text{in}} = 1$ bar, $p_{\text{CH}_4,\text{in}} = p_{\text{H}_2\text{O},\text{in}} = 0$ bar, $\tau_{\text{mod,CO}_2} = 2$ kg·s/mol (open symbols) and $\tau_{\text{mod,CO}_2} = 10$ kg·s/mol (closed symbols)).

Between 200 and 300 °C, the integral CO₂ reaction rate is almost doubled for each temperature increase of 20 K. For all H₂/CO₂ ratios, the temperature dependence is the same, and apparent activation energies of 73 to 78 kJ/mol can be derived from the experiments. These activation energies are typical for the CO₂ methanation reaction [27, 35, 111], which confirms that the experiments were performed in absence of mass and heat transfer limitations [51]. Additionally, Figure 6.2 shows that $\bar{r}_{2\text{PM}}$ increases with increasing H₂/CO₂ ratio. This results from the positive influence of increasing H₂ partial pressure on the CO₂ reaction rates, as shown in Figure 6.3.

Figure 6.2 also shows that the influence of H₂/CO₂ ratio is more pronounced for small H₂/CO₂ ratios. This effect can be explained by the higher production of CO at small H₂/CO₂ ratios: at 240 °C the CO selectivity is about 1 % for H₂/CO₂ = 1, while it is about 0.4 % for higher H₂/CO₂ ratios. The same trend can be observed for the other investigated temperatures. As

the presence of even a few ppm of CO is known to mitigate the CO₂ methanation [35], the higher CO production for H₂/CO₂ = 1 leads to stronger mitigation of the CO₂ methanation reaction kinetics as compared to higher H₂/CO₂ ratios.

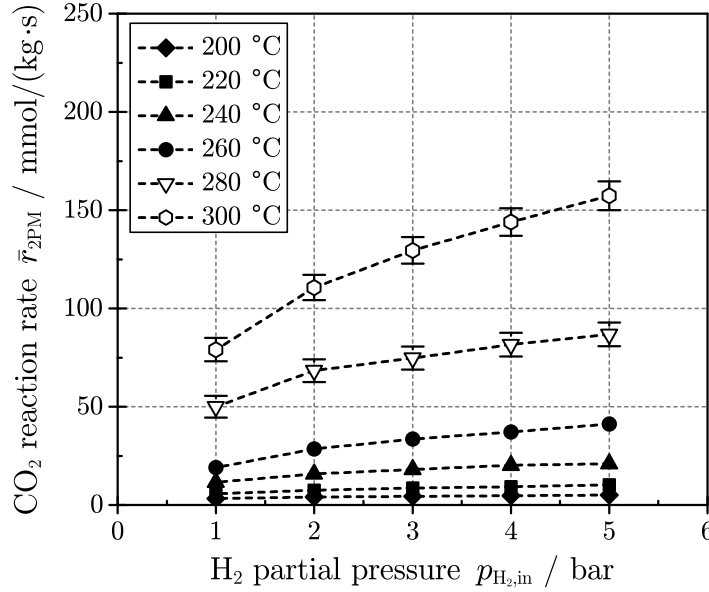


Figure 6.3: Influence of inlet H₂ partial pressure on the CO₂ reaction rate for temperatures between 200 and 300 °C ($p_{\text{R}} = 9.2$ bar, $p_{\text{CO}_2, \text{in}} = 1$ bar, $p_{\text{CH}_4, \text{in}} = p_{\text{H}_2\text{O}, \text{in}} = 0$ bar, $\tau_{\text{mod}, \text{CO}_2} = 2$ kg·s/mol (open symbols) and $\tau_{\text{mod}, \text{CO}_2} = 10$ kg·s/mol (closed symbols)).

The influence of inlet H₂ partial pressure $p_{\text{H}_2, \text{in}}$ on the CO₂ reaction rate $\bar{r}_{2\text{PM}}$ is shown in Figure 6.3 for temperatures ranging from 200 to 300 °C. An increase in $p_{\text{H}_2, \text{in}}$ has a positive influence on $\bar{r}_{2\text{PM}}$, which is confirmed by several publications [32, 35, 105, 106, 110, 111]. At 300 °C, $\bar{r}_{2\text{PM}}$ is enhanced by 70 % when $p_{\text{H}_2, \text{in}}$ is increased from 1 to 4 bar. As previously reported, the increase in $\bar{r}_{2\text{PM}}$ is more pronounced for $p_{\text{H}_2, \text{in}}$ in the range of 1 to 2 bar as compared to higher $p_{\text{H}_2, \text{in}}$. With a logarithmic linearization of the experimental data depicted in Figure 6.3, the order of reaction for H₂ was determined for each investigated temperature. This order of reaction increases with increasing temperature from 0.33 to 0.42. In literature, H₂ reaction orders ranging from 0.21 to 1 have been reported [35–37, 104–107, 111].

In Figure 6.4, the influence of inlet CO₂ partial pressure $p_{\text{CO}_2, \text{in}}$ on the CO₂ reaction rate $\bar{r}_{2\text{PM}}$ is shown for an inlet H₂ partial pressure of 4 bar. An increase in $p_{\text{CO}_2, \text{in}}$ has a positive effect on $\bar{r}_{2\text{PM}}$. At 300 °C, $\bar{r}_{2\text{PM}}$ is increased by ca. 17 % when $p_{\text{CO}_2, \text{in}}$ rises from 0.75 to 1.25 bar. This trend is more significant for higher temperatures. Accordingly, the CO₂ reaction order derived from logarithmic linearization of the experimental data shown in Figure 6.4 rises from 0.07 to 0.3 between 200 and 300 °C. In literature, a positive influence of p_{CO_2} on the CO₂ reaction rate has been reported, and most of the published reaction rate equations for CO₂ methanation use a CO₂ reaction order between 0.3 and 1 [35, 36, 104–107, 111].

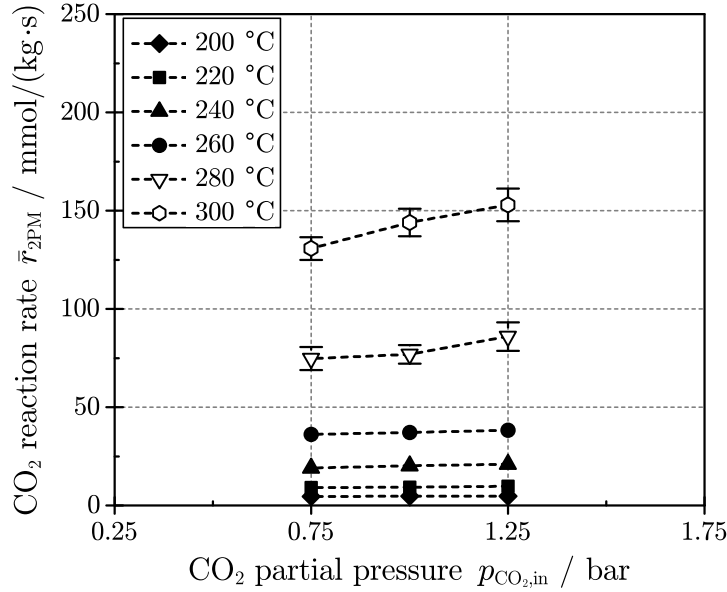


Figure 6.4: Influence of inlet CO₂ partial pressure on the CO₂ reaction rate for temperatures between 200 and 300 °C ($p_{\text{R}} = 9.2$ bar, $p_{\text{H}_2, \text{in}} = 4$ bar, $p_{\text{CH}_4, \text{in}} = p_{\text{H}_2\text{O}, \text{in}} = 0$ bar, $\tau_{\text{mod}, \text{CO}_2} = 1.6 - 2.7$ kg·s/mol (open symbols) and $\tau_{\text{mod}, \text{CO}_2} = 8 - 13$ kg·s/mol (closed symbols)).

In Figure 6.4, the influence of $p_{\text{CO}_2, \text{in}}$ on the CO₂ reaction rate is shown for near stoichiometric H₂/CO₂ ratios of 3 to 5, typical of two-phase methanation conditions. However, the findings of Figure 6.4 may not be relevant for a technical three-phase methanation process, as H₂/CO₂ ratios between 1 and 2 are typical for three-phase CO₂ methanation conditions at the catalyst surface. The effect of $p_{\text{CO}_2, \text{in}}$ on the CO₂ reaction rate for a H₂/CO₂ ratio between 0.8 and 6.6 (i.e. $p_{\text{H}_2, \text{in}}$ between 1 and 5 bar) and a temperature of 260 °C is shown in Figure 6.5. For sub-stoichiometric conditions, an increase in $p_{\text{CO}_2, \text{in}}$ leads to a small increase in $\bar{r}_{2\text{PM}}$, while the increase in $\bar{r}_{2\text{PM}}$ is more significant for $p_{\text{H}_2, \text{in}} \geq 4$ bar. The CO₂ reaction order derived from these experiments is 0.07 for sub-stoichiometric H₂/CO₂ ratios (i.e. three-phase methanation conditions), and 0.13 for H₂/CO₂ ratios ≥ 4 (i.e. two-phase methanation conditions). According to our knowledge, this observation has never been reported in the literature, because CO₂ methanation is usually investigated for stoichiometric H₂/CO₂ ratios. This effect was proven by reproduced experiments for both investigated catalyst samples and for different space time velocities. The reduced influence of $p_{\text{CO}_2, \text{in}}$ on $\bar{r}_{2\text{PM}}$ for substoichiometric H₂/CO₂ ratios can be explained by the lack of adsorbed H₂ on the catalyst surface relative to adsorbed carbon species.

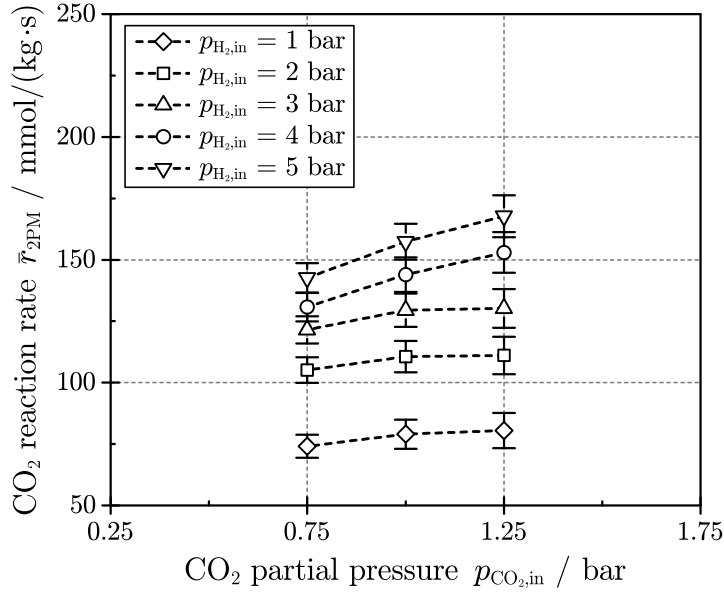


Figure 6.5: Influence of inlet CO₂ partial pressure on the CO₂ reaction rate for inlet H₂ partial pressures between 1 and 5 bar ($p_R = 9.2$ bar, $T = 260$ °C, $p_{\text{CH}_4, \text{in}} = p_{\text{H}_2\text{O}, \text{in}} = 0$ bar, $\tau_{\text{mod}, \text{CO}_2} = 1.6 - 2.7$ kg·s/mol).

The influence of inlet CH₄ partial pressure on the CO₂ reaction rate is shown in Figure 6.6 for $p_{\text{CO}_2, \text{in}} = 1$ bar, a H₂/CO₂ ratio of 4 and temperatures ranging from 200 to 300 °C. As expected, the CO₂ reaction rate is insensitive to $p_{\text{CH}_4, \text{in}}$ at any investigated temperature, which is in agreement with most literature [27, 110].

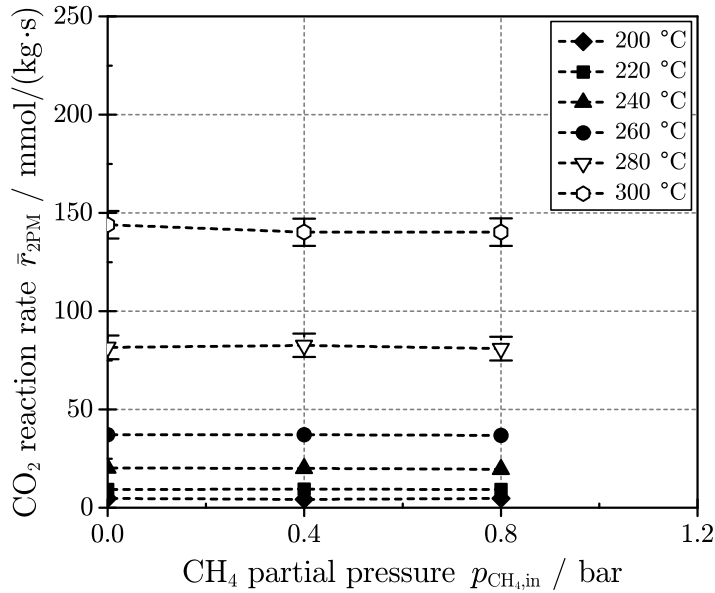


Figure 6.6: Influence of inlet CH₄ partial pressure on the CO₂ reaction rate for temperatures between 200 and 300 °C ($p_R = 9.2$ bar, $p_{\text{CO}_2, \text{in}} = 1$ bar, $p_{\text{H}_2, \text{in}} = 4$ bar, $p_{\text{H}_2\text{O}, \text{in}} = 0$ bar, $\tau_{\text{mod}, \text{CO}_2} = 2$ (open symbols) and $\tau_{\text{mod}, \text{CO}_2} = 10$ kg·s/mol (closed symbols)).

In Figure 6.7, the effect of inlet H_2O partial pressure $p_{\text{H}_2\text{O},\text{in}}$ on $\bar{r}_{2\text{PM}}$ is depicted for temperatures ranging from 240 to 300 °C as well as a CO_2 partial pressure of 1 bar and a H_2/CO_2 ratio of 4. At 300 °C, a H_2O partial pressure of 0.4 bar results in a strong decrease in $\bar{r}_{2\text{PM}}$ of ca. 30 %. This decrease is less pronounced with decreasing temperature. However, a further increase in $p_{\text{H}_2\text{O},\text{in}}$ from 0.4 bar to higher partial pressures leads only to a further reduction in $\bar{r}_{2\text{PM}}$ of about 10 %. This trend has already been observed by Lim et al. [110]. A strong adsorption of H_2O on the catalyst active sites preventing adsorption of reactants can explain the effect of H_2O on the CO_2 reaction rates. The oxidation of catalyst active sites with increasing $p_{\text{H}_2\text{O}}$, as reported in Fischer-Tropsch synthesis [223], represents another explanation. Temperature programmed experiments as well as spectroscopic investigations may help clarifying this phenomenon. However, this is out of the scope of this kinetic study.

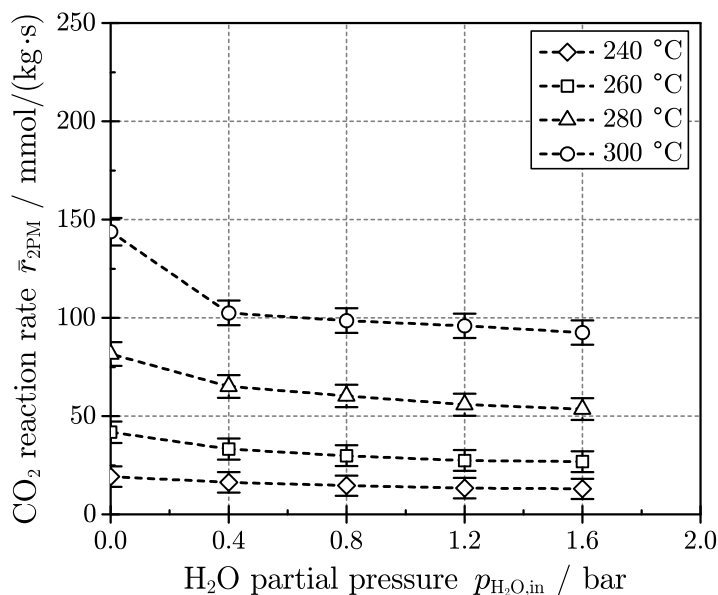


Figure 6.7: Influence of inlet H_2O partial pressure on the CO_2 reaction rate for temperatures between 240 and 300 °C ($p_{\text{R}} = 9.2$ bar, $p_{\text{CO}_2,\text{in}} = 1$ bar, $p_{\text{H}_2,\text{in}} = 4$ bar, $p_{\text{CH}_4,\text{in}} = 0$ bar, $\tau_{\text{mod},\text{CO}_2} = 2$ kg·s/mol).

Experimental data shown in Figure 6.7 were obtained for a H_2/CO_2 ratio of 4. In order to see the influence of H_2O for different H_2/CO_2 ratios further experiments were carried out. The results of the corresponding investigations are shown in Figure 6.8, where the inlet H_2O partial pressure is varied from 0 to 0.8 bar for H_2/CO_2 ratios ranging from 3 to 5 at a temperature of 280 °C. Similar trends can be observed for all investigated H_2/CO_2 ratios. Thus, contrary to the CO_2 influence, the H_2O effect on the CO_2 reaction rates does not depend on the H_2/CO_2 ratio. Altogether, the experimental H_2O reaction order derived from logarithmic linearization does not vary significantly with temperature or H_2/CO_2 ratio; it is about 0.1. Considering that the negative influence of $p_{\text{H}_2\text{O},\text{in}}$ on the CO_2 methanation reaction kinetics is due to an adsorption effect, the low variation of H_2O reaction order with temperature is characteristic of a small adsorption enthalpy.

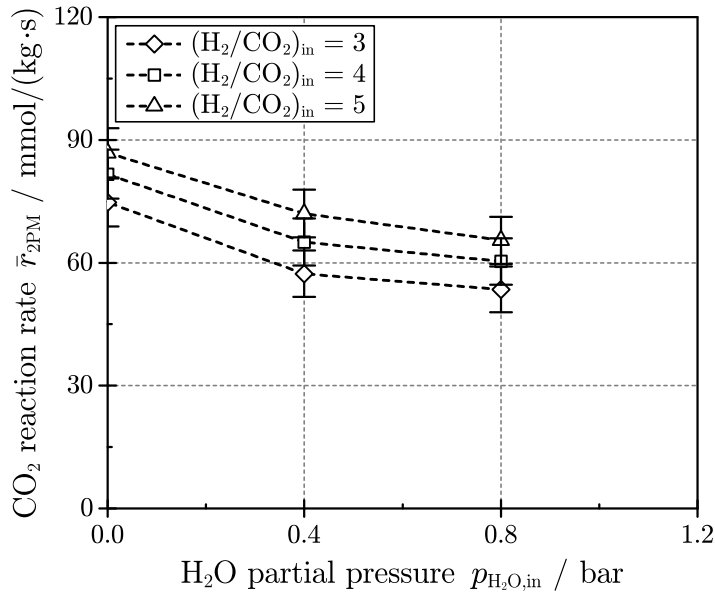


Figure 6.8: Influence of inlet H₂O partial pressure on the CO₂ reaction rate for H₂/CO₂ ratios between 3 and 5 ($p_R = 9.2$ bar, $T = 280$ °C, $p_{\text{CO}_2,\text{in}} = 1$ bar, $p_{\text{CH}_4,\text{in}} = 0$ bar, $\tau_{\text{mod,CO}_2} = 2$ kg·s/mol).

6.4.2 Reaction rate equation

Using the experimental results described in section 6.4.1, excluding the experiments with H₂O in the reactor feed, a power law kinetic rate equation has been derived from least-square minimization. The resulting rate equation is shown in Eq. 6.13 (see Notation for the parameter units).

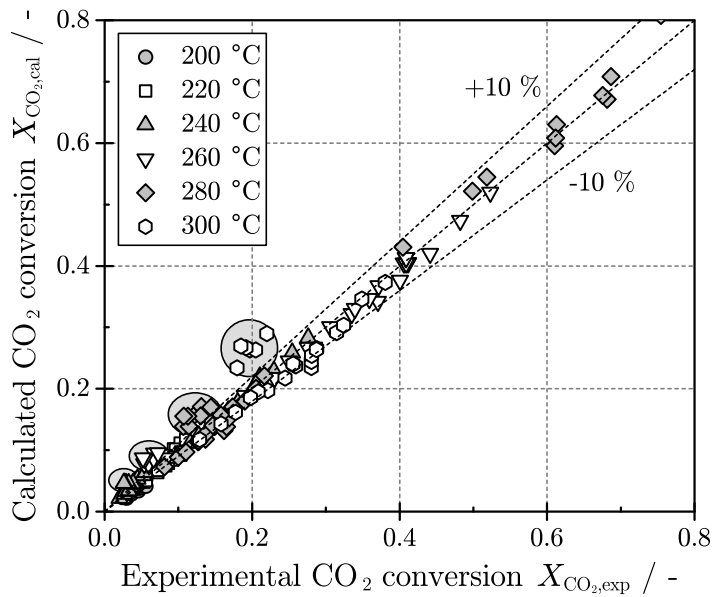


Figure 6.9: Parity plot between experimental and calculated CO₂ conversions. Calculated CO₂ conversions using Eq. 6.13. Grey-marked areas represent the experiments for which H₂O is present in the reactor feed.

$$r_{2\text{PM}} = 4.54469 \cdot 10^5 \cdot \exp\left(\frac{-79378}{R \cdot T}\right) \cdot \frac{c_{\text{H}_2}^{0.4} \cdot c_{\text{CO}_2}^{0.1}}{(1 + 1 \cdot c_{\text{H}_2\text{O}})^{0.1}} \cdot K \quad (6.13)$$

An activation energy of $E_A = 79$ kJ/mol - typical for CO₂ methanation - is retrieved. The parity plot between the experimental CO₂ conversion $X_{\text{CO}_2,\text{exp}}$ and the CO₂ conversion $X_{\text{CO}_2,\text{cal}}$ calculated with Eq. 6.13 is illustrated in Figure 6.9. A good agreement of experimental results and model is obtained. A standard deviation between $X_{\text{CO}_2,\text{exp}}$ and $X_{\text{CO}_2,\text{cal}}$ of 7.6 % is achieved, assessing a normal distribution.

Experiments with H₂O in the reactor feed (grey-marked areas in Figure 6.9) cannot be modeled properly with the rate equation described in Eq. 6.13. The calculated CO₂ conversions are systematically 30 % higher than the experimental CO₂ conversions. This corresponds to the effect described in section 6.4.1: addition of water to the reactor feed drastically reduces $r_{2\text{PM}}$ by ca. 30 %. As the rate equation described in Eq. 6.13 cannot properly describe the H₂O experiments, another rate equation has been derived for these experiments with least-square minimization. It is expressed in Eq. 6.14. This new rate equation can predict experiments with H₂O with a standard deviation of 13.3 %. The only difference between Eq. 6.13 and Eq. 6.14 is the pre-exponential factor k_0 . Eq. 6.14 is also very similar to the kinetic rate equation developed for three-phase CO₂ methanation (see Eq. 5.18 in chapter 5). A detailed comparison between two-phase and three-phase methanation kinetics is carried out in the following section.

$$r_{2\text{PM,H}_2\text{O}} = 3.2462 \cdot 10^5 \cdot \exp\left(\frac{-79378}{R \cdot T}\right) \cdot \frac{c_{\text{H}_2}^{0.4} \cdot c_{\text{CO}_2}^{0.1}}{(1 + 1 \cdot c_{\text{H}_2\text{O}})^{0.1}} \cdot K \quad (6.14)$$

Another type of kinetic rate equation, e.g. a Langmuir-Hinshelwood type, might solve the issue related to H₂O but the simplicity of Eq. 6.7 was preferred, as only two sets of kinetic parameters depending on the reactor feed composition, i.e. dry or wet feed, are sufficient to describe the experimental data over a broad parameter range.

To understand the discrepancies between calculated and experimental reaction rates represented in Figure 6.9, a sensitivity analysis was carried out on the reaction rate equation given in Eq. 6.13. For this analysis, the reaction temperature and the CO₂, H₂ and H₂O concentrations were varied according to the corresponding uncertainties listed in Table 6.2. An extreme case scenario was obtained by setting simultaneously the uncertainty of the parameters to their maximum or minimum value. These uncertainties were calculated using the differential method described in the Appendix N.

Table 6.2: Measurement uncertainties for the sensitivity analysis.

Parameters	Variation
T	± 2 K
c_i	± 4 %

Figure 6.10 shows the influence of measurement uncertainties on the true CO_2 reaction rate. Temperature has the strongest impact on $r_{2\text{PM}}$ followed by c_{H_2} , c_{CO_2} , and $c_{\text{H}_2\text{O}}$. The decreasing influence of gas concentration from H_2 to H_2O is directly related to the gas species reaction order illustrated in Eq. 6.13, while the temperature impact is related to the activation energy of reaction. Considering the extreme case scenario, the measurement uncertainties can lead to a deviation in $r_{2\text{PM}}$ of ca. 9 %. These uncertainties can therefore explain the standard deviation between experimental and calculated X_{CO_2} observed in Figure 6.9.

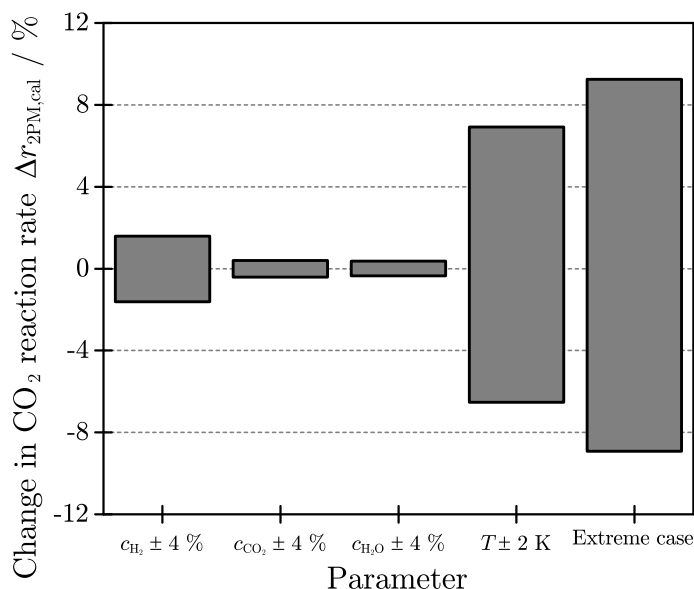


Figure 6.10: Sensitivity analysis on the reaction kinetic rate equation given in Eq. 6.13, valid when no H_2O is present in the reactor feed.

6.4.3 Comparison of two-phase and three-phase methanation kinetics

To verify the postulate of chapter 5, two-phase and three-phase CO_2 methanation were compared to each other: in absence of liquid phase influence on CO_2 methanation reaction kinetics and if gas concentration in the liquid phase is the relevant kinetic parameter to describe CO_2 methanation reaction kinetics, similar reaction rates should be obtained at similar operating conditions in both reaction systems. It was not possible to compare directly the CO_2 reaction rates measured in two-phase and three-phase systems, as different types of reactors were used for the experiments (PFR and CSTR, respectively). However, it was possible to compare CO_2 reaction rates derived from kinetic rate equations. In order to do this, the two-phase methanation kinetic rate equation expressed in Eq. 6.14 was used to calculate three-phase CO_2 reaction rates based on experimental data gathered in chapter 5, i.e. temperatures and gas concentrations in the liquid phase from three-phase experiments were implemented in Eq. 6.14. The rate equation described in Eq. 6.14 was preferred to the rate equation expressed in Eq. 6.13, as it takes into account the presence of H_2O in the reactor feed. Indeed, three-phase methanation experiments were conducted in a CSTR. As such, H_2O was always present in the reaction system. The results of this study are shown in a parity plot illustrated in Figure

6.11.

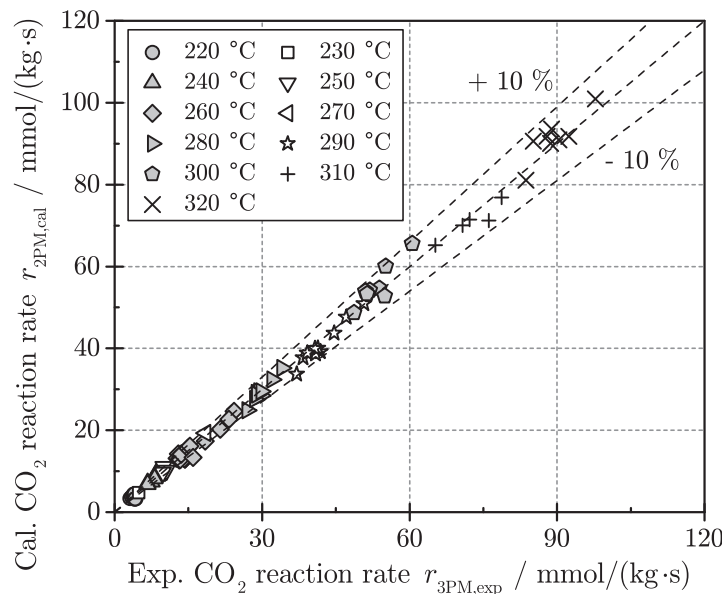


Figure 6.11: Parity plot between CO₂ reaction rates measured in a three-phase system and CO₂ reaction rates calculated with a two-phase kinetic rate equation. Calculated reaction rates are determined with Eq. 6.14.

Figure 6.11 shows that a very good agreement between 91 experimental three-phase CO₂ reaction rates, $r_{3PM,exp}$, and CO₂ reaction rates calculated from two-phase methanation rate equation, $r_{3PM,cal}$, is obtained. Assuming a normal distribution, a standard deviation between experimental and calculated reaction rates of 5.3 % is reached. As a two-phase kinetic rate equation is able to describe three-phase methanation experiments, it is confirmed that the liquid phase employed in three-phase methanation has no relevant influence on the CO₂ methanation kinetics. Figure 6.11 also confirms that gas concentrations in the liquid phase and not gas partial pressures in the gas phase are the relevant parameters to describe the three-phase CO₂ methanation reaction kinetics.

6.5 Summary

The objective of this chapter was to validate the postulate of chapter 5 that a liquid phase does not influence the intrinsic CO₂ methanation reaction rate. For this purpose, CO₂ methanation experiments were carried out using a plug flow laboratory fixed-bed reactor, i.e. a reaction system without liquid phase.

Using the results of 213 validated experiments, a power law kinetic rate equation has been developed, which describes two-phase methanation kinetics on a commercially available catalyst for inlet CO₂ partial pressures of 1 bar and temperatures between 200 °C and 300 °C (see Eq. 6.14).

The two-phase methanation kinetic rate equation can describe three-phase methanation experiments with good agreement (see Figure 6.11), i.e. a liquid-phase does not influence the

intrinsic reaction rate but the concentration of reacting species on the catalyst surface and gas concentration, not gas partial pressure, is the relevant parameter to describe the CO₂ methanation reaction kinetics.

7 Performance of a slurry bubble column reactor for transient CO₂ methanation

In order to exploit all the benefits of the PtG technology - foremost the time-scale decoupling of renewable energy supply and final utilization - the methanation step involved in the PtG process has to be a transient process. Rönsch et al. [7] have already shown that adiabatic fixed-bed reactors with interstage cooling and gas recirculation, which are state-of-the-art steady-state reactors for commercial CO methanation plants, have thermal runaway issues when they are operated under transient conditions.

Hence, new reactor concepts are required for the PtG process. The current benchmark PtG facility in Werlte (Germany) uses a tube bundle reactor (TBR) for catalytic methanation of CO₂ from a biogas plant (see Figure 7.1) [205]. However, the literature related to this facility is scarce and little information is available regarding the transient behavior of this reactor. A slurry bubble column reactor (SBCR) represents a promising alternative to fixed-bed technology. The advantages of a SBCR are the high heat capacity of the slurry phase as well as the excellent mixing in the reactor, which results in well-controlled, almost uniform temperature profile even under transient operating conditions [144].

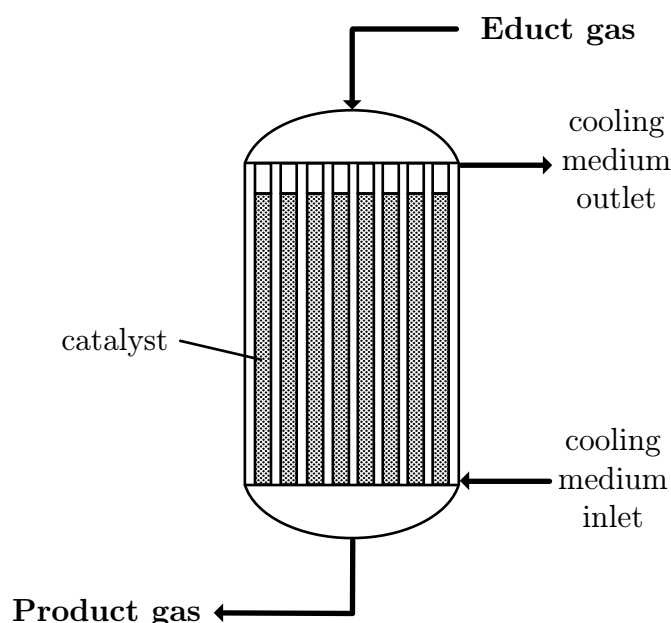


Figure 7.1: Scheme of a tube bundle reactor.

The aim of this chapter was to identify the potential of a SBCR used as CO₂ methanation reactor for the PtG process. For this purpose, a SBCR was modeled based on experimental data gathered in chapters 4 and 5, as well as on literature data related to fluid dynamics: i.e. gas holdup, axial dispersion, volumetric gas/liquid mass transfer coefficient and heat transfer coefficient for a SBCR. Then, the performance of the SBCR and a benchmark TBR were compared for steady-state and transient PtG operation to assess the expected advantages of the SBCR over the benchmark methanation reactor.

7.1 Literature review on reactor modeling

In the following, a literature review is performed on the recent publications related to SBCR and fixed-bed reactor modeling.

7.1.1 Slurry bubble column reactor

Basha et al. [142] differentiate three types of bubble column reactor (BCR) and SBCR models: axial dispersion models (ADM), multiple cell circulation models (MCCM), and computational fluid dynamics (CFD) models. Most of the SBCR models available in the literature are ADM that have been developed for Fischer-Tropsch synthesis (FTS) application.

In ADM integral parameters known as axial dispersion coefficients $D_{i,ax}$ are used to describe the different mixing behaviors within the three phases involved in a SBCR. These axial dispersion coefficients are implemented in the partial differential equations describing a SBCR (see e.g. Eq. 7.5). Some authors chose to simulate SBCR assuming ideal reactor behavior. Often, the gas phase is treated as a PFR ($D_{i,ax} = 0$), while the slurry phase is described as CSTR ($D_{i,ax} = \infty$) [239–249]. Other authors implemented axial dispersion coefficients from correlations available in the literature, as ideal reactor behavior is not able to represent correctly the real phase mixing within SBCR [144, 156, 250–256].

In MCCM a BCR [257–269] or a SBCR [270, 271] is divided into several cells with defined mixing behavior, e.g. assuming a better mixing in the bottom and the top of the liquid phase as compared to the rest of the reactor. MCCM require the detailed knowledge of cell number as well as cell mixing behavior. However, these data are experimentally hard to measure and to verify, and therefore scarce in literature [142].

CFD models can provide more detailed SBCR modeling through consideration of the fluid dynamics of the three phases. Two approaches for CFD modeling have been made so far: the Euler-Euler (gas and liquid are treated as fluid, solid are assumed as fluid or uniformly distributed) approach [272–292] and the Euler-Lagrange (gas is treated as fluid or particle, liquid is assumed as fluid, and solid is treated as particle) approach [293–299]. Nevertheless, the later approach is usually not suited for the simulation of a whole SBCR, as CPU time is extremely high. This is the reason why the Euler-Euler approach is usually preferred. CFD models require drag coefficient models to simulate the flow fields inside a SBCR. However, drag coefficient models for two- and three-phase systems are scarce and usually not applicable,

because coalescence and break-up of gas bubbles in BCR/SBCR are still not well-understood [142].

Simulation of SBCR was performed for transient FTS operation [144, 156, 256]. For these simulations, de Swart et al. [144] and Rados et al. [156] used an ADM operating in the heterogeneous flow regime. They considered the flow of large gas bubbles as PFR, while they assumed the small gas bubbles to follow the slurry phase flow. Solid particles were either uniformly distributed in the reactor [156] or the solid concentration was assumed to follow an exponential decay with increasing reactor height [144]. The authors concluded that SBCR are suited for transient FTS, as they do not undergo thermal runaway. Nevertheless, they emphasized the need for accurate investigation of the liquid phase backmixing in SBCR.

In this chapter, the transient behavior of the SBCR for CO₂ methanation was simulated with a model based on the ADM of Rados et al. [156].

7.1.2 Tube bundle reactor

Fixed-bed reactors are state of the art. As such a large number of fixed-bed reactor models have been developed. In this work, only the recent publications related to fixed-bed reactors for catalytic CO₂ methanation are reviewed.

Fixed-bed reactor models can be classified into homogeneous and heterogeneous models [238]. Homogeneous models neglect local concentration and temperature difference between the catalyst and the gas phase. This assumption is valid when there is no mass or heat transfer limitation within the reactor. These limitations are usually estimated with the Mears' and Anderson's criteria [236, 237] as well as the Thiele modulus [300] (see the Appendices C and E). If these criteria are not fulfilled, concentration or temperature differences are expected between the catalyst and gas phase. In this case, heterogeneous models are to be considered. These models treat each phase separately, i.e. concentrations and temperature in the catalyst particle are different from the concentrations and temperature of the bulk gas phase. These models offer a higher degree of precision but require much higher CPU time, as the number of partial differential equations is doubled.

Fixed-bed reactor models can be further categorized into one-dimensional (1D) and two-dimensional (2D) models [238]. 1D models do not consider any gradients along the radial axis of the reactor. However, as the temperature of fixed-bed reactors may be controlled by a heat exchanger at the reactor tube wall, radial temperature and concentration gradients may be observed in these reactors. 2D models consider these radial gradients and describe the evolution of concentration and temperature along the vertical and radial axes. Though 2D models offer more detailed results as compared to 1D models, they need much higher calculation times, as computers must solve partial differential equations with two spatial coordinates.

Schlereth et al. [301] investigated the influence of model types on the simulation results of a steady-state fixed-bed reactor for CO₂ methanation. They investigated 1D and 2D homogeneous models as well as a 1D heterogeneous model. They showed that simple 1D homogeneous models are able to describe qualitatively the behavior of a methanation fixed-bed reactor.

However, 2D homogeneous models are better suited for detailed and quantitative description of methanation reactors.

Even more recently, Sun et al. [302, 303] investigated the transient behavior of a fixed-bed reactor for CO₂ methanation using a 1D homogeneous reactor model. Attention was not paid to dynamic operation but to catalyst deactivation over time.

In this chapter, the transient behavior of the TBR was modeled with a 1D homogeneous model. A 2D homogeneous model was also prepared but resulted in excessive calculation times.

7.2 Reactor modeling

The SBCR and the TBR were designed to reach a CO₂ conversion of 0.9 at 20 bar with a feed gas composition H₂/CO₂/CH₄ of 4/1/1 at a volume flow rate of 900 m³/h (STP) under steady-state operation. These process parameters correspond to a medium-size biogas fermenter of 300 m³/h (STP) biogas output. The feed gas composition is representative of a typical biogas composition with a CO₂/CH₄ ratio of 1, which is enriched by H₂ for complete CO₂ conversion to CH₄. All relevant input parameters for the two reactor models are summarized in Table 7.1.

Table 7.1: Input parameters for the two reactor models

Parameter	Value
$\dot{V}_{in,STP}$	900 m ³ /h
p	20 bar
$y_{H_2,in}$	4/6
$y_{CO_2,in}$	1/6
$y_{CH_4,in}$	1/6
ρ_S	1050 kg/m ³
$c_{p,S}$	1000 J/(kg·K)
λ_S	0.2 W/(m·K)
ε_S	0.4

In this work, the response of the SBCR and TBR for transient CO₂ methanation was simulated for very fast inlet gas velocity changes taking place within 1 s. This situation aims to represent a PtG facility responding to a sudden surplus of renewable electricity if no H₂ buffer tank is integrated. This situation represents a worst case scenario, as the volume of pipings and intermediate devices are neglected. The aim of this study was to assess the evolution of reactor temperature and outlet gas quality resulting from the gas velocity change.

The following gas load changes were considered to model this situation:

1. From 25 to 50 % of the maximum methanation reactor capacity, i.e. 25 % load in 1 s;
2. From 50 to 100 % of the maximum methanation reactor capacity, i.e. 50 % load in 1 s;
3. From 75 to 100 % of the maximum methanation reactor capacity, i.e. 25 % load in 1 s;

4. Reverse load changes for each of the three above-mentioned load changes.

Harsh gas load changes are usually not performed on TBR, as they are sensitive to a change in superficial gas velocity. In practice, a well-defined and mild change over time of gas velocity and cooling medium temperature is implemented. However, this means that an expensive H₂ tank is required to buffer the H₂ volume flow rate from the electrolyzer. Götz et al. [304] have shown that it is more economical to operate a methanation reactor under transient operating conditions as compared to build a H₂ buffer tank. Consequently, the worst case scenario in terms of gas load change - without H₂ buffer tank - is considered in this work. A minimum gas load corresponding to 25 % of the maximum reactor capacity is assumed, as lower gas loads would lead to a change in SBCR hydrodynamic regime which is not considered in the SBCR model.

Both reactor models were implemented in Matlab[®] R2015a using an ode15s solver with a relative and absolute tolerance of 0.1 %. The time step increment was set to 1 s. A sufficiently long period of time was simulated in order to reach steady state. In the following a detailed description of the SBCR and TBR model is given.

7.2.1 Slurry bubble column reactor model

Model structure

The ADM model for SBCR is schematically represented in Figure 7.2. This model uses axial dispersion coefficients for the gas and liquid phase $D_{G,ax}$ and $D_{L,ax}$, respectively, and considers two bubble classes, “small” and “large”, assuming that large bubbles flow upwards as a PFR, while small bubbles recirculate with the liquid phase entrained by the large bubble flow. The gas holdup ε_G , i.e. the relative gas phase volume in the reactor, is therefore divided into large bubbles ($\varepsilon_{G,large}$) and small bubbles ($\varepsilon_{G,small}$). Mass transfer takes place between the bubbles and the slurry phase and depends on the volumetric gas/liquid mass transfer coefficient $k_L a_i$ and the dimensionless Henry’s law constant $H_{i,cc}$ of a gas species i . The chemical reaction takes place at the surface of the catalyst, while the heat exchange takes place between the slurry phase and an internal cooling surface area which is equally distributed along the reactor. The external heat transfer, i.e. on the cooling medium side, is neglected and the cooling medium temperature is set constant.

The SBCR was simulated under the heterogeneous flow regime in order to allow for a high gas hourly space velocity ($GHSV$, see Eq. 7.1). The reactor was operated as semi-batch reactor, i.e. no fresh or recycled slurry was circulated in the reactor ($u_L = 0$ m/s). Only the gas phase flowed through the SBCR. A perforated plate, which was designed based on previous hydrodynamic measurements [8, 138], was used as gas sparger.

$$GHSV = \frac{\dot{V}_{in,STP}}{V_R} \quad (7.1)$$

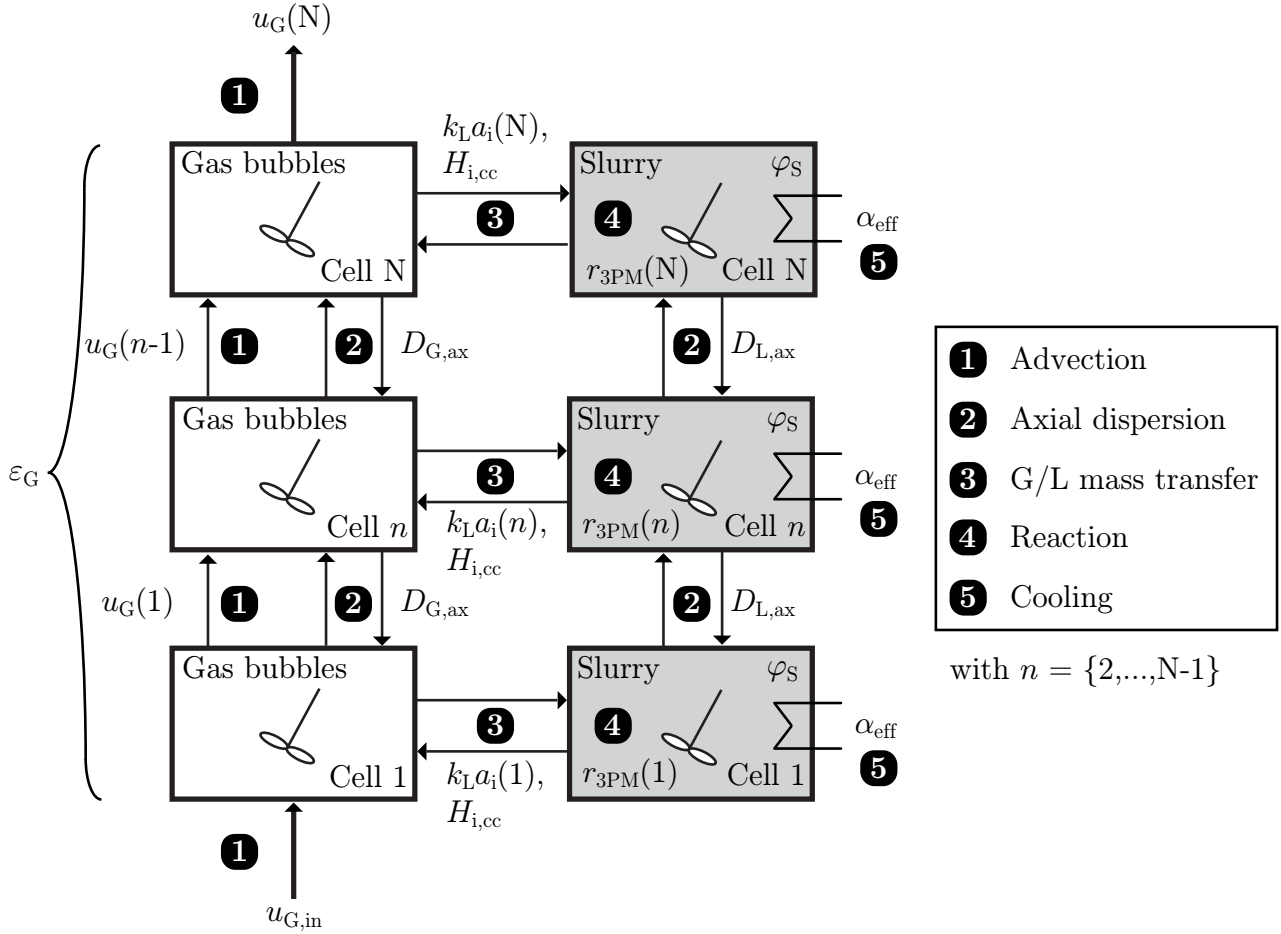


Figure 7.2: Structure of the slurry bubble column reactor model, including the parameters influencing the mass and heat transfer phenomena.

Model assumptions

The SBCR model incorporates the following assumptions. Assumptions 1 to 4 are illustrated in Figure 7.3.

1. Gas phase is assumed ideal and Raoult's law can be applied, i.e. $c_{i,G} = p_i / (RT)$;
2. Mass transfer resistance between the gas and liquid phase is located in the liquid phase only, i.e. the gas concentration at the G/L interphase $c_{i,G}^*$ equals the gas concentration in the bulk gas phase $c_{i,G}$;
3. Gas/liquid equilibrium is reached for each gas species, i.e. Henry's law expressed in Eq. 7.2 is applicable at the gas/liquid interphase;
4. Mass transfer resistance between the liquid phase and solid phase (catalyst) is neglected, i.e. the gas concentration at the L/S interphase $c_{i,S}^*$ equals the gas concentration in the bulk liquid phase $c_{i,L}$;
5. There is no radial concentration and temperature gradient, i.e. the reactor is discretized only in the vertical direction z (1D model);
6. Catalyst is uniformly distributed in the liquid phase, i.e. $\partial \varphi_S / \partial z = 0$.

7. There is no direct contact between the catalyst and the gas phase, i.e. no reaction in the gas phase;
8. The three phases are in thermal equilibrium, i.e. $T_G(z) = T_L(z) = T_S(z) = T(z)$;
9. The gas phase is neglected in the energy balance, i.e. $\sum_j \rho_j \cdot c_{p,j} \cdot T = \rho_{SL} \cdot c_{p,SL} \cdot T$.

Model assumptions are discussed in Appendix M.1.

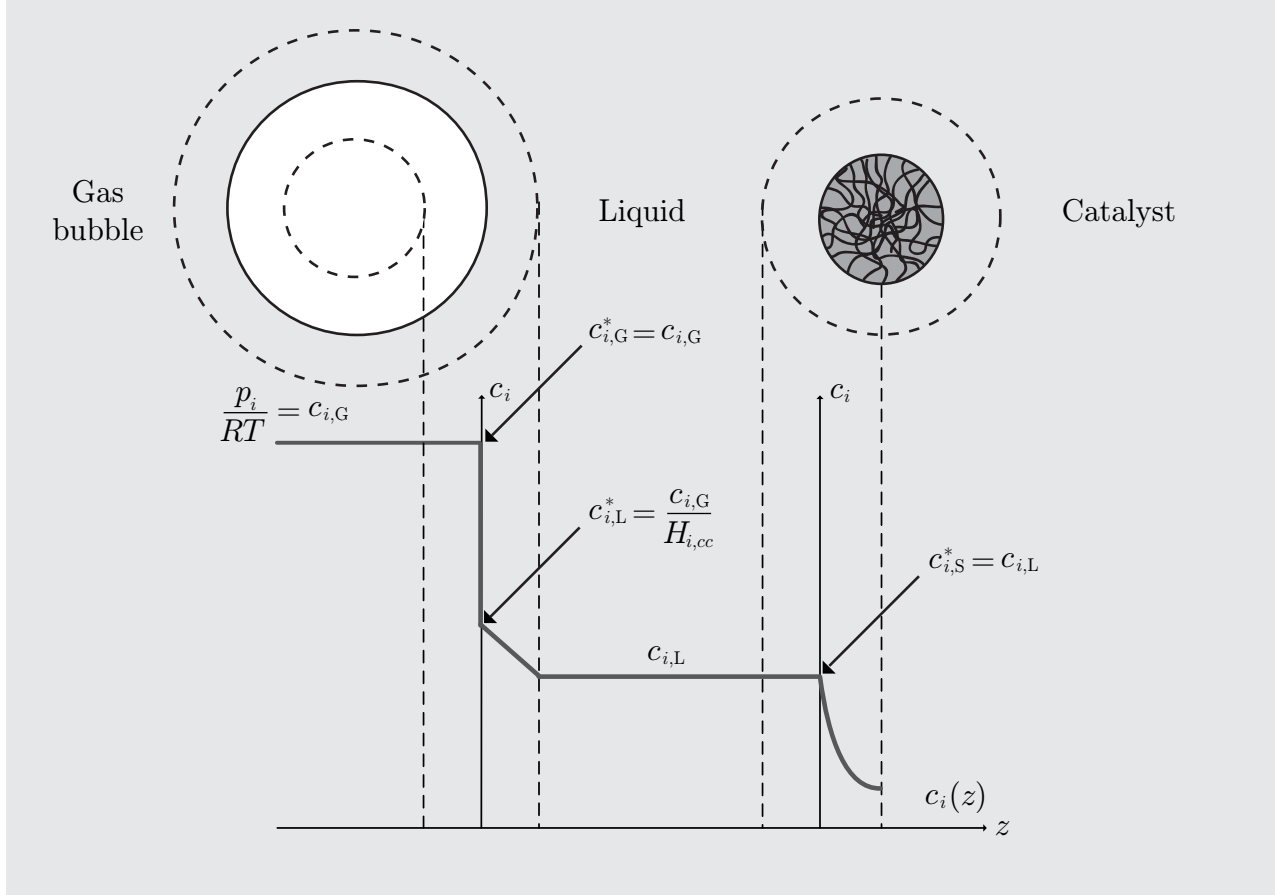


Figure 7.3: Concentration profile of an educt gas species along the three phases of the slurry bubble column reactor model.

Mole and energy balance

With these assumptions, the mole and energy balances around the SBCR can be written as shown in Eq. 7.5 to 7.9. Hereby, the dimensionless Henry's law constant $H_{i,cc}$ describes the concentration of gas species i dissolved in the liquid phase $c_{i,L}^*$ (see Eq. 7.2).

$$H_{i,cc} = \frac{c_{i,G}}{c_{i,L}^*} = H_{i,pc} \cdot \frac{1}{R \cdot T} \quad (7.2)$$

The superficial velocity of small bubbles $u_{G,small}$ is defined in Eq. 7.3,

$$u_{G,small} = \frac{\varepsilon_{G,small}}{\varepsilon_G} \cdot u_G \quad (7.3)$$

while the superficial velocity of large bubbles is defined in Eq. 7.4.

$$u_{G,\text{large}} = u_G - u_{G,\text{small}} \quad (7.4)$$

Mole balance for a gas species i in the large bubbles (Eq. 7.5):

$$\underbrace{\frac{\partial}{\partial t} (\varepsilon_{G,\text{large}} \cdot c_{i,G,\text{large}})}_{\text{Accumulation}} = \underbrace{\frac{\partial}{\partial z} \left(\varepsilon_{G,\text{large}} \cdot D_{G,\text{ax},\text{large}} \cdot \frac{\partial c_{i,G,\text{large}}}{\partial z} \right)}_{\text{Axial dispersion}} - \underbrace{\frac{\partial}{\partial z} (u_{G,\text{large}} \cdot c_{i,G,\text{large}})}_{\text{Advection}} - \underbrace{k_L a_{i,\text{large}} \cdot \left(\frac{c_{i,G,\text{large}}}{H_{i,cc}} - c_{i,L} \right)}_{\text{G/L mass transfer}} \quad (7.5)$$

Mole balance for a gas species i in the small bubbles (Eq. 7.6):

$$\underbrace{\frac{\partial}{\partial t} (\varepsilon_{G,\text{small}} \cdot c_{i,G,\text{small}})}_{\text{Accumulation}} = \underbrace{\frac{\partial}{\partial z} \left(\varepsilon_{G,\text{small}} \cdot D_{G,\text{ax},\text{small}} \cdot \frac{\partial c_{i,G,\text{small}}}{\partial z} \right)}_{\text{Axial dispersion}} - \underbrace{\frac{\partial}{\partial z} (u_{G,\text{small}} \cdot c_{i,G,\text{small}})}_{\text{Advection}} - \underbrace{k_L a_{i,\text{small}} \cdot \left(\frac{c_{i,G,\text{small}}}{H_{i,cc}} - c_{i,L} \right)}_{\text{G/L mass transfer}} \quad (7.6)$$

Mole balance around the whole gas phase, i.e. small and large bubbles together (Eq. 7.7):

$$\underbrace{\frac{\partial}{\partial t} (\varepsilon_G \cdot c_G)}_{\text{Accumulation}} = \underbrace{-\frac{\partial}{\partial z} (u_G \cdot c_G)}_{\text{Advection}} - \underbrace{\sum_i k_L a_i \cdot \left(\frac{c_{i,G}}{H_{i,cc}} - c_{i,L} \right)}_{\text{G/L mass transfer}} \quad (7.7)$$

Mole balance for a gas species i in the slurry phase (Eq. 7.8):

$$\underbrace{\frac{\partial}{\partial t} (\varepsilon_{SL} \cdot c_{i,L})}_{\text{Accumulation}} = \underbrace{\frac{\partial}{\partial z} \left(\varepsilon_{SL} \cdot D_{SL,\text{ax}} \cdot \frac{\partial c_{i,L}}{\partial z} \right)}_{\text{Axial dispersion}} + \underbrace{k_L a_{i,\text{large}} \cdot \left(\frac{c_{i,G,\text{large}}}{H_{i,cc}} - c_{i,L} \right) + k_L a_{i,\text{small}} \cdot \left(\frac{c_{i,G,\text{small}}}{H_{i,cc}} - c_{i,L} \right)}_{\text{G/L mass transfer}} + \underbrace{\nu_1 \cdot \eta_{\text{cat}} \cdot \varphi_S \cdot \rho_S \cdot r_{3\text{PM}}}_{\text{Reaction}} \quad (7.8)$$

Slurry phase energy balance (Eq. 7.9):

$$\underbrace{\rho_{\text{SL}} \cdot c_{p,\text{SL}} \cdot \varepsilon_{\text{SL}} \cdot \frac{\partial T}{\partial t}}_{\text{Accumulation}} = \underbrace{\frac{\partial}{\partial z} \left(\varepsilon_{\text{SL}} \cdot \lambda_{\text{SL,eff}} \cdot \frac{\partial T}{\partial z} \right)}_{\text{Axial dispersion}} + \underbrace{\eta_{\text{cat}} \cdot \varphi_{\text{S}} \cdot \rho_{\text{S}} \cdot r_{3\text{PM}} \cdot (-\Delta h_{\text{r}})}_{\text{Reaction heat}} - \underbrace{\alpha_{\text{eff}} \cdot a_{\text{cool}} \cdot (T - T_{\text{cool}})}_{\text{Cooling}} \quad (7.9)$$

The slurry holdup ε_{SL} is defined in Eq. 7.10,

$$\varepsilon_{\text{SL}} = \frac{V_{\text{S}} + V_{\text{L}}}{V_{\text{R}}} = 1 - \varepsilon_{\text{G}} \quad (7.10)$$

while the effective slurry heat conductivity $\lambda_{\text{SL,eff}}$ is defined in Eq. 7.11.

$$\lambda_{\text{SL,eff}} = \rho_{\text{SL}} \cdot c_{p,\text{SL}} \cdot D_{\text{SL,ax}} \quad (7.11)$$

Hydrodynamics and mass transfer

The gas holdups ε_{G} , $\varepsilon_{\text{G,large}}$ and $\varepsilon_{\text{G,small}}$ in Eq. 7.5 to Eq. 7.7 were calculated with the correlation developed by Behkish et al. [171], while the volumetric mass transfer coefficients $k_{\text{L}}a_{i,\text{large}}$ and $k_{\text{L}}a_{i,\text{small}}$ in Eq. 7.5 to Eq. 7.7 were calculated with the correlation developed by Lemoine et al. [186]. These correlations were chosen because they were the only available correlations that cover the relevant range of three-phase methanation operating conditions (see the Appendices G and H).

It is well-known that correlations for SBCR dispersion coefficients available in the literature were validated for bubble columns without solid phase and for small reactor diameter (< 0.2 m) and are less relevant for technical SBCR [148–155]. Nevertheless, dispersion coefficients are necessary, because fully ideal reactor models (PFR or CSTR) are not suitable to represent technical SBCR [144, 254]. The axial dispersion coefficient correlation developed by Deckwer and Buckhart [155] (see Eq. 2.14 in chapter 2) was implemented in this work to calculate the axial dispersion coefficients of the small bubbles $D_{\text{G,ax,small}}$ and the slurry phase $D_{\text{SL,ax}}$, as it is often applied in the literature to model SBCR for FTS [144, 254]. The axial dispersion coefficient of the large bubbles $D_{\text{G,ax,large}}$ was set to 0, as the behavior of these bubbles is considered as PFR.

The decrease in superficial gas velocity along the reactor height due to chemical reaction was calculated by solving Eq. 7.7.

Reaction rate

The intrinsic reaction rate $r_{3\text{PM}}$ was calculated using a kinetic rate equation based on the measurements shown in chapter 5 (see Eq. 5.18), while the catalyst efficiency was calculated through estimation of the Thiele modulus (see Eq. C.6 and C.7 in the Appendix).

Heat transfer

The effective heat transfer coefficient α_{eff} was calculated with a correlation developed by Deckwer et al. [189] (see Eq. 2.24 in chapter 2), as the SBCR modelled in this chapter operates within the validity range of Deckwer's correlation. The volumetric heat exchanger surface area a_{cool} was set to $10 \text{ m}^2/\text{m}^3$, which is an average value of volumetric heat exchanger surface areas suggested by de Swart et al. [144]. Considering the reactor design calculated in section 7.3.1.1, a_{cool} of $10 \text{ m}^2/\text{m}^3$ corresponds to 10 cooling tubes of outer diameter 0.03 m vertically placed inside the SBCR. These cooling tubes occupy less than 8 % of the reactor volume.

The slurry properties (density, viscosity, heat capacity and conductivity as well as gas diffusion coefficient) were calculated with Eq. B.13 to Eq. B.17 in the Appendix, as the validity range of these correlations covers the CO_2 methanation operating conditions. The liquid used in the SBCR is dibenzyltoluene as it proved to be a suitable liquid for three-phase methanation. The maximum allowed temperature for DBT is $350 \text{ }^\circ\text{C}$. As CO_2 methanation experiments were carried up to a maximum temperature of $320 \text{ }^\circ\text{C}$ (see chapter 5), the SBCR was designed for an average slurry temperature of $320 \text{ }^\circ\text{C}$. Pure dibenzyltoluene properties (viscosity, surface tension, density and heat capacity) can be found in the Appendix A.2 and in chapter 4.

Numerical procedure

In the Matlab[®] ode15s solver, Eq. 7.7 to Eq. 7.9 were solved with the method of lines (MOL), i.e. the partial differential equations (PDE) along the vertical axis were discretized, while the solver integrated the ordinary differential equations (ODE) along time. The reactor was discretized in $N = 100$ cells resulting in $13 \times 100 = 1300$ ODE. For a number of cells larger than 100, modeling results did not vary significantly from the $N = 100$ case (see Figure M.1 in the Appendix).

Reactor design strategy

To simplify the design of a methanation SBCR, several boundary conditions had to be fixed. These boundary conditions as well as their justification are listed in Table 7.2.

Table 7.2: Slurry bubble column reactor boundary conditions.

Parameter	Value	Justification
\bar{T}_{SL}	$320 \text{ }^\circ\text{C}$	Derived from own experiments (see chapter 5)
$T_{\text{SL,max}}$	$350 \text{ }^\circ\text{C}$	Taken from DBT safety data sheet [305]
$T_{\text{G,in}}$	\bar{T}_{SL}	Reduction of reactor variables
d_{P}	$75 \cdot 10^{-6} \text{ m}$	Derived from own experiments (see chapter 5)
d_{hole}	$1 \cdot 10^{-4} \text{ m}$	Derived from previous experiments [138]
$a_{\text{free}} = 1 - \frac{A_{\text{hole}}}{A_{\text{gas sparger}}}$	$7.2 \cdot 10^{-3}$	Derived from previous experiments [138]
N_{hole}	83095	Derived from a_{free} and d_{hole}
$u_{\text{G,in,max}}$	0.3 m/s	Taken from literature [306]
d_{R}	0.34 m	Derived from $u_{\text{G,in,max}}$ and $\dot{V}_{\text{G,in,STP}}$
a_{cool}	$10 \text{ m}^2/\text{m}^3$	Taken from literature [144]

In order to reach a CO_2 conversion of 0.9 and a mean slurry temperature \bar{T}_{SL} of $320 \text{ }^\circ\text{C}$

(see definition in Eq. 7.12), three parameters could be adjusted: the catalyst concentration φ_S , the reactor height h_R and the cooling medium temperature T_{cool} . The following strategy was used to achieve the desired CO_2 conversion and reactor temperature. First, φ_S , h_R and T_{cool} were guessed and the Matlab[®] model solved the PDE and delivered a result. If the resulting CO_2 conversion and the mean slurry temperature were not satisfying, φ_S , h_R and T_{cool} were iteratively varied until the desired CO_2 conversion and mean slurry temperature were achieved. This algorithm is illustrated in Figure M.16 in the Appendix.

$$\bar{T}_{\text{SL}} = \frac{1}{h_R} \int_0^{h_R} T_{\text{SL}}(z) dz \quad (7.12)$$

7.2.2 Tube bundle reactor model

Model structure

The TBR was modeled as a 1D homogeneous tube bundle reactor which is schematically represented in Figure 7.4. The educt gases enter at the top of the reactor tubes and react along the reactor at the catalyst surface. Each reactor tube is cooled by the cooling medium with a constant temperature T_{cool} .

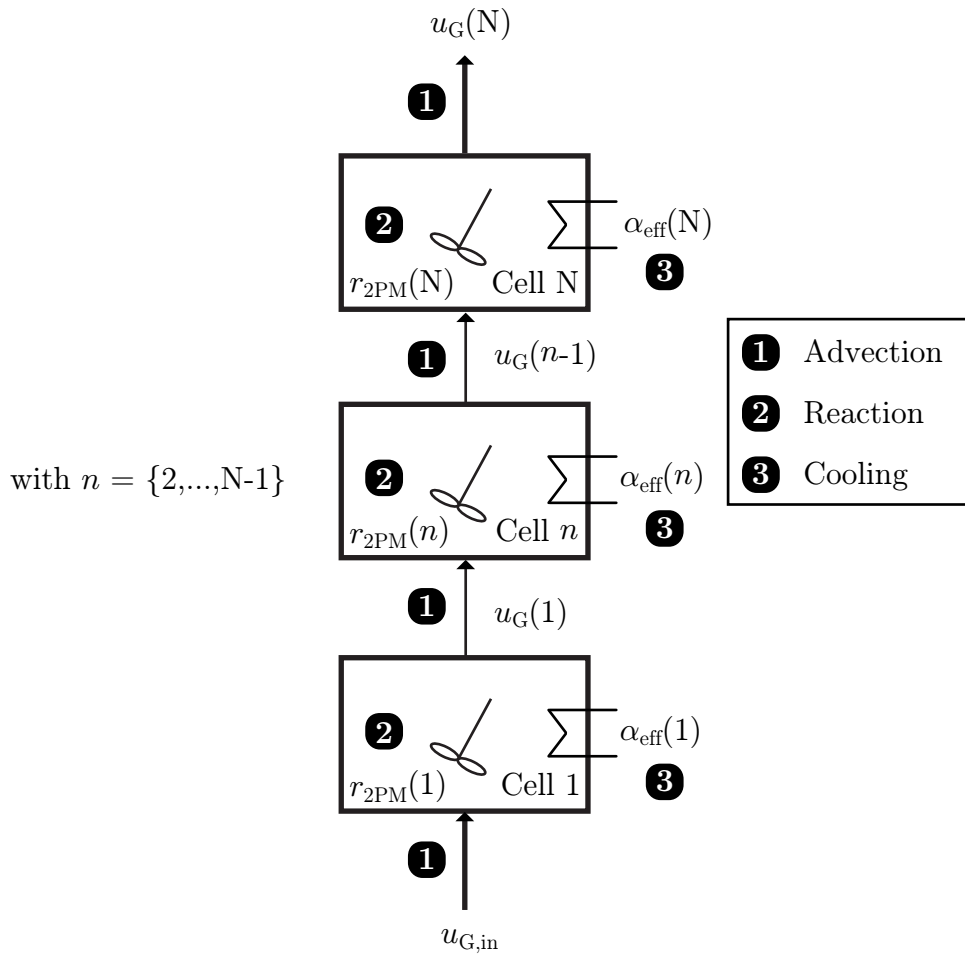


Figure 7.4: Structure of the tube bundle reactor model, including the parameters influencing the mass and heat transfer phenomena.

Model assumptions

The TBR model incorporates the following assumptions:

1. Gas phase is assumed ideal, i.e. $c_{i,G} = p_i / (RT)$;
2. No distinction is made between concentration or temperature in the bulk gas phase and catalyst phase; only the intra-particle mass transfer is taken into account with the catalyst efficiency η_{cat} , i.e. $c_{i,S}(z) = \eta_{\text{cat}} \cdot c_{i,G}(z)$ and $T_G(z) = T_S(z) = T(z)$;
3. Plug flow is assumed, i.e. mass dispersion in the axial direction is neglected;
4. Thermal heat conduction, i.e. heat dispersion in the axial direction is neglected;
5. Reactor wall is not taken into account for energy balance (accumulation term) and heat transfer.

Model assumptions are discussed in Appendix M.1.

Mole and energy balance

Using these assumptions, the mole and energy balances for the TBR can be written as follows.

Mole balance for the gas phase (Eq. 7.13):

$$\underbrace{\varepsilon_{\text{bed}} \cdot \frac{\partial c_G}{\partial t}}_{\text{Accumulation}} = - \underbrace{\frac{\partial}{\partial z} (u_G \cdot c_G)}_{\text{Advection}} + \underbrace{\sum_i \nu_i \cdot \eta_{\text{cat}} \cdot (1 - \varepsilon_{\text{bed}}) \cdot \rho_S \cdot r_{2\text{PM}}}_{\text{Reaction}} \quad (7.13)$$

Mole balance for a gas species i in the gas phase (Eq. 7.14):

$$\underbrace{\varepsilon_{\text{bed}} \cdot \frac{\partial c_{i,G}}{\partial t}}_{\text{Accumulation}} = - \underbrace{\frac{\partial}{\partial z} (u_G \cdot c_{i,G})}_{\text{Advection}} + \underbrace{\nu_i \cdot \eta_{\text{cat}} \cdot (1 - \varepsilon_{\text{bed}}) \cdot \rho_S \cdot r_{2\text{PM}}}_{\text{Reaction}} \quad (7.14)$$

Energy balance (Eq. 7.15):

$$\underbrace{(\rho_G \cdot c_{p,G} \cdot \varepsilon_{\text{bed}} + \rho_S \cdot c_{p,S} \cdot (1 - \varepsilon_{\text{bed}})) \cdot \frac{\partial T}{\partial t}}_{\text{Accumulation}} = - \underbrace{\frac{\partial}{\partial z} (\rho_G \cdot c_{p,G} \cdot u_G \cdot T)}_{\text{Advection}} + \underbrace{+ \eta_{\text{cat}} \cdot (1 - \varepsilon_{\text{bed}}) \cdot \rho_S \cdot r_{2\text{PM}} \cdot (-\Delta h_r)}_{\text{Reaction heat}} - \underbrace{\frac{4 \cdot \alpha_{\text{eff}}}{d_{\text{tube}}} \cdot (T - T_{\text{cool}})}_{\text{Cooling}} \quad (7.15)$$

Reaction rate

The intrinsic reaction rate $r_{2\text{PM}}$ was calculated using the kinetic rate equation based on the measurements shown in chapter 6 (see Eq. 6.13), while the catalyst efficiency was calculated through estimation of the Thiele modulus (see Eq. C.6 and Eq. C.7 in the Appendix).

Heat transfer

The effective heat transfer coefficient was calculated with Eq. 7.16:

$$\alpha_{\text{eff}} = \frac{1}{\frac{1}{\alpha_{\text{wall}}} + \frac{d_{\text{tube}}}{8 \cdot \lambda_{r,\text{eff}}}} \quad (7.16)$$

The wall heat transfer coefficient α_{wall} was calculated using a correlation developed by Martin and Nilles [307] for heat transfer in fixed-bed reactors (see Appendix B.3). This correlation is valid for a Peclet number Pe between 1 and 10000 and d_{tube}/d_P between 1.2 and 51. In this work, Pe lies between 100 and 400, while d_{tube}/d_P is 6.6. Thus, the correlation of Martin and Nilles is valid for this TBR simulation. The heat transfer coefficient on the cooling side of the reactor was assumed to be high and not limiting. Furthermore, the cooling medium temperature was assumed to be constant due to a large cooling medium flow rate.

The effective radial heat conductivity $\lambda_{r,\text{eff}}$ of the bed material (solid and gas phases) was calculated with the so-called α_w heat transfer model, assuming constant heat conductivity along the radial coordinates (see Appendix B.3). More detailed information on this model can be found in [238].

Momentum balance

Along Eq. 7.13 to Eq. 7.15, the momentum balance expressed in Eq. 7.17 (Ergun equation [308]) had to be solved to account for the pressure drop along the fixed bed.

$$\frac{\partial p}{\partial z} = -\frac{u_G}{d_P} \cdot \frac{1 - \varepsilon_{\text{bed}}}{\varepsilon_{\text{bed}}^3} \cdot \left(1.75 \cdot \rho_G \cdot u_G + 150 \cdot \frac{\mu_G}{d_P} \cdot (1 - \varepsilon_{\text{bed}}) \right) \quad (7.17)$$

The decrease in superficial gas velocity along the reactor height due to chemical reaction was calculated by solving Eq. 7.13.

Numerical procedure

In the Matlab[®] ode15s solver, Eq. 7.13 to Eq. 7.15 were solved with the MOL, i.e. the PDE along the vertical axis were discretized, while the solver integrated the ODE along time. The reactor was discretized in cells with a height $dz = 0.005$ m.

Reactor design strategy

A TBR design optimizing heat transfer was chosen: the pellet catalyst ($d_P = 0.003$ m) is distributed over several tubes ($d_{\text{tube,in}} = 0.02$ m) reaching a packed-bed porosity ε_{bed} of 0.4. The maximum inlet gas velocity in each tube $u_{G,\text{in}}$, was set to 1.0 m/s in order to mitigate pressure drop, leading to a number of tubes N_{tube} of 80. The maximum catalyst temperature allowed for continuous operation is 510 °C. The TBR was designed accordingly. The TBR boundary conditions as well as their justification are listed in Table 7.3.

In order to reach a CO₂ conversion of 0.9 and keep the maximum reactor temperature below 510 °C, two parameters could be varied: the reactor length L_R and the cooling medium temperature T_{cool} . First, these two parameters were guessed and the Matlab[®] solver was started. L_R and T_{cool} were then iteratively varied until the desired CO₂ conversion and

maximum reactor temperature were achieved. This algorithm is illustrated in Figure M.15 in the Appendix.

Table 7.3: Tube bundle reactor boundary conditions.

Parameter	Value	Justification
T_{in}	T_{cool}	Reduction of reactor variables*
$d_{\text{tube,in}}$	$2 \cdot 10^{-2}$ m	Optimal heat transfer
$u_{\text{G,in,max}}$	≤ 1 m/s	Pressure drop mitigation
N_{tube}	80	Derived from $u_{\text{G,in,max}}$ and $\dot{V}_{\text{in,STP}}$
ε_{bed}	0.4	Reaction and heat transfer enhancement

* This corresponds to a reactor design where the cooling medium preheats the inlet gas flow. The influence of inlet gas temperature on the performance of the TBR is shown in Figure M.2 in the Appendix.

7.3 Results and discussion

Aim of this chapter was to study the behavior of a SBCR and a TBR for transient PtG operations. Beforehand, reactor designs had to be determined using the boundary conditions given in Table 7.2 and 7.3; these designs are presented in section 7.3.1. Once the reactor designs were established, the evolution of local reactor temperature as well as CO₂ conversion integrated along the vertical axis of each reactor were discussed for both reactors. Then, a sensitivity analysis was performed to assess the reliability of each reactor model. To conclude section 7.3.1, a reactor control strategy was defined for the different gas loads applied for transient PtG operation.

The results of transient PtG operation are presented in section 7.3.2. First, the effect of a gas load increase on methanation reactor performance was studied with dimensionless numbers. Once this effect was clarified, results of transient methanation reactor operation were discussed. Finally, solutions to improve the performance of both methanation reactors were proposed.

7.3.1 Determination of methanation reactor design

7.3.1.1 Slurry bubble column reactor design

Aim of the following study was to find the combination of $h_{\text{R}}/d_{\text{R}}$ and φ_{S} maximizing the reactor $GHSV$, i.e. the reactor performance, for a maximum volume flow rate of 900 m³/h and a CO₂ conversion X_{CO_2} of 0.9. The results of this study are shown in Figure 7.5. For $0 \leq \varphi_{\text{S}} \leq 0.12$, $h_{\text{R}}/d_{\text{R}}$ rapidly decreases from 55 to 8, while $GHSV$ rapidly increases from 500 to 3500 1/h. For $0.12 \leq \varphi_{\text{S}} \leq 0.2$, $h_{\text{R}}/d_{\text{R}}$ decreases slowly, while $GHSV$ increases slowly until an optimum is reached with $h_{\text{R}}/d_{\text{R}} = 7.4$ and $GHSV = 3918$ 1/h. A further increase in φ_{S} leads to a slow increase in $h_{\text{R}}/d_{\text{R}}$ and a decrease in $GHSV$.

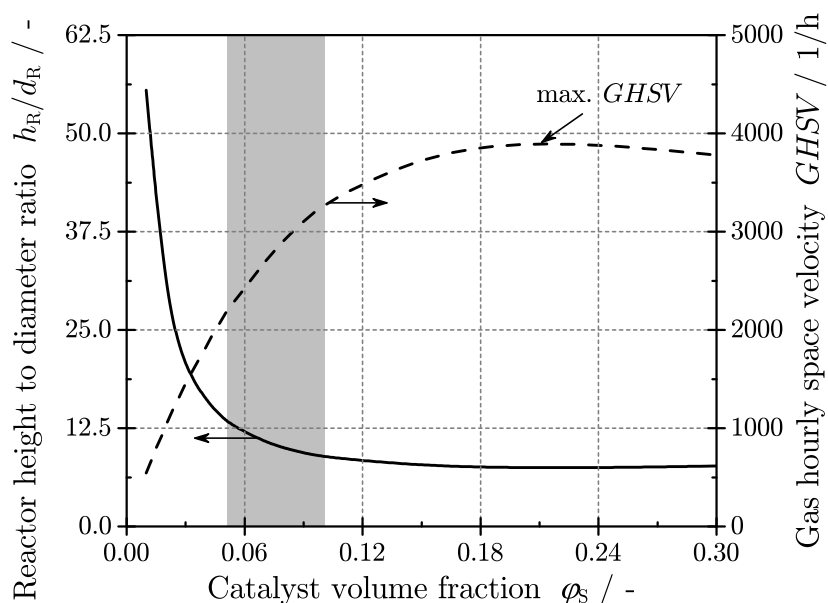


Figure 7.5: Combinations of catalyst volume fraction, required reactor height-to-diameter ratio and gas hourly space velocity of the slurry bubble column reactor which allow a CO₂ conversion of 0.9 with a feed H₂/CO₂/CH₄ of 4/1/1 and a volume flow rate of 900 m³/h ($\bar{T}_{\text{SL}} = 320$ °C, $p_{\text{out}} = 20$ bar, $u_{\text{G,in}} = 0.3$ m/s). Grey-marked area corresponds to the range of catalyst volume fraction for an investment/operation cost optimization.

A SBCR is usually either limited by chemical reaction rate or by gas/liquid mass transfer [136, 137]. Chemical reaction rate is enhanced by increasing catalyst volume fraction (see Eq. 7.8), while gas/liquid mass transfer is decreased by increasing catalyst volume fraction [186] (see Eq. 2.22 in chapter 2). The limiting reaction step can be identified in Figure 7.5; for $\varphi_{\text{S}} \leq 0.2$ the chemical reaction is the limiting reaction step, as an increase in φ_{S} leads to higher *GHSV*. However, for $\varphi_{\text{S}} > 0.2$ an increase in φ_{S} no longer enhances *GHSV*; the SBCR is limited by gas/liquid mass transfer.

Furthermore, a grey area is pictured in Figure 7.5 which corresponds to the range of φ_{S} for an investment/operation cost optimization: at $\varphi_{\text{S}} < 0.05$ the resulting SBCR is too large to be cost effective, while at $\varphi_{\text{S}} > 0.1$ an increase in catalyst volume fraction does not lead to a substantial decrease in reactor volume. The catalyst concentration of a commercial SBCR for three-phase CO₂ methanation lies therefore in this range. Nevertheless, in this work both SBCR and TBR are compared using a reactor design maximizing *GHSV*, i.e. maximizing the specific reaction heat release which corresponds to the most challenging scenario in terms of heat management. As a consequence, a catalyst volume fraction of 0.2 corresponding to a $h_{\text{R}}/d_{\text{R}}$ of 7.4 and a *GHSV* of 3918 1/h are used as SBCR design parameters for the following simulations. All SBCR design parameters are summarized in Table 7.4.

Table 7.4: Slurry bubble column reactor design parameters to reach a CO₂ conversion of 0.9 for a feed H₂/CO₂/CH₄ of 4/1/1 with a volume flow rate of 900 m³/h (STP).

Parameter	Value
\bar{T}_{SL}	320 °C
$T_{\text{SL,max}}$	350 °C
$T_{\text{G,in}}$	\bar{T}_{SL}
d_{P}	$75 \cdot 10^{-6}$ m
d_{hole}	$1 \cdot 10^{-4}$ m
a_{free}	$7.2 \cdot 10^{-3}$
N_{hole}	83095
$u_{\text{G,in,max}}$	0.3 m/s
a_{cool}	10 m ² /m ³
d_{R}	0.34 m
φ_{S}	0.2
h_{R}	2.53 m
$GHSV$	3918 1/h

Based on this study, the evolution of local slurry temperature $T_{\text{SL}}(z)$ as well as CO₂ conversion $X_{\text{CO}_2}(z)$ integrated along the vertical axis of the SBCR was calculated. The results are shown in Figure 7.6.

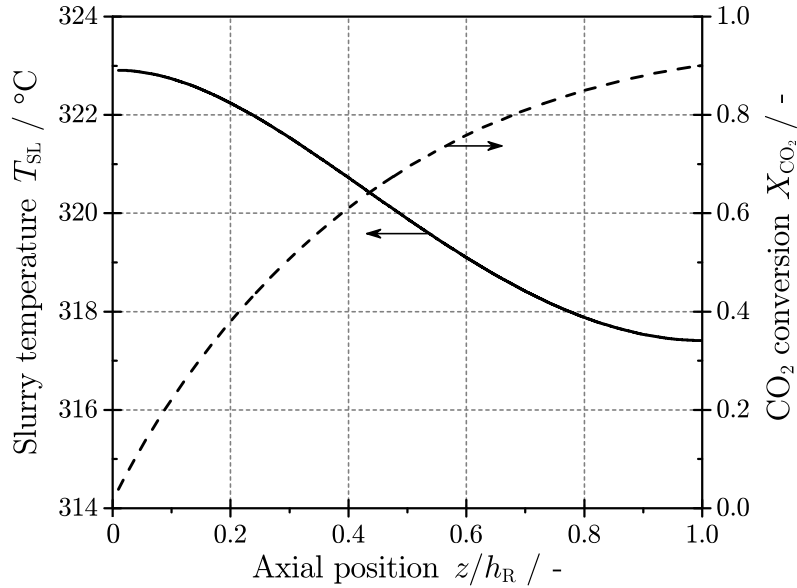


Figure 7.6: Evolution of local slurry temperature and CO₂ conversion integrated along the axial direction of the slurry bubble column reactor for a feed H₂/CO₂/CH₄ of 4/1/1 (Reactor design parameters are summarized in Table 7.4, $T_{\text{cool}} = 269$ °C).

From the bottom to the top of the SBCR, T_{SL} decreases from 323 to 317 °C. Hence, the SBCR can be considered as quasi isothermal. The evolution of T_{SL} is correlated to X_{CO_2} and the corresponding reaction heat release: 50 % of the CO₂ conversion takes place in the first 30 % of reactor volume (bottom), while only 10 % of the CO₂ conversion takes place in

the last 30 % of reactor volume (top). Considering that cooling occurs in the slurry phase with constant specific heat transfer area and constant cooling medium temperature, T_{SL} is accordingly higher than 320 °C at the reactor bottom and lower than 320 °C at the reactor top.

To assess the reliability of the SBCR model, a sensitivity analysis was carried out on the most critical SBCR model parameters, i.e. the parameters controlling the effective reaction rate; the gas holdup ε_G , the gas/liquid mass transfer coefficient $k_L a_i$, and the intrinsic CO₂ methanation reaction rate r_{3PM} . The uncertainty of ε_G , $k_L a_i$ and r_{3PM} were taken from literature, [171, 186, 207]. These uncertainties were $\pm 42\%$, $\pm 36\%$, and $\pm 10.6\%$, respectively. An extreme case scenario was obtained by setting simultaneously the uncertainty of each parameter to its maximum or minimum value. The results of the sensitivity analysis are shown in Figure 7.7.

The reaction rate is the least sensitive parameter, followed by $k_L a_i$ and ε_G . This order was expected, as the SBCR is mass-transfer limited and not chemical-reaction limited. As a consequence, a change in r_{CO_2} of $\pm 10.6\%$ has a small influence on X_{CO_2} (around ± 0.01). The gas/liquid mass transfer $k_L a_i$ has a much higher influence as it controls the reaction limiting step: a decrease in $k_L a_i$ of -36% results in a decrease in X_{CO_2} of ca. 0.11. The influence of ε_G on X_{CO_2} is even higher than the influence of $k_L a_i$. In the $k_L a_i$ correlation developed by Lemoine et al. [186] $k_L a_i$ is proportional to $\varepsilon_G^{1.21}$. As a consequence, an uncertainty in ε_G results in an even higher uncertainty in $k_L a_i$. Considering the extreme case scenario, the parameter uncertainties can lead to a deviation in X_{CO_2} of 0.35. This shows the current need for more accurate ε_G and $k_L a_i$ correlations.

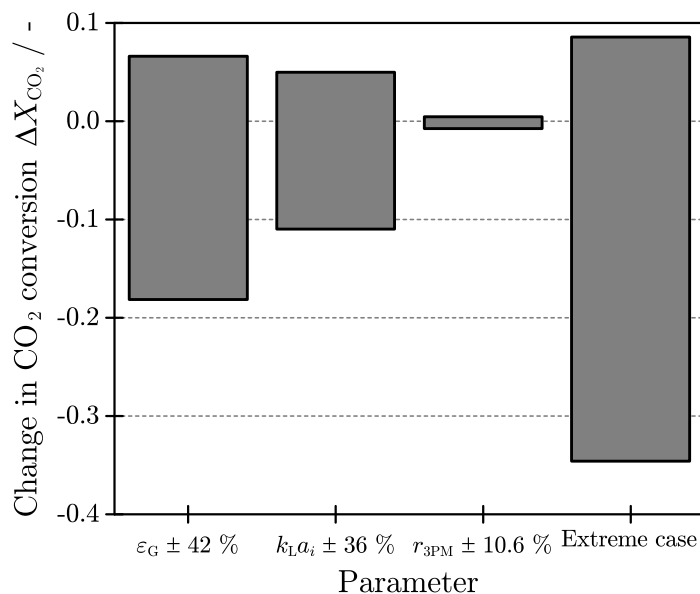


Figure 7.7: Sensitivity analysis based on the uncertainties of gas holdup and gas/liquid mass transfer coefficient correlations as well as kinetic rate equation for the slurry bubble column reactor with a feed H₂/CO₂/CH₄ of 4/1/1 (Reactor design parameters are summarized in Table 7.4, reference $X_{CO_2} = 0.9$).

However, if a reactor design with a volumetric catalyst concentration of 0.07 had been chosen, i.e. in the economical range (see Figure 7.5), the results of a sensitivity analysis should be

different. For this catalyst concentration, the reactor is limited by chemical reaction and not by mass transfer. As a consequence, $\varphi_S = 0.07$ the reactor should be much more sensitive to a change in r_{3PM} .

7.3.1.2 Tube bundle reactor design

Aim of the following study was to identify a combination of reactor length L_R and cooling medium temperature T_{cool} which maximizes $GHSV$ for a maximum volume flow rate of 900 m³/h and a CO₂ conversion X_{CO_2} of 0.9, while keeping T_{max} below 510 °C. The results of this study are shown in Figure 7.8. For increasing T_{cool} , both T_{max} and $GHSV$ increase. Furthermore, for 227 °C < T_{cool} < 245 °C, the increase in T and $GHSV$ is higher. Increasing temperatures enhance chemical reaction rate. An increase in T_{cool} results in higher reactor temperatures which enhance the reaction rate and allow for higher $GHSV$.

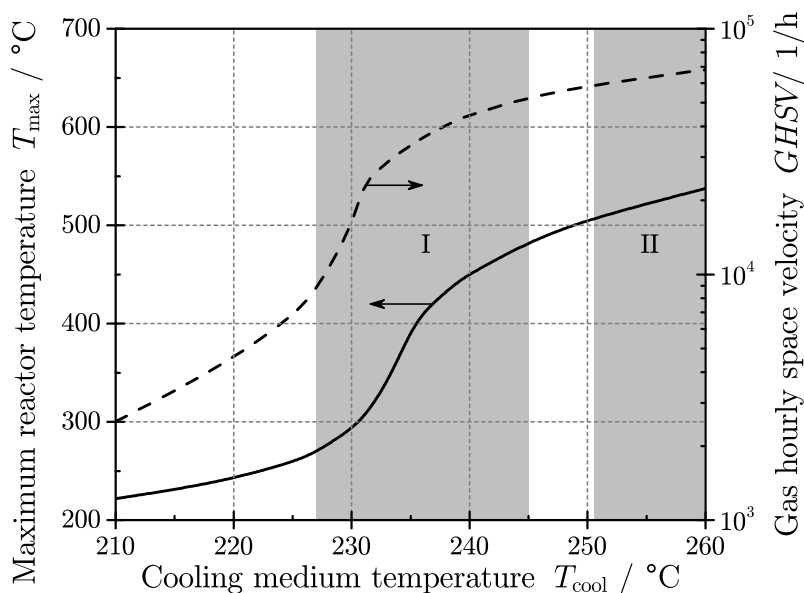


Figure 7.8: Combinations of cooling medium temperature, maximum reactor temperature and gas hourly space velocity of the tube bundle reactor which allow for a CO₂ conversion of 0.9 with a feed H₂/CO₂/CH₄ of 4/1/1 and a volume flow rate of 900 m³/h ($p_{in} = 20$ bar, $u_{G,in} = 0.97$ m/s). Grey-marked areas correspond to non-acceptable operating conditions (I: high sensitivity to cooling, II: thermal catalyst degradation).

The two grey areas marked in Figure 7.8 (I and II) correspond to operating conditions which are not desired for the design of a TBR for CO₂ methanation. Area I is characterized by $\Delta T_{max}/\Delta T_{cool} > 5$: a small increase in T_{cool} results in a high change in T_{max} . It is critical to design a TBR in area I, considering that a change in cooling temperature of less than 1 K may lead to change in reactor temperature between 5 and 25 K. As such the cooling medium temperature range $227 \text{ °C} \leq T_{cool} \leq 245 \text{ °C}$ is not desirable. Area II is characterized by $T_{max} > 510 \text{ °C}$, i.e. temperatures which favor thermal catalyst degradation according to the specifications of the catalyst supplier. Thus, conditions with T_{cool} higher than 252 °C are not

acceptable. Higher cooling temperature could be chosen, if a catalyst with higher temperature stability can be implemented.

Two ranges of cooling temperature can be used for the design of the TBR: $T_{\text{cool}} < 227$ °C, and 245 °C $< T_{\text{cool}} < 252$ °C. Choosing $T_{\text{cool}} < 227$ °C results in a TBR with low *GHSV* (< 2500 1/h). The maximum possible *GHSV* of about 59,683 1/h is achieved at $T_{\text{cool}} = 251$ °C and $L_{\text{R}} = 0.6$ m. These parameters are in consequence used as TBR design parameters for further simulations. All the TBR design parameters are summarized in Table 7.5.

Table 7.5: Tube bundle reactor design parameters.

Parameter	Value
T_{in}	T_{cool}
$d_{\text{tube,in}}$	$2 \cdot 10^{-2}$ m
$u_{\text{G,in,max}}$	0.97 m/s
N_{tube}	80
ε_{bed}	0.4
L_{R}	0.6 m
<i>GHSV</i>	59,683 1/h

Based on this study, the evolution of the local reactor temperature $T_{\text{R}}(z)$ and CO_2 conversion $X_{\text{CO}_2}(z)$ integrated along the vertical axis of the TBR is shown in Figure 7.9. Between 0 and 60 % of the reactor volume, T_{R} rises slowly from 251 °C to 350 °C, which results in an increase in X_{CO_2} of only 0.35. Between 60 and 80 % of the reactor volume, the increase in T_{R} is significant: $\Delta T_{\text{R}} = 230$ K. It results in a considerable increase in X_{CO_2} of 0.45. Between 80 and 100 % of the reactor volume, T_{R} decreases while X_{CO_2} slowly rises from 0.8 to 0.9. Under these conditions, the chemical reaction rate slows down due to thermodynamic limitation.

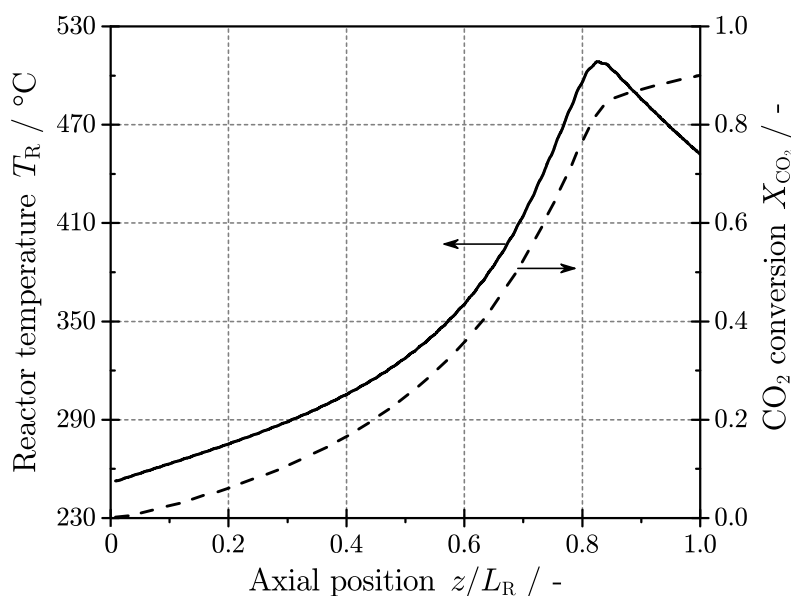


Figure 7.9: Evolution of local reactor temperature and CO_2 conversion integrated along the axial direction of the tube bundle reactor for a feed $\text{H}_2/\text{CO}_2/\text{CH}_4$ of 4/1/1 (Reactor design parameters are summarized in Table 7.5, $T_{\text{cool}} = 251$ °C).

A sensitivity analysis was carried out on the most critical parameters of the TBR model to assess the simulation reliability. These parameters control the reaction rate or the heat transfer: the tube wall heat transfer coefficient α_{wall} , the effective radial heat conductivity $\lambda_{r,\text{eff}}$, and the kinetic rate equation for CO_2 methanation $r_{2\text{PM}}$.

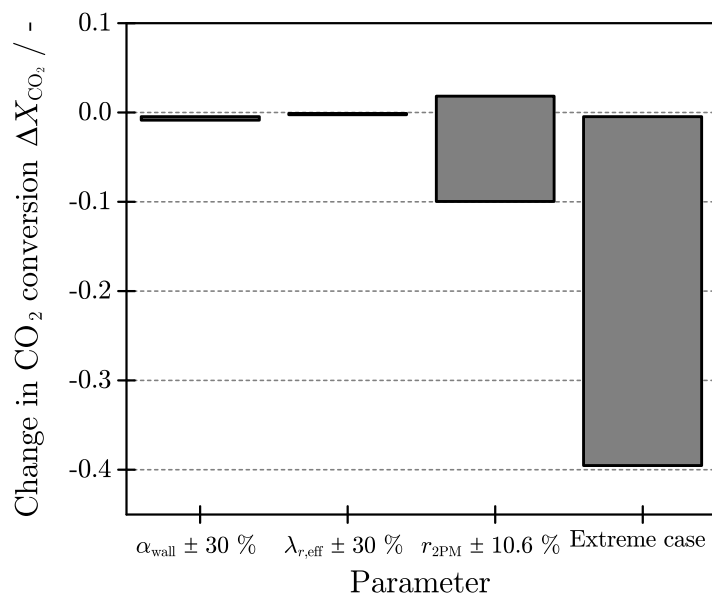


Figure 7.10: Sensitivity analysis based on the uncertainties of heat transfer coefficient and radial heat conductivity correlations as well as kinetic rate equation for the methanation tube bundle reactor with a feed $\text{H}_2/\text{CO}_2/\text{CH}_4$ of 4/1/1 (Reactor design parameters are summarized in Table 7.5, reference $X_{\text{CO}_2} = 0.9$).

The uncertainties of α_{wall} and $r_{2\text{PM}}$ were taken from literature and are $\pm 30\%$ and $\pm 10.6\%$, respectively. The uncertainty related to $\lambda_{r,\text{eff}}$ correlation could not be found in the literature (see Appendix B.3.3). Thus, the uncertainty of $\lambda_{r,\text{eff}}$ was set to $\pm 30\%$. An extreme case scenario is obtained by setting simultaneously the uncertainty of each parameter to its maximum or minimum value. The results of this sensitivity analysis are shown in Figure 7.10.

The uncertainties related to α_{wall} and $\lambda_{r,\text{eff}}$ have almost no influence on X_{CO_2} : a change of only ± 0.01 is observed. However, the maximum reactor temperature T_{max} does change ca. ± 30 K. A rise in α_{wall} and $\lambda_{r,\text{eff}}$ increases the effective heat transfer coefficient. Hence, the reactor temperature decreases as well as the effective reaction rate and the gas superficial velocity. The decrease in u_G results in higher gas residence time, which compensates for the lower reaction rates and results in almost no change in X_{CO_2} . A decrease in $r_{2\text{PM}}$ of -10.6% has a higher impact on the achievable X_{CO_2} with a change of ca. -0.1 . The TBR simulated in this work is a polytropic reactor and is strongly affected by a change in $r_{2\text{PM}}$ which impacts the evolution of temperature and gas concentrations along the whole reactor length. An increase in $r_{2\text{PM}}$ of $+10.6\%$ has less impact on X_{CO_2} because X_{CO_2} is already high and the reaction is limited by thermodynamic equilibrium and not chemical reaction kinetics. Finally, considering an extreme case scenario, a simultaneous increase in α_{wall} , $\lambda_{r,\text{eff}}$ and $r_{2\text{PM}}$ results in a significant decrease in X_{CO_2} of ca. 0.4 . Under these conditions, the cooling rate is strongly enhanced, which mitigates the formation of a hot spot: a maximum reactor temperature of

only 353 °C is reached. As a consequence lower reaction rates are achieved which decrease X_{CO_2} .

7.3.1.3 Reactor control strategy

For PtG applications, a methanation reactor must be able to adapt to a fluctuating H_2 volume flow rate, while maintaining a constant H_2/CO_2 ratio of 4. For a given gas volume flow rate, the cooling medium temperature must be adapted, so that the methanation reactor respects its boundary conditions ($X_{\text{CO}_2} \geq 0.9$, as well as all parameters given Table 7.2 and 7.3). For transient operation, the previously designed SBCR and TBR should operate between 25 and 100 % of the maximum gas load. The corresponding cooling medium temperatures derived from steady-state simulations are summarized in Table 7.6.

Table 7.6: Reactor cooling medium temperature for different gas loads. Reactor design parameters are summarized in Table 7.4 and 7.5.

Load / %	SBCR		TBR	
	$T_{\text{cool}} / ^\circ\text{C}$	$X_{\text{CO}_2} / -$	$T_{\text{cool}} / ^\circ\text{C}$	$X_{\text{CO}_2} / -$
25	300	0.975	206	0.968
50	289	0.964	226	0.942
75	278	0.933	240	0.92
100	269	0.9	251	0.9

Table 7.6 shows that X_{CO_2} decreases in both reactors for increasing gas load. However, the SBCR requires a reduced T_{cool} for increasing gas load, while the TBR needs increased T_{cool} ; this behavior is explained in section 7.3.2.1. Furthermore, at 25 % of the maximum gas load the TBR is characterized by $\Delta T_{\text{max}}/\Delta T_{\text{cool}} > 5$. As safe steady-state operation cannot be guaranteed under this operating condition (see Figure 7.8), transient TBR operation at gas loads below 50 % is not considered.

To summarize, the SBCR is an almost isothermal reactor which is limited by gas/liquid mass transfer. On the other hand, the TBR is mostly limited by heat transfer. Contrary to the SBCR, the TBR is a polytropic reactor which offers higher reaction rates. Hence, much higher $GHSV$ can be reached in a TBR (in this case, ca. 60,000 1/h) compared to a SBCR ($GHSV = 4000$ 1/h). For steady-state operation, a TBR is to be preferred to a SBCR. However, a TBR may not be suited for transient operation, as it is very sensitive to a gas load variation, leading to significant changes in advective heat transfer and cooling rate.

7.3.2 Transient Power-to-Gas operation

7.3.2.1 Effect of gas load increase on methanation reactor performance

As preliminary for transient PtG operation, a study was carried out to understand the effect of gas load increase on the SBCR and the TBR performance via comparison of dimensionless numbers for mass and heat transfer. These dimensionless numbers are derived from the differential equations describing the mass and heat balance of the reactor (SBCR: Eq. 7.8 and 7.9, TBR: Eq. 7.14 and 7.15)). They compare axial dispersion, gas/liquid mass transfer, chemical reaction or convective heat transfer with advection. These dimensionless numbers are:

- $1/Pe'$, i.e. diffusive mass transfer vs. advective mass transfer;
- $1/Pe$, i.e. diffusive heat transfer vs. advective heat transfer;
- Sh/Pe' , i.e. gas/liquid mass transfer vs. advective mass transfer;
- Da_I , i.e. reaction rate vs. advective mass transfer;
- Da_{III} , i.e. reaction heat release rate vs. advective heat transfer;
- St , i.e. convective heat transfer vs. advective heat transfer.

The results of this study are shown in Figures M.3 to M.6 in the Appendix and are summarized in Table 7.7 and 7.8.

Table 7.7: Effect of gas load increase on SBCR performance for a constant cooling medium temperature.

Reactor	Phenomena	Change	Effect
SBCR	Advection	↗↗↗	Lower gas residence time
	Axial dispersion	↗	Lower axial c_i and T gradient
	G/L mass transfer	↗↗	Higher $c_{i,L}$
	Chemical reaction	↗↗	Higher reaction rate and heat release rate
	Convective heat transfer	-	Constant heat transfer coefficient

Table 7.7 shows that a gas load in a SBCR increase leads to a rise in axial dispersion and gas/liquid mass transfer, which results in lower axial gradients of gas concentrations and temperature, and higher gas concentrations in the liquid phase, respectively. Due to the higher gas concentrations in the liquid phase the overall reaction rate increases, which also results in higher reaction heat release rate. The convective heat transfer of a SBCR is insensitive to an increase in gas load for gas superficial velocity higher than 0.1 m/s. As a consequence, the heat transfer coefficient of the SBCR is unchanged. These phenomena result in a small increase in SBCR temperature and small decrease in CO_2 conversion X_{CO_2} .

Table 7.8: Effect of gas load increase on TBR performance for a constant cooling medium temperature.

Reactor	Phenomena	Change	Effect
TBR	Advection	↗↗↗	Lower gas residence time, and hot spot translation to higher z
	Chemical reaction	↗↗	Higher reaction rate and heat release rate
	Convective heat transfer	↗↗↗	Higher heat transfer coefficient

Table 7.8 shows that a gas load increase results also in lower gas residence time. Besides, it displaces the reactor hot spot to higher axial coordinates. The overall reaction rate is increased by the higher gas concentrations, which results in higher reaction heat release rate. However, the convective heat transfer is also largely increased, which results in much higher cooling rate. The resulting cooling rate is higher than the reaction heat release rate. Consequently, the temperature of the TBR as well as CO_2 conversion decrease significantly.

7.3.2.2 Transient slurry bubble column reactor

The evolution of the mean slurry temperature \bar{T}_{SL} over time is shown in Figure 7.11 for a gas load step increase from 75 to 100 % of the maximum reactor gas load.

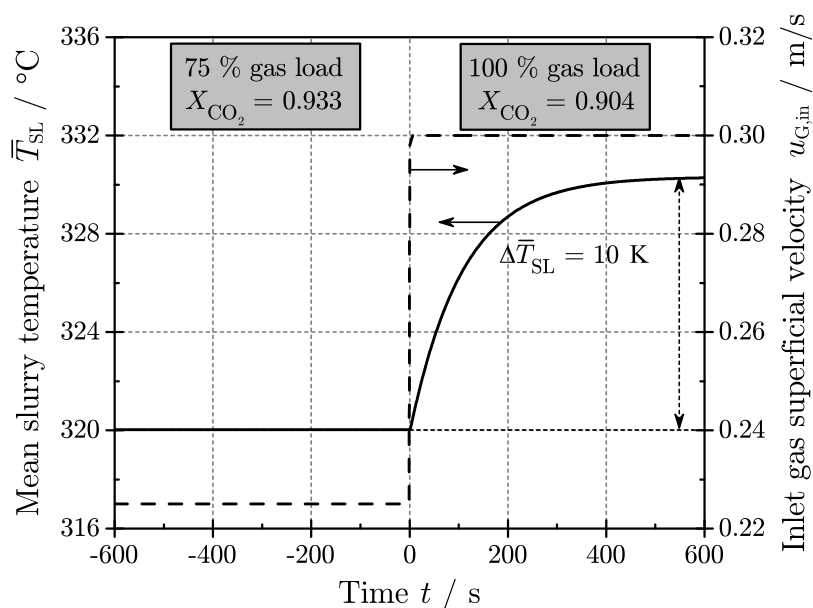


Figure 7.11: Slurry temperature as function of time after a gas load step change from 75 to 100 % for a feed $\text{H}_2/\text{CO}_2/\text{CH}_4$ of 4/1/1 (Reactor design parameters are summarized in Table 7.4, $T_{\text{cool}} = 278$ °C).

The new load is reached after 1 s. Following this change \bar{T}_{SL} increases from 320 to 330 °C; a stationary state is reached after ca. 600 s. Due to the high heat transfer coefficient (ca. $2300 \text{ W}/(\text{m}^2\cdot\text{K})$) and the high heat capacity of the slurry phase (ca. $1600 \text{ kJ}/(\text{m}^3\cdot\text{K})$), a minor increase in \bar{T}_{SL} of only 10 K takes place, while X_{CO_2} decreases from 0.933 to 0.904.

Due to the increase in gas velocity, the gas residence time is reduced, while the increased slurry temperature leads to higher reaction rates. Altogether, the higher reaction rates do not compensate for the shorter residence time, which results in a lower X_{CO_2} . However, at any time $X_{\text{CO}_2} > 0.9$ and $T_{\text{SL}} < 350$ °C is given. Hence, all SBCR boundary conditions are respected: the SBCR design is adequate for this transient operation.

The evolution of the mean slurry temperature \bar{T}_{SL} over time after a gas load decrease from 100 to 75 % is shown in Figure M.7 in the Appendix. Similar results are obtained: the SBCR design is suitable for this transient methanation operation. This statement applies also for the other gas load changes shown in Figures M.8 to M.11. Even for the large gas load change of ± 50 %, the SBCR boundary conditions are respected. As such the SBCR designed in this work is a suitable CO_2 methanation reactor for the suggested transient PtG operating conditions.

7.3.2.3 Transient tube bundle reactor

The evolution of the maximum reactor temperature T_{max} over time is shown in Figure 7.12 for a gas load increase from 75 to 100 % of the maximum reactor gas load. The new load is reached in 1 s. Following this change, T_{max} rises from 510 to 579 °C within 7 s and then decreases to 351 °C within the next 11 s. After 18 s the TBR has reached the new steady-state: the TBR response is 33 times faster than the SBCR response.

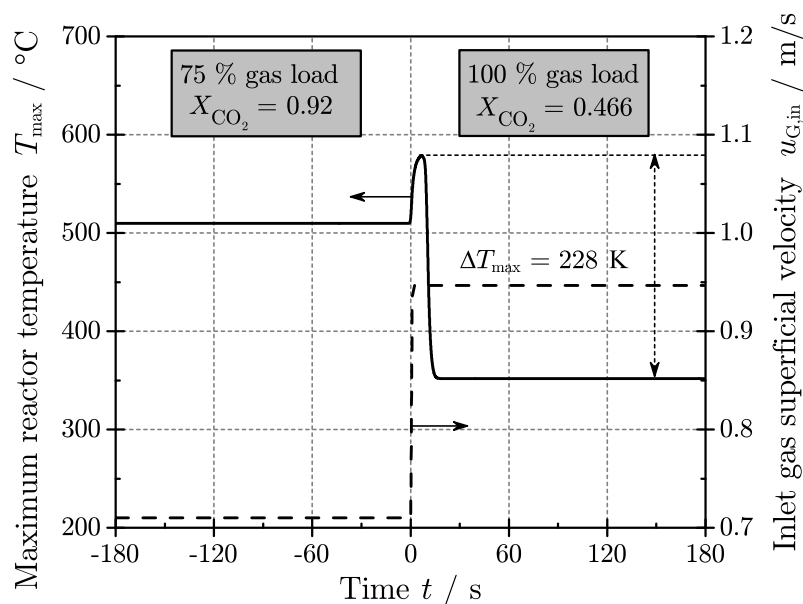


Figure 7.12: Maximum reactor temperature of the tube bundle reactor as function of time after a gas load step change from 75 to 100 % for a feed $\text{H}_2/\text{CO}_2/\text{CH}_4$ of 4/1/1 (Reactor design parameters are summarized in Table 7.5, $T_{\text{cool}} = 240$ °C).

The evolution of T_{max} over time is related to the combination of mass-transfer and heat-transfer phenomena, which are illustrated in Figure 7.13. An increase in gas inlet velocity enhances the advective mass transfer: a higher amount of educts can react in the reactor which results in an increase in reaction heat release rate. As a consequence T_{max} increases. Following the gas velocity increase, advective heat transfer and cooling rate are also increased. The increased

cooling rate results in lower reactor temperature, while the increased advective heat transfer shifts the reactor hot spot to the reactor outlet. Hence, the hot spot progressively disappears from the reactor and T_{\max} decreases.

Figure 7.13 shows also that X_{CO_2} decreases from 0.92 to 0.466 comparing the two stationary states. The lower X_{CO_2} is related to the lower reactor temperature as well as the decreased gas residence time. The TBR response to a gas load change is not satisfying the design requirements. First, the catalyst reaches a temperature higher than the maximum of 510 °C. Then, the catalyst undergoes a high temperature change within a short period of time, which may result in mechanical stress leading to catalyst crushing and deactivation. Finally, the outlet gas quality ($X_{\text{CO}_2} < 0.9$) is not satisfying the design requirements.

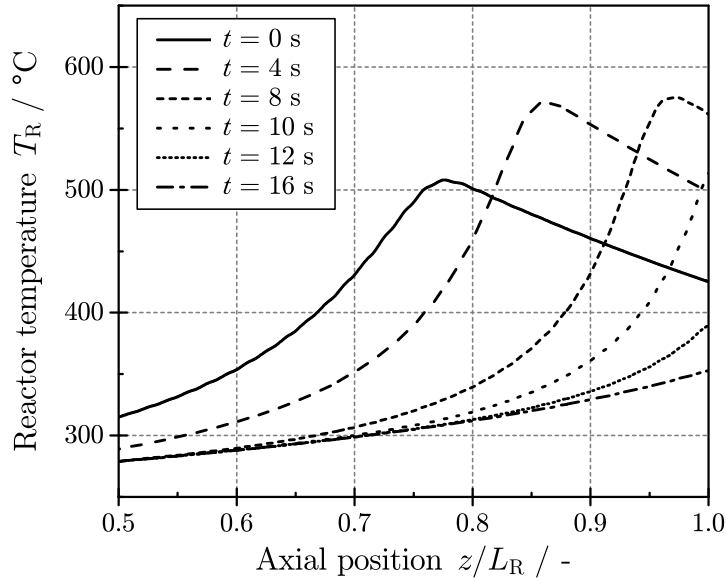


Figure 7.13: Evolution of the reactor temperature along the axial direction of the tube bundle reactor after a gas velocity step change from 0.71 to 0.95 m/s ($p_{\text{in}} = 20$ bar, $L_{\text{R}} = 0.6$ m, $T_{\text{cool}} = 240$ °C).

The evolution of the maximum reactor temperature T_{\max} over time after a gas load decrease from 100 to 75 % is shown in Figure M.13. Again, the transient TBR response does not satisfy the design requirements. Although X_{CO_2} fulfills the required gas quality, T_{\max} is above the maximum allowed catalyst temperature of 510 °C. Besides, the catalyst undergoes a temperature change of 84 K within 15 s which may result in catalyst crushing and deactivation.

The other gas load variations show similar results (see Figures M.12 to M.14). Altogether the TBR design suggested in this work is not suitable for transient PtG operation. Solutions to overcome this issue are suggested in the following section.

7.3.3 Reactor improvement considerations

Dimensionless numbers are useful to characterize and understand the interaction between mass transfer, heat transfer, and chemical reaction involved in reaction engineering. In this work, the Damköhler numbers II and III as well as the Stanton number are of special interest to understand the process involved in steady-state and transient operations of a SBCR and a TBR for CO₂ methanation.

The Damköhler number II, Da_{II} , compares chemical reaction rate with mass-transfer phenomena as shown in Eq. 7.18. The volumetric gas/particle mass transfer coefficient $k_G a_{CO_2}$ of the TBR was calculated using Eq. C.2 in the Appendix, while the volumetric gas/liquid mass transfer coefficient for the SBCR $k_L a_{CO_2}$ was calculated with Eq. 2.22.

$$Da_{II} = \frac{\varphi_S \cdot \rho_S \cdot r_{CO_2}}{k_j a_{CO_2} \cdot c_{CO_2,G}} \quad (7.18)$$

The evolution of Da_{II} with increasing gas load is shown in Figure 7.14 for both SBCR and TBR. $Da_{II,SBCR} > 1$, while $Da_{II,TBR} \ll 1$ over the whole range of gas load, i.e. the SBCR is moderately limited by gas/liquid mass transfer while the inter-particle mass transfer is not limiting the TBR. To improve the efficiency of the SBCR, efforts should be made to enhance the gas/liquid mass transfer e.g. by increasing the specific gas/liquid interfacial area [136, 137].

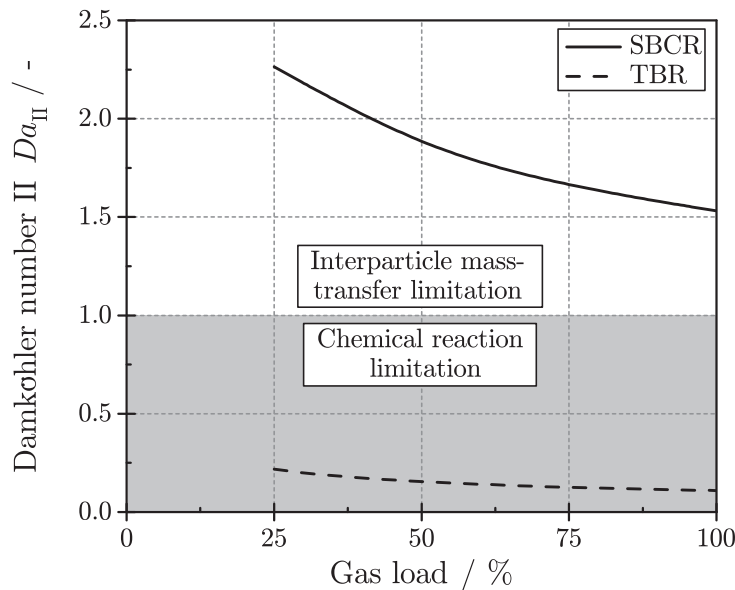


Figure 7.14: Influence of gas load on Damköhler number II of the slurry bubble column reactor and the tube bundle reactor for a gas atmosphere H₂/CO₂/CH₄ of 4/1/1 ($p_R = 20$ bar; $\varphi_S = 0.2$, $T_{SBCR} = 320$ °C; $T_{TBR} = 350$ °C).

The transient Stanton number St' compares cooling rate with reactor heat accumulation as shown in Eq. 7.19. In Eq. 7.19, $\Delta T_R/\Delta t$ is set for both reactors to 40 K/h which corresponds to the maximum catalyst heating rate recommended by the catalyst supplier. However, as the reactors are compared with each other, the value of $\Delta T_R/\Delta t$ is not relevant.

$$St' = \frac{\alpha_{\text{eff}} \cdot a_{\text{cool}} \cdot (T_{\text{R}} - T_{\text{cool}})}{\rho \cdot c_p \cdot \frac{\Delta T_{\text{R}}}{\Delta t}} \quad (7.19)$$

The evolution of St' with increasing gas load is shown in Figure 7.15. For both reactors, $St' \gg 1$: the heat accumulation is sensitive to a change in cooling rate. However, St'_{TBR} is 15 to 53 times higher than St'_{SBCR} . This explains the reactor response time shown in Figure 7.11 and Figure 7.12. As St'_{TBR} is high, the TBR reaches steady state after ca. 20 s, while the SBCR requires ca. 600 s to reach steady-state.

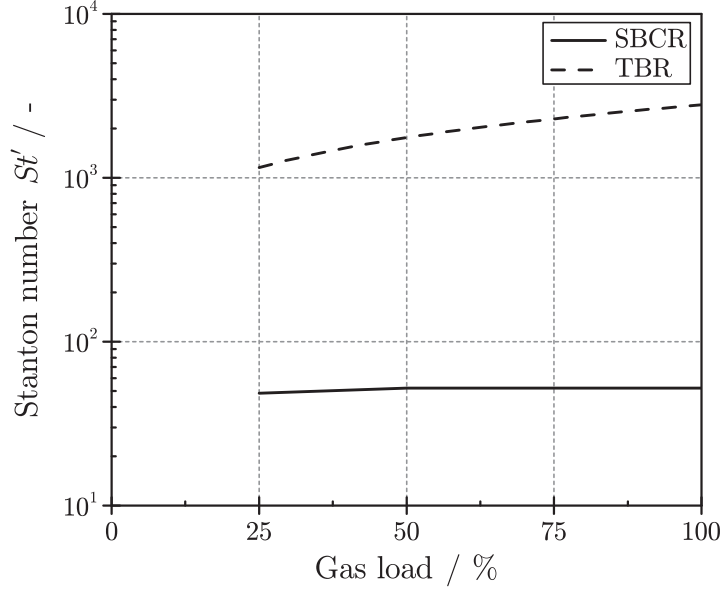


Figure 7.15: Influence of gas load on transient Stanton number of the slurry bubble column reactor and the tube bundle reactor for a gas atmosphere $\text{H}_2/\text{CO}_2/\text{CH}_4$ of 4/1/1 ($p_{\text{R}} = 20$ bar, $\Delta T_{\text{R}}/\Delta t = 40$ K/h; $\varphi_{\text{S}} = 0.2$, $T_{\text{SBCR}} = 320$ °C, $T_{\text{cool,SBCR}} = 270$ °C; $T_{\text{TBR}} = 350$ °C, $T_{\text{cool,TBR}} = 250$ °C).

Finally, the transient Damköhler number III Da'_{III} compares heat release rate from reaction with heat accumulation as shown in Eq. 7.20.

$$Da'_{\text{III}} = \frac{\varphi_{\text{S}} \cdot \rho_{\text{S}} \cdot r_{\text{CO}_2} \cdot |\Delta h_{\text{r}}|}{\rho \cdot c_p \cdot \frac{\Delta T_{\text{R}}}{\Delta t}} \quad (7.20)$$

The evolution of Da'_{III} with increasing gas load is shown in Figure 7.16 for both reactors. In both cases is $Da'_{\text{III}} \gg 1$: the heat accumulation is sensitive to a change in reaction heat release rate. Nevertheless, $Da'_{\text{III,TBR}}$ is ca. 45 times higher than $Da'_{\text{III,SBCR}}$. Combined with St'_{TBR} , $Da'_{\text{III,TBR}}$ can explain the poor transient behavior of this TBR: this reactor is very sensitive to a change in reaction heat release rate and cooling rate, which results in significant variations in reactor temperature during transient operation. On the contrary, St'_{SBCR} and $Da'_{\text{III,SBCR}}$ are much lower due to the high heat capacity of the slurry phase: the SBCR is much less sensitive to change in reaction heat release rate or cooling rate and can successfully be operated under transient operating conditions.

Options to improve the transient behavior of the TBR are to reduce the catalyst volume fraction φ_S , to use a catalyst showing a lower methanation activity or to mix the catalyst with high heat capacity inert material in order to decrease Da'_{III} . However, this will reduce the reactor $GHSV$.

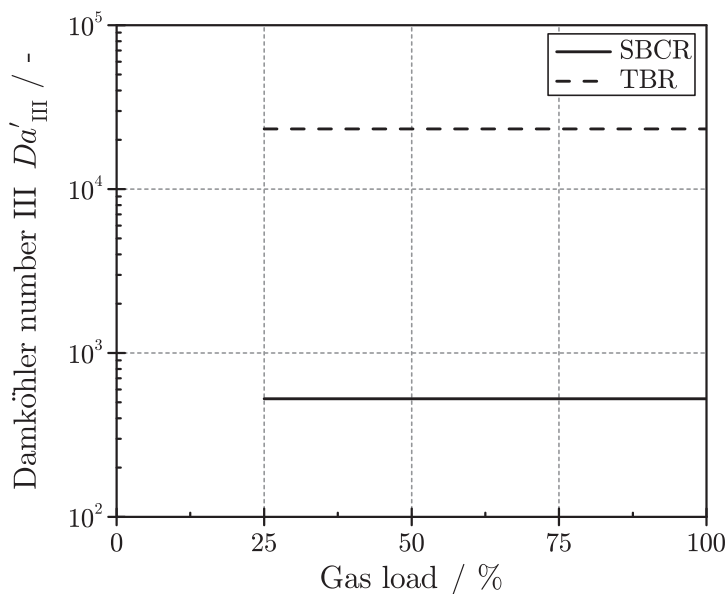


Figure 7.16: Influence of gas load on transient Damköhler number III of the slurry bubble column reactor and the tube bundle reactor for a gas atmosphere $H_2/CO_2/CH_4$ of 4/1/1 ($p_R = 20$ bar, $\Delta T_R/\Delta t = 40$ K/h; $\varphi_S = 0.2$, $T_{SBCR} = 320$ °C; $T_{TBR} = 350$ °C).

7.4 Summary

The objective of this chapter was to assess the performance of a SBCR for transient CO_2 methanation, as part of a PtG process chain. For this purpose, an axial dispersion model based on literature data and experimental data gathered in chapters 4 to 6 was developed. The SBCR performance was compared to a state-of-the-art TBR for steady-state and transient PtG operation. Transient PtG operation was modeled using gas load step changes between 25 and 100 % of the reactor maximum capacity, while the TBR was modeled with a 1D homogeneous fixed-bed reactor model.

For steady-state operation the TBR allows for much higher gas hourly space velocities ($GHSV$) as compared to the SBCR (see Figures 7.5 and 7.8). In addition, sensitivity analyses showed that under the relevant reaction conditions the TBR is limited by heat transfer, while the SBCR is limited by gas/liquid mass transfer (see Figures 7.7 and 7.10).

For transient PtG operation the TBR undergoes significant temperature changes within a short time resulting in undesired outlet gas qualities violating product gas specifications (see Figure 7.12). The TBR is not adapted to gas load step changes but could be operated under transient operation using well-defined and slow change in cooling medium temperature as well as gas velocity. As a consequence, the related PtG facility would require a larger H_2 buffer

tank resulting in significantly lower process economics. On the contrary, the SBCR is adapted to transient PtG operations: the SBCR temperature is kept under control and changes slowly over time, while the outlet gas composition sticks to the gas quality requirements (see Figure 7.11).

Finally, measures to improve the efficiency of both reactors were proposed considering dimensionless numbers. The *GHSV* of the SBCR can be enhanced by increasing the specific interfacial area controlling gas/liquid mass transfer (see Figure 7.14), while the transient behavior of the TBR can be improved by reducing the catalyst concentration/activity or by mixing the catalyst with high heat capacity inert material in detriment of the *GHSV* (see Figures 7.15 and 7.16).

Altogether a SBCR for CO₂ methanation is a promising reactor concept, if transient operating conditions are considered.

8 Summary

The share of renewable energy sources like wind and sun is rising in the EU to mitigate the impact of human beings on climate change [309]. However, this type of renewable energy is intermittent as well as fluctuating, which could result in a mismatch between power production and demand in the future. To tackle this issue, Power-to-Gas (PtG) processes which aim at transforming renewable electrical energy into chemical energy carriers with high energy density [2] can be implemented. The PtG process chain considered in this work aims for transforming electrical energy into methane through the reaction of carbon dioxide with hydrogen produced by water electrolysis (see Eq. 8.1). Methane is the main component of synthetic natural gas (SNG), which can be injected into the natural gas grid. SNG can be used for a wide range of applications in highly efficient final energy conversion technologies, e.g. decentralized/central combined heat and power units and mobility (compressed natural gas and liquefied natural gas).



To minimize the size of a H_2 buffer between the electrolysis and methanation steps, which represents the main invest cost of a PtG facility after the electrolyzer [304], the methanation reactor should be operated under transient operating conditions. This represents a challenge for reaction engineering: reactor temperature as well as outlet gas composition must always be kept under control, whatever the current reactor gas load is. The current benchmark PtG facility in Werlte [205] uses a tube bundle methanation reactor with CO_2 from biogas used as carbon source and H_2 from two 3 MW alkali electrolyzers. The literature related to this facility is scarce and little information is available regarding the transient behavior of the methanation reactor. Considering the electrolyzer technology as well as the methanation reactor type of the Werlte facility only minimal flexibility of this PtG process can be expected.

An alternative methanation reactor concept is the slurry bubble column reactor (SBCR). In this reactor, the catalyst is suspended in a liquid and fluidized by the rising gas bubbles. The high heat capacity as well as the good mixing of the slurry phase allow for very efficient heat removal and almost isothermal operating conditions. The main reactor drawback is linked to the additional mass transfer resistance from the gas to the liquid phase. The transient behavior of a SBCR has already been successfully tested for Fischer-Tropsch synthesis application [144]. Nevertheless, Fischer-Tropsch synthesis SBCR differs from CO_2 methanation SBCR; in Fischer-Tropsch synthesis the feed gas is diluted with recirculation gas and a smaller conversion per pass is achieved as compared to CO_2 methanation. Consequently, the reaction heat release rate in a Fischer-Tropsch synthesis SBCR is less pronounced.

The aim of this thesis was to understand and predict the behavior of a SBCR operated under transient CO₂ methanation condition using detailed experimental data as well as literature. To fulfill this task, the following pieces of information were required:

- Reactor hydrodynamics;
- Gas/liquid mass transfer;
- Heat transfer;
- CO₂ methanation reaction rate.

In a previous PhD Thesis carried out at Engler-Bunte-Institut, Fuel Technology, Manuel Götz demonstrated the feasibility of three-phase CO₂ methanation in a 10 kW SBCR laboratory facility using a commercial nickel catalyst and dibenzyltoluene (C₂₁H₂₀) as liquid phase for temperatures between 250 and 320 °C and pressures up to 20 bar [8]. In addition, Götz measured the solubility of CO₂ and H₂ in dibenzyltoluene for temperatures relevant for three-phase CO₂ methanation. However, some pieces of data were missing to develop a complete SBCR simulation tool for CO₂ methanation. First, the solubilities of the CO₂ methanation product gases, i.e. CH₄ and H₂O, were not known in the chosen liquid phase dibenzyltoluene (DBT). Then, SBCR hydrodynamics, gas/liquid mass transfer and heat transfer for the operating conditions relevant for CO₂ methanation were not fully described. Finally, the CO₂ methanation reaction kinetics in a three-phase system was not established. Especially, the influence of a liquid phase on a gaseous reaction like methanation was not clear. In this PhD thesis, experiments focused on the determination of CH₄ and H₂O solubilities in DBT as well as on the development of a kinetic rate equation for three-phase CO₂ methanation.

A laboratory facility was built for the determination of methanation product gas solubilities, and verified with well-defined CO₂ solubility experiments in pure water. Then, the solubilities of CH₄ and H₂O in DBT were determined for pressures and temperatures relevant for CO₂ methanation:

- The Henry's law constant of CH₄ in DBT $H_{\text{CH}_4,px}$ decreases from 550 to 538 bar in the temperature range of 240 to 320 °C and for pressures up to 12 bar;
- The Henry's law constant of H₂O in DBT $H_{\text{H}_2\text{O},px}$ increases from 143 to 180 bar in the temperature range of 250 to 290 °C and for pressures up to 9 bar.

Thereafter, to clarify the influence of a liquid phase on the CO₂ methanation reaction kinetics, three-phase CO₂ methanation experiments were carried out in a continuous stirred-tank reactor for liquid phases showing different gas solubilities for CO₂, H₂, CH₄, and H₂O. The following results were gathered for a CO₂ partial pressure of 1 bar and temperature of 230 °C:

- At same reactant partial pressures, different reaction rates are observed for different liquid phases;
- At same reactant concentrations in the liquid phase, similar reaction rates are observed;

Thus, the relevant parameter to describe CO₂ methanation reaction kinetics in a three-phase system is gas concentration in the liquid phase, which can be calculated from the gas partial pressure and the corresponding Henry's law constant.

Then, further three-phase CO₂ methanation kinetic experiments were carried out in the continuous stirred-tank reactor in DBT for a wide range of technically relevant operating conditions (see Chapter 5, Table 5.3). Based on these experiments, the kinetic rate equation shown in Eq. 8.2 was developed to describe three-phase CO₂ methanation reaction kinetics. The constant K describes the chemical equilibrium limitation, while $c_{i,L}$ represents the concentration of gas species i in the liquid phase.

$$r_{\text{CO}_2} = 3.2462 \cdot 10^5 \cdot \exp\left(\frac{-79378}{R \cdot T}\right) \cdot \frac{c_{\text{H}_2,L}^{0.4} \cdot c_{\text{CO}_2,L}^{0.1}}{(1 + 1 \cdot c_{\text{H}_2\text{O},L})^{0.1}} \cdot K \quad (8.2)$$

Finally, a SBCR was modeled for catalytic CO₂ methanation in the PtG process with a one-dimensional axial dispersion reactor model using own experimental data related to gas solubilities and CO₂ methanation reaction kinetics, as well as literature data related to reactor hydrodynamics, gas/liquid mass transfer and heat transfer within a SBCR. The performances of the SBCR and a state-of-the-art tube bundle reactor (TBR) simulated with a one-dimensional homogeneous fixed-bed reactor model were compared for steady-state and transient PtG operations. Transient PtG conditions were modeled using gas load step changes in the range of 25 to 100 % of the maximum reactor capacities, while maintaining the cooling medium temperature constant.

For steady-state PtG operation, the following results were obtained:

- The TBR offers high gas hourly space velocities ($GHSV$) up to 60,000 1/h; it is limited by heat transfer;
- The SBCR can reach $GHSV$ up to 4,000 1/h; it is limited by gas/liquid mass transfer.

Hence, the TBR is more efficient than the SBCR for steady-state PtG operation.

For transient PtG operation, i.e. 25 or 50 % load change in 1 s, the following results were obtained:

- The TBR undergoes significant temperature changes of 200 K within 20 s resulting in undesired outlet gas qualities;
- The SBCR undergoes moderate temperature changes of 10 K within 10 min, while the outlet gas composition sticks to the gas quality requirements.

Therefore, the SBCR is more efficient than the TBR for these transient PtG operations.

To conclude, options to improve the efficiency of both reactors were proposed and discussed based on theoretical consideration:

- The $GHSV$ of the SBCR can be enhanced by increasing the specific interfacial area controlling gas/liquid mass transfer;
- The transient behavior of the TBR can be improved by reducing the catalyst concentration/activity or by mixing the catalyst with high heat capacity inert material in detriment of $GHSV$ of the TBR.

9 Zusammenfassung

Der Anteil der erneuerbaren Energien wie Wind und Sonne steigt in der EU kontinuierlich an und leistet damit einen Beitrag zur Minimierung der anthropogenen Einflüsse auf den Klimawandel [309]. Bei all den positiven Effekten der Nutzung regenerativer Energien muss jedoch bedacht werden, dass diese zeitlich intermittierend und fluktuierend anfallen und daher die bereits heute auftretenden Diskrepanzen zwischen Energieerzeugung und Nutzung mit zunehmender Substitution der gut speicherbaren fossilen Energieträger weiter zunehmen wird. Um das Problem der schlechten Speicherbarkeit elektrischer Energie in den Griff zu bekommen, könnten zukünftig Power-to-Gas (PtG) Prozesse einen wertvollen Beitrag leisten. Bei diesen wird schlecht speicherbare elektrische Energie in einen gut speicher- und nutzbaren gasförmigen Energieträger mit hoher Energiedichte umgewandelt [2]. Die in dieser Arbeit betrachtete PtG-Prozesskette nutzt hierzu die Umwandlung von Kohlenstoffdioxid mit regenerativ erzeugtem Wasserstoff aus einer Wasserelektrolyse, um mit Hilfe der Methanisierungsreaktion (siehe Gl. 9.1) synthetisches Methan zu erzeugen. Dieses kann anschließend als Substitute Natural Gas (SNG) in das Erdgasnetz eingespeist und auf diesem Weg transportiert, gespeichert und genutzt werden. Für die Nutzung stehen alle Erdgasanwendungen offen, was vor allem Kraft-Wärme-Kopplung oder die Nutzung im Mobilitätssektor als CNG (Compressed Natural Gas) oder LNG (Liquefied Natural Gas) einschließt.



Innerhalb einer PtG-Prozesskette stellt der Wasserstoff(zwischen)speicher eine der Hauptinvestitionen dar. Dessen Größe lässt sich minimieren, wenn der nachfolgende Syntheseprozess den transient anfallenden Eduktströmen folgen kann, was bei katalytischen Synthesen eher die Ausnahme ist. Hauptproblem dabei ist, dass sowohl die Reaktortemperatur als auch die Eduktgaszusammensetzungen ständig mit dem jeweiligen Lastzustand korrelieren müssen. Thermische Runaways oder unzulässige Produktzusammensetzungen müssen unter allen Umständen vermieden werden, was zusammen eine bisher nur unzureichend gelöste technische Herausforderung darstellt. Die aktuelle Benchmark-PtG-Anlage in Werlte [205] nutzt einen mit einer Salzsäure gekühlten Festbettreaktor. Als Kohlenstoffquelle wird CO_2 aus einer Biogasanlage genutzt, der notwendige Wasserstoff stammt aus zwei 3 MW Alkali Elektrolyseuren. Leider finden sich in der Literatur nur wenige technische Details zu dieser Anlage. Die bekannten technischen Daten legen aber den Schluss nahe, dass diese Anlage nur bedingt dynamisch betreibbar ist und daher diese Technologie für die angesprochenen Anforderungen unzureichend ist.

Ein alternativer Methanisierungsreaktor-konzept ist der Blasensäulenreaktor (SBCR). In diesem Reaktor ist der Katalysator in einer Flüssigkeit suspendiert und durch die steigenden Gasblasen fluidisiert. Die hohe Wärmekapazität sowohl als auch die gute Durchmischung der Slurryphase ermöglichen eine sehr effiziente Wärmeabfuhr und fast isotherme Betriebsbedingungen. Der Hauptnachteil dieses Reaktors ist mit dem zusätzlichem Gas/Flüssigkeit-Stoffübergangswiderstand verbunden. Das transiente Verhalten eines SBCR wurde schon zur Fischer-Tropsch-Synthese erfolgreich getestet [144]. Nichtsdestotrotz unterscheidet sich ein SBCR zur Fischer-Tropsch-Synthese von einem SBCR zur CO₂-Methanisierung: im Vergleich zur CO₂-Methanisierung ist das Feedgas in Fischer-Tropsch-Synthese mit Rezirkulationsgas verdünnt und eine kleinere Konversion pro Pass ist erzielt. Deswegen ist die Reaktionswärme-freisetzung in einem SBCR zur in Fischer-Tropsch-Synthese weniger ausgeprägt.

Ziel dieser Dissertation war, das transiente Verhalten eines SBCR zur CO₂-Methanisierung durch Einsatz experimenteller Daten sowie Daten aus der Literatur zu verstehen und vorherzusagen. Für diesen Zweck mussten offene Fragen zu den folgenden Punkten geklärt werden:

- Reaktorhydrodynamik;
- Gas/Flüssigkeit-Stoffübergang
- Wärmeübergang;
- Reaktionskinetik der CO₂-Methanisierung.

In seiner am Engler-Bunte-Institut geb durchgeführte Dissertation zeigte Manuel Götz die Machbarkeit der Dreiphasen-CO₂-Methanisierung in einem 10 kW SBCR-Laborapparat mit einem kommerziell verfügbaren Nickelkatalysator und Dibenzyltoluol (C₂₁H₂₀) als Flüssigkeit bei Temperaturen zwischen 250 and 320 °C und Drücken bis zu 20 bar [8]. Darüber hinaus maß Götz die Löslichkeit von CO₂ und H₂ bei Temperaturen relevant für die Dreiphasen-CO₂-Methanisierung. Jedoch fehlen einige wesentliche Daten zur Erstellung eines brauchbaren Simulationswerkzeuges zur Beschreibung eines SBCR-Reaktors. So sind beispielsweise keine Daten zur Löslichkeit der Methanisierungsprodukte CH₄ und H₂O in der Flüssigphase (DBT) verfügbar. Auch sind weder die SBCR-Hydrodynamik noch der Gas-/Flüssigkeits-Stoff- und -Wärmeübergang unter den Bedingungen der CO₂-Methanisierung bekannt und mathematisch beschrieben. Auch die Reaktionskinetik der CO₂-Methanisierung im dreiphasigen System aus Gas, festem Katalysator und Flüssigphase wurde bisher nicht ermittelt, ist jedoch für die Modellierung und Prozessbetrachtung von zentraler Wichtigkeit.

Zur Bestimmung der Löslichkeiten der Prozessgase unter Methanisierungsbedingungen wurde eine geeignete Apparatur errichtet. Zur Verifizierung des Versuchsaufbaus wurden Literatur-ergebnisse zur Löslichkeit von CO₂ in Wasser durchgeführt, die zufriedenstellende Ergebnisse lieferten. Anschließend wurden mit dem verifizierten Versuchsaufbau Löslichkeiten von CH₄ und H₂O in DBT unter relevanten Prozessdrücken und -temperaturen bestimmt und bewertet:

- Der Henry-Koeffizient von CH₄ in DBT $H_{\text{CH}_4,px}$ nimmt von 550 bis 538 bar zwischen 240 und 320 °C bei Drücken bis zu 12 bar ab;
- Der Henry-Koeffizient von H₂O in DBT $H_{\text{H}_2\text{O},px}$ steigt von 143 bis 180 bar zwischen 250 und 290 °C bei Drücken bis zu 9 bar an.

Danach wurden Dreiphasenmethanisierungsexperimente in einem komplett rückvermischtem Rührkessel mit verschiedenen Flüssigkeiten und dadurch verschiedenen Gaslöslichkeiten für CO_2 , H_2 , CH_4 , und H_2O durchgeführt, um den Einfluss einer Flüssigkeit auf die Reaktionskinetik der CO_2 -Methanisierung zu klären. Die folgenden Ergebnisse wurden bei einem CO_2 -Partialdruck von 1 bar und 230 °C gesammelt:

- Bei gleichen Reaktantpartialdrücken wurden unterschiedliche Reaktionsgeschwindigkeiten für verschiedene Flüssigkeiten beobachtet;
- Bei gleichen Reaktantkonzentrationen in der Flüssigkeit wurden ähnliche Reaktionsgeschwindigkeiten beobachtet;

Auf Basis dieser Ergebnisse kann davon ausgegangen werden, dass die Gaskonzentration in der Flüssigphase der relevante Parameter zur Beschreibung der CO_2 -Reaktionskinetik ist. Diese Konzentration kann bei den relevanten Betriebsbedingungen der Dreiphasen-Methanisierung aus den Gasphasen-Partialdrücken und den bekannten bzw. in dieser Arbeit ermittelten Henry-Koeffizienten berechnet werden.

Im Anschluss an diese ersten Dreiphasenmethanisierungsexperimente erfolgte die experimentelle Ermittlung der Reaktionskinetik der CO_2 -Methanisierung. Hierzu wurde Versuche in einem idealen Labor-Rührkesselreaktor durchgeführt (siehe Kapitel 5, Tabelle 5.3). Mit den daraus erhaltenen Ergebnissen wurde der in Gl. 9.2 gezeigte reaktionskinetische Ansatz aufgestellt, in welchem die Konstante K die Annäherung an das thermodynamische Gleichgewicht und $c_{i,L}$ die Konzentrationen der beteiligten Gasspezies in der Flüssigphase darstellen.

$$r_{\text{CO}_2} = 3.2462 \cdot 10^5 \cdot \exp\left(\frac{-79378}{R \cdot T}\right) \cdot \frac{c_{\text{H}_2,L}^{0.4} \cdot c_{\text{CO}_2,L}^{0.1}}{(1 + 1 \cdot c_{\text{H}_2\text{O},L})^{0.1}} \cdot K \quad (9.2)$$

Unter Nutzung der reaktionskinetischen Daten und der zuvor ermittelten Stoffparameter und hydrodynamischen Größen wurde abschließend ein Modell zur Beschreibung eines SBCR aufgestellt und mit diesem ein Dreiphasen-Reaktor innerhalb einer PtG-Prozesskette simuliert. Diese Ergebnisse wurden mit denen eines 1D homogenen Festbettreaktormodells (TBR) verglichen, welches für die gleichen Rahmenbedingungen erstellt wurde. Für die Betrachtung der Dynamikfähigkeit beider Reaktorkonzepte wurde jeweils eine Laständerung zwischen 25 und 100 % der Auslegungsgröße betrachtet, die innerhalb einer Sekunde auftritt und dabei die Temperatur des Kühlmediums konstant lässt.

Für stationären PtG-Betrieb wurden die folgenden Ergebnisse erhalten:

- Der TBR ermöglicht hohe gas hourly space velocities ($GHSV$) bis zu 60.000 1/h; er ist durch den Wärmeübergang limitiert;
- Der SBCR kann bei einer maximalen $GHSV$ von 4.000 1/h betrieben werden; er ist durch den Gas/Flüssigkeit-Stoffübergang limitiert.

Für einen stationären Betrieb ist daher der TBR effizienter als der SBCR.

Für den transienten Betrieb folgt aus dem Vergleich der beiden Reaktorkonzepte:

- Im TBR treten Temperaturspitzen von 200 K innerhalb von 20 Sekunden auf, was zur Schädigung des Katalysators und/oder der Reaktorrohre führen kann. Außerdem können bei diesen erhöhten Temperaturen die erforderlichen Produktgasspezifikationen nicht eingehalten werden;
- Im SBCR beträgt der maximale Temperaturanstieg durch Lasterhöhung 10 K in 10 Minuten. Es treten keine unzulässigen Temperaturspitzen auf und die Produktgaszusammensetzung erfüllt alle Spezifikationen.

Für einen transienten Betrieb ist daher der SBCR deutlich effizienter als der TBR. Es können dynamische Betriebsweisen realisiert werden, die bei einem TBR aus verschiedenen Gründen unmöglich sind.

Zum Schluss wurden Optionen zur Verbesserung der Effizienz beider Reaktoren an Hand von theoretischen Überlegungen vorgeschlagen und diskutiert:

- Die *GHSV* des SBCR kann durch Erhöhung der spezifischen Grenzfläche, die den Gas/Flüssigkeit-Stoffübergang kontrolliert, vergrößert werden;
- Das transiente Verhalten des TBR kann durch Abnahme der Katalysatorkonzentration, bzw. -Aktivität oder durch Mischung des Katalysators mit einem inerten Material, das eine hohe Wärmekapazität besitzt, verbessert werden. Nachteil ist eine zwangsläufige Abnahme des *GHSV* des Reaktors.

10 Outlook

In this PhD thesis research focused on the determination of methanation gas solubilities in dibenzyltoluene, on the development of a kinetic rate equation for three-phase CO₂ methanation as well as on the understanding of the effect of a liquid phase on a gas phase reaction like CO₂ methanation. For a better understanding of the behavior of a SBCR operated under transient CO₂ methanation condition, further experimental investigations related to reactor hydrodynamics as well as mass and heat transfer should be performed.

For this purpose, a three-phase methanation pilot facility is under construction for the so-called Karlsruhe Institute of Technology Energy-Lab 2.0 project. The characteristics of this pilot plant are as following:

- Up to 50 m³/h (STP) inlet gas volume flow rate;
- H₂ from a 1 MW PEM electrolyzer, CO₂ from a tank, and syngas from a 5 MW entrained flow gasifier;
- SBCR diameter of 0.25 m and height of 2.5 m ($h_R/d_R = 10$);
- Up to 10 m³/h (STP) methane output.

This facility will also allow for confrontation of the transient SBCR simulation results with experimental data.

Verification of the contribution from the co-authors

Title: A study on Three-phase CO₂ Methanation Reaction kinetics in a Continuous Stirred-tank Slurry Reactor

Journal: Fuel

Authors: Jonathan Lefebvre, Nike Trudel, Siegfried Bajohr and Thomas Kolb

Position in the dissertation:

The content of this paper has been included in Chapters 4 and 5.

Contribution of Jonathan Lefebvre:

- conceived the concept
- designed the experiments
- conducted the gas solubility experiments
- conducted the CO₂ methanation experiments: 80 %
- analyzed and discussed the results/data: 80 %
- wrote and corrected the manuscript

Contribution of Nike Trudel:

- conducted the CO₂ methanation experiments: 20 %
- analyzed and discussed the results/data: 20 %
- read and corrected the manuscript

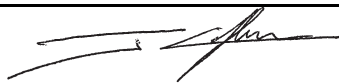



Contribution of Siegfried Bajohr:

- read and corrected the manuscript

Contribution of Thomas Kolb:

- supervised the research
- read and corrected the manuscript

Signature of the authors:

Author	Electronic signature
Jonathan Lefebvre	
Nike Trudel	
Siegfried Bajohr	
Thomas Kolb	

Title: A Comparison of Two-phase and Three-phase CO₂ Methanation Reaction Kinetics

Journal: Fuel

Authors: Jonathan Lefebvre, Siegfried Bajohr and Thomas Kolb

Position in the dissertation:

The content of this paper has been included in Chapter 6.

Contribution of Jonathan Lefebvre:

- conceived the concept
- designed and conducted the experiments
- analyzed and discussed the results/data
- wrote and corrected the manuscript

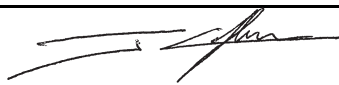


Contribution of Siegfried Bajohr:

- read and corrected the manuscript

Contribution of Thomas Kolb:

- supervised the research
- read and corrected the manuscript

Signature of the authors:

Author	Electronic signature
Jonathan Lefebvre	
Siegfried Bajohr	
Thomas Kolb	

Publication list

Journal publications sorted by year

- J. Lefebvre, S. Bajohr, and T. Kolb, “A Comparison of Two-phase and Three-phase CO₂ Methanation Reaction Kinetics”, *Fuel*, vol. 239, pp. 896-904, 2019, ISSN: 0016-2361. DOI: 10.1016/j.fuel.2018.11.051.
- J. Lefebvre, N. Trudel, S. Bajohr, and T. Kolb, “A study on three-phase CO₂ methanation reaction kinetics in a continuous stirred-tank slurry reactor”, *Fuel*, vol. 217, pp. 151-159, 2018, ISSN: 0016-2361. DOI: 10.1016/j.fuel.2017.12.082.
- M. Götz, J. Lefebvre, F. Mörs, F. Ortloff, R. Reimert, S. Bajohr, and T. Kolb, “Novel gas holdup correlation for slurry bubble column reactors operated in the homogeneous regime”, *Chemical Engineering Journal*, vol. 308, pp. 1209-1224, 2017, ISSN: 1385-8947. DOI: 10.1016/j.cej.2016.09.101.
- S. Rönsch, J. Schneider, S. Matthischke, M. Schlüter, M. Götz, J. Lefebvre, P. Prabhakaran, and S. Bajohr, “Review on methanation - from fundamentals to current projects”, *Fuel*, vol. 166, pp. 276-296, 2016, ISSN: 0016-2361. DOI: 10.1016/j.fuel.2015.10.111.
- M. Götz, J. Lefebvre, F. Mörs, R. Reimert, F. Graf, and T. Kolb, “Hydrodynamics of organic and ionic liquids in a slurry bubble column reactor operated at elevated temperatures”, *Chemical Engineering Journal*, vol. 286, pp. 348-360, 2016, ISSN: 1385-8947. DOI: 10.1016/j.cej.2015.10.044.
- M. Götz, J. Lefebvre, F. Mörs, A. McDaniel Koch, F. Graf, S. Bajohr, R. Reimert, and T. Kolb, “Renewable Power-to-Gas: A technological and economic review”, *Renewable Energy*, vol. 85, pp. 1371-1390, 2016, ISSN: 0960-1481. DOI: 10.1016/j.renene.2015.07.066.
- J. Lefebvre, M. Götz, S. Bajohr, R. Reimert, and T. Kolb, “Improvement of three-phase methanation reactor performance for steady-state and transient operation”, *Fuel Processing Technology*, vol. 132, no. 0, pp. 83-90, 2015, ISSN: 0378-3820. DOI: 10.1016/j.fuproc.2014.10.040.
- M. Götz, F. Graf, J. Lefebvre, S. Bajohr, and R. Reimert, “Speicherung elektrischer Energie aus regenerativen Quellen im Erdgasnetz - Arbeitspaket 5: Betrachtungen des Gesamtsystems im Hinblick auf Dynamik und Prozessintegration” *Energie-, Wasser-Praxis*, vol. 65, no. 11, pp. 51-55, 2014, ISSN: 1436-6134.
- M. Götz, F. Graf, J. Lefebvre, S. Bajohr, and R. Reimert, “Speicherung elektrischer Energie aus regenerativen Quellen im Erdgasnetz - Arbeitspaket 2a: Drei-Phasen-

Methanisierung” *Energie-, Wasser-Praxis*, vol. 65, no. 11, pp. 41-43, 2014, ISSN: 1436-6134.

Conference contributions sorted by year

Oral presentations

- J. Lefebvre, S. Bajohr, and T. Kolb, “CO₂ Methanation in a Slurry Bubble Column Reactor - Influence of the Liquid Phase on the Reaction Kinetics and the Reactor Design”, ProcessNet-Jahrestagung und 32. DECHEMA-Jahrestagung der Biotechnologen 2016, Aachen, Germany, 12 - 15/09/2016.
- J. Lefebvre, S. Bajohr, and T. Kolb, “Three-phase methanation - From lab-scale to pilot-plant”, 3rd Nuremberg Methanation Workshop and Second Generation Fuels, Nürnberg, 19 - 20/05/2016.

Poster presentations

- J. Lefebvre, S. Bajohr, and T. Kolb, “CO₂ Methanation in a Slurry Bubble Column Reactor - Reactor dynamics and reaction kinetics”, Jahrestreffen Reaktionstechnik 2017 der Dechema, Würzburg, Germany, 22 - 24/05/2017.

Curriculum vitae

Personal information

Name: Jonathan Lefebvre
Date of birth: 10/06/1988
Place of birth: Pontoise (France)
Nationality: French

Professional experience

Since 07/2018 Research Engineer, BASF SE, Germany

05/2013 - 05/2018 Research assistant at Engler-Bunte-Institut Fuel Technology, Karlsruhe Institute of Technology, Germany

09/2011 - 02/2013 R&D Process Engineer, Alstom Carbon Capture GmbH, Germany

Education

Since 05/2013 PhD thesis at Engler-Bunte-Institut Fuel Technology, Karlsruhe Institute of Technology, Germany

03/2010 - 09/2011 Double Engineer Diploma, Process engineering, thermal and energy process specialization, University of Technology of Braunschweig (TUBS), Germany

09/2006 - 09/2011 Engineer Diploma, Process engineering, thermal and energy process specialization, University of Technology of Compiegne (UTC), France

06/2006 "French Baccalauréat" (specialty mathematics and physics) with distinction, Lycée N.D. de la Compassion, Pontoise (95), France

Appendix

A Material properties

A.1 Gas purity

Table A.1: Supplier and purity of the gases used in this work.

Gases	Supplier	Purity
Ar	Air Liquide	99.997 %
N ₂	Air Liquide	99.999 %
H ₂	Basi	99.999 %
CO ₂	Basi	99.995 %
CH ₄	Air Liquide	99.999 %

A.2 Dibenzyltoluene properties

Dibenzyltoluene properties are as following [305].

Boiling range at 1013 mbar: ca. 385 - 395 °C.

Pour point: ca. -34 °C.

Flash point: ca. 200 °C.

Ignition temperature: ca. 500 °C.

Permissible heater film temperature: 350 °C.

Table A.2: Dibenzyltoluene properties relevant for the design of a slurry bubble column reactor for three-phase CO₂ methanation [305].

T °C	ρ kg·m ⁻³	c_p J·kg ⁻¹ ·K ⁻¹	λ W·m ⁻¹ ·K ⁻¹	ν m ² ·s ⁻¹	p_v bar
0	1058	1.48·10 ³	0.133	3.21·10 ⁻⁴	-
20	1044	1.55·10 ³	0.131	4.70·10 ⁻⁵	-
100	987	1.85·10 ³	0.120	3.10·10 ⁻⁶	-
200	915	2.22·10 ³	0.062	9.2·10 ⁻⁷	0.005
220	901	2.29·10 ³	0.060	7.7·10 ⁻⁷	0.012
240	887	2.37·10 ³	0.059	6.5·10 ⁻⁷	0.027
260	873	2.44·10 ³	0.057	5.7·10 ⁻⁷	0.054
280	858	2.52·10 ³	0.055	5.0·10 ⁻⁷	0.098
300	844	2.59·10 ³	0.054	4.5·10 ⁻⁷	0.200
320	830	2.67·10 ³	0.053	4.0·10 ⁻⁷	0.315
340	815	2.74·10 ³	0.051	3.6·10 ⁻⁷	0.560
360	801	2.82·10 ³	0.050	3.2·10 ⁻⁷	0.860

B Calculation of physical properties

B.1 Gas properties

B.1.1 Gas density, ρ_G

The density of the gas mixture in kg/m³ is calculated with the ideal gas law, see Eq. B.1.

$$\rho_G = \frac{p \cdot M_G}{R \cdot T} \quad (\text{B.1})$$

with

$$M_G = \sum y_i \cdot M_i \quad (\text{B.2})$$

B.1.2 Dynamic viscosity, μ_G

The dynamic viscosity of a gaseous component in Pa·s is calculated with the following Equation B.3 [310]:

$$\mu_{i,G} = A + B \cdot T + C \cdot T^2 + D \cdot T^3 + E \cdot T^4 \quad (\text{B.3})$$

For the calculation of the viscosity of a gaseous mixture, the following formula is applied (Eq. B.4):

$$\mu_G = \sum y_i \cdot \mu_{i,G} \quad (\text{B.4})$$

B.1.3 Specific heat capacity, $c_{p,G}$

The specific heat capacity of a gas mixture in J/kg is estimated using Eq. B.5.

$$c_{p,G} = \frac{\sum y_i \cdot M_i \cdot c_{p,i}}{\sum y_i \cdot M_i} \quad (\text{B.5})$$

The specific heat capacity of each gas component $c_{p,i}$ is calculated according to Equation B.6. This correlation is taken from [311].

$$c_{p,i} = A + B \cdot T + C \cdot T^2 + D \cdot T^3 + \frac{E}{T^2} \quad (\text{B.6})$$

B.1.4 Thermal conductivity, λ_G

The thermal conductivity in W/(m·K) of a gas mixture is calculated as following (Eq. B.7):

$$\lambda_G = \sum_i y_i \cdot \lambda_i \quad (\text{B.7})$$

The thermal conductivity of each gaseous component in W/m/K is estimated using Eq. B.8 [310].

$$\lambda_i = A + B \cdot T + C \cdot T^2 + D \cdot T^3 + E \cdot T^4 \quad (\text{B.8})$$

B.1.5 Binary molecular diffusion coefficient, D_{12}

The binary diffusion coefficient in cm²/s can be estimated with Eq. B.9 from [311] Da 27:

$$D_{12} = \frac{0.00143 \cdot T^{1.75} ((M_1)^{-1} + (M_2)^{-1})^{1/2}}{p \sqrt{2} ((\Delta_{v1})^{1/3} + (\Delta_{v2})^{1/3})^2} \quad (\text{B.9})$$

Δ_{vi} is the diffusion volume. For H₂ Δ_{vi} is 6.12 and 26.9 for CO₂ [311].

B.1.6 Parameters for Peng Robinson equation of state

The parameter b in the Peng Robinson equation of state is defined in Eq. B.10 [208].

$$b = \frac{0.0778 \cdot R \cdot T_{\text{crit}}}{p_{\text{crit}}} \quad (\text{B.10})$$

The acentric function $\theta(T, \omega)$ in the Peng Robinson equation of state is defined in Eq. B.11 [208].

$$\theta(T, \omega) = \frac{0.45724 \cdot R^2 \cdot T_{\text{crit}}^2}{p_{\text{crit}}} \cdot (1 + \kappa \cdot (1 - T_r^{0.5}))^2 \quad (\text{B.11})$$

With κ defined in Eq. B.12 [208].

$$\kappa = 0.37464 + 1.54226 \cdot \omega - 0.26922 \cdot \omega^2 \quad (\text{B.12})$$

Table B.1: Parameters for Peng Robinson equation of state [209].

		H ₂	CO ₂	Ar	CH ₄	H ₂ O
T_{crit}	K	33.18	304.19	150.72	190.66	647.66
p_{crit}	bar	13.13	73.82	48.636	46.4017838	22.423574
ω	-	-0.220	0.228	-0.002	0.013	0.348

B.2 Slurry properties

B.2.1 Slurry density, ρ_{SL}

Slurry density can be calculated with Eq. B.13:

$$\rho_{\text{SL}} = \rho_{\text{L}} \cdot (1 - \varphi_{\text{S}}) + \rho_{\text{P}} \cdot \varphi_{\text{S}} \quad (\text{B.13})$$

B.2.2 Slurry dynamic viscosity, μ_{SL}

Slurry viscosity can be calculated with Eq. B.14 [312]:

$$\mu_{\text{SL}} = \mu_{\text{L}} \cdot (1 + 4.5 \cdot \varphi_{\text{S}}) \quad (\text{B.14})$$

B.2.3 Slurry heat capacity, $c_{p,\text{SL}}$

Slurry heat capacity can be calculated with Eq. B.15 [189]:

$$c_{p,\text{SL}} = c_{p,\text{L}} \cdot (1 - w_{\text{S}}) + c_{p,\text{S}} \cdot w_{\text{S}} \quad (\text{B.15})$$

B.2.4 Slurry heat conductivity, λ_{SL}

Slurry heat conductivity can be calculated with Eq. B.16 [189]:

$$\lambda_{\text{SL}} = \lambda_{\text{L}} \frac{2\lambda_{\text{L}} + \lambda_{\text{S}} - 2\varphi_{\text{S}} \cdot (\lambda_{\text{L}} - \lambda_{\text{S}})}{2\lambda_{\text{L}} + \lambda_{\text{S}} + \varphi_{\text{S}} \cdot (\lambda_{\text{L}} - \lambda_{\text{S}})} \quad (\text{B.16})$$

B.2.5 Gas diffusion coefficient in liquid phase, $D_{i,L}$

The gas diffusion coefficient in liquid phase $D_{i,L}$ can be estimated with Eq. B.17 [313] (see publication for units):

$$D_{i,L} = \frac{7.4 \cdot 10^{-8} \cdot T \cdot M_L^{0.5}}{\mu_L \cdot V_{i,molecule}^{0.6}} \quad (\text{B.17})$$

$V_{i,molecule}$ is the molecule volume. For CO_2 , this volume is $34 \text{ cm}^3/(\text{g}\cdot\text{mol})$ [313].

B.3 Fixed-bed properties

B.3.1 Thermal conductivity of the catalyst bed, λ_{bed}

The thermal conductivity of the catalyst bed λ_{bed} is calculated using the correlation proposed by Tsotsas [238] (see Eq. B.18 to B.22).

$$\lambda_{bed} = \lambda_G \cdot (1 - \sqrt{1 - \varepsilon_{bed}} + \sqrt{1 - \varepsilon_{bed}} \cdot k_c) \quad (\text{B.18})$$

with

$$k_c = \frac{2}{N} \cdot \left(\frac{B}{N^2} \cdot \frac{k_P - 1}{k_P} \cdot \ln \frac{k_P}{B} - \frac{B + 1}{2} - \frac{B - 1}{N} \right) \quad (\text{B.19})$$

and

$$N = 1 - \frac{B}{k_P} \quad (\text{B.20})$$

with B calculated for catalyst particles assuming spheres.

$$B = 1.25 \cdot \left(\frac{1 - \varepsilon_{bed}}{\varepsilon_{bed}} \right)^{10/9} \quad (\text{B.21})$$

with

$$k_P = \frac{\lambda_P}{\lambda_G} \quad (\text{B.22})$$

B.3.2 Effective radial thermal conductivity of the catalyst bed, $\lambda_{eff,r}$

The effective radial thermal conductivity of the catalyst bed is calculated according to Tsotsas [238] (see Eq. B.23).

$$\lambda_{eff,r} = \lambda_{bed} + \frac{Pe \cdot \lambda_G}{8} \quad (\text{B.23})$$

with Pe the Peclet number defined with Eq. B.24:

$$Pe = \frac{u_G \cdot \rho_G \cdot c_{p,G} \cdot d_P}{\lambda_G} \quad (\text{B.24})$$

B.3.3 Heat transfer coefficient at the internal reactor wall, α_{wall}

The heat transfer coefficient in a fixed-bed reactor α_{wall} is calculated using the correlation of Martin and Nilles [307] (see Eq. B.25).

$$\alpha_{\text{wall}} = \left(1.3 + 5 \cdot \frac{d_P}{d_{\text{tube}}}\right) \cdot \frac{\lambda_{\text{bed}}}{d_P} + 0.19 \cdot \frac{\lambda_G}{d_P} \cdot Re_0^{0.75} \cdot Pr^{0.33} \quad (\text{B.25})$$

Re_0 is the Reynolds number defined for a catalyst particle (see Eq. B.26):

$$Re_0 = \frac{u_G \cdot \rho_G \cdot d_P}{\mu_G} \quad (\text{B.26})$$

and Pr is the Prandtl number defined according to Eq. B.27.

$$Pr = \frac{\mu_G \cdot c_{p,G}}{\lambda_G} \quad (\text{B.27})$$

C Mass transfer in and around catalyst particles

C.1 Mass transfer coefficient gas-catalyst particle, k_G

The mass transfer coefficient between gas phase (bulk) and the catalyst particle can be estimated with Eq. C.1 and C.2 [314]:

$$k_G = \frac{Sh \cdot D_{12}}{d_P} \quad (\text{C.1})$$

$$Sh = \frac{1.15}{\sqrt{\varepsilon_P}} \cdot Re_0^{0.5} \cdot Sc^{1/3} \quad (\text{C.2})$$

C.2 Effective pore diffusion coefficient in a catalyst particle, $D_{i,\text{eff}}$

The effective pore diffusion coefficient can be calculated using Eq. C.3, in which ε_P is the catalyst porosity estimated to be 0.4:

$$D_{i,\text{eff}} = D_{\text{pore}} \cdot \varepsilon_P^{1.5} \quad (\text{C.3})$$

Assuming one cylindrical pore, the effective pore diffusion coefficient depends on the Knudsen diffusion and the molecular diffusion (see sections B.1.5 and B.2.5). This is represented in Eq. C.4.

$$\frac{1}{D_{\text{pore}}} = \frac{1}{D_{12}} + \frac{1}{D_{\text{Kn}}} \quad (\text{C.4})$$

The Knudsen diffusion for mesopores can be calculated with C.5 (units are SI).

$$D_{\text{Kn}} = 9.7 \cdot r_{\text{pore}} \cdot \sqrt{\frac{T}{M_G}} \quad (\text{C.5})$$

Where T is the temperature in K and M_G is the molar mass in g/mol. In this work, the molar mass of CO_2 is used as it results in conservative diffusion constant.

The average r_{pore} derived from BET experiments is $5 \cdot 10^{-9}$ m.

C.3 Catalyst efficiency, η_{cat}

The catalyst efficiency can be calculated using Eq. C.6 [300]:

$$\eta_{\text{cat}} = \frac{3}{\Phi} \cdot \left(\frac{1}{\tanh \Phi} - \frac{1}{\Phi} \right) \quad (\text{C.6})$$

Φ is the Thiele modulus defined with Eq. C.7 [300].

$$\Phi = \frac{d_P}{2} \cdot \sqrt{\frac{r_i \cdot \rho_P}{c_i \cdot D_{i,\text{eff}}}} \quad (\text{C.7})$$

D Criterion for plug flow reactor behavior

A fixed-bed reactor can be assumed as a plug flow reactor (no axial dispersion), when the Bodenstein number Bo is at least higher than 100. The Bodenstein number is a function of the axial Peclet number (see Eq. D.1)

$$Bo = Pe'_{\text{ax}} \cdot \frac{L_R}{d_P} \quad (\text{D.1})$$

The axial Peclet number can be calculated using Eq. D.2 [238].

$$\frac{1}{Pe'_{\text{ax}}} = \frac{1 - \sqrt{1 - \varepsilon_{\text{bed}}}}{Pe'} + \frac{1}{2} \quad (\text{D.2})$$

with Pe' the Peclet number defined as following (Eq. D.3):

$$Pe' = \frac{u_G \cdot d_P}{D_{1,2}} \quad (\text{D.3})$$

E Criteria for estimation of absence of mass and heat transfer limitation

The reaction rate of heterogeneous catalytic reaction can be limited by the chemical reaction itself or by mass and heat transfer. To identify the limiting reaction process, different criteria have been developed to estimate if the effective reaction rate $r_{i,\text{eff}}$ is controlled by mass- and heat transfer. The following criteria are valid for a reaction order of 1.

First of all the Weisz-Prater criterium has to be fulfilled to assure the absence of intraparticle mass-transfer limitations [235].

$$\frac{r_{i,\text{eff}} \cdot \rho_p \cdot d_p^2}{4c_i \cdot D_{i,\text{eff}}} < 1. \quad (\text{E.1})$$

Then, external mass-transfer can be neglected if the Mears criterium is valid [237]:

$$\frac{r_{i,\text{eff}} \cdot \rho_p \cdot d_p}{c_i \cdot k_G} < 0.3. \quad (\text{E.2})$$

The absence of heat-transfer limitations inside the catalyst can be assumed when the Anderson criterium is fulfilled [236]:

$$\frac{r_{i,\text{eff}} \cdot |\Delta h_r| \cdot \rho_p \cdot d_p^2}{4\lambda_{\text{eff}} \cdot T} < \frac{RT}{E_A}. \quad (\text{E.3})$$

Finally, external heat-transfer around the catalyst particle can be neglected when the second Mears criterium is valid [237]:

$$\frac{r_{i,\text{eff}} \cdot |\Delta h_r| \cdot \rho_p \cdot d_p}{\alpha_{\text{eff}} \cdot T} < \frac{0.3RT}{E_A}. \quad (\text{E.4})$$

F Evaluation of minimum gas velocity for complete solid suspension in a slurry bubble column reactor

The range of minimum gas velocity for complete solid suspension in a three-phase CO₂ methanation slurry bubble column reactor is shown in Table F.1. The corresponding SBCR design is described in chapter 7.

Table F.1: Evaluation of of minimum gas velocity for complete solid suspension in a slurry bubble column reactor for three-phase CO₂ methanation.

Parameter	Units	Minimum	Maximum
ρ_P	kg/m ³	1050	1050
ρ_L	kg/m ³	818	892
d_P	10 ⁻⁶ m	50	100
d_R	m	0.34	0.34
φ_S	-	0.01	0.3
μ_L	10 ⁻³ Pa·s	0.344	0.574
σ_L	10 ⁻³ N/m	13.2	21.9
Ar	10 ⁻³ -	1.97	4.2
$u_{P,set}$	10 ⁻³ m/s	0.66	1.1
$u_{G,min}$	10 ⁻³ m/s	0.64	2.1

G Supporting materials for gas holdup correlations

The following pieces of information are related to the gas holdup correlation developed by Behkish et al. [171] (see section 2.2.1.4).

The parameter Γ takes into account the influence of gas sparger geometry on the gas holdup (Eq. G.1).

$$\Gamma = K_d \cdot N_{\text{hole}} \cdot d_{\text{hole}}^{\alpha_{\text{sparger}}} \quad (\text{G.1})$$

K_d represents the gas sparger coefficient and is equal to $1.363 \text{ m}^{-\alpha_{\text{sparger}}}$ for perforated plates. α_{sparger} is the gas sparger coefficient.

$$a_{\text{free}} = N_{\text{hole}} \cdot \left(\frac{d_{\text{hole}}}{d_R} \right)^2 \quad (\text{G.2})$$

For perforated plates α_{sparger} depends on the free hole area a_{free} defined in Eq. G.2. $\alpha_{\text{sparger}} = 0.017$ for $a_{\text{free}} < 5.5 \cdot 10^{-4}$ and $\alpha_{\text{sparger}} = 0.0293$ for $a_{\text{free}} > 3 \cdot 10^{-3}$, else $\alpha_{\text{sparger}} = 0.303$.

The parameter Y_1 describes the influence of the solids on the gas holdup (Eq. G.3, units are SI). The parameter $w_{\text{mc,L}}$ represents the mass fraction of the main liquid in case two liquids are present in the system. If only one liquid is present, then $w_{\text{mc,L}} = 1$.

$$Y_1 = -2.231 \cdot \varphi_S - 0.157 \cdot \rho'_P \cdot d_P - 0.242 \cdot w_{mc,L} \quad (\text{G.3})$$

ρ'_P represents the skeletal density of the solid particles. In addition, Behkish et al. [171] define the heterogeneous regime for $\varepsilon'_G > (F_{\text{het}})^{6.25}$. The parameter F_{het} is defined according to Eq. G.4 (units are SI).

$$F_{\text{het}} = 1 - 3.04 \cdot 10^{-6} \cdot \left(\frac{\rho_L^{0.97}}{\mu_L^{0.16}} \right) \cdot \exp(-4.5 \cdot \varphi_S + 4.5 \cdot w_{mc,L}) \quad (\text{G.4})$$

Table G.1: Comparison between the validity range of Behkish's gas holdup correlation and the three-phase methanation operating conditions.

Parameter	Units	Correlation validity range	3PM operating conditions
T	$^{\circ}\text{C}$	2 - 265	225 - 325
p	10^5 Pa	1 - 150	5 - 20
u_G	m/s	0.0035 - 0.574	0 - 0.3
d_R	m	0.0382 - 5.5	< 0.15
p_v	10^3 Pa	0 - 700	1.6 - 33.1
$w_{mc,L}$	-	0.5 - 1.0	1.0
ρ_L	kg/m^3	633.4 - 1583	818 - 892
μ_L	$10^{-3} \text{ Pa}\cdot\text{s}$	0.189 - 398.8	0.344 - 0.574
σ_L	$10^{-3} \text{ N}/\text{m}$	8.4 - 75	13.2 - 21.9
M_L	$10^{-3} \text{ kg}/\text{mol}$	18 - 730	272.4
M_G	$10^{-3} \text{ kg}/\text{mol}$	2 - 44	2 - 44
ρ_G	kg/m^3	0.06 - 177.3	1.05 - 10.48
ρ'_P	kg/m^3	700 - 4000	3962.5
d_P	10^{-6} m	5 - 300	50 - 100
φ_S	-	0 - 0.36	0.01 - 0.3

H Supporting materials for volumetric mass transfer correlations

The following pieces of information are related to the volumetric gas/liquid mass-transfer correlation developed by Lemoine et al. [186] (see section 2.2.2).

Lemoine et al. [186] estimates the diameter of bubbles in the homogeneous regime with Eq. H.3 (units are SI).

$$d_B = 37.19 \cdot \frac{\sigma_L^{1.22} \cdot \rho_G^{0.02} \cdot \mu_L^{0.08} \cdot T^{1.66}}{\rho_L^{1.52} \cdot M_G^{0.12}} u_G^{0.14} \cdot (1 - \varepsilon_G)^{1.56} \cdot \Gamma^{-0.02} \left(\frac{d_R}{1 + d_R} \right)^{0.3} e^Y \quad (\text{H.1})$$

In Eq. H.1, Y describes the influence of solids on d_B (Eq. H.2, units are SI):

$$Y = 2.81 \cdot \varphi_S + 2.77 \cdot \rho_P' \cdot d_P - 2.29 \cdot w_{mc,L} \quad (\text{H.2})$$

Lemoine et al. [186] estimates the diameter of large bubbles for heterogeneous regime with Eq. H.3 (units are SI).

$$d_{B,\text{large}} = d_B^{0.96} \cdot \left(1 - 10^{-5} \cdot \rho_L^{0.22} \cdot \mu_L^{0.03} \cdot \sigma_L^{8.6} \cdot u_G^{0.04} \cdot \varepsilon_G^{2.37} \cdot \varepsilon_{G,\text{large}}^{2.74} \right) \quad (\text{H.3})$$

Table H.1: Comparison between the validity range of Lemoine's $k_L a$ correlation and the three-phase methanation operating conditions.

Parameter	Units	Correlation validity range	3PM operating conditions
T	°C	3 - 265	225 - 325
p	10^5 Pa	1 - 198	5 - 20
u_G	m/s	0.0035 - 0.574	0 - 0.3
d_R	m	0.0382 - 5.5	< 0.15
h_R / d_R	-	4 - 20	5 - 15
p_v	10^3 Pa	0 - 700	1.6 - 33.1
$w_{mc,L}$	-	0.5 - 1.0	1.0
ρ_L	kg/m ³	633 - 1583	818 - 892
μ_L	10^{-3} Pa·s	0.16 - 398.8	0.344 - 0.574
σ_L	10^{-3} N/m	8.4 - 75	13.2 - 21.9
$D_{i,L}$	10^{-9} m ² /s	0.0125 - 27.8	7.37 - 43.1
M_L	10^{-3} kg/mol	18 - 730	272.4
M_G	10^{-3} kg/mol	2 - 44	2 - 44
ρ_G	kg/m ³	0.06 - 223.77	1.05 - 10.48
ρ_P'	kg/m ³	700 - 4000	3962.5
d_P	10^{-6} m	42 - 300	50 - 100
φ_S	-	0 - 0.36	0.01 - 0.3

I Evaluation of mass-transfer resistance in a slurry bubble column reactor

Considering a first order reaction, the effective reaction rate within a SBCR depends on gas-side mass transfer resistance (1), liquid-side mass transfer resistance (2), solid-side mass transfer resistance (3) and chemical reaction rate resistance (4) and can be described by Eq. I.1:

$$\frac{1}{V} \frac{\partial n_i}{\partial t} = \frac{c_{i,G}}{\underbrace{\frac{1}{k_G a_i}}_{(1)} + \underbrace{\frac{H_{i,cc}}{k_L a_i}}_{(2)} + \underbrace{\frac{H_{i,cc}}{k_S a_i}}_{(3)} + \underbrace{\frac{H_{i,cc}}{\eta_{\text{cat}} \cdot \varphi_S \cdot \rho_S \cdot r_{3\text{PM}}}}_{(4)}} \quad (\text{I.1})$$

The effective reaction rate is limited by the highest mass-transfer resistance and it is therefore of great interest to assess the above-mentioned mass-transfer resistances for three-phase methanation operating conditions (see Table I.1).

Table I.1: Evaluation of mass-transfer resistance in a slurry bubble column reactor for three-phase CO₂ methanation. $T = 320$ °C, $c_{\text{CO}_2,\text{G}} = 63.83$ mol/m³, $(\text{H}_2/\text{CO}_2)_{\text{G}} = 4/1$, $u_{\text{G}} = 0.075 - 0.3$ m/s, $\varphi_{\text{S}} = 0.2$, $\rho_{\text{S}} = 1100$ kg/m³.

$\frac{1}{k_{\text{G}}a_{\text{CO}_2}}$	$\frac{H_{\text{CO}_2,cc}}{k_{\text{L}}a_{\text{CO}_2}}$	$\frac{H_{\text{CO}_2,cc}}{k_{\text{S}}a_{\text{CO}_2}}$	$\frac{H_{\text{CO}_2,cc}}{\eta_{\text{cat}} \cdot \varphi_{\text{S}} \cdot \rho_{\text{P}} \cdot r_{3\text{PM}}}$
0.075 - 0.13 s	2.3 - 3.4 s	0.038 - 0.051 s	0.56 s

Table I.1 shows that the main transfer resistances are the liquid-side mass transfer and the reaction rate. Hence, the gas and solid-side mass transfer can be neglected for the design of a three-phase CO₂ methanation SBCR.

k_{G,CO_2} is calculated assuming complete diffusion limitation, i.e. $Sh_{\text{G}} = 2$. The bubble diameter d_{B} is evaluated using Eq. H.1 and H.3. $k_{\text{L}}a_{\text{CO}_2}$ is calculated using Eq. 2.22, while $a_{\text{G}/\text{L}}$ is evaluated using the relation expressed in Eq. I.2.

$$a_{\text{G}/\text{L}} = \frac{6 \cdot \varepsilon_{\text{G}}}{d_{\text{B}}} \quad (\text{I.2})$$

The dimensionless Henry's law constant of CO₂ in DBT is calculated using Eq. 4.12 and the corresponding parameters listed in Table 4.4. k_{S,CO_2} is calculated using the correlation developed by Sanger and Deckwer [315].

The specific liquid-solid interphase $a_{\text{L}/\text{S}}$ can be calculated with Eq. I.3 assuming spheric catalyst particles.

$$a_{\text{L}/\text{S}} = \frac{6 \cdot m_{\text{cat}}}{d_{\text{P}} \cdot \rho_{\text{P}} \cdot V_{\text{R}}} \quad (\text{I.3})$$

η_{cat} is calculated with Eq. C.6, while $r_{3\text{PM}}$ is evaluated with Eq. 5.18.

J Supporting results: gas solubility experiments

In the following, additional information is given for the gas solubility experiments performed in chapter 4.

J.1 Exemplary gas solubility experiment

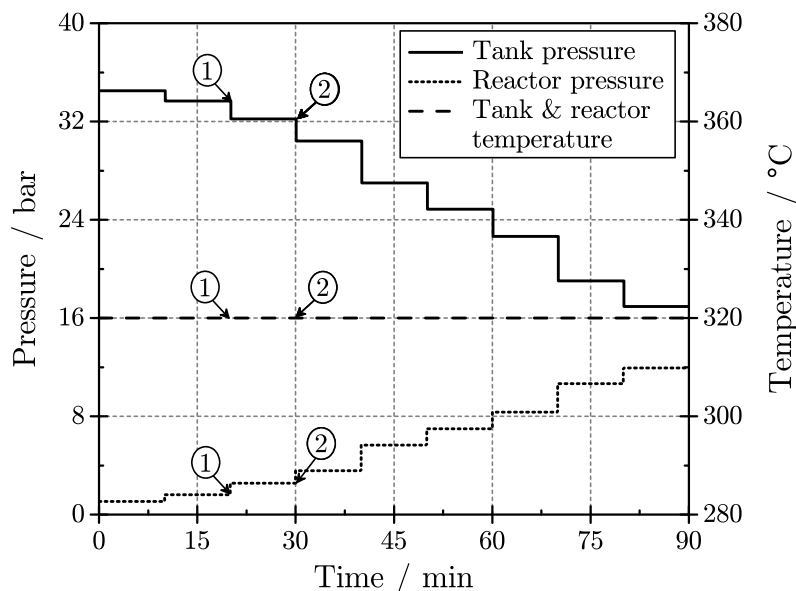


Figure J.1: Evolution of reactor and tank pressure as well as temperature as function of time in the experimental measurement of CH_4 solubility in dibenzyltoluene at $320\text{ }^\circ\text{C}$. (1) describes the situation before the gas discharge from the feed tank into the reactor. (2) describes the situation after the discharge when gas dissolution is fully achieved.

J.2 Validation of the experimental procedure

The validation of the experimental procedure with CO_2 solubility experiments in H_2O is pictured in Figure J.2. It can be seen that all experiments are in agreement with Henry's law, as the worst fit has a R^2 of 0.9997. In addition, Figure J.2 shows that the slope of each curve increases with increasing temperature, which means that CO_2 solubility decreases with increasing temperature. This trend is also reported in the literature [316–318].

The CO_2 Henry's law constants $H_{\text{CO}_2,px}$ derived from Figure J.2 are summarized in Table J.1 and compared to literature data. As can be seen in Table J.1, $H_{\text{CO}_2,px}$ estimated in this work are in good agreement with the data from the literature. The largest relative error δ of -9.7% is obtained at $30\text{ }^\circ\text{C}$. The other experiments conducted between 40 and $80\text{ }^\circ\text{C}$ show a relative error of only $\pm 5\%$. As CO_2 solubility data from the literature can be reproduced, the experimental setup and procedure employed in this work are validated and can be used for the determination of Henry's law constants.

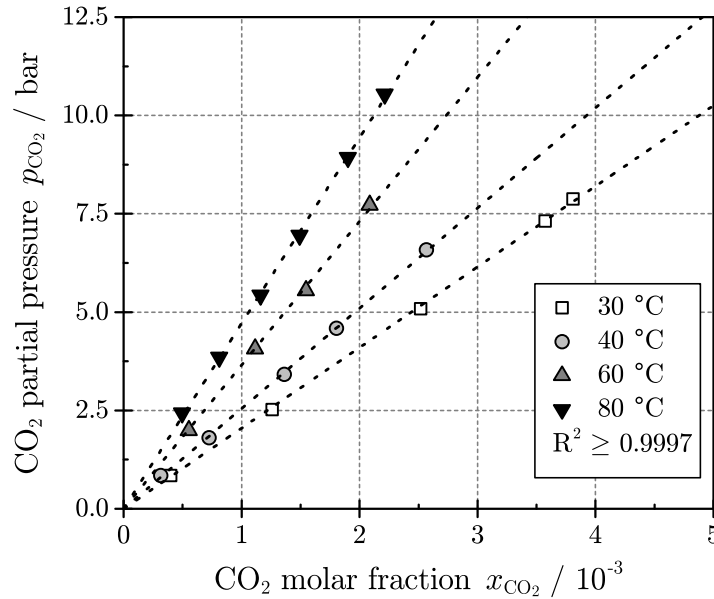


Figure J.2: CO₂ solubility in distilled water conducted at different temperatures. Dashed lines corresponds to the fit $p_{\text{CO}_2} = H_{\text{CO}_2,pc} \cdot x_{\text{CO}_2}$.

Table J.1: Experimental Henry's law constant of CO₂ in H₂O and comparison with literature data [316–318].

T °C	$H_{\text{CO}_2,px,\text{exp}}$ bar	$H_{\text{CO}_2,px,\text{lit}}$ bar	δ %
30	2024.9	1845.7	-9.7
40	2487.9	2379.9	-4.5
60	3517	3330.5	-5.6
80	4095	4306.5	5

J.3 Ar solubility in dibenzyltoluene

Figure J.3 shows the results of Ar solubility experiments carried out at temperatures ranging from 240 to 270 °C in DBT. For these experiments, the worst fit exhibits a R^2 of 0.9994. Therefore, the Henry's law is valid. Furthermore, the slopes of each fit are in the range 690 to 711 bar: Ar solubility shows almost no temperature dependency for the investigated temperature range. Results of solubility experiments in organic oils are very scarce in the literature and - to the author knowledge - there are no data available in the literature for Ar solubility in organic oils.

Table J.2 sums up the Henry's law constants $H_{\text{Ar},px}$ and $H_{\text{Ar},pc}$ obtained from Figure J.3. The small temperature dependency of Ar Henry's law constant is quantified as following: there is an increase in $H_{\text{Ar},px}$ of ca. 3 % for a temperature increase of 30 K. Measurement uncertainty is also satisfactory with ca. ± 2 %. This is due to the instrumental accuracy as well as the relatively low Henry's law constant, i.e. high Ar solubility in DBT.

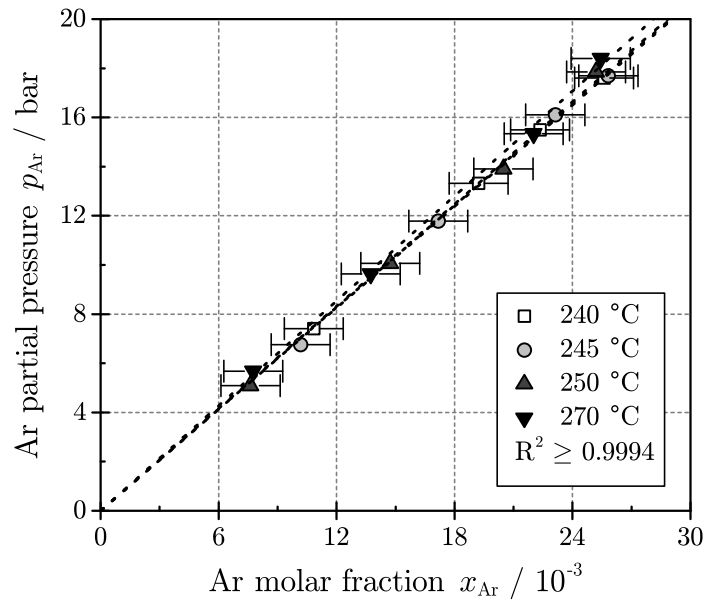


Figure J.3: Ar solubility in DBT for temperatures between 240 and 270 °C. Dashed lines corresponds to the fit $p_{\text{Ar}} = H_{\text{Ar},pc} \cdot x_{\text{Ar}}$.

Table J.2: Experimental Henry's law constant of Ar in DBT for temperatures between 240 and 270 °C.

T °C	$H_{\text{Ar},px}$ bar	$H_{\text{Ar},pc}$ bar·m ³ /mol
240	690.1 ± 10.9	0.174 ± 0.003
245	687.8 ± 11.5	0.174 ± 0.003
250	693.3 ± 14.8	0.176 ± 0.004
270	711.4 ± 15.2	0.183 ± 0.004

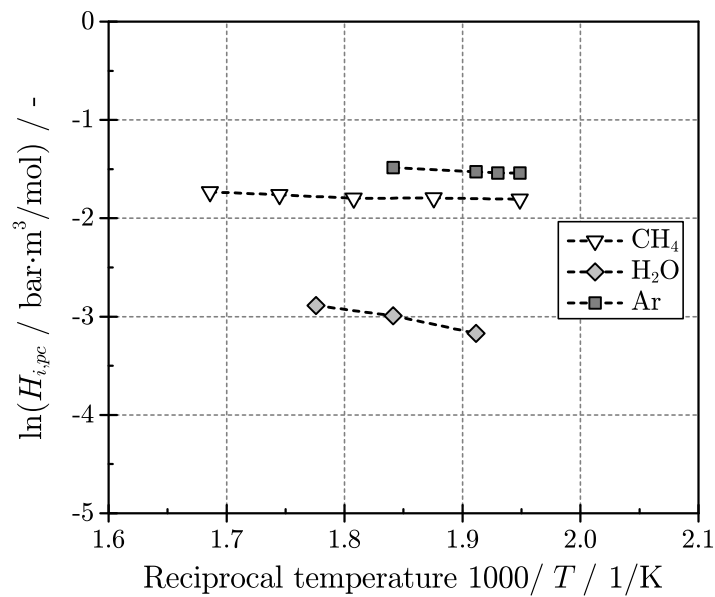


Figure J.4: Temperature dependency of Henry's law constant $H_{i,pc}$ in DBT.

Ar solubility in DBT has been investigated in a narrowed temperature range which does not cover the whole temperature range relevant for CO₂ methanation. Nevertheless, Ar does not play a role in CO₂ methanation reaction kinetics and Ar solubility in DBT is not significantly temperature dependent. This is the reason why no further Ar solubility experiments have been carried out in this work.

K Chemical equilibrium of three-phase CO₂ methanation

The chemical equilibrium constant K_{eq} is the product of the activities of the reacting species. For three-phase CO₂ methanation, the reacting system can be divided into gas phase and liquid phase, i.e. K_{eq} can be expressed as product of the activities in the gas phase (see Eq. K.1) or in the liquid phase (see Eq. K.2).

$$K_{\text{eq,G}} = \frac{p_{\text{H}_2\text{O}}^2 \cdot p_{\text{CH}_4}}{p_{\text{H}_2}^4 \cdot p_{\text{CO}_2}} \cdot p_0^2 \quad (\text{K.1})$$

$$K_{\text{eq,L}} = \frac{c_{\text{H}_2\text{O,L}}^2 \cdot c_{\text{CH}_4,\text{L}}}{c_{\text{H}_2,\text{L}}^4 \cdot c_{\text{CO}_2,\text{L}}} \cdot \left(\sum^i c_{i,\text{L}} \right)^2 \quad (\text{K.2})$$

As both gas and liquid phases are in phase equilibrium, chemical equilibrium of three-phase CO₂ methanation is reached in the phase that results in the maximum CO₂ conversion.

Another definition of chemical equilibrium states that chemical equilibrium is reached when the sum of chemical potential of the reacting species have reached a minimum, i.e. K_{eq} is linked to the system free Gibb's enthalpy ΔG_0 as shown in Eq. K.3.

$$K_{\text{eq}} = \exp\left(\frac{-\Delta G_0}{RT}\right) \quad (\text{K.3})$$

The Gibb's enthalpies of the gas species can be calculated using gas enthalpy and entropy correlations from NIST Chemistry WebBook [231]. Using Eq. K.3 as well as Eq. K.1 and Eq. K.2, the equilibrium CO₂ conversion in the gas and liquid phase, respectively $X_{\text{CO}_2,\text{G,eq}}$ and $X_{\text{CO}_2,\text{L,eq}}$, can be calculated. This calculation is carried at the experimental conditions summarized in Table K.1. Under these conditions, a CO₂ methanation experiment was carried out in the lab facility shown in chapter 5 and the experimental CO₂ conversion $X_{\text{CO}_2,\text{exp}}$ was calculated.

Table K.1 shows that $X_{\text{CO}_2,\text{L,eq}}$ is lower than $X_{\text{CO}_2,\text{G,eq}}$ and $X_{\text{CO}_2,\text{exp}}$. Hence, $K_{\text{eq,L}}$ is not relevant to describe the chemical equilibrium of three-phase CO₂ methanation. On the contrary, $K_{\text{eq,G}}$ can be the relevant chemical equilibrium constant for three-phase CO₂ methanation, as $X_{\text{CO}_2,\text{exp}} \leq X_{\text{CO}_2,\text{G,eq}}$.

Table K.1: Operating conditions and comparison between theoretical and experimental CO₂ conversions.

Parameters	Value	units
T	320	°C
$p_{\text{CO}_2,\text{in}}$	2.38	bar
$p_{\text{H}_2,\text{in}}$	9.45	bar
$p_{\text{H}_2\text{O},\text{in}}$	0.32	bar
$p_{\text{CH}_4,\text{in}}$	0	bar
$c_{\text{CO}_2,\text{L},\text{in}}$	18.3	mol/m ³
$c_{\text{H}_2,\text{L},\text{in}}$	30.86	mol/m ³
$c_{\text{H}_2\text{O},\text{L},\text{in}}$	5.42	mol/m ³
$c_{\text{CH}_4,\text{L},\text{in}}$	0	mol/m ³
$X_{\text{CO}_2,\text{G},\text{eq}}$	0.96	-
$X_{\text{CO}_2,\text{L},\text{eq}}$	0.39	-
$X_{\text{CO}_2,\text{exp}}$	0.64	-

To confirm this assessment, it is recommended to carry out batch three-phase CO₂ methanation experiments. If the assessment is correct, the experimental CO₂ conversion should be equal to the equilibrium CO₂ conversion calculated with $K_{\text{eq,G}}$.

Another way to tackle the issue of calculating the chemical equilibrium constant of three-phase CO₂ methanation is to get rid of the term K in the kinetic rate equations Eq. 5.12 and 6.7. To do so, it is necessary to measure the reaction kinetics of steam reforming, i.e. the CO₂ methanation reverse reaction. However, the main carbon product of steam reforming is CO and not CO₂. Accordingly, the reaction kinetics of CO methanation must be also investigated. The chemical equilibrium of three-phase CO₂ methanation can be then described as combination of CO₂ and CO methanation as well as steam reforming reaction kinetics (see e.g. the publication of Xu and Froment [102]).

L Supporting results: three-phase methanation kinetic experiments

In the following, additional information is given for the three-phase methanation kinetic experiments performed in chapter 5.

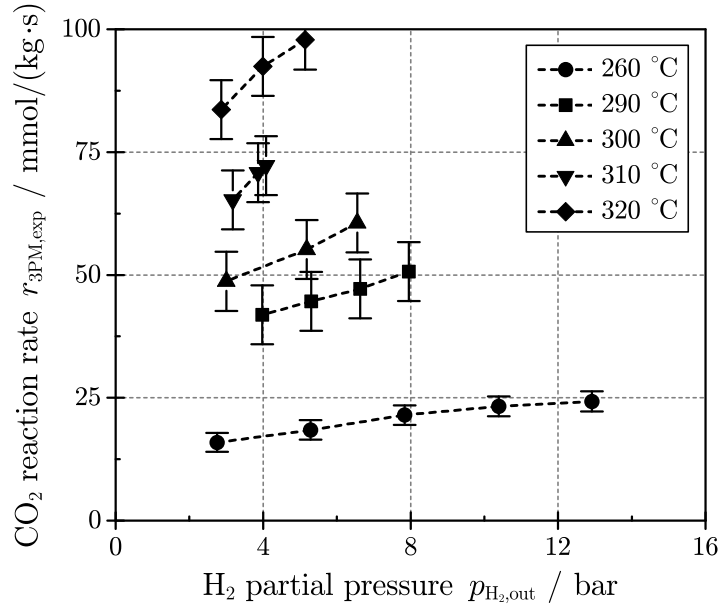


Figure L.1: Influence of H₂ partial pressure on the CO₂ reaction rate for temperatures between 260 and 320 °C ($p_R = 10.5 - 14.7$ bar, $p_{\text{CO}_2,\text{out}} = 1$ bar, $p_{\text{CH}_4,\text{out}} = 0.1 - 0.2$ bar, $p_{\text{H}_2\text{O},\text{out}} = 0.3 - 0.5$ bar, $\tau_{\text{mod},\text{CO}_2} = 1.8 - 2.7$ kg·s/mol).

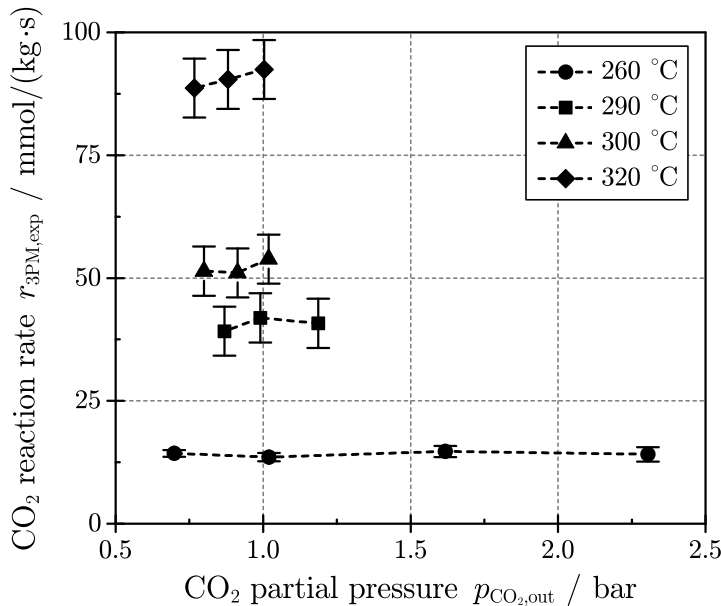


Figure L.2: Influence of CO₂ partial pressure on the CO₂ reaction rate for temperatures between 260 and 320 °C ($p_R = 10 - 14.7$ bar, $p_{\text{H}_2,\text{out}} = 4$ bar, $p_{\text{CH}_4,\text{out}} = 0.1 - 0.2$ bar, $p_{\text{H}_2\text{O},\text{out}} = 0.2 - 0.5$ bar, $\tau_{\text{mod},\text{CO}_2} = 1.8 - 3$ kg·s/mol).

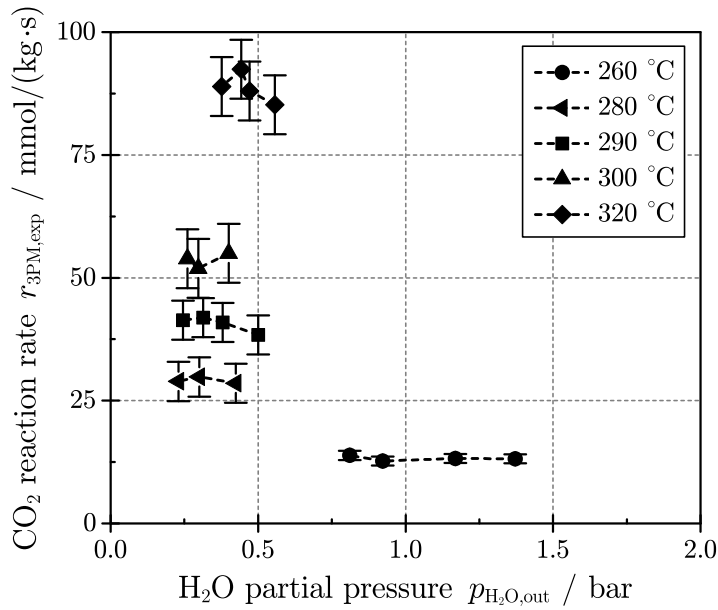


Figure L.3: Influence of H₂O partial pressure on the CO₂ reaction rate for temperatures between 260 and 320 °C ($p_R = 10 - 14.7$ bar, $p_{\text{CO}_2,\text{out}} = 1$ bar, $p_{\text{H}_2,\text{out}} = 4$ bar, $p_{\text{CH}_4,\text{out}} = 0.1 - 0.2$ bar, $\tau_{\text{mod,CO}_2} = 1.8 - 2.7$ kg.s/mol).

M Supporting results: modeling of CO₂ methanation reactors

In the following, additional information is given for the methanation reactor modelings performed in chapter 7.

M.1 Model assumptions

In the following, assumptions related to the SBCR (see page 74) and TBR models (see page 80) are discussed.

The SBCR is operated at an absolute pressure of 20 bar. At this pressure, ideal gas behavior (assumption 1) deviates less than 1 % from real gas behavior (Peng Robinson equation of state). Gas-side mass transfer resistance can take place if the reacting gas is highly diluted in the gas bubbles, i.e. representing only few ppm [139]. However, for three-phase CO₂ methanation, 100 % CO₂ conversion is impossible due to chemical equilibrium limitations. At 320 °C, the maximum CO₂ conversion is e.g. 98 %. Hence, methanation gas educts are not highly diluted and gas-side mass transfer resistance can be neglected. Solid-side mass transfer resistance can be neglected considering the superior volumetric surface area of catalyst particles compared to gas bubbles, which is at least two orders of magnitude higher (i.e. error is less than 1 %). Assumptions 5 to 7 are justified by the good mixing behavior of a SBCR. Finally, assumption 8 is acceptable, as the gas phase accounts for less than 1 % of the total energy balance.

The TBR is operated an absolute pressure of 20 bar. At this pressure, ideal gas behavior (assumption 1) deviates less than 1 % from real gas behavior (Peng Robinson equation of state). Assumption 2 (no heat and mass transfer limitation) is verified via the calculation of the Mears' and Anderson's criteria [236, 237]. For all investigated parameters, these criteria are respected. Hence, the pseudo-homogeneous model is justified for the modeling of this TBR. The catalyst efficiency accounting for the intra-particle mass transfer limitation is calculated with the Thiele modulus [300]. The plug flow behavior of the reactor of assumption 3 is verified through calculation of the Bodenstein number Bo . For all simulations, Bo is higher than 100 and justifies the plug flow assumption [238]. In this catalytic packed-bed reactor the axial convective heat transfer is two orders of magnitude higher than the axial heat conduction, i.e. neglecting the axial heat conduction results in less than 1 % error. The reactor tube temperature is considered equal to the cooling medium temperature, as the reactor wall conductivity (steel) is high and the external heat transfer is assumed very high.

M.2 Influence of cell number on CO₂ conversion using the slurry bubble column reactor model

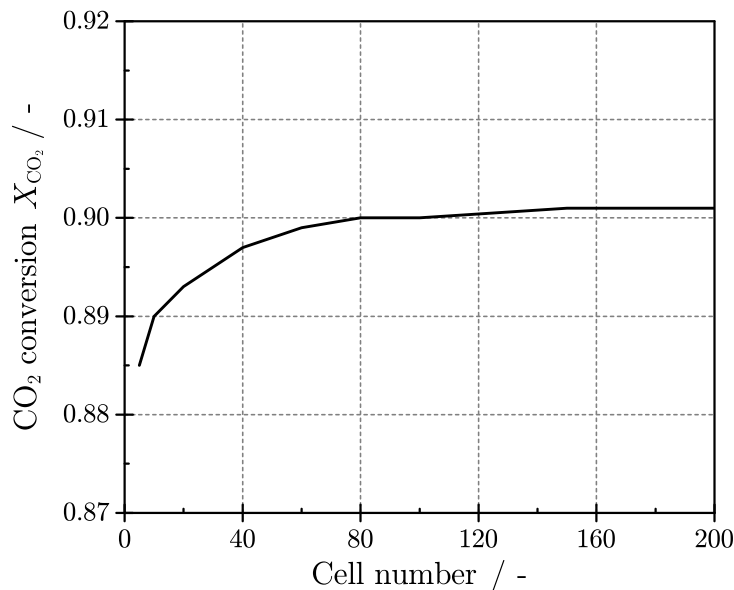


Figure M.1: Evolution of the CO₂ conversion in the slurry bubble column reactor as function of cell number ($\bar{T}_{SL} = 320$ °C, $p_{out} = 20$ bar, $h_R/d_R = 7.2$, $\varphi_S = 0.2$, $T_{cool} = 269$ °C).

M.3 Influence of inlet gas temperature on the performance of the tube bundle reactor

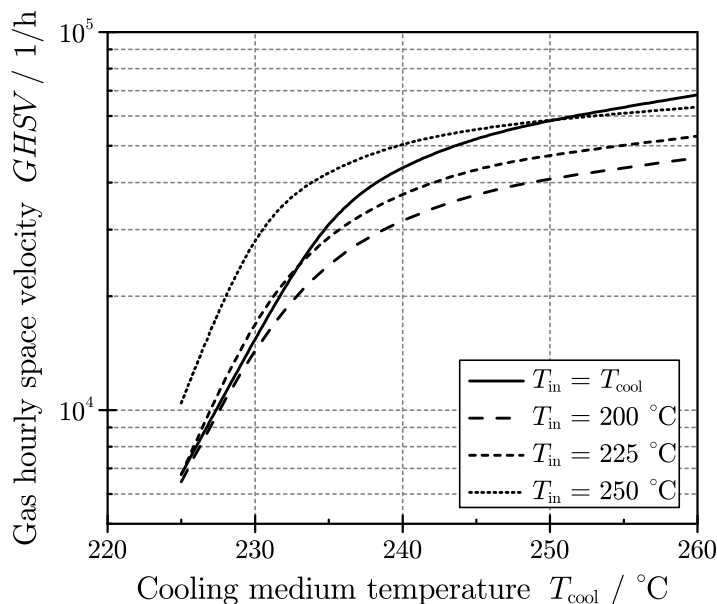


Figure M.2: Influence of cooling medium temperature on the gas hourly space velocity of the tube bundle reactor for different inlet gas temperatures. Calculation for: CO₂ conversion of 0.9, feed composition H₂/CO₂/CH₄ of 4/1/1, $p_{\text{in}} = 20$ bar.

M.4 Effect of gas load on slurry bubble column reactor reactor

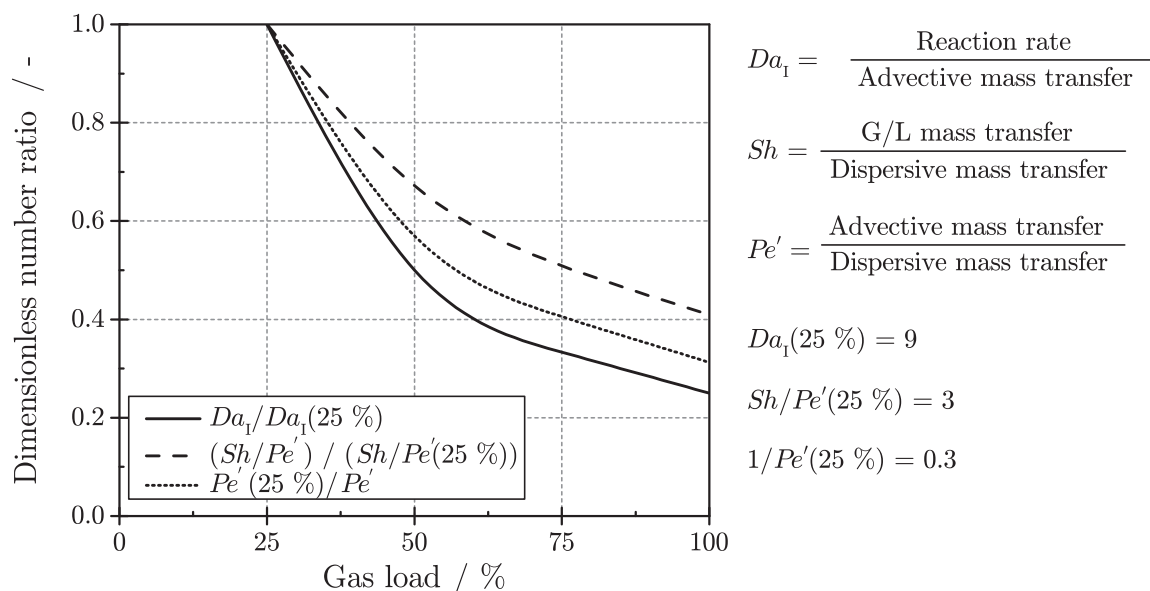


Figure M.3: Dimensionless numbers for mass transfer in the the slurry bubble column reactor as function of gas load for a feed H₂/CO₂/CH₄ of 4/1/1 ($\bar{T}_{\text{SL}} = 320$ °C, $p_{\text{out}} = 20$ bar, $\varphi_{\text{S}} = 0.2$).

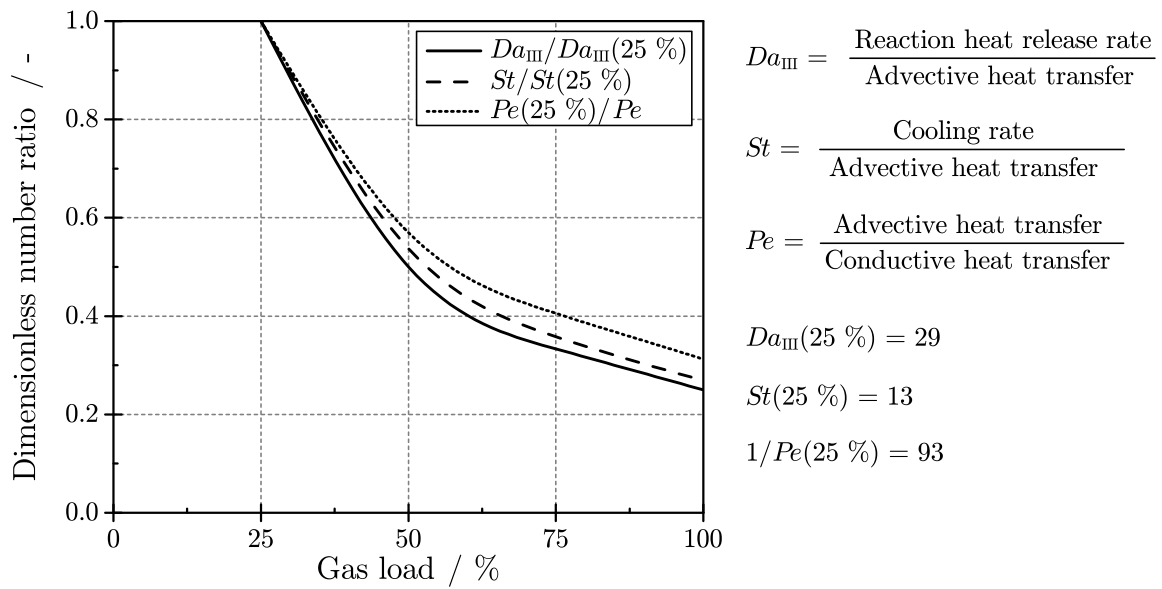


Figure M.4: Dimensionless numbers for heat transfer in the the slurry bubble column reactor as function of gas load for a feed $H_2/CO_2/CH_4$ of 4/1/1 ($\bar{T}_{SL} = 320\text{ }^\circ\text{C}$, $p_{out} = 20\text{ bar}$, $\varphi_S = 0.2$).

M.5 Effect of gas load on tube bundle reactor

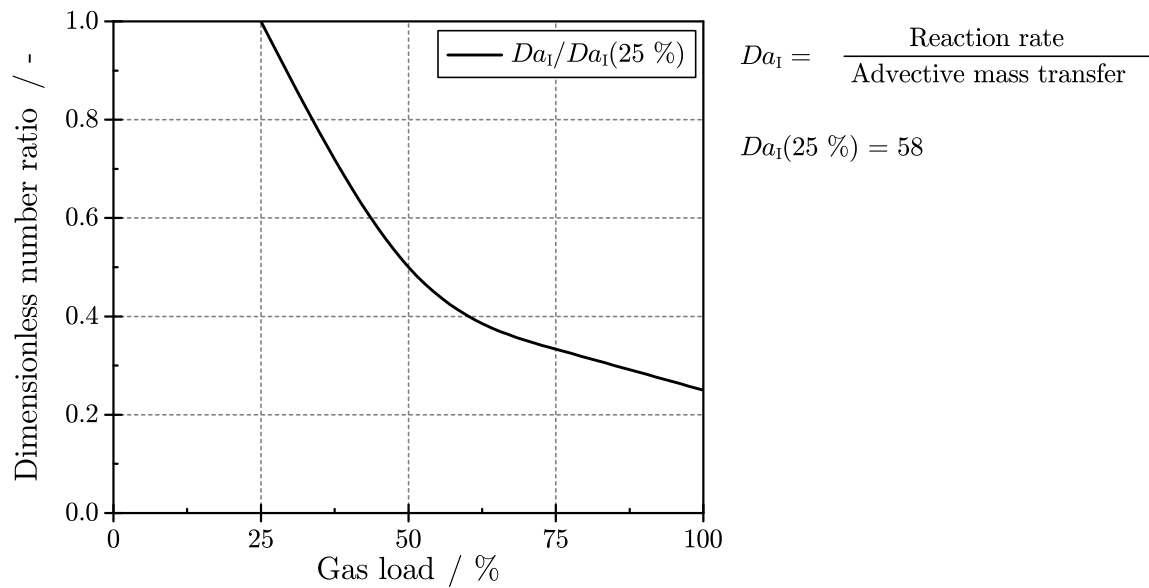


Figure M.5: Dimensionless numbers for mass transfer in the tube bundle reactor as function of gas load for a feed $H_2/CO_2/CH_4$ of 4/1/1 ($T_R = 350\text{ }^\circ\text{C}$, $p_{in} = 20\text{ bar}$).

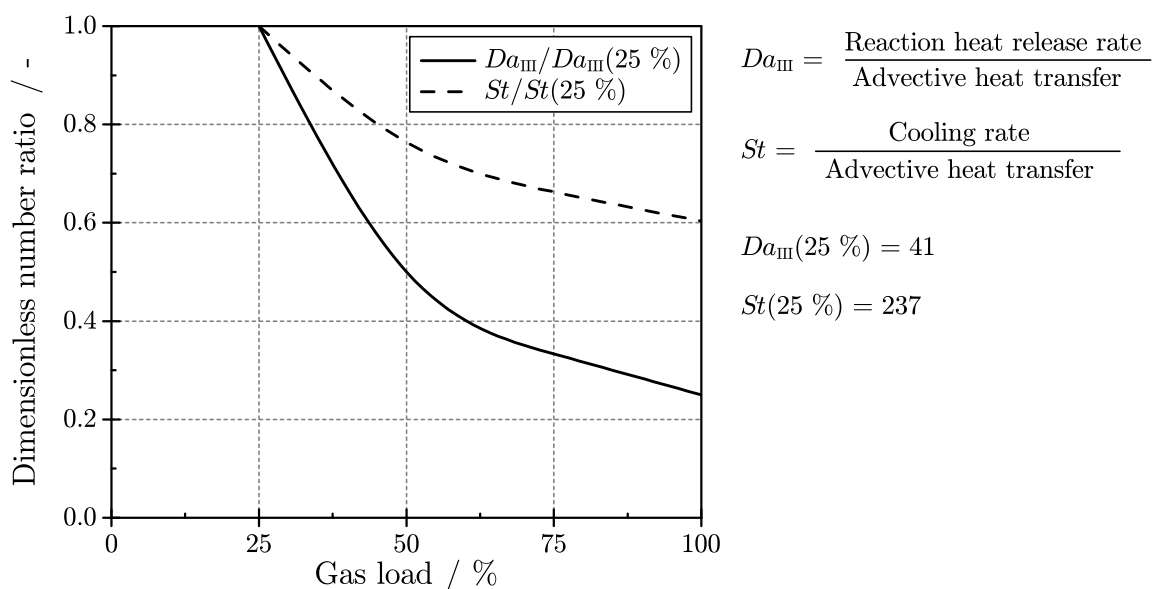


Figure M.6: Dimensionless numbers for heat transfer in the tube bundle reactor as function of gas load for a feed $\text{H}_2/\text{CO}_2/\text{CH}_4$ of 4/1/1 ($T_R = 350\text{ }^\circ\text{C}$, $p_{in} = 20\text{ bar}$).

M.6 Effect of gas load step change on slurry bubble column reactor

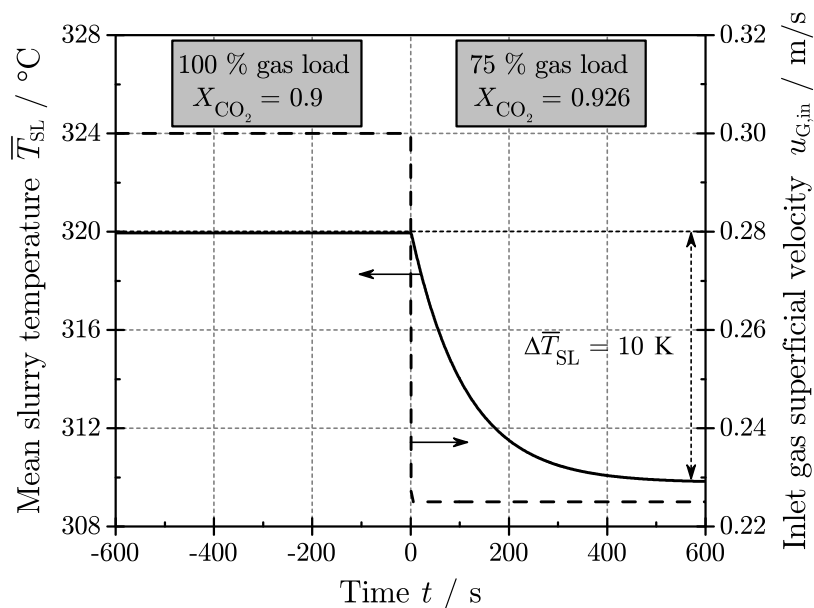


Figure M.7: Slurry temperature as function of time after a gas load step change from 100 to 75 % for a feed $\text{H}_2/\text{CO}_2/\text{CH}_4$ of 4/1/1 (Reactor design parameters are summarized in Table 7.4, $T_{cool} = 269\text{ }^\circ\text{C}$).

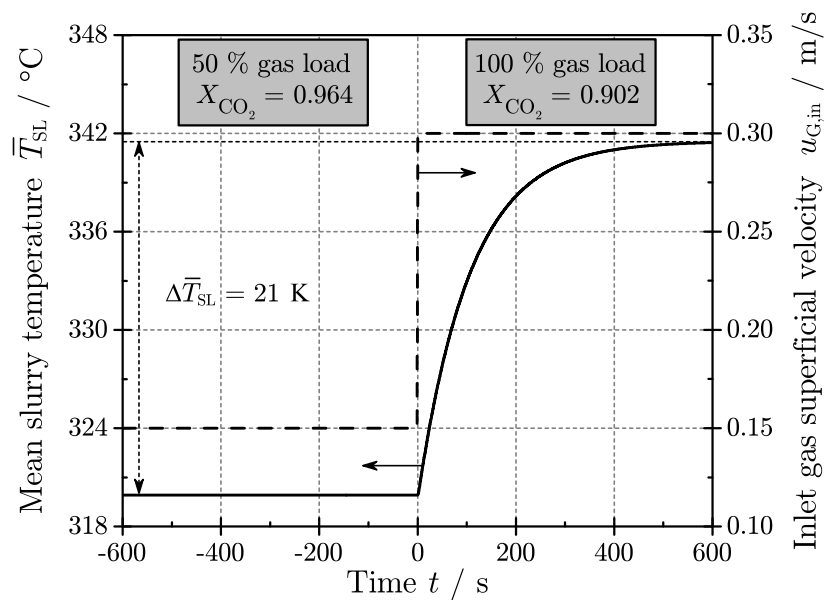


Figure M.8: Slurry temperature as function of time after a gas load step change from 50 to 100 % for a feed $\text{H}_2/\text{CO}_2/\text{CH}_4$ of 4/1/1 (Reactor design parameters are summarized in Table 7.4, $T_{\text{cool}} = 269 \text{ }^\circ\text{C}$).

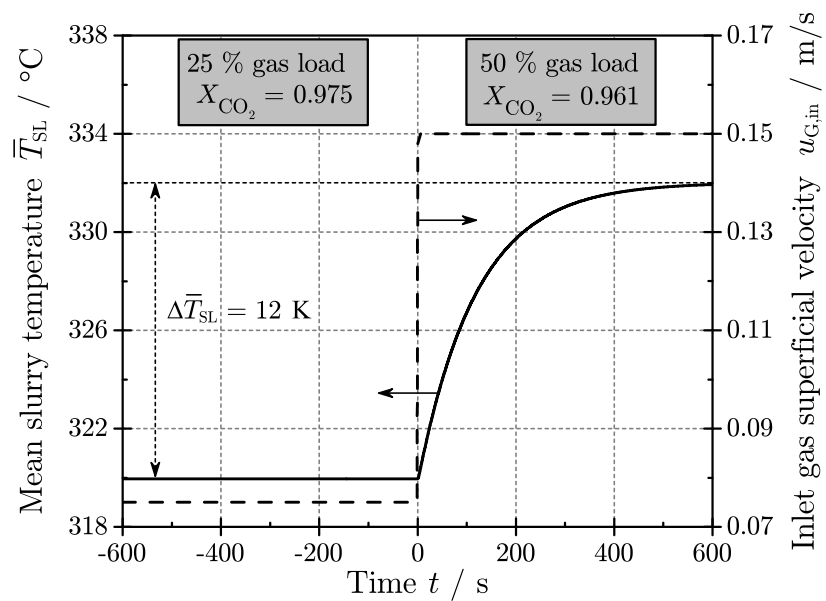


Figure M.9: Slurry temperature as function of time after a gas load step change from 25 to 50 % for a feed $\text{H}_2/\text{CO}_2/\text{CH}_4$ of 4/1/1 (Reactor design parameters are summarized in Table 7.4, $T_{\text{cool}} = 300 \text{ }^\circ\text{C}$).

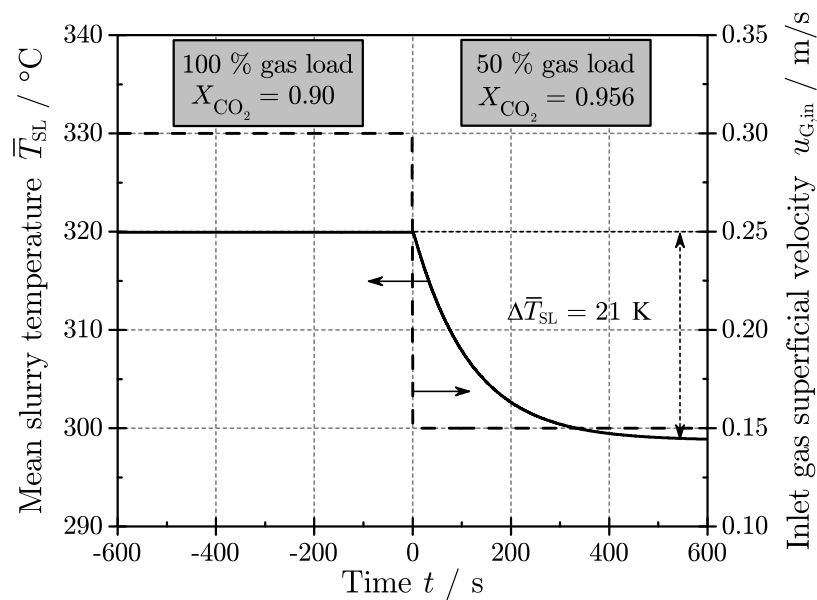


Figure M.10: Slurry temperature as function of time after a gas load step change from 100 to 50 % for a feed $\text{H}_2/\text{CO}_2/\text{CH}_4$ of 4/1/1 (Reactor design parameters are summarized in Table 7.4, $T_{\text{cool}} = 269 \text{ }^\circ\text{C}$).

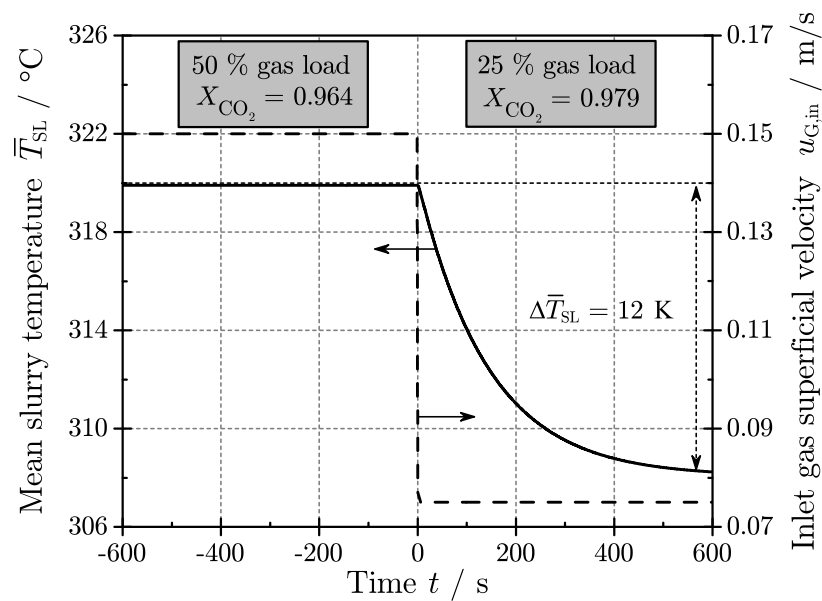


Figure M.11: Slurry temperature as function of time after a gas load step change from 50 to 25 % for a feed $\text{H}_2/\text{CO}_2/\text{CH}_4$ of 4/1/1 (Reactor design parameters are summarized in Table 7.4, $T_{\text{cool}} = 289 \text{ }^\circ\text{C}$).

M.7 Effect of gas load step change on tube bundle reactor

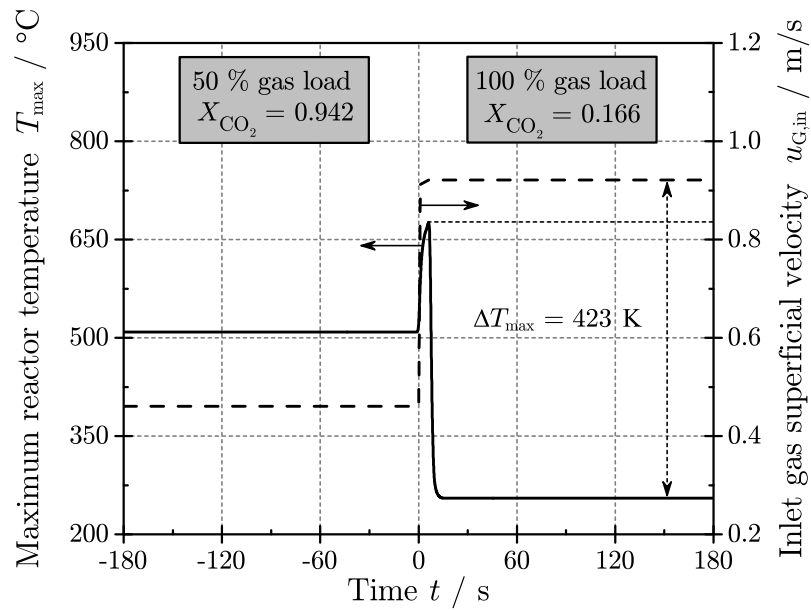


Figure M.12: Maximum reactor temperature of the tube bundle reactor as function of time after a gas load step change from 50 to 100 % for a feed $\text{H}_2/\text{CO}_2/\text{CH}_4$ of 4/1/1 (Reactor design parameters are summarized in Table 7.5, $T_{\text{cool}} = 240$ °C).

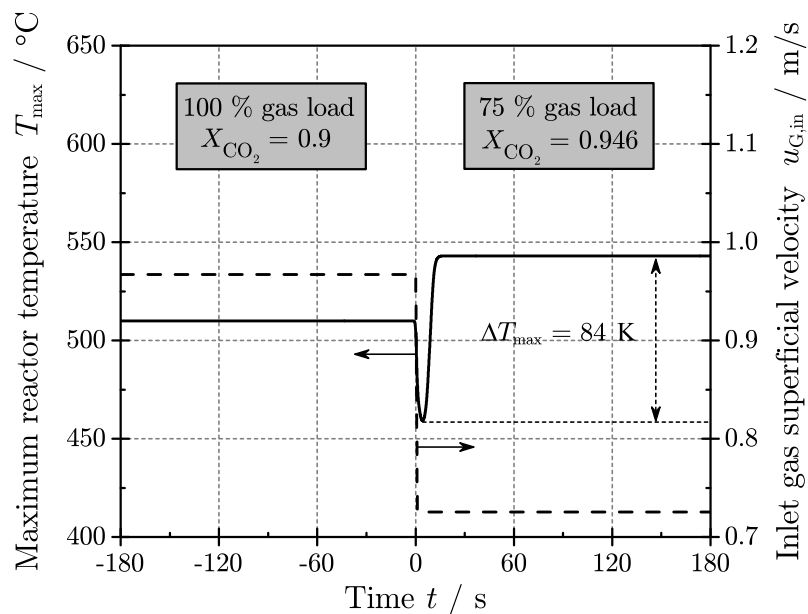


Figure M.13: Maximum reactor temperature of the tube bundle reactor as function of time after a gas load step change from 100 to 75 % for a feed $\text{H}_2/\text{CO}_2/\text{CH}_4$ of 4/1/1 (Reactor design parameters are summarized in Table 7.5, $T_{\text{cool}} = 251$ °C).

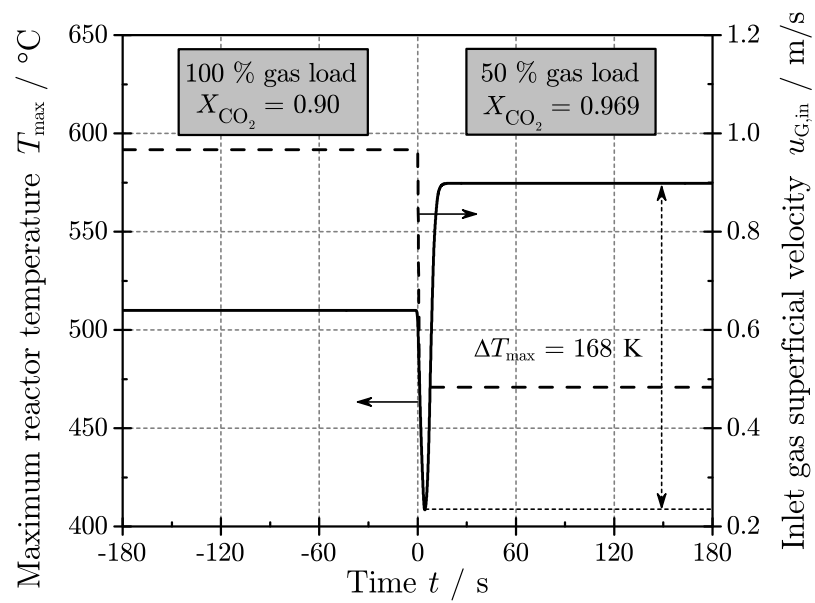


Figure M.14: Maximum reactor temperature of the tube bundle reactor as function of time after a gas load step change from 100 to 50 % for a feed $\text{H}_2/\text{CO}_2/\text{CH}_4$ of 4/1/1 (Reactor design parameters are summarized in Table 7.5, $T_{\text{cool}} = 251$ °C).

M.8 Design algorithm

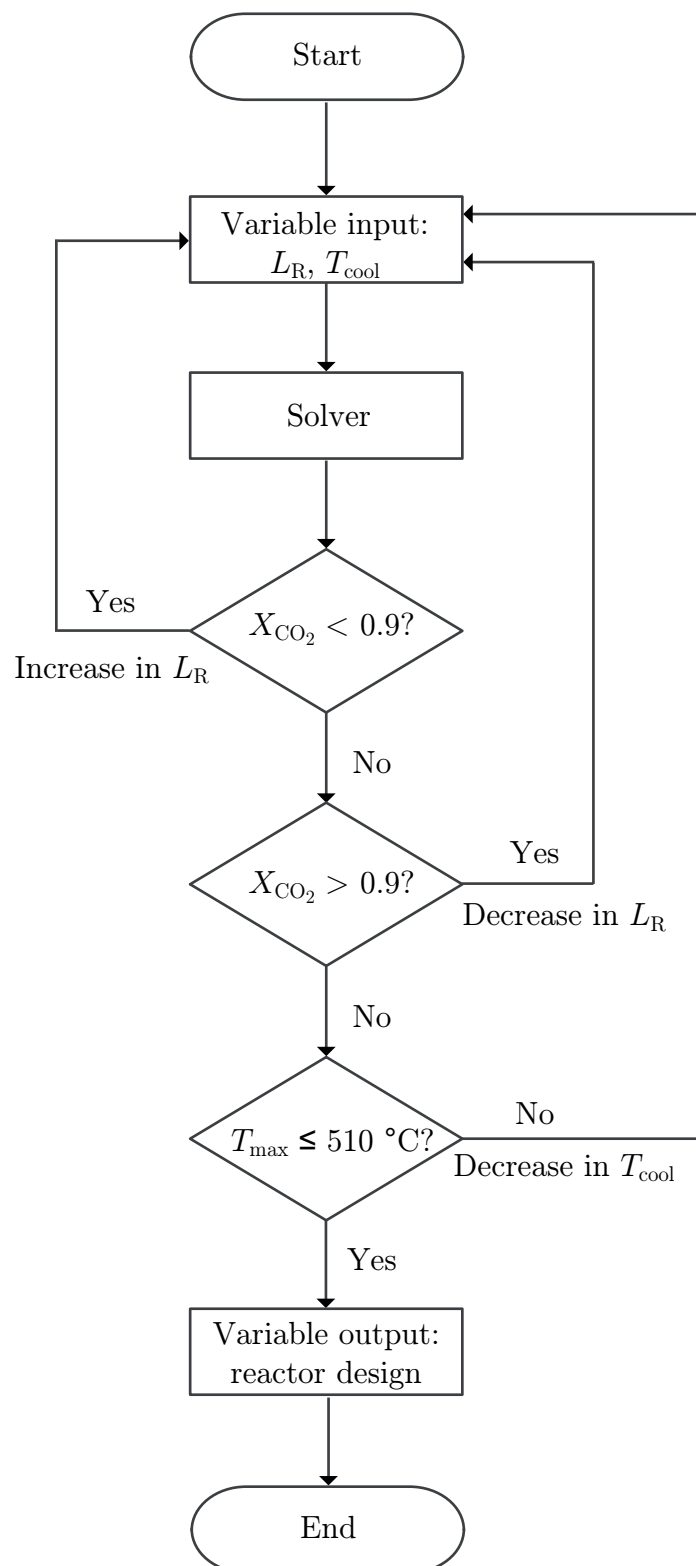


Figure M.15: Algorithm for the design of the tube bundle reactor with a CO_2 conversion of 0.9 and a maximum reactor temperature of $510 \text{ }^\circ\text{C}$.

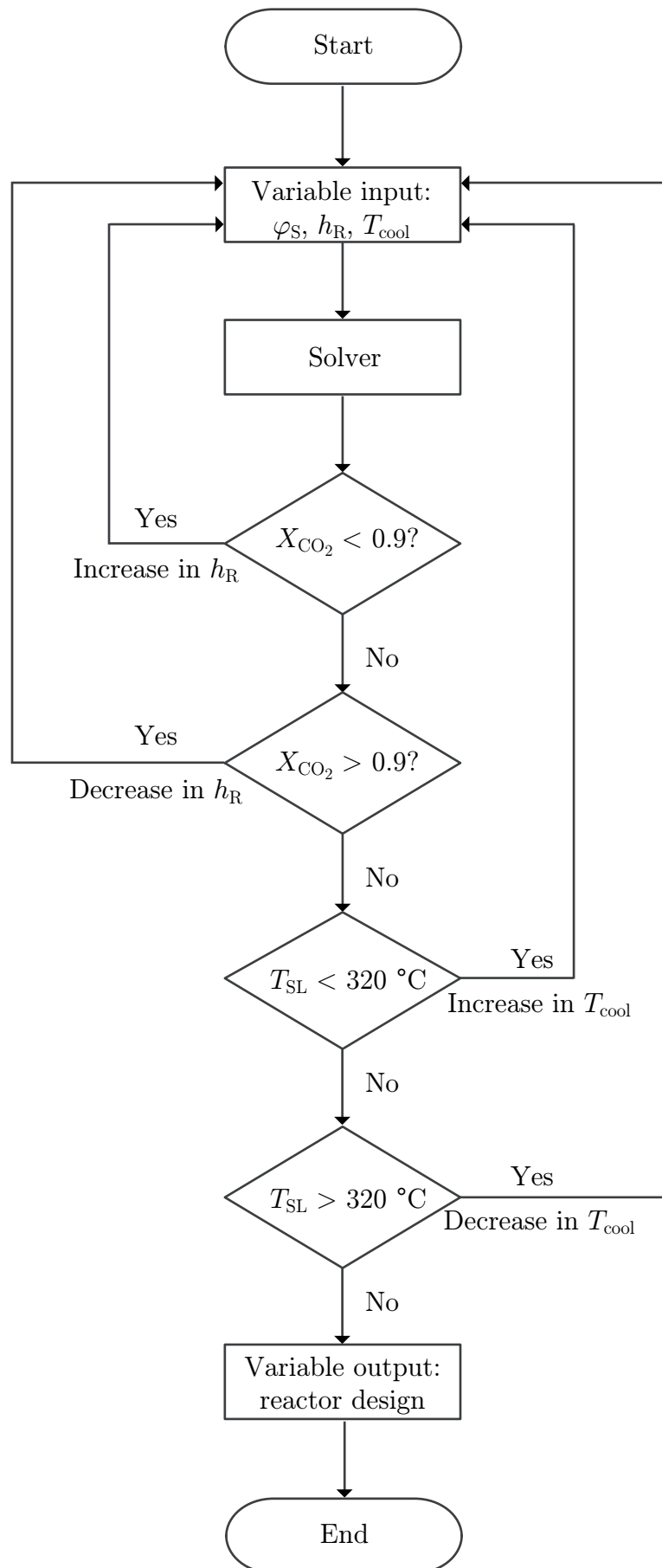


Figure M.16: Algorithm for the design of the slurry bubble column reactor with a CO_2 conversion of 0.9 and a mean slurry temperature of $320\text{ }^\circ\text{C}$.

N Evaluation of data accuracy

In this work, the data accuracy has been calculated with the differential method. An example is given below for X_{CO_2} . The CO_2 conversion X_{CO_2} is defined as following (Eq. N.1):

$$X_{\text{CO}_2} = \frac{\dot{n}_{\text{CO}_2,\text{in}} - \dot{n}_{\text{CO}_2,\text{out}}}{\dot{n}_{\text{CO}_2,\text{in}}} \quad (\text{N.1})$$

Eq. N.1 can be rewritten as following (Eq. N.2):

$$\ln(X_{\text{CO}_2}) = \ln(\dot{n}_{\text{CO}_2,\text{in}} - \dot{n}_{\text{CO}_2,\text{out}}) - \ln(\dot{n}_{\text{CO}_2,\text{in}}) \quad (\text{N.2})$$

Then, Eq. N.2 is differentiated to obtain Eq. N.3:

$$\frac{dX_{\text{CO}_2}}{X_{\text{CO}_2}} = \frac{d\dot{n}_{\text{CO}_2,\text{in}}}{\dot{n}_{\text{CO}_2,\text{in}} - \dot{n}_{\text{CO}_2,\text{out}}} - \frac{d\dot{n}_{\text{CO}_2,\text{out}}}{\dot{n}_{\text{CO}_2,\text{in}} - \dot{n}_{\text{CO}_2,\text{out}}} - \frac{d\dot{n}_{\text{CO}_2,\text{in}}}{\dot{n}_{\text{CO}_2,\text{in}}} \quad (\text{N.3})$$

Eq. N.3 can be then rewritten to obtain Eq. N.4

$$\frac{dX_{\text{CO}_2}}{X_{\text{CO}_2}} = \frac{d\dot{n}_{\text{CO}_2,\text{in}}}{\dot{n}_{\text{CO}_2,\text{in}}} \cdot \frac{1 - X_{\text{CO}_2}}{X_{\text{CO}_2}} - \frac{d\dot{n}_{\text{CO}_2,\text{out}}}{\dot{n}_{\text{CO}_2,\text{out}}} \cdot \frac{1 - X_{\text{CO}_2}}{X_{\text{CO}_2}} \quad (\text{N.4})$$

Finally, the relative accuracy $\Delta X_{\text{CO}_2}/X_{\text{CO}_2}$ can be expressed as following (Eq. N.5):

$$\frac{\Delta X_{\text{CO}_2}}{X_{\text{CO}_2}} = \frac{\Delta \dot{n}_{\text{CO}_2,\text{in}}}{\dot{n}_{\text{CO}_2,\text{in}}} \cdot \frac{1 - X_{\text{CO}_2}}{X_{\text{CO}_2}} + \frac{\Delta \dot{n}_{\text{CO}_2,\text{out}}}{\dot{n}_{\text{CO}_2,\text{out}}} \cdot \frac{1 - X_{\text{CO}_2}}{X_{\text{CO}_2}} \quad (\text{N.5})$$

Following the same method, the accuracy of r_i , p_i and $He_{i,px}$ can be estimated with the following Eq. N.6 to N.12.

$$\frac{\Delta r_{3\text{PM}}}{r_{3\text{PM}}} = \frac{\Delta r_{2\text{PM}}}{r_{2\text{PM}}} = \frac{\Delta X_{\text{CO}_2}}{X_{\text{CO}_2}} + \frac{\Delta m_{\text{cat}}}{m_{\text{cat}}} + \frac{\Delta \dot{n}_{\text{CO}_2,\text{in}}}{\dot{n}_{\text{CO}_2,\text{in}}} \quad (\text{N.6})$$

$$\frac{\Delta p_i}{p_i} = \frac{\Delta y_i}{y_i} + \frac{\Delta p}{p} \quad (\text{N.7})$$

$$\frac{\Delta He_{i,px}}{He_{i,px}} = \frac{\Delta p}{p} + \frac{\Delta n_L}{n_L} + \frac{\Delta n_{i,L}}{n_{i,L}} \quad (\text{N.8})$$

$$\frac{\Delta n_L}{n_L} = \frac{\Delta m_L}{m_L} \quad (\text{N.9})$$

$$\frac{\Delta n_{i,L}}{n_{i,L}} = \frac{\Delta n_{i,\text{Tank},1} + \Delta n_{i,\text{Tank},2} + \Delta n_{i,\text{R},2} + \Delta n_{i,\text{R},1}}{(n_{i,\text{Tank},1} - n_{i,\text{Tank},2}) - (n_{i,\text{R},2} - n_{i,\text{R},1})} \quad (\text{N.10})$$

$$\frac{\Delta n_{\text{Tank}}}{n_{\text{Tank}}} = \frac{\Delta p_{\text{Tank}}}{p_{\text{Tank}}} + \frac{\Delta T_{\text{Tank}}}{T_{\text{Tank}}} + \frac{\Delta V_{\text{Tank}}}{V_{\text{Tank}}} \quad (\text{N.11})$$

$$\frac{\Delta n_R}{n_R} = \frac{\Delta p_R}{p_R} + \frac{\Delta T_R}{T_R} + \frac{\Delta V_R}{V_R} \quad (\text{N.12})$$

The accuracy of the experimental parameters used in this work is listed in Table N.1.

Table N.1: Accuracy of experimental parameters according to the device suppliers.

Measurement device	Parameter	Units	Accuracy
MFC	$\Delta \dot{n}_{\text{CO}_2, \text{in}}$	$\text{mol} \cdot \text{s}^{-1}$	$\pm 0.01 \cdot \dot{n}_{\text{CO}_2, \text{in}}$
GC	$\Delta \dot{n}_{\text{CO}_2, \text{out}}$	$\text{mol} \cdot \text{s}^{-1}$	$\pm 0.01 \cdot \dot{n}_{\text{CO}_2, \text{out}}$
GC	Δy_i	-	$\pm 0.01 \cdot y_i$
Electronic sensor	Δp	bar	$\pm 0.025 \cdot p_{\text{max, sensor}}$
Thermocouple type K	ΔT	K or °C	± 1.5
Thermocouple Pt-100	ΔT	K or °C	± 0.8
Balance (catalyst)	Δm	kg	$\pm 1 \cdot 10^{-6}$
Balance (liquid)	Δm	kg	$\pm 1 \cdot 10^{-4}$

O Technical drawings

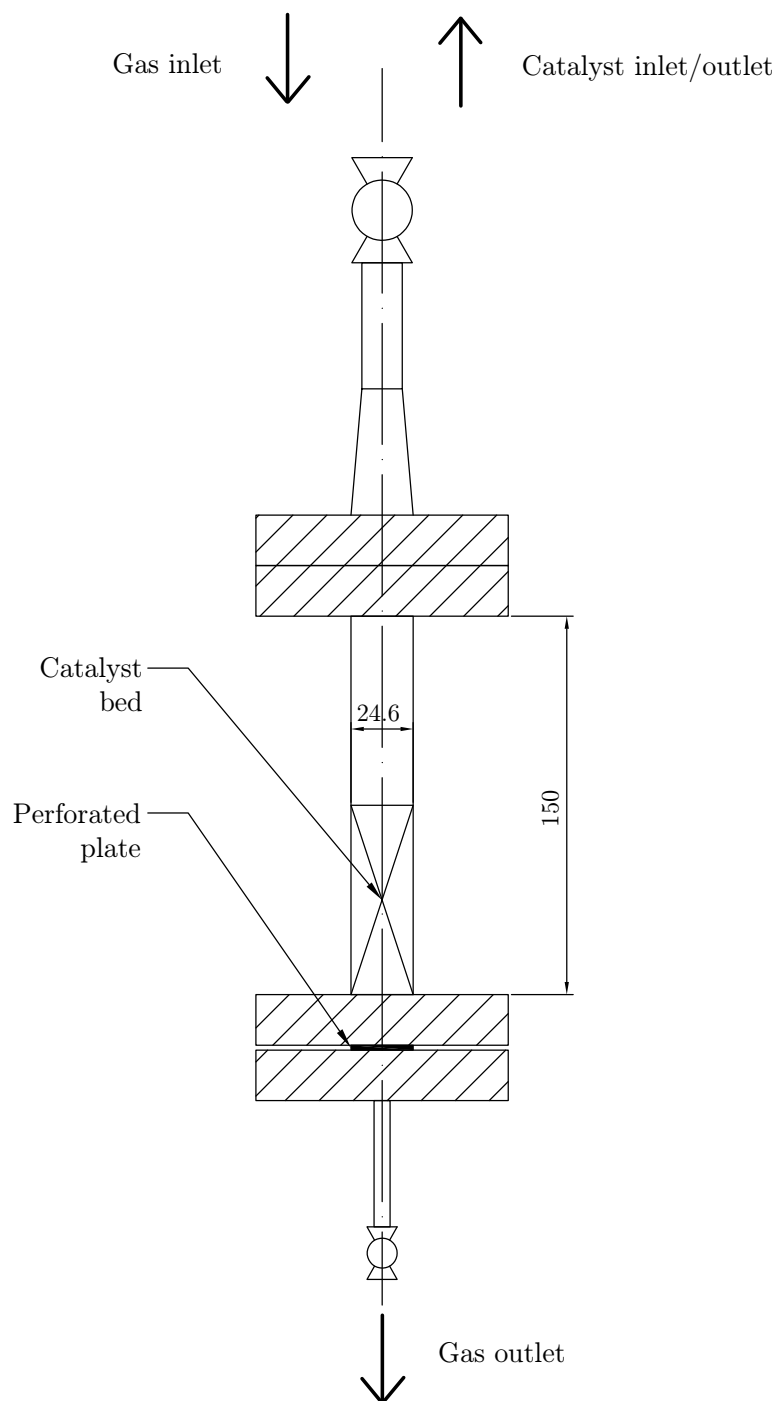


Figure O.1: Scheme of the reduction reactor. Dimensions are given in mm

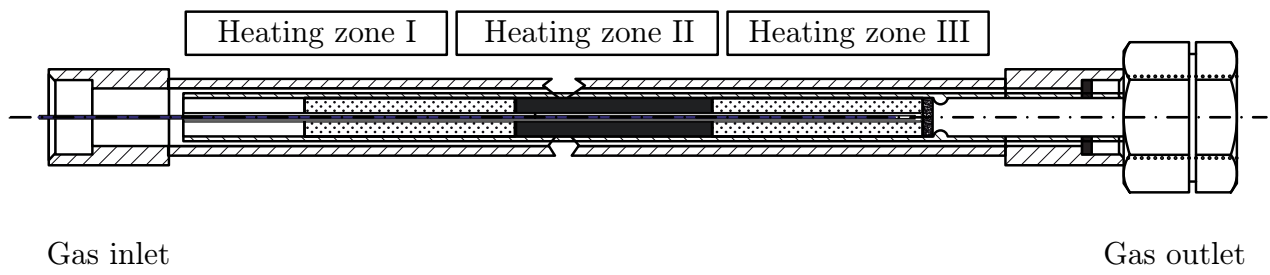


Figure O.2: Schematic illustration of the lab-scale fixed-bed reactor adapted from [234]

References

- [1] UNFCCC. *Adoption of the Paris Agreement*. 2015.
- [2] Manuel Götz et al. “Renewable Power-to-Gas: A technological and economic review”. In: *Renewable Energy* 85 (2016), pp. 1371–1390. ISSN: 0960-1481. DOI: 10.1016/j.renene.2015.07.066.
- [3] Manuel Bailera et al. “Power to Gas projects review: Lab, pilot and demo plants for storing renewable energy and CO₂”. In: *Renewable and Sustainable Energy Reviews* 69 (2017), pp. 292–312. ISSN: 1364-0321. DOI: 10.1016/j.rser.2016.11.130.
- [4] Michael Sterner and Ingo Stadler. *Energiespeicher - Bedarf, Technologien, Integration*. SpringerLink : Bücher. Berlin: Springer Vieweg, 2014. ISBN: 978-3-642-37379-4.
- [5] Koji Hashimoto et al. “The production of renewable energy in the form of methane using electrolytic hydrogen generation”. In: *Energy, Sustainability and Society* 4.1 (2014), p. 17. ISSN: 2192-0567. DOI: 10.1186/s13705-014-0017-5.
- [6] Stefan Rönsch et al. “Review on methanation -- From fundamentals to current projects”. In: *Fuel* 166 (2016), pp. 276–296. ISSN: 0016-2361. DOI: 10.1016/j.fuel.2015.10.111.
- [7] S. Rönsch et al. “Dynamische Simulation von Reaktoren zur Festbettmethanisierung: Dynamic Simulation of Fixed-Bed Methanation Reactors”. In: *Chemie Ingenieur Technik* 86.8 (2014), pp. 1198–1204. ISSN: 1522-2640. DOI: 10.1002/cite.201300046.
- [8] Manuel Götz. “Methanisierung im Dreiphasen-Reaktor”. PhD thesis. Karlsruhe: Karlsruher Institut für Technologie (KIT), 2014.
- [9] Jan Kopyscinski, Tilman J. Schildhauer, and Serge M. A. Biollaz. “Production of synthetic natural gas (SNG) from coal and dry biomass -- A technology review from 1950 to 2009”. In: *Fuel* 89.8 (2010), pp. 1763–1783. ISSN: 0016-2361. DOI: 10.1016/j.fuel.2010.01.027.
- [10] Jiajian Gao et al. “Recent advances in methanation catalysts for the production of synthetic natural gas”. In: *RSC Adv* 5.29 (2015), pp. 22759–22776. DOI: 10.1039/C4RA16114A.
- [11] Wei Wang et al. “Recent advances in catalytic hydrogenation of carbon dioxide”. In: *Chemical Society Reviews* 40.7 (2011), pp. 3703–3727. ISSN: 0306-0012. DOI: 10.1039/c1cs15008a.
- [12] G. A. Mills and F. W. Steffgen. “Catalytic Methanation”. In: *Catalysis Reviews* 8.1 (1974), pp. 159–210. DOI: 10.1080/01614947408071860.

- [13] Xiong Su et al. “Catalytic carbon dioxide hydrogenation to methane: A review of recent studies”. In: *Journal of Energy Chemistry* 25.4 (2016), pp. 553–565. ISSN: 2095-4956. DOI: 10.1016/j.jechem.2016.03.009.
- [14] L. M. Aparicio. “Transient Isotopic Studies and Microkinetic Modeling of Methane Reforming over Nickel Catalysts”. In: *Journal of Catalysis* 165.2 (1997), pp. 262–274. ISSN: 0021-9517. DOI: 10.1006/jcat.1997.1468.
- [15] R. A. Dalla Betta, A. G. Piken, and M. Shelef. “Heterogeneous methanation: Steady-state rate of CO hydrogenation on supported ruthenium, nickel and rhenium”. In: *Journal of Catalysis* 40.2 (1975), pp. 173–183. ISSN: 0021-9517. DOI: 10.1016/0021-9517(75)90244-4.
- [16] D. C. Gardner and C. H. Bartholomew. “Kinetics of carbon deposition during methanation of carbon monoxide”. In: *Ind. Eng. Chem. Process Des. Develop.*; 20.1 (1981), pp. 80–87. DOI: 10.1021/i300001a007.
- [17] Craig K. Vance and Calvin H. Bartholomew. “Hydrogenation of carbon dioxide on group viii metals: III, Effects of support on activity/selectivity and adsorption properties of nickel”. In: *Applied Catalysis* 7.2 (1983), pp. 169–177. DOI: 10.1016/0166-9834(83)80005-0.
- [18] Sibel Z. Ozdogan, Paul D. Gochis, and John L. Falconer. “Carbon and carbon monoxide hydrogenation on nickel: Support effects”. In: *Journal of Catalysis* 83.2 (1983), pp. 257–266. ISSN: 0021-9517. DOI: 10.1016/0021-9517(83)90053-2.
- [19] Calvin H. Bartholomew and Craig K. Vance. “Effects of support on the kinetics of carbon hydrogenation on nickel”. In: *Journal of Catalysis* 91.1 (1985), pp. 78–84. ISSN: 0021-9517. DOI: 10.1016/0021-9517(85)90290-8.
- [20] Dacheng Hu et al. “Enhanced Investigation of CO Methanation over Ni/Al₂O₃ Catalysts for Synthetic Natural Gas Production”. In: *Ind. Eng. Chem. Res.* 51.13 (2012), pp. 4875–4886. ISSN: 0888-5885. DOI: 10.1021/ie300049f.
- [21] Sònia Abelló, César Berrueco, and Daniel Montané. “High-loaded nickel--alumina catalyst for direct CO₂ hydrogenation into synthetic natural gas (SNG)”. In: *Fuel* 113.0 (2013), pp. 598–609. ISSN: 0016-2361. DOI: 10.1016/j.fuel.2013.06.012.
- [22] Jiajian Gao et al. “Ni/Al₂O₃ catalysts for CO methanation: Effect of Al₂O₃ supports calcined at different temperatures”. In: *Journal of Energy Chemistry* 22.6 (2013), pp. 919–927. ISSN: 2095-4956. DOI: 10.1016/S2095-4956(14)60273-4.
- [23] Guoquan Zhang et al. “A comparison of Ni/SiC and Ni/Al₂O₃ catalyzed total methanation for production of synthetic natural gas”. In: *Applied Catalysis A: General* 462-463 (2013), pp. 75–81. ISSN: 0926-860X. DOI: 10.1016/j.apcata.2013.04.037.
- [24] Xiaobo Bai et al. “Influence of Operating Conditions on Carbon Deposition Over a Ni Catalyst for the Production of Synthetic Natural Gas (SNG) from Coal”. In: *Catalysis Letters* 144.12 (2014), pp. 2157–2166. ISSN: 1011-372X. DOI: 10.1007/s10562-014-1379-1.
- [25] J. Barrientos et al. “Deactivation of supported nickel catalysts during CO methanation”. In: *Applied Catalysis A: General* 486.0 (2014), pp. 143–149. ISSN: 0926-860X. DOI: 10.1016/j.apcata.2014.08.021.

- [26] Gabriella Garbarino et al. “A study of the methanation of carbon dioxide on Ni/Al₂O₃ catalysts at atmospheric pressure”. In: *International Journal of Hydrogen Energy* 39.22 (2014), pp. 11557–11565. ISSN: 0360-3199. DOI: 10.1016/j.ijhydene.2014.05.111.
- [27] Franz Koschany, David Schlereth, and Olaf Hinrichsen. “On the kinetics of the methanation of carbon dioxide on coprecipitated NiAl(O)_x”. In: *Applied Catalysis B: Environmental* 181 (2016), pp. 504–516. ISSN: 0926-3373. DOI: 10.1016/j.apcatb.2015.07.026.
- [28] Yakun Li et al. “Metal-foam-structured Ni–Al₂O₃ catalysts: Wet chemical etching preparation and syngas methanation performance”. In: *Applied Catalysis A: General* 510 (2016), pp. 216–226. ISSN: 0926-860X. DOI: 10.1016/j.apcata.2015.11.034.
- [29] Hiroki Muroyama et al. “Carbon dioxide methanation over Ni catalysts supported on various metal oxides”. In: *Journal of Catalysis* 343 (2016), pp. 178–184. ISSN: 0021-9517. DOI: 10.1016/j.jcat.2016.07.018.
- [30] Wangxin Nie et al. “CeO₂-assisted Ni nanocatalysts supported on mesoporous Al₂O₃ for the production of synthetic natural gas”. In: *Fuel* 202.Supplement C (2017), pp. 135–143. ISSN: 0016-2361. DOI: 10.1016/j.fuel.2017.04.026.
- [31] Chalachew Mebrahtu et al. “CO₂ methanation over Ni catalysts based on ternary and quaternary mixed oxide: A comparison and analysis of the structure-activity relationships”. In: *Catalysis and synthetic fuels: state of the art and outlook* (2017). ISSN: 0920-5861. DOI: 10.1016/j.cattod.2017.08.060.
- [32] Dew, J. N., White, R. R., and Sliepcevich, C. M. “Hydrogenation of Carbon Dioxide on Nickel-Kieselguhr Catalyst”. In: *Ind. Eng. Chem.* 47.1 (1955), pp. 140–146. ISSN: 0019-7866. DOI: 10.1021/ie50541a044.
- [33] John L. Falconer and A. Ercüment ZaC Cşli. “Adsorption and methanation of carbon dioxide on a nickel/silica catalyst”. In: *Journal of Catalysis* 62.2 (1980), pp. 280–285. ISSN: 0021-9517. DOI: 10.1016/0021-9517(80)90456-X.
- [34] Gordon D. Weatherbee and Calvin H. Bartholomew. “Hydrogenation of CO₂ on group VIII metals: I. Specific activity of NiSiO₂”. In: *Journal of Catalysis* 68.1 (1981), pp. 67–76. ISSN: 0021-9517. DOI: 10.1016/0021-9517(81)90040-3.
- [35] Gordon D. Weatherbee and Calvin H. Bartholomew. “Hydrogenation of CO₂ on group VIII metals: II. Kinetics and mechanism of CO₂ hydrogenation on nickel”. In: *Journal of Catalysis* 77.2 (1982), pp. 460–472. ISSN: 0021-9517. DOI: 10.1016/0021-9517(82)90186-5.
- [36] J. A. Dalmon and G. A. Martin. “The Kinetics and Mechanism of Carbon Monoxide Methanation over Silica-Supported Nickel Catalysts”. In: *Journal of Catalysis* 84 (1983), pp. 45–54. ISSN: 0021-9517.
- [37] Jeng H. Chiang and Jack R. Hopper. “Kinetics of the hydrogenation of carbon dioxide over supported nickel”. In: *Ind. Eng. Chem. Prod. Res. Dev.* 22.2 (1983), pp. 225–228. ISSN: 0196-4321. DOI: 10.1021/i300010a011.
- [38] Xiaoliang Yan et al. “Methanation over Ni/SiO₂: Effect of the catalyst preparation methodologies”. In: *International Journal of Hydrogen Energy* 38.5 (2013), pp. 2283–2291. ISSN: 0360-3199. DOI: 10.1016/j.ijhydene.2012.12.024.

- [39] Xu Zhang, Wen-jing Sun, and Wei Chu. “Effect of glow discharge plasma treatment on the performance of Ni/SiO₂ catalyst in CO₂ methanation”. In: *Journal of Fuel Chemistry and Technology* 41.1 (2013), pp. 96–101. ISSN: 1872-5813. DOI: 10.1016/S1872-5813(13)60012-2.
- [40] M. Aziz et al. “Highly active Ni-promoted mesostructured silica nanoparticles for CO₂ methanation”. In: *Applied Catalysis B: Environmental* 147 (2014), pp. 359–368. ISSN: 0926-3373. DOI: 10.1016/j.apcatb.2013.09.015.
- [41] M. Aziz et al. “Methanation of carbon dioxide on metal-promoted mesostructured silica nanoparticles”. In: *Applied Catalysis A: General* 486 (2014), pp. 115–122. ISSN: 0926-860X. DOI: 10.1016/j.apcata.2014.08.022.
- [42] Xiao Chen et al. “Silicon--nickel intermetallic compounds supported on silica as a highly efficient catalyst for CO methanation”. In: *Catal. Sci. Technol.* 4.1 (2014), pp. 53–61. ISSN: 2044-4753. DOI: 10.1039/C3CY00743J.
- [43] M. Aziz et al. “CO₂ methanation over Ni-promoted mesostructured silica nanoparticles: Influence of Ni loading and water vapor on activity and response surface methodology studies”. In: *Chemical Engineering Journal* 260 (2015), pp. 757–764. ISSN: 1385-8947. DOI: 10.1016/j.cej.2014.09.031.
- [44] Xiaoliang Yan et al. “Dielectric barrier discharge plasma for preparation of Ni-based catalysts with enhanced coke resistance: Current status and perspective”. In: *Plasmas for enhanced catalytic processes (ISPCEM 2014)* 256, Part 1 (2015), pp. 29–40. ISSN: 0920-5861. DOI: 10.1016/j.cattod.2015.04.045.
- [45] Vijay M. Shinde and Giridhar Madras. “CO methanation toward the production of synthetic natural gas over highly active Ni/TiO₂ catalyst”. In: *AIChE Journal* 60.3 (2014), pp. 1027–1035. ISSN: 1547-5905. DOI: 10.1002/aic.14304.
- [46] Christoph Schild et al. “Carbon dioxide hydrogenation over nickel/zirconia catalysts from amorphous precursors: on the mechanism of methane formation”. In: *J. Phys. Chem.* 95.16 (1991), pp. 6341–6346. DOI: 10.1021/j100169a049.
- [47] Nina Perkas et al. “Methanation of Carbon Dioxide on Ni Catalysts on Mesoporous ZrO₂ Doped with Rare Earth Oxides”. In: *Catalysis Letters* 130.3-4 (2009), pp. 455–462. ISSN: 1011-372X. DOI: 10.1007/s10562-009-9952-8.
- [48] Yan-Hui Huang et al. “Highly efficient Ni-ZrO₂ catalyst doped with Yb₂O₃ for co-methanation of CO and CO₂”. In: *Applied Catalysis A: General* 466 (2013), pp. 300–306. ISSN: 0926-860X. DOI: 10.1016/j.apcata.2013.06.021.
- [49] Aihua Chen et al. “High catalytic performance of mesoporous zirconia supported nickel catalysts for selective CO methanation”. In: *Catalysis Science & Technology* 4.8 (2014), p. 2508. ISSN: 2044-4753. DOI: 10.1039/C4CY00461B.
- [50] Cuili Guo et al. “CO methanation over ZrO₂/Al₂O₃ supported Ni catalysts: A comprehensive study”. In: *Fuel Processing Technology* 124 (2014), pp. 61–69. ISSN: 0378-3820. DOI: 10.1016/j.fuproc.2014.02.017.
- [51] Zhenhua Li et al. “High CO methanation activity on zirconia-supported molybdenum sulfide catalyst”. In: *Journal of Energy Chemistry* 23.5 (2014), pp. 625–632. ISSN: 2095-4956. DOI: 10.1016/S2095-4956(14)60193-5.

- [52] Fanhui Meng et al. “Effect of ZrO₂ on catalyst structure and catalytic methanation performance over Ni-based catalyst in slurry-bed reactor”. In: *International Journal of Hydrogen Energy* 40.29 (2015), pp. 8833–8843. ISSN: 0360-3199. DOI: 10.1016/j.ijhydene.2015.05.057.
- [53] H. Takano et al. “CO₂ methanation of Ni catalysts supported on tetragonal ZrO₂ doped with Ca²⁺ and Ni²⁺ ions”. In: *International Journal of Hydrogen Energy* 40.26 (2015), pp. 8347–8355. ISSN: 0360-3199. DOI: 10.1016/j.ijhydene.2015.04.128.
- [54] Carla de Leitenburg, Alessandro Trovarelli, and Jan Kašpar. “A Temperature-Programmed and Transient Kinetic Study of CO₂ Activation and Methanation over CeO₂ Supported Noble Metals”. In: *Journal of Catalysis* 166.1 (1997), pp. 98–107. ISSN: 0021-9517. DOI: 10.1006/jcat.1997.1498.
- [55] Shohei Tada et al. “Ni/CeO₂ catalysts with high CO₂ methanation activity and high CH₄ selectivity at low temperatures”. In: *XII International Symposium on Polymer Electrolytes: New Materials for Application in Proton Exchange Membrane Fuel Cells* 37.7 (2012), pp. 5527–5531. ISSN: 0360-3199. DOI: 10.1016/j.ijhydene.2011.12.122.
- [56] Ussa Aldana, P. A. et al. “Catalytic CO₂ valorization into CH₄ on Ni-based ceria-zirconia. Reaction mechanism by operando IR spectroscopy”. In: *Catalysis and synthetic fuels: state of the art and outlook* 215.0 (2013), pp. 201–207. ISSN: 0920-5861. DOI: 10.1016/j.cattod.2013.02.019.
- [57] Ming-Yue Ding et al. “Bio-syngas methanation towards synthetic natural gas (SNG) over highly active Al₂O₃--CeO₂ supported Ni catalyst”. In: *Fuel Processing Technology* 134.0 (2015), pp. 480–486. ISSN: 0378-3820. DOI: 10.1016/j.fuproc.2015.03.006.
- [58] Mingyue Ding et al. “Enhancement of methanation of bio-syngas over CeO₂-modified Ni/Al₂O₃ catalysts”. In: *Biomass and Bioenergy* 85 (2016), pp. 12–17. DOI: 10.1016/j.biombioe.2015.11.025.
- [59] L. Atzori et al. “CO₂ methanation on hard-templated NiOCeO₂ mixed oxides”. In: *International Journal of Hydrogen Energy* 42.32 (2017), pp. 20689–20702. ISSN: 0360-3199. DOI: 10.1016/j.ijhydene.2017.06.198.
- [60] Guilin Zhou et al. “Methanation of carbon dioxide over Ni/CeO₂ catalysts: Effects of support CeO₂ structure”. In: *International Journal of Hydrogen Energy* 42.25 (2017), pp. 16108–16117. ISSN: 0360-3199. DOI: 10.1016/j.ijhydene.2017.05.154.
- [61] GunDae Lee et al. “Raney Ni catalysts derived from different alloy precursors Part II. CO and CO₂ methanation activity”. In: *Korean Journal of Chemical Engineering* 22.4 (2005), pp. 541–546. DOI: 10.1007/BF02706639.
- [62] Mei-Ting Fan et al. “Mg-Al oxide supported Ni catalysts with enhanced stability for efficient synthetic natural gas from syngas”. In: *Applied Surface Science* 307 (2014), pp. 682–688. ISSN: 01694332. DOI: 10.1016/j.apsusc.2014.04.098.
- [63] Meng Guo and Gongxuan Lu. “The effect of impregnation strategy on structural characters and CO₂ methanation properties over MgO modified Ni/SiO₂ catalysts”. In: *Catalysis Communications* 54 (2014), pp. 55–60. ISSN: 1566-7367. DOI: 10.1016/j.catcom.2014.05.022.

- [64] Jiao Liu et al. “Intercorrelation of structure and performance of Ni-Mg/Al₂O₃ catalysts prepared with different methods for syngas methanation”. In: *Catal. Sci. Technol.* 4.2 (2014), pp. 472–481. ISSN: 2044-4753. DOI: 10.1039/C3CY00601H.
- [65] Maria C. Bacariza et al. “Magnesium as Promoter of CO₂ Methanation on Ni-Based USY Zeolites”. In: *Energy & Fuels* 31.9 (2017), pp. 9776–9789. ISSN: 0887-0624. DOI: 10.1021/acs.energyfuels.7b01553.
- [66] Rotgerink, H. G. J. Lansink et al. “Studies on the promotion of nickel---alumina coprecipitated catalysts: II. Lanthanum oxide”. In: *Applied Catalysis* 45.2 (1988), pp. 257–280. DOI: 10.1016/S0166-9834(00)83033-X.
- [67] Qing Liu et al. “Enhanced catalytic performances of Ni/Al₂O₃ catalyst via addition of V₂O₃ for CO methanation”. In: *Applied Catalysis A: General* 488 (2014), pp. 37–47. ISSN: 0926-860X. DOI: 10.1016/j.apcata.2014.09.028.
- [68] Qing Liu et al. “Highly active and stable Ni/[gamma]-Al₂O₃ catalysts selectively deposited with CeO₂ for CO methanation”. In: *RSC Adv* 4.31 (2014), pp. 16094–16103. DOI: 10.1039/C4RA00746H.
- [69] Calvin H. Bartholomew. “Mechanism of catalyst deactivation”. In: *Applied Catalysis A: General* 212 (2001), pp. 17–60. ISSN: 0926-860X.
- [70] Maya Kiskinova and D. Wayne Goodman. “Modification of chemisorption properties by electronegative adatoms: H₂ and CO on chlorided, sulfided, and phosphided Ni(100)”. In: *Surface Science* 108.1 (1981), pp. 64–76. DOI: 10.1016/0039-6028(81)90358-7.
- [71] Nguyen, T. T. M., L. Wissing, and M. S. Skjoeth-Rasmussen. “High temperature methanation: Catalyst considerations”. In: *Catalysis and synthetic fuels: state of the art and outlook* 215.0 (2013), pp. 233–238. ISSN: 0920-5861. DOI: 10.1016/j.cattod.2013.03.035.
- [72] W. M. Shen, J. A. Dumesic, and C. G. Hill. “Criteria for stable Ni particle size under methanation reaction conditions: Nickel transport and particle size growth via nickel carbonyl”. In: *Journal of Catalysis* 68.1 (1981), pp. 152–165. ISSN: 0021-9517. DOI: 10.1016/0021-9517(81)90048-8.
- [73] J.A Moulajn, A.E van Diepen, and F. Kapteijn. “Catalyst deactivation: is it predictable? What to do?” In: *Applied Catalysis A: General* 212.1-2 (2001), pp. 3–16. ISSN: 0926-860X. DOI: 10.1016/S0926-860X(00)00842-5.
- [74] D. E. Peebles, D. W. Goodman, and J. M. White. “Methanation of carbon dioxide on nickel(100) and the effects of surface modifiers”. In: *The Journal of Physical Chemistry* 87.22 (1983), pp. 4378–4387. ISSN: 0022-3654. DOI: 10.1021/j100245a014.
- [75] S. Fujita et al. “Methanation of carbon monoxide and carbon dioxide over nickel catalyst under the transient state”. In: *Reaction Kinetics and Catalysis Letters* 33.1 (1987), pp. 179–184. ISSN: 0133-1736. DOI: 10.1007/BF02066720.
- [76] Todd K. Campbell and John L. Falconer. “Carbon dioxide hydrogenation on potassium-promoted nickel catalysts”. In: *Applied Catalysis* 50.1 (1989), pp. 189–197. DOI: 10.1016/S0166-9834(00)80835-0.

- [77] S. Fujita et al. “Mechanisms of methanation of carbon monoxide and carbon dioxide over nickel”. In: *Industrial & Engineering Chemistry Research* 30.6 (1991), pp. 1146–1151. DOI: 10.1021/ie00054a012.
- [78] Shin-ichiro Fujita et al. “Mechanisms of methanation of carbon dioxide and carbon monoxide over nickel/alumina catalysts”. In: *Applied Catalysis A: General* 104.1 (1993), pp. 87–100. ISSN: 0926-860X. DOI: 10.1016/0926-860X(93)80212-9.
- [79] Michel Marwood et al. “Transient drift spectroscopy for the determination of the surface reaction kinetics of CO₂ methanation”. In: *Chemical Engineering Science* 49.24 (1994), pp. 4801–4809. ISSN: 0009-2509. DOI: 10.1016/S0009-2509(05)80060-0.
- [80] Michel Marwood et al. “Periodic operation applied to the kinetic study of CO₂ methanation”. In: *Catalysis Today* 20.3 (1994), pp. 437–448. ISSN: 0920-5861. DOI: 10.1016/0920-5861(94)80137-1.
- [81] Song Qin et al. “Theoretical Study on the Reaction Mechanism of the Gas-Phase H₂/CO₂/Ni(3D) System”. In: *J. Phys. Chem. A* 109.29 (2005), pp. 6498–6502. ISSN: 1089-5639. DOI: 10.1021/jp0506585.
- [82] Jun Ren et al. “Insights into the mechanisms of CO₂ methanation on Ni(111) surfaces by density functional theory”. In: *Applied Surface Science* 351 (2015), pp. 504–516. ISSN: 01694332. DOI: 10.1016/j.apsusc.2015.05.173.
- [83] Pallavi Bothra, Ganga Periyasamy, and Swapan K. Pati. “Methane formation from the hydrogenation of carbon dioxide on Ni(110) surface - a density functional theoretical study”. In: *Phys. Chem. Chem. Phys.* 15.15 (2013), pp. 5701–5706. ISSN: 1463-9076. DOI: 10.1039/C3CP44495C.
- [84] E. Vesselli et al. “Catalytic CO₂ Hydrogenation on Nickel: Novel Insight by Chemical Transient Kinetics”. In: *J. Phys. Chem. C* 115.4 (2011), pp. 1255–1260. ISSN: 1932-7447. DOI: 10.1021/jp106551r.
- [85] Qiushi Pan et al. “Insight into the reaction route of CO₂ methanation: Promotion effect of medium basic sites”. In: *Catalysis Communications* 45.0 (2014), pp. 74–78. ISSN: 1566-7367. DOI: 10.1016/j.catcom.2013.10.034.
- [86] Qiushi Pan et al. “In situ FTIR spectroscopic study of the CO₂ methanation mechanism on Ni/Ce_{0.5}Zr_{0.5}O₂”. In: *Catal. Sci. Technol.* 4.2 (2014), pp. 502–509. ISSN: 2044-4753. DOI: 10.1039/C3CY00868A.
- [87] M. Araki and V. Ponec. “Methanation of carbon monoxide on nickel and nickel-copper alloys”. In: *Journal of Catalysis* 44.3 (1976), pp. 439–448. ISSN: 0021-9517. DOI: 10.1016/0021-9517(76)90421-8.
- [88] Sa van Ho and Peter Harriott. “The kinetics of methanation on nickel catalysts”. In: *Journal of Catalysis* 64.2 (1980), pp. 272–283. ISSN: 0021-9517. DOI: 10.1016/0021-9517(80)90502-3.
- [89] R. van Meerten et al. “The kinetics and mechanism of the methanation of carbon monoxide on a nickel-silica catalyst”. In: *Applied Catalysis* 3.1 (1982), pp. 29–56. DOI: 10.1016/0166-9834(82)80221-2.

- [90] Toshiaki Mori et al. “Kinetics, isotope effects, and mechanism for the hydrogenation of carbon monoxide on supported nickel catalysts”. In: *J. Phys. Chem.* 86.14 (1982), pp. 2753–2760. DOI: 10.1021/j100211a039.
- [91] R. E. Hayes and W. J. Thomas. “Catalyst Deactivation By Carbon Formation In Methanation”. In: *Studies in Surface Science and Catalysis : Catalysis on the Energy Scene*. Ed. by S. Kaliaguine and A. Mahay. Vol. Volume 19. Elsevier, 1984, pp. 463–470. ISBN: 0167-2991. DOI: 10.1016/S0167-2991(09)60130-0.
- [92] I. Alstrup. “On the Kinetics of CO Methanation on Nickel Surfaces”. In: *Journal of Catalysis* 151.1 (1995), pp. 216–225. ISSN: 0021-9517. DOI: 10.1006/jcat.1995.1023.
- [93] Jens Sehested et al. “Methanation of CO over Nickel: Mechanism and Kinetics at High H₂/CO Ratios”. In: *The Journal of Physical Chemistry B* 109.6 (2005), pp. 2432–2438. ISSN: 1520-6106. DOI: 10.1021/jp040239s.
- [94] M. A. Vannice. “The Catalytic Synthesis of Hydrocarbons from Carbon Monoxide and Hydrogen”. In: *Catalysis Reviews* 14.1 (1976), pp. 153–191. DOI: 10.1080/03602457608073410.
- [95] C. P. Huang and J. T. Richardson. “Alkali promotion of nickel catalysts for carbon monoxide methanation”. In: *Journal of Catalysis* 51.1 (1978), pp. 1–8. ISSN: 0021-9517. DOI: 10.1016/0021-9517(78)90232-4.
- [96] Coenen, J. W. E. et al. “The dynamics of methanation of carbon monoxide on nickel catalysts”. In: *Applied Catalysis* 25.1 (1986), pp. 1–8. DOI: 10.1016/S0166-9834(00)81215-4.
- [97] V. Sanchez-Escribano et al. “On the mechanisms and the selectivity determining steps in syngas conversion over supported metal catalysts: An IR study”. In: *Applied Catalysis A: General* 316.1 (2007), pp. 68–74. ISSN: 0926-860X. DOI: 10.1016/j.apcata.2006.09.020.
- [98] M. P. Andersson et al. “Structure sensitivity of the methanation reaction: H₂-induced CO dissociation on nickel surfaces”. In: *Journal of Catalysis* 255.1 (2008), pp. 6–19. ISSN: 0021-9517. DOI: 10.1016/j.jcat.2007.12.016.
- [99] Benjamin Mutz et al. “Methanation of CO₂: Structural response of a Ni-based catalyst under fluctuating reaction conditions unraveled by operando spectroscopy”. In: *Journal of Catalysis* 327.0 (2015), pp. 48–53. ISSN: 0021-9517. DOI: 10.1016/j.jcat.2015.04.006.
- [100] Benjamin Mutz et al. “Surface Oxidation of Supported Ni Particles and Its Impact on the Catalytic Performance during Dynamically Operated Methanation of CO₂”. In: *Catalysts* 7.9 (2017). ISSN: 2073-4344. DOI: 10.3390/catal7090279.
- [101] Benjamin Mutz et al. “Operando Raman spectroscopy on CO₂ methanation over alumina-supported Ni, Ni₃Fe and NiRh_{0.1} catalysts: Role of carbon formation as possible deactivation pathway”. In: *Applied Catalysis A: General* 556 (2018), pp. 160–171. ISSN: 0926-860X. DOI: <https://doi.org/10.1016/j.apcata.2018.01.026>.
- [102] Jianguo Xu and Gilbert F. Froment. “Methane steam reforming, methanation and water-gas shift: I. Intrinsic kinetics”. In: *AIChE Journal* 35.1 (1989), pp. 88–96. ISSN: 1547-5905. DOI: 10.1002/aic.690350109.

- [103] G. G. Binder and R. R. White. “Synthesis of methane from carbon dioxide and hydrogen”. In: *Chemical Engineering Process* 46.11 (1950), pp. 563–574.
- [104] T. van Herwijnen, H. van Doesburg, and De Jong, W. A. “Kinetics of the methanation of CO and CO₂ on a nickel catalyst”. In: *Journal of Catalysis* 28.3 (1973), pp. 391–402. ISSN: 0021-9517. DOI: 10.1016/0021-9517(73)90132-2.
- [105] H. Inoue and M. Funakoshi. “Kinetics of methanation of carbon monoxide and carbon dioxide”. In: *Journal of Chemical Engineering of Japan* 17.6 (1984), pp. 602–610. DOI: 10.1252/jcej.17.602.
- [106] Takami Kai, Takeshige Takahashi, and Shintaro Furusaki. “Kinetics of the methanation of carbon dioxide over a supported Ni-La₂O₃ catalyst”. In: *The Canadian Journal of Chemical Engineering* 66.2 (1988), pp. 343–347. ISSN: 1939-019X. DOI: 10.1002/cjce.5450660226.
- [107] M. Šolc. “Kinetik der hydrierung des kohlendioxyds zu methan an einem nickel-chrom(III)-oxyd-katalysator”. In: *Collection of Czechoslovak Chemical Communications* 27.11 (1962), pp. 2621–2627. ISSN: 0010-0765. DOI: 10.1135/cccc19622621.
- [108] Klaus Kaltenmaier. “Untersuchungen zur Kinetik der Methanisierung von CO₂-reichen Gasen bei höheren Drücken”. PhD thesis. Karlsruhe: Universität Karlsruhe (TH), 1988.
- [109] Dominik Schollenberger. “Nutzung von Wabenreaktoren zur Methanisierung bei PtG-Prozessen”. MA thesis. Karlsruhe: Karlsruher Institut für Technologie (KIT), 2013.
- [110] Jin Yang Lim et al. “Kinetic studies of CO₂ methanation over a Ni/Al₂O₃ catalyst using a batch reactor”. In: *Chemical Engineering Science* 141 (2016), pp. 28–45. ISSN: 0009-2509. DOI: 10.1016/j.ces.2015.10.026.
- [111] Z. A. Ibraeva et al. “Kinetics of methanation of carbon dioxide on a nickel catalyst”. In: *Theoretical and Experimental Chemistry* 26.5 (1991), pp. 584–588. ISSN: 0040-5760. DOI: 10.1007/BF00531916.
- [112] R. A. Hubble, J. Y. Lim, and J. S. Dennis. “Kinetic studies of CO₂ methanation over a Ni/[gamma]-Al₂O₃ catalyst”. In: *Faraday Discussions* 192.0 (2016), pp. 529–544. ISSN: 1359-6640. DOI: 10.1039/C6FD00043F.
- [113] S. Rönsch and A. Ortwein. “Methanisierung von Synthesegasen - Grundlagen und Verfahrensentwicklungen”. In: *Chemie Ingenieur Technik* 83.8 (2011), pp. 1200–1208. ISSN: 1522-2640. DOI: 10.1002/cite.201100013.
- [114] J. P. Strakey, A. J. Forney, and W. P. Haynes. *Methanation in coal gasification processes*. 1.01.1975.
- [115] John M. Panek and John Grasser. *Practical Experience Gained During the First Twenty Years of Operation of the Great Plains Gasification Plant and Implications for Future Projects*. 2006.
- [116] Bernd Höhle. *Methanation pilot plant ADAM I (NFE project) and other methanation pilot plants*. Zentralbibliothek d. Kernforschungsanlage Jülich GmbH, 1978.
- [117] Hans Harms, Bernd Höhle, and Allan Skov. “Methanisierung kohlenmonoxidreicher Gase beim Energie-Transport”. In: *Chemie Ingenieur Technik* 52.6 (1980), pp. 504–515. ISSN: 1522-2640.

- [118] W. P. Haynes and A. J. Forney. *High BTU gas from coal: Status and prospects*. 1.01.1976.
- [119] R. Lohmüller. *Methansynthese mit kombinierten isothermen und adiabaten Reaktoren*. 1977.
- [120] M. Buxbaum. “Methanisierungsreaktor”. Pat. DE102011121930A1. 2013.
- [121] David Schlereth, Philipp J. Donaubauer, and Olaf Hinrichsen. “Metallic Honeycombs as Catalyst Supports for Methanation of Carbon Dioxide”. In: *Chemical Engineering & Technology* 38.10 (2015), pp. 1845–1852. ISSN: 1521-4125. DOI: 10.1002/ceat.201400717.
- [122] Choji Fukuhara et al. “A novel nickel-based structured catalyst for CO₂ methanation: A honeycomb-type Ni/CeO₂ catalyst to transform greenhouse gas into useful resources”. In: *Applied Catalysis A: General* 532 (2017), pp. 12–18. ISSN: 0926-860X. DOI: 10.1016/j.apcata.2016.11.036.
- [123] C. Janke et al. “Catalytic and adsorption studies for the hydrogenation of CO₂ to methane”. In: *Applied Catalysis B: Environmental* 152–153.0 (2014), pp. 184–191. ISSN: 0926-3373. DOI: 10.1016/j.apcatb.2014.01.016.
- [124] O. Görke, P. Pfeifer, and K. Schubert. “Highly selective methanation by the use of a microchannel reactor”. In: *Catalytic Microstructured Reactors Catalytic Microstructured Reactors* 110.1--2 (2005), pp. 132–139. ISSN: 0920-5861. DOI: 10.1016/j.cattod.2005.09.009.
- [125] Kriston P. Brooks et al. “Methanation of carbon dioxide by hydrogen reduction using the Sabatier process in microchannel reactors”. In: *Chemical Engineering Science* 62.4 (2007), pp. 1161–1170. ISSN: 0009-2509. DOI: 10.1016/j.ces.2006.11.020.
- [126] Zhihong Liu et al. “Total methanation of syngas to synthetic natural gas over Ni catalyst in a micro-channel reactor”. In: *Fuel* 95 (2012), pp. 599–605. ISSN: 0016-2361. DOI: 10.1016/j.fuel.2011.12.045.
- [127] K. Müller et al. “Sabatier-based CO₂-methanation by catalytic conversion”. In: *Environmental Earth Sciences* (2013). ISSN: 1866-6280. DOI: 10.1007/s12665-013-2609-3.
- [128] Andreas Borgschulte et al. “Sorptions enhanced CO₂ methanation”. In: *Phys. Chem. Chem. Phys.* 15.24 (2013), pp. 9620–9625. ISSN: 1463-9076. DOI: 10.1039/C3CP51408K.
- [129] Stéphane Walspurger et al. “Sorptions enhanced methanation for substitute natural gas production: Experimental results and thermodynamic considerations”. In: *Chemical Engineering Journal* 242.0 (2014), pp. 379–386. ISSN: 1385-8947. DOI: 10.1016/j.cej.2013.12.045.
- [130] Joachim Werther. “Fluidized-Bed Reactors”. In: *Ullmann’s Encyclopedia of Industrial Chemistry*. Weinheim, Germany: Wiley-VCH Verlag GmbH & Co. KGaA, 2000. ISBN: 9783527306732. DOI: 10.1002/14356007.b04_239.pub2.
- [131] Martin C. Seemann, Tilman J. Schildhauer, and Biollaz, Serge M. A. “Fluidized Bed Methanation of Wood-Derived Producer Gas for the Production of Synthetic Natural Gas”. In: *Ind. Eng. Chem. Res.* 49.15 (2010), pp. 7034–7038. ISSN: 0888-5885. DOI: 10.1021/ie100510m.

- [132] Jan Kopyscinski, Tilman J. Schildhauer, and Serge M.A. Biollaz. “Methanation in a fluidized bed reactor with high initial CO partial pressure: Part I—Experimental investigation of hydrodynamics, mass transfer effects, and carbon deposition”. In: *Chemical Engineering Science* 66.5 (2011), pp. 924–934. ISSN: 0009-2509. DOI: 10.1016/j.ces.2010.11.042.
- [133] D.B Blum, M.B Sherwin, and M.E Frank. “Liquid phase methanation of high concentration CO synthesis gas”. In: *Journal Name: Am. Chem. Soc., Div. Fuel Chem., Prepr.; (United States); Journal Volume: 19:3* (1974), Medium: X; Size: Pages: 44–56.
- [134] J. W. Martin. *Liquid-phase methanation/shift process development—final technical report*. 1.01.1982.
- [135] Jonathan Lefebvre et al. “Improvement of three-phase methanation reactor performance for steady-state and transient operation”. In: *Fuel Processing Technology* 132.0 (2015), pp. 83–90. ISSN: 0378-3820. DOI: 10.1016/j.fuproc.2014.10.040.
- [136] N. G. Deen et al. “Bubble Columns”. In: *Ullmann’s Encyclopedia of Industrial Chemistry*. Weinheim, Germany: Wiley-VCH Verlag GmbH & Co. KGaA, 2000. ISBN: 9783527306732. DOI: 10.1002/14356007.b04_275.pub2.
- [137] Stoyan Nedeltchev and Adrian Schumpe. “Slurry Reactors”. In: *Handbook of Heterogeneous Catalysis*. Wiley-VCH Verlag GmbH & Co. KGaA, 2008. ISBN: 9783527610044. DOI: 10.1002/9783527610044.hetcat0113.
- [138] Manuel Götz et al. “Hydrodynamics of organic and ionic liquids in a slurry bubble column reactor operated at elevated temperatures”. In: *Chemical Engineering Journal* 286 (2016), pp. 348–360. ISSN: 1385-8947. DOI: 10.1016/j.cej.2015.10.044.
- [139] Wolf-Dieter Deckwer. *Reaktionstechnik in Blasensäulen*. 1. Aufl. Grundlagen der chemischen Technik. Frankfurt am Main and Aarau: Salle and Sauerländer, 1985. ISBN: 978-3-79-355540-7.
- [140] Philipp Rollbusch et al. “Bubble columns operated under industrial relevant conditions -- current understanding of design parameters”. In: *Chemical Engineering Science* (2014). ISSN: 0009-2509. DOI: 10.1016/j.ces.2014.11.061.
- [141] R. V. Chaudhari and P. A. Ramachandran. “Three phase slurry reactors”. In: *AIChE Journal* 26.2 (1980), pp. 177–201. ISSN: 1547-5905. DOI: 10.1002/aic.690260202.
- [142] Omar M. Basha et al. “Fischer--Tropsch Synthesis in Slurry Bubble Column Reactors: Experimental Investigations and Modeling -- A Review: Review”. In: *International Journal of Chemical Reactor Engineering* 13.3 (2015). DOI: 10.1515/ijcre-2014-0146.
- [143] Behnam Khadem-Hamedani et al. “Mathematical modeling of a slurry bubble column reactor for hydrodesulfurization of diesel fuel: Single- and two-bubble configurations”. In: *Chemical Engineering Research and Design* 100 (2015), pp. 362–376. ISSN: 0263-8762. DOI: 10.1016/j.cherd.2015.05.023.
- [144] J.W.A. de Swart and R. Krishna. “Simulation of the transient and steady state behaviour of a bubble column slurry reactor for Fischer--Tropsch synthesis”. In: *Chemical Engineering and Processing: Process Intensification* 41.1 (2002), pp. 35–47. ISSN: 0255-2701. DOI: 10.1016/S0255-2701(00)00159-8.

- [145] Kozo Koide et al. “Critical Gas Velocity Required For Complete Suspension Of Solid Particles In Solid-Suspended Bubble Columns”. In: *Journal of Chemical Engineering of Japan* 16 (1983), pp. 7–12.
- [146] Holger Martin. “Wärme- und Stoffübertragung in der Wirbelschicht”. In: *Chemie Ingenieur Technik* 52.3 (1980), pp. 199–209. ISSN: 1522-2640. DOI: 10.1002/cite.330520303.
- [147] Y. T. Shah, G. J. Stiegel, and M. M. Sharma. “Backmixing in gas-liquid reactors”. In: *AIChE Journal* 24.3 (1978), pp. 369–400. ISSN: 00011541. DOI: 10.1002/aic.690240302.
- [148] T. Reith, S. Renken, and B. A. Israël. “Gas hold-up and axial mixing in the fluid phase of bubble columns”. In: *17th International Symposium of Chemical Reaction Engineering (IS CRE 17)* 23.6 (1968), pp. 619–629. ISSN: 0009-2509. DOI: 10.1016/0009-2509(68)89007-4.
- [149] Yoshihiro Ohki and HAKUAI INOUE. “Longitudinal mixing of the liquid phase in bubble columns”. In: *17th International Symposium of Chemical Reaction Engineering (IS CRE 17)* 25.1 (1970), pp. 1–16. ISSN: 0009-2509. DOI: 10.1016/0009-2509(70)85016-3.
- [150] Y. Kato. “Longitudinal dispersion coefficient of a liquid in a bubble column”. In: *International Chemical Engineering* 12.1 (1972), pp. 182–187.
- [151] G. D. Towell and G. H. Ackerman, eds. *Axial mixing of liquid and gas in large bubble reactors*. 1972.
- [152] Kiyomi Akita and Fumitake Yoshida. “Gas Holdup and Volumetric Mass Transfer Coefficient in Bubble Columns. Effects of Liquid Properties”. In: *Industrial & Engineering Chemistry Process Design and Development* 12.1 (1973), pp. 76–80. ISSN: 0196-4305. DOI: 10.1021/i260045a015.
- [153] Reiner Badura et al. “Durchmischung in Blasensäulen”. In: *Chemie Ingenieur Technik* 46.9 (1974), p. 399. ISSN: 1522-2640. DOI: 10.1002/cite.330460909.
- [154] H. Hikita and H. Kikukawa. “Liquid-phase mixing in bubble columns: Effect of liquid properties”. In: *The Chemical Engineering Journal* 8.3 (1974), pp. 191–197. ISSN: 0300-9467. DOI: 10.1016/0300-9467(74)85024-0.
- [155] W.-D. Deckwer, R. Burckhart, and G. Zoll. “Mixing and mass transfer in tall bubble columns”. In: *17th International Symposium of Chemical Reaction Engineering (IS CRE 17)* 29.11 (1974), pp. 2177–2188. ISSN: 0009-2509. DOI: 10.1016/0009-2509(74)80025-4.
- [156] Novica Rados, Muthanna H. Al-Dahhan, and Milorad P. Dudukovic. “Modeling of the Fischer–Tropsch synthesis in slurry bubble column reactors”. In: *Catalysis Today* 79-80 (2003), pp. 211–218. ISSN: 0920-5861. DOI: 10.1016/S0920-5861(03)00007-5.
- [157] S. D. Kim, C. G. I. Baker, and M. A. Bergougnou. “Phase holdup characteristics of three phase fluidized beds”. In: *The Canadian Journal of Chemical Engineering* 53.1 (1975), pp. 134–139. ISSN: 1939-019X. DOI: 10.1002/cjce.5450530126.

- [158] Masao Kito, Koichi Tabei, and Koichi Murata. “Gas and Liquid Holdups in Mobile Beds under the Countercurrent Flow of Air and Liquid”. In: *Ind. Eng. Chem. Proc. Des. Dev.* 17.4 (1978), pp. 568–571. ISSN: 0196-4305. DOI: 10.1021/i260068a030.
- [159] J. B. Joshi and M. M. Sharma. “A Circulation Cell Model for Bubble Columns”. In: *Trans IChemE* 57 (1979), pp. 244–252.
- [160] Kozo Koide et al. “Gas holdup and volumetric liquid-phase mass transfer coefficient in solid-suspended bubble columns”. In: *Journal of Chemical Engineering of Japan* 17.5 (1984), pp. 459–466.
- [161] D. N. SMITH et al. “Bubble Behavior in a Slurry Bubble Column Reactor Model”. In: *Chemical and Catalytic Reactor Modeling*. Ed. by Milorad P. Duduković and Patrick L. Mills. Vol. 237. ACS Symposium Series. Washington, D.C.: American Chemical Society, 1984, pp. 125–147. ISBN: 0-8412-0815-8. DOI: 10.1021/bk-1984-0237.ch008.
- [162] I. G. Reilly et al. “A correlation for gas holdup in turbulent coalescing bubble columns”. In: *The Canadian Journal of Chemical Engineering* 64.5 (1986), pp. 705–717. ISSN: 1939-019X. DOI: 10.1002/cjce.5450640501.
- [163] Dragomir B. Bukur and James G. Daly. “Gas hold-up in bubble columns for Fischer-Tropsch synthesis”. In: *17th International Symposium of Chemical Reaction Engineering (IS CRE 17)* 42.12 (1987), pp. 2967–2969. ISSN: 0009-2509. DOI: 10.1016/0009-2509(87)87064-1.
- [164] S. L. P. Lee and H. I. de Lasa. “Phase holdups in three-phase fluidized beds”. In: *AIChE Journal* 33.8 (1987), pp. 1359–1370. ISSN: 00011541. DOI: 10.1002/aic.690330813.
- [165] Thomas Sauer and Dietmar-Christian Hempel. “Fluid dynamics and mass transfer in a bubble column with suspended particles”. In: *Chemical Engineering & Technology - CET* 10.1 (1987), pp. 180–189. ISSN: 0930-7516. DOI: 10.1002/ceat.270100123.
- [166] A. Schumpe, A. K. Saxena, and L. K. Fang. “Gas/liquid mass transfer in a slurry bubble column”. In: *17th International Symposium of Chemical Reaction Engineering (IS CRE 17)* 42.7 (1987), pp. 1787–1796. ISSN: 0009-2509. DOI: 10.1016/0009-2509(87)80183-5.
- [167] L.-S. Fan et al. “Some aspects of high-pressure phenomena of bubbles in liquids and liquid–solid suspensions”. In: *17th International Symposium of Chemical Reaction Engineering (IS CRE 17)* 54.21 (1999), pp. 4681–4709. ISSN: 0009-2509. DOI: 10.1016/S0009-2509(99)00348-6.
- [168] R. Krishna and S. T. Sie. “Design and scale-up of the Fischer–Tropsch bubble column slurry reactor”. In: *2012 International Workshop on Clean Technologies of Coal and Biomass Utilization* 64.1-3 (2000), pp. 73–105. ISSN: 0378-3820. DOI: 10.1016/S0378-3820(99)00128-9.
- [169] Chia-Min Chen and Lii-Ping Leu. “Hydrodynamics and mass transfer in three-phase magnetic fluidized beds”. In: *Powder Technology* 117.3 (2001), pp. 198–206. ISSN: 0032-5910. DOI: 10.1016/S0032-5910(00)00370-3.
- [170] K. Ramesh and T. Murugesan. “Minimum fluidization velocity and gas holdup in gas-liquid-solid fluidized bed reactors”. In: *Journal of Chemical Technology & Biotechnology* 77.2 (2002), pp. 129–136. ISSN: 1097-4660. DOI: 10.1002/jctb.533.

- [171] Arsam Behkish et al. “Novel correlations for gas holdup in large-scale slurry bubble column reactors operating under elevated pressures and temperatures”. In: *Chemical Engineering Journal* 115.3 (2006), pp. 157–171. ISSN: 1385-8947. DOI: 10.1016/j.cej.2005.10.006.
- [172] H. M. Jena, G. K. Roy, and B. C. Meikap. “Prediction of gas holdup in a three-phase fluidized bed from bed pressure drop measurement”. In: *Chemical Engineering Research and Design* 86.11 (2008), pp. 1301–1308. ISSN: 0263-8762. DOI: 10.1016/j.cherd.2008.05.007.
- [173] V. Sivakumar, K. Senthilkumar, and T. Kannadasan. “Prediction of gas holdup in the three-phase fluidized bed: Air/Newtonian and non-Newtonian liquid systems”. In: *Polish Journal of Chemical Technology* 12.4 (2010). ISSN: 1899-4741. DOI: 10.2478/v10026-010-0053-7.
- [174] Laurent Sehabiague and Badie I. Morsi. “Hydrodynamic and Mass Transfer Characteristics in a Large-Scale Slurry Bubble Column Reactor for Gas Mixtures in Actual Fischer–Tropsch Cuts”. In: *International Journal of Chemical Reactor Engineering* 11.1 (2013), pp. 1–20. DOI: 10.1515/ijcre-2012-0042.
- [175] Manuel Götz et al. “Novel gas holdup correlation for slurry bubble column reactors operated in the homogeneous regime”. In: *Chemical Engineering Journal* 308 (2017), pp. 1209–1224. ISSN: 1385-8947. DOI: 10.1016/j.cej.2016.09.101.
- [176] Nigar Kantarci, Fahir Borak, and Kutlu O. Ulgen. “Bubble column reactors: Review”. In: *Process Biochemistry* 40.7 (2005), pp. 2263–2283. ISSN: 13595113. DOI: 10.1016/j.procbio.2004.10.004.
- [177] Wolfgang Gestrich, Helmut Esenwein, and Werner Krauss. “Der flüssigkeitsseitige Stoffübergangskoeffizient in Blasenschichten”. In: *Chemie Ingenieur Technik* 48.5 (1976), pp. 399–407. ISSN: 1522-2640. DOI: 10.1002/cite.330480509.
- [178] Miki Fukuma, Katsuhiko Muroyama, and Akira Yasunishi. “Specific gas-liquid interfacial area and liquid-phase mass transfer coefficient in a slurry bubble column”. In: *Journal of Chemical Engineering of Japan* 20.3 (1987), pp. 321–324. ISSN: 1881-1299. DOI: 10.1252/jcej.20.321.
- [179] Jonathan L. Salvacion et al. “Effects of alcohols on gas holdup and volumetric liquid-phase mass transfer coefficient in gel-particle-suspended bubble column”. In: *JOURNAL OF CHEMICAL ENGINEERING OF JAPAN* 28.4 (1995), pp. 434–442. ISSN: 0021-9592. DOI: 10.1252/jcej.28.434.
- [180] P. H. Calderbank and M. B. Moo-Young. “The continuous phase heat and mass transfer properties of dispersions”. In: *17th International Symposium of Chemical Reaction Engineering (IS CRE 17)* 50.24 (1995), pp. 3921–3934. ISSN: 0009-2509. DOI: 10.1016/0009-2509(96)81823-9.
- [181] Gonzalo Vázquez et al. “Surface Tension of Binary Mixtures of Water + Monoethanolamine and Water + 2-Amino-2-methyl-1-propanol and Tertiary Mixtures of These Amines with Water from 25 °C to 50 °C”. In: *J. Chem. Eng. Data* 42.1 (1997), pp. 57–59. ISSN: 0021-9568. DOI: 10.1021/je960238w.

- [182] I. Dewes and A. Schumpe. “Gas density effect on mass transfer in the slurry bubble column”. In: *Chemical Engineering Science* 52.21-22 (1997), pp. 405–4109. ISSN: 0009-2509.
- [183] Favio Neme, Liliana Coppola, and Ursula Böhm. “Gas holdup and mass transfer in solid suspended bubble columns in presence of structured packings”. In: *Chemical Engineering & Technology - CET* 20.5 (1997), pp. 297–303. ISSN: 0930-7516. DOI: 10.1002/ceat.270200503.
- [184] Y.X Guo, M.N Rathor, and H.C Ti. “Hydrodynamics and mass transfer studies in a novel external-loop airlift reactor”. In: *Catalytic Reaction and Reactor Engineering EuropaCat V Limerick, Sept 2-7 2001* 67.3 (1997), pp. 205–214. ISSN: 1385-8947. DOI: 10.1016/S1385-8947(97)00043-0.
- [185] Weiguo Yang, J. Wang, and Y. Jin. “Mass Transfer Characteristics of Syn-gas Components in Slurry System at Industrial Conditions”. In: *Chemical Engineering & Technology - CET* 24.6 (2001), pp. 651–657. ISSN: 0930-7516. DOI: 10.1002/1521-4125(200106)24:6<651::AID-CEAT651>3.0.CO;2-X.
- [186] Romain Lemoine et al. “An algorithm for predicting the hydrodynamic and mass transfer parameters in bubble column and slurry bubble column reactors”. In: *Fuel Processing Technology* 89.4 (2008), pp. 322–343. ISSN: 0378-3820. DOI: 10.1016/j.fuproc.2007.11.016.
- [187] Stoyan Nedeltchev and Adrian Schumpe. “New Approaches for Theoretical Estimation of Mass Transfer Parameters in Both Gas-Liquid and Slurry Bubble Columns”. In: *Mass Transfer in Steelmaking Operations*. Ed. by Roberto Parreiras Tavares. INTECH Open Access Publisher, 2011. ISBN: 978-953-307-215-9. DOI: 10.5772/14721.
- [188] C.G.J. Baker, E. R. Armstrong, and M. A. Bergougnou. “Heat transfer in three-phase fluidized beds”. In: *Powder Technology* 21.2 (1978), pp. 195–204. ISSN: 0032-5910. DOI: 10.1016/0032-5910(78)80089-8.
- [189] W.-D. Deckwer. “On the mechanism of heat transfer in bubble column reactors”. In: *17th International Symposium of Chemical Reaction Engineering (IS CRE 17)* 35.6 (1980), pp. 1341–1346. ISSN: 0009-2509. DOI: 10.1016/0009-2509(80)85127-X.
- [190] Y. Kato et al. “Liquid holdup and heat transfer coefficient between bed and wall in liquid solid and gas-liquid-solid fluidized beds”. In: *Powder Technology* 28.2 (1981), pp. 173–179. ISSN: 0032-5910. DOI: 10.1016/0032-5910(81)87040-4.
- [191] Tai-Ming Chiu and E. N. Ziegler. “Heat transfer in three-phase fluidized beds”. In: *AIChE Journal* 29.4 (1983), pp. 677–685. ISSN: 1547-5905. DOI: 10.1002/aic.690290424.
- [192] K. Muroyama, M. Fukuma, and A. Yasunishi. “Wall-to-bed heat transfer coefficient in gas-liquid-solid fluidized beds”. In: *The Canadian Journal of Chemical Engineering* 62.2 (1984), pp. 199–208. ISSN: 1939-019X. DOI: 10.1002/cjce.5450620207.
- [193] Tai-Ming Chiu and E. N. Ziegler. “Liquid holdup and heat transfer coefficient in liquid-solid and three-phase fluidized beds”. In: *AIChE Journal* 31.9 (1985), pp. 1504–1509. ISSN: 1547-5905. DOI: 10.1002/aic.690310913.

- [194] M. Saberian-Broudjenni et al. “Contribution à l’étude du transfert de chaleur à la paroi dans les réacteurs à lit fluidisé gaz-liquide-solide à faible vitesse de liquide”. In: *The Canadian Journal of Chemical Engineering* 63.4 (1985), pp. 553–564. ISSN: 1939-019X. DOI: 10.1002/cjce.5450630405.
- [195] I. S. Suh, G. T. Jin, and S. D. Kim. “Heat transfer coefficients in three phase fluidized beds”. In: *International Journal of Multiphase Flow* 11.2 (1985), pp. 255–259. ISSN: 03019322. DOI: 10.1016/0301-9322(85)90049-7.
- [196] S. D. Kim, Y. Kang, and H. K. Kwon. “Heat transfer characteristics in two- and three-phase slurry-fluidized beds”. In: *AIChE Journal* 32.8 (1986), pp. 1397–1400. ISSN: 1547-5905. DOI: 10.1002/aic.690320820.
- [197] Maria Magiliotou, Ye-Mon Chen, and Liang-Shih Fan. “Bed-immersed object heat transfer in a three-phase fluidized bed”. In: *AIChE Journal* 34.6 (1988), pp. 1043–1047. ISSN: 1547-5905. DOI: 10.1002/aic.690340620.
- [198] Jong O. Kim, Dae H. Park, and Sang D. Kim. “Heat transfer and wake characteristics in three-phase fluidized beds with floating bubble breakers”. In: *Chemical Engineering and Processing: Process Intensification* 28.2 (1990), pp. 113–119. ISSN: 0255-2701. DOI: 10.1016/0255-2701(90)80007-R.
- [199] A. Zaidi et al. “Hydrodynamics and heat transfer in three-phase fluidized beds with highly viscous pseudoplastic solutions”. In: *17th International Symposium of Chemical Reaction Engineering (IS CRE 17)* 45.8 (1990), pp. 2235–2238. ISSN: 0009-2509. DOI: 10.1016/0009-2509(90)80100-S.
- [200] S. C. Saxena, N. S. Rao, and A. C. Saxena. “Estimation of heat transfer coefficient for immersed surfaces in bubble columns involving fine powders”. In: *Powder Technology* 63.2 (1990), pp. 197–202. ISSN: 0032-5910. DOI: 10.1016/0032-5910(90)80042-W.
- [201] Samir Kumar and L.-S. Fan. “Heat-transfer characteristics in viscous gas-liquid and gas-liquid-solid systems”. In: *AIChE Journal* 40.5 (1994), pp. 745–755. ISSN: 1547-5905. DOI: 10.1002/aic.690400502.
- [202] G. Q. Yang et al. “Heat-Transfer Characteristics in Slurry Bubble Columns at Elevated Pressures and Temperatures”. In: *Ind. Eng. Chem. Res.* 39.7 (2000), pp. 2568–2577. ISSN: 0888-5885. DOI: 10.1021/ie990774s.
- [203] Patnail, K. S. K. R., ed. *Heat transfer coefficients in three-phase sparged reactors: A unified correlation*. 2007.
- [204] Manuel Götz et al. “Evaluation of Organic and Ionic Liquids for Three-Phase Methanation and Biogas Purification Processes”. In: *Energy & Fuels* 27.8 (2013), pp. 4705–4716. ISSN: 0887-0624. DOI: 10.1021/ef400334p.
- [205] Reinhard Otten. “Das Audi e-gas-Projekt: Die Energiewende im CNG-Tank”. In: *13. Erdgas Mobil Symposium*. Audi AG. Berlin, May 2013.
- [206] Simone Nagel. “Untersuchung der Reaktionskinetik der CO₂-Methanisierung in einem Slurry-Reaktor”. MA thesis. Karlsruhe: Karlsruher Institut für Technologie (KIT), 2015.

- [207] Jonathan Lefebvre et al. “A study on three-phase CO₂ methanation reaction kinetics in a continuous stirred-tank slurry reactor”. In: *Fuel* 217 (2018), pp. 151–159. ISSN: 0016-2361. DOI: 10.1016/j.fuel.2017.12.082.
- [208] Ding-Yu Peng and Donald B. Robinson. “A New Two-Constant Equation of State”. In: *Industrial & Engineering Chemistry Fundamentals* 15.1 (1976), pp. 59–64. DOI: 10.1021/i160057a011.
- [209] Kenneth S. Pitzer. *Molecular structure and statistical thermodynamics: Selected papers of Kenneth S. Pitzer*. Vol. vol. 1. World Scientific series in 20th century chemistry. Singapore: World Scientific Pub. Co, 1993. ISBN: 9812795960.
- [210] C. C. Chappelow and J. M. Prausnitz. “Solubilities of gases in high-boiling hydrocarbon solvents”. In: *AIChE Journal* 20.6 (1974), pp. 1097–1104. ISSN: 1547-5905. DOI: 10.1002/aic.690200606.
- [211] Geert H. Graaf et al. “Gas-liquid solubilities of the methanol synthesis components in various solvents”. In: *J. Chem. Eng. Data* 37.2 (1992), pp. 146–158. ISSN: 0021-9568. DOI: 10.1021/je00006a004.
- [212] Daniela Kerlé. “Untersuchung der Löslichkeit von Gasen in ionischen Flüssigkeiten mit Methoden der Molekulardynamischen Simulation”. PhD thesis. Rostock: Universität Rostock, 2013.
- [213] C. Reichardt and T. Welton. *Solvents and solvent effects in organic chemistry*. 4. ed. Wiley-VCH Verlag GmbH, 2011. ISBN: 978-3-527-63222-0.
- [214] J.M Prausnitz, R.N Lichtenthaler, and E. deG. Azevedo. *Molecular thermodynamics of fluid-phase equilibria*. 3. ed. Upper Saddle River: Prentice Hall, 1999. ISBN: 0139777458.
- [215] Svenja Heling. “Investigation of the limiting processes involved in three-phase methanation”. MA thesis. Karlsruhe: Karlsruher Institut für Technologie (KIT), 2014.
- [216] J. Francis et al. “Design of improved hydrocracking catalysts by increasing the proximity between acid and metallic sites”. In: *Applied Catalysis A: General* 409–410.0 (2011), pp. 140–147. ISSN: 0926-860X. DOI: 10.1016/j.apcata.2011.09.040.
- [217] S. Toppinen et al. “Liquid-Phase Hydrogenation Kinetics of Aromatic Hydrocarbon Mixtures”. In: *Ind. Eng. Chem. Res.* 36.6 (1997), pp. 2101–2109. ISSN: 0888-5885. DOI: 10.1021/ie960263v.
- [218] Xin Qin et al. “Interaction between metal and support: Effects of support acidity on adspecies of co over Ru”. In: *Reaction Kinetics and Catalysis Letters* 31.2 (1986), pp. 279–283. ISSN: 0133-1736. DOI: 10.1007/BF02072957.
- [219] Min Hye Youn et al. “Hydrogen production by auto-thermal reforming of ethanol over nickel catalysts supported on metal oxides: Effect of support acidity”. In: *Applied Catalysis B: Environmental* 98.1–2 (2010), pp. 57–64. ISSN: 0926-3373. DOI: 10.1016/j.apcatb.2010.05.002.
- [220] Antonymuthu Stanislaus and Barry H. Cooper. “Aromatic Hydrogenation Catalysis: A Review”. In: *Catalysis Reviews* 36.1 (1994), pp. 75–123. DOI: 10.1080/01614949408013921.

- [221] R. J. Madon, J. P. O'Connell, and Michel Boudart. "Catalytic hydrogenation of cyclohexene: Part II. Liquid phase reaction on supported platinum in a gradientless slurry reactor". In: *AIChE Journal* 24.5 (1978), pp. 904–911. ISSN: 1547-5905. DOI: 10.1002/aic.690240516.
- [222] E. E. Gonzo and M. Boudart. "Catalytic hydrogenation of cyclohexene: Gas-phase and liquid-phase reaction on supported palladium". In: *Journal of Catalysis* 52.3 (1978), pp. 462–471. ISSN: 0021-9517. DOI: 10.1016/0021-9517(78)90352-4.
- [223] Iglesias G. , M. et al. "Chemical energy storage in gaseous hydrocarbons via iron Fischer-Tropsch synthesis from H₂/CO₂: Kinetics, selectivity and process considerations". In: *Catalysis Today* 242, Part A (2015), pp. 184–192. ISSN: 0920-5861. DOI: 10.1016/j.cattod.2014.05.020.
- [224] Hilko Eilers, Maria Iglesias González, and Georg Schaub. "Lab-scale experimental studies of Fischer--Tropsch kinetics in a three-phase slurry reactor under transient reaction conditions". In: *Syngas Convention – Fuels and Chemicals from Synthesis Gas: State of the Art 2* 275 (2016), pp. 164–171. ISSN: 0920-5861. DOI: 10.1016/j.cattod.2015.11.011.
- [225] G. H. Graaf et al. "Kinetics of the three phase methanol synthesis". In: *Chemical Engineering Science* 43.8 (1988), pp. 2161–2168. ISSN: 0009-2509. DOI: 10.1016/0009-2509(88)87098-2.
- [226] G. H. Graaf, E. J. Stamhuis, and A.A.C.M. Beenackers. "Kinetics of low-pressure methanol synthesis". In: *Chemical Engineering Science* 43.12 (1988), pp. 3185–3195. ISSN: 0009-2509. DOI: 10.1016/0009-2509(88)85127-3.
- [227] Daniel Safai. "Katalysatorenscreening für die Dreiphasen-Methanisierung". MA thesis. Karlsruhe: Karlsruher Institut für Technologie (KIT), 2014.
- [228] Nike Trudel. "Bestimmung der Reaktionskinetik der CO₂-Methanisierung in einem Slurry-Reaktor". MA thesis. Karlsruhe: Karlsruher Institut für Technologie, 2016.
- [229] Ulli Hammann. "Untersuchung des Einflusses einer Suspensionsflüssigkeit auf die Reaktionskinetik der CO₂-Methanisierung". MA thesis. Karlsruhe: Karlsruher Institut für Technologie (KIT), 2016.
- [230] C.V. Miguel, A. Mendes, and L.M. Madeira. "Intrinsic kinetics of CO₂ methanation over an industrial nickel-based catalyst". In: *Journal of CO₂ Utilization* 25 (2018), pp. 128–136. ISSN: 2212-9820. DOI: <https://doi.org/10.1016/j.jcou.2018.03.011>.
- [231] W. G. Mallard and P. J. Linstrom. "NIST chemistry webbook". In: *NIST Standard Reference Database* 69 (1998).
- [232] G. H. Graaf et al. "Chemical equilibria in methanol synthesis". In: *Chemical Engineering Science* 41.11 (1986), pp. 2883–2890. ISSN: 0009-2509. DOI: 10.1016/0009-2509(86)80019-7.
- [233] Jonathan Lefebvre, Siegfried Bajohr, and Thomas Kolb. "A comparison of two-phase and three-phase CO₂ methanation reaction kinetics". In: *Fuel* 239 (2019), pp. 896–904. ISSN: 0016-2361. DOI: <https://doi.org/10.1016/j.fuel.2018.11.051>.

- [234] María Iglesias González. “Gaseous Hydrocarbon Synfuels from H₂/CO₂ based on Renewable Electricity: Kinetics, Selectivity and Fundamentals of Fixed-Bed Reactor Design for Flexible Operation”. PhD thesis. Karlsruhe: Karlsruher Institut für Technologie (KIT), 2015. DOI: 10.5445/IR/1000051662.
- [235] P. B. Weisz and C. D. Prater. “Interpretation of Measurements in Experimental Catalysis”. In: *Advances in Catalysis* 6 (1954), pp. 143–196. ISSN: 0360-0564. DOI: 10.1016/S0360-0564(08)60390-9.
- [236] Anderson, J. B. A. “Criterion for Isothermal Behaviour of a Catalyst Pellet”. In: *Chem. Eng. Sci.* 18 (1963), p. 147.
- [237] Mears, D. E. “Tests for Transport Limitations in Experimental Catalytic Reactors”. In: *Ind. Eng. Chem. Proc. Des. Dev.* 10.4 (1971), pp. 541–547. ISSN: 0196-4305. DOI: 10.1021/i260040a020.
- [238] Evangelos Tsotsas. “M7 Wärmeleitung und Dispersion in durchströmten Schüttungen”. In: *VDI-Wärmeatlas*. Berlin, Heidelberg: Springer Berlin Heidelberg, 2013, pp. 1517–1534. ISBN: 978-3-642-19981-3. DOI: 10.1007/978-3-642-19981-3_102.
- [239] Charles N. Satterfield and George A. Huff. “25 Effects of mass transfer on Fischer-Tropsch synthesis in slurry reactors”. In: *17th International Symposium of Chemical Reaction Engineering (IS CRE 17)* 35.1 (1980), pp. 195–202. ISSN: 0009-2509. DOI: 10.1016/0009-2509(80)80087-X.
- [240] W. D. Deckwer et al. “On the relevance of mass transfer limitations in the Fischer-Tropsch slurry process”. In: *17th International Symposium of Chemical Reaction Engineering (IS CRE 17)* 36.4 (1981), pp. 773–774. ISSN: 0009-2509. DOI: 10.1016/0009-2509(81)85092-0.
- [241] Dragomir B. Bukur. “Some comments on models for Fischer-Tropsch reaction in slurry bubble column reactors”. In: *17th International Symposium of Chemical Reaction Engineering (IS CRE 17)* 38.3 (1983), pp. 440–446. ISSN: 0009-2509. DOI: 10.1016/0009-2509(83)80161-4.
- [242] David Stern, Alexis T. Bell, and Heinz Heinemann. “Effects of mass transfer on the performance of slurry reactors used for fischer-tropsch synthesis”. In: *17th International Symposium of Chemical Reaction Engineering (IS CRE 17)* 38.4 (1983), pp. 597–605. ISSN: 0009-2509. DOI: 10.1016/0009-2509(83)80119-5.
- [243] C. Maretto and R. Krishna. “Modelling of a bubble column slurry reactor for Fischer-Tropsch synthesis”. In: *Catalysis Today* 52.2--3 (1999), pp. 279–289. ISSN: 0920-5861. DOI: 10.1016/S0920-5861(99)00082-6.
- [244] Gerard P. van der Laan, Antonie A. C. M. Beenackers, and Rajamani Krishna. “Multicomponent reaction engineering model for Fe-catalyzed Fischer-Tropsch synthesis in commercial scale slurry bubble column reactors”. In: *Chemical Engineering Science* 54.21 (1999), pp. 5013–5019. ISSN: 0009-2509. DOI: 10.1016/S0009-2509(99)00225-0.
- [245] Hyun-Seob Song et al. “Multiplicity and sensitivity analysis of Fischer-Tropsch bubble column slurry reactors: Plug-flow gas and well-mixed slurry model”. In: *17th International Symposium of Chemical Reaction Engineering (IS CRE 17)* 58.12 (2003), pp. 2759–2766. ISSN: 0009-2509.

- [246] Hyun-Seob Song et al. “Operating strategies for Fischer-Tropsch reactors: A model-directed study”. In: *Korean Journal of Chemical Engineering* 21.2 (2004), pp. 308–317. ISSN: 0256-1115. DOI: 10.1007/BF02705414.
- [247] Fabiano A. N. Fernandes. “Modeling and Product Grade Optimization of Fischer–Tropsch Synthesis in a Slurry Reactor”. In: *Ind. Eng. Chem. Res.* 45.3 (2006), pp. 1047–1057. ISSN: 0888-5885. DOI: 10.1021/ie0507732.
- [248] Yu Wang et al. “Modeling of the Fischer--Tropsch synthesis in slurry bubble column reactors”. In: *Chemical Engineering and Processing: Process Intensification* 47.2 (2008), pp. 222–228. ISSN: 0255-2701. DOI: 10.1016/j.cep.2007.02.011.
- [249] Robert Guettel and Thomas Turek. “Comparison of different reactor types for low temperature Fischer--Tropsch synthesis: A simulation study”. In: *17th International Symposium of Chemical Reaction Engineering (IS CRE 17)* 64.5 (2009), pp. 955–964. ISSN: 0009-2509. DOI: 10.1016/j.ces.2008.10.059.
- [250] Wolf Dieter Deckwer et al. “Modeling the Fischer-Tropsch synthesis in the slurry phase”. In: *Ind. Eng. Chem. Proc. Des. Dev.* 21.2 (1982), pp. 231–241. ISSN: 0196-4305.
- [251] David Stern, Alexis T. Bell, and Heinz Heinemann. “A theoretical model for the performance of bubble-column reactors used for Fischer-Tropsch synthesis”. In: *17th International Symposium of Chemical Reaction Engineering (IS CRE 17)* 40.9 (1985), pp. 1665–1677. ISSN: 0009-2509. DOI: 10.1016/0009-2509(85)80027-0.
- [252] J. R. Turner and P. L. Mills. “Comparison of axial dispersion and mixing cell models for design and simulation of fischer-tropsch slurry bubble column reactors”. In: *17th International Symposium of Chemical Reaction Engineering (IS CRE 17)* 45.8 (1990), pp. 2317–2324. ISSN: 0009-2509. DOI: 10.1016/0009-2509(90)80111-Q.
- [253] A. Prakash. “On the effects of syngas composition and water-gas-shift reaction rate on FT synthesis over iron based catalyst in a slurry reactor”. In: *Chemical Engineering Communications* 128.1 (1994), pp. 143–158. ISSN: 0098-6445.
- [254] Novica Rados, Muthanna H. Al-Dahhan, and Milorad P. Duduković. “Dynamic Modeling of Slurry Bubble Column Reactors”. In: *Industrial & Engineering Chemistry Research* 44.16 (2005), pp. 6086–6094. DOI: 10.1021/ie040227t.
- [255] Laurent Sehabiague et al. “Modeling and optimization of a large-scale slurry bubble column reactor for producing 10,000 t/day of Fischer--Tropsch liquid hydrocarbons: Festschrift Issue In honor of Professor Shiao-Hung Chiang”. In: *Journal of the Chinese Institute of Chemical Engineers* 39.2 (2008), pp. 169–179. ISSN: 0368-1653. DOI: 10.1016/j.jcice.2007.11.003.
- [256] Siavash Seyednejadian et al. “Power to Fuels: Dynamic Modeling of a Slurry Bubble Column Reactor in Lab-Scale for Fischer Tropsch Synthesis under Variable Load of Synthesis Gas”. In: *Applied Sciences* 8.4 (2018). ISSN: 2076-3417. DOI: 10.3390/app8040514.
- [257] K. Rietema. “Science and technology of dispersed two-phase systems---I and II”. In: *17th International Symposium of Chemical Reaction Engineering (IS CRE 17)* 37.8 (1982), pp. 1125–1150. ISSN: 0009-2509. DOI: 10.1016/0009-2509(82)85058-6.

- [258] Peter Zehner. “Impuls-, Stoff- und Wärmetransport in Blasensäulen”. In: *Chemie Ingenieur Technik* 54.3 (1982), pp. 248–251. ISSN: 1522-2640. DOI: 10.1002/cite.330540311.
- [259] Karl G. Anderson and Richard G. Rice. “Local turbulence model for predicting circulation rates in bubble columns”. In: *AIChE Journal* 35.3 (1989), pp. 514–518. ISSN: 1547-5905. DOI: 10.1002/aic.690350321.
- [260] H.-E Gasche et al. “Hydrodynamics in bubble columns”. In: *Chemical Engineering and Processing: Process Intensification* 26.2 (1989), pp. 101–109. ISSN: 0255-2701. DOI: 10.1016/0255-2701(89)90002-0.
- [261] N. N. Clark, J. W. van Egmond, and E. P. Nebiolo. “The drift-flux model applied to bubble columns and low velocity flows”. In: *International Journal of Multiphase Flow* 16.2 (1990), pp. 261–279. ISSN: 03019322. DOI: 10.1016/0301-9322(90)90058-Q.
- [262] Richard G. Rice and Nicholas W. Geary. “Prediction of liquid circulation in viscous bubble columns”. In: *AIChE Journal* 36.9 (1990), pp. 1339–1348. ISSN: 00011541. DOI: 10.1002/aic.690360907.
- [263] N. W. Geary and R. G. Rice. “Circulation in bubble columns: Corrections for distorted bubble shape”. In: *AIChE Journal* 37.10 (1991), pp. 1593–1594. ISSN: 1547-5905. DOI: 10.1002/aic.690371018.
- [264] Nicholas W. Geary and Richard G. Rice. “Circulation and scale-up in bubble columns”. In: *AIChE Journal* 38.1 (1992), pp. 76–82. ISSN: 1547-5905. DOI: 10.1002/aic.690380108.
- [265] J. Grienberger and H. Hofmann. “Investigations and modelling of bubble columns”. In: *17th International Symposium of Chemical Reaction Engineering (IS CRE 17)* 47.9 (1992), pp. 2215–2220. ISSN: 0009-2509. DOI: 10.1016/0009-2509(92)87037-Q.
- [266] H. F. Svendsen, H. A. Jakobsen, and R. Torvik. “Local flow structures in internal loop and bubble column reactors”. In: *17th International Symposium of Chemical Reaction Engineering (IS CRE 17)* 47.13 (1992), pp. 3297–3304. ISSN: 0009-2509. DOI: 10.1016/0009-2509(92)85038-D.
- [267] V. V. Ranade. “Flow in bubble columns: Some numerical experiments”. In: *17th International Symposium of Chemical Reaction Engineering (IS CRE 17)* 47.8 (1992), pp. 1857–1869. ISSN: 0009-2509. DOI: 10.1016/0009-2509(92)80304-U.
- [268] A. Sokolichin and G. Eigenberger. “Gas--liquid flow in bubble columns and loop reactors: Part I. Detailed modelling and numerical simulation”. In: *17th International Symposium of Chemical Reaction Engineering (IS CRE 17)* 49.24 (1994), pp. 5735–5746. ISSN: 0009-2509. DOI: 10.1016/0009-2509(94)00289-4.
- [269] Marco Millies and Dieter Mewes. “Calculation of circulating flows in bubble columns”. In: *17th International Symposium of Chemical Reaction Engineering (IS CRE 17)* 50.13 (1995), pp. 2093–2106. ISSN: 0009-2509. DOI: 10.1016/0009-2509(94)00500-Q.
- [270] E. Delnoij, J.A.M. Kuipers, and W.P.M. van Swaaij. “Dynamic simulation of gas-liquid two-phase flow: Effect of column aspect ratio on the flow structure”. In: *17th International Symposium of Chemical Reaction Engineering (IS CRE 17)* 52.21 (1997), pp. 3759–3772. ISSN: 0009-2509. DOI: 10.1016/S0009-2509(97)00222-4.

- [271] E. Delnoij et al. “Dynamic simulation of dispersed gas-liquid two-phase flow using a discrete bubble model”. In: *17th International Symposium of Chemical Reaction Engineering (IS CRE 17)* 52.9 (1997), pp. 1429–1458. ISSN: 0009-2509. DOI: 10.1016/S0009-2509(96)00515-5.
- [272] S. Grevskott et al. “Liquid circulation, bubble size distributions, and solids movement in two- and three-phase bubble columns”. In: *17th International Symposium of Chemical Reaction Engineering (IS CRE 17)* 51.10 (1996), pp. 1703–1713. ISSN: 0009-2509. DOI: 10.1016/0009-2509(96)00029-2.
- [273] D. Mitra-Majumdar, B. Farouk, and Y. T. Shah. “Hydrodynamic modeling of three-phase flows through a vertical column”. In: *17th International Symposium of Chemical Reaction Engineering (IS CRE 17)* 52.24 (1997), pp. 4485–4497. ISSN: 0009-2509. DOI: 10.1016/S0009-2509(97)00293-5.
- [274] Wen Jianping and Xu Shonglin. “Local hydrodynamics in a gas-liquid-solid three-phase bubble column reactor”. In: *Catalytic Reaction and Reactor Engineering EuropaCat V Limerick, Sept 2-7 2001* 70.1 (1998), pp. 81–84. ISSN: 1385-8947. DOI: 10.1016/S1385-8947(97)00120-4.
- [275] Nely T. Padial et al. “Three-dimensional simulation of a three-phase draft-tube bubble column”. In: *17th International Symposium of Chemical Reaction Engineering (IS CRE 17)* 55.16 (2000), pp. 3261–3273. ISSN: 0009-2509. DOI: 10.1016/S0009-2509(99)00587-4.
- [276] Diana Matonis, Dimitri Gidaspow, and Mitra Bahary. “CFD simulation of flow and turbulence in a slurry bubble column”. In: *AIChE Journal* 48.7 (2002), pp. 1413–1429. ISSN: 1547-5905. DOI: 10.1002/aic.690480706.
- [277] Volker Michele and Dietmar C. Hempel. “Liquid flow and phase holdup---measurement and CFD modeling for two-and three-phase bubble columns”. In: *Chemical Engineering Science* 57.11 (2002), pp. 1899–1908. ISSN: 0009-2509. DOI: 10.1016/S0009-2509(02)00051-9.
- [278] Mohan R. Rampure, Vivek V. Buwa, and Vivek V. Ranade. “Modelling of Gas-Liquid/Gas-Liquid-Solid Flows in Bubble Columns: Experiments and CFD Simulations”. In: *The Canadian Journal of Chemical Engineering* 81.3-4 (2003), pp. 692–706. ISSN: 1939-019X. DOI: 10.1002/cjce.5450810348.
- [279] Isaac K. Gamwo et al. “CFD models for methanol synthesis three-phase reactors: Reactor optimization”. In: *Catalytic Reaction and Reactor Engineering EuropaCat V Limerick, Sept 2-7 2001* 93.2 (2003), pp. 103–112. ISSN: 1385-8947. DOI: 10.1016/S1385-8947(02)00192-4.
- [280] G.M Cartland Glover and S.C Generalis. “Gas--liquid--solid flow modelling in a bubble column”. In: *Chemical Engineering and Processing: Process Intensification* 43.2 (2004), pp. 117–126. ISSN: 0255-2701. DOI: 10.1016/S0255-2701(03)00009-6.
- [281] Wei Feng et al. “Local hydrodynamics of gas--liquid-nanoparticles three-phase fluidization”. In: *17th International Symposium of Chemical Reaction Engineering (IS CRE 17)* 60.24 (2005), pp. 6887–6898. ISSN: 0009-2509. DOI: 10.1016/j.ces.2005.06.006.

- [282] D. Wiemann and D. Mewes. “Calculation of flow fields in two and three-phase bubble columns considering mass transfer”. In: *17th International Symposium of Chemical Reaction Engineering (IS CRE 17)* 60.22 (2005), pp. 6085–6093. ISSN: 0009-2509. DOI: 10.1016/j.ces.2005.04.054.
- [283] Jörg Schallenberg, Jan H. Enß, and Dietmar C. Hempel. “The important role of local dispersed phase hold-ups for the calculation of three-phase bubble columns”. In: *Chemical Engineering Science* 60.22 (2005), pp. 6027–6033. ISSN: 0009-2509. DOI: 10.1016/j.ces.2005.02.017.
- [284] Khanh-Toan Nguyen and Shyh-Chour Huang. “Simulation of hydrodynamic characteristics of glass beads in gas-liquid-solid three phase fluidized beds by computational fluid dynamics”. In: *J Eng Technol Educ* 2 (2007), pp. 248–261.
- [285] R. Panneerselvam, S. Savithri, and G. D. Surender. “CFD simulation of hydrodynamics of gas-liquid-solid fluidised bed reactor”. In: *17th International Symposium of Chemical Reaction Engineering (IS CRE 17)* 64.6 (2009), pp. 1119–1135. ISSN: 0009-2509. DOI: 10.1016/j.ces.2008.10.052.
- [286] Perumalsamy Muthiah, Kalaichelvi Ponnusamy, and T. K. Radhakrishnan. “CFD modeling of flow pattern and phase holdup of three phase fluidized bed contactor”. In: *Chemical Product and Process Modeling* 4.1 (2009), p. 36.
- [287] Peter J. O’Rourke, Paul Zhao, and Dale Snider. “A model for collisional exchange in gas/liquid/solid fluidized beds”. In: *17th International Symposium of Chemical Reaction Engineering (IS CRE 17)* 64.8 (2009), pp. 1784–1797. ISSN: 0009-2509. DOI: 10.1016/j.ces.2008.12.014.
- [288] Andrey A. Troshko and Franz Zdravistch. “CFD modeling of slurry bubble column reactors for Fisher-Tropsch synthesis”. In: *Chemical Engineering Science* 64.5 (2009), pp. 892–903. ISSN: 0009-2509. DOI: 10.1016/j.ces.2008.10.022.
- [289] K. Sivaguru, K. Meera SheriffaM. Begum, and N. Anantharaman. “Hydrodynamic studies on three-phase fluidized bed using CFD analysis”. In: *Catalytic Reaction and Reactor Engineering EuropaCat V Limerick, Sept 2-7 2001* 155.1--2 (2009), pp. 207–214. ISSN: 1385-8947. DOI: 10.1016/j.cej.2009.07.037.
- [290] E. M. Matos et al. “Modeling and simulation of a pseudo-three-phase slurry bubble column reactor applied to the process of petroleum hydrodesulfurization”. In: *Computers & Chemical Engineering* 33.6 (2009), pp. 1115–1122. ISSN: 0098-1354. DOI: 10.1016/j.compchemeng.2008.12.011.
- [291] Mohsen Hamidipour, Jinwen Chen, and FaiCcal Larachi. “CFD study on hydrodynamics in three-phase fluidized beds---Application of turbulence models and experimental validation”. In: *17th International Symposium of Chemical Reaction Engineering (IS CRE 17)* 78 (2012), pp. 167–180. ISSN: 0009-2509. DOI: 10.1016/j.ces.2012.05.016.
- [292] Basha Omar M et al. *CFD Modeling with Experimental Validation of the Internal Hydrodynamics in a Pilot-Scale Slurry Bubble Column Reactor*. 2016. DOI: 10.1515/ijcre-2015-0165.

- [293] Yong Li, Jianping Zhang, and Liang-Shih Fan. “Numerical simulation of gas-liquid-solid fluidization systems using a combined CFD-VOF-DPM method: Bubble wake behavior”. In: *17th International Symposium of Chemical Reaction Engineering (IS CRE 17)* 54.21 (1999), pp. 5101–5107. ISSN: 0009-2509. DOI: 10.1016/S0009-2509(99)00263-8.
- [294] Jianping Zhang, Yong Li, and Liang-Shih Fan. “Numerical studies of bubble and particle dynamics in a three-phase fluidized bed at elevated pressures”. In: *Powder Technology* 112.1–2 (2000), pp. 46–56. ISSN: 0032-5910. DOI: 10.1016/S0032-5910(99)00304-6.
- [295] Jianping Zhang, Yong Li, and Liang-Shih Fan. “Discrete phase simulation of gas-liquid-solid fluidization systems: Single bubble rising behavior”. In: *Powder Technology* 113.3 (2000), pp. 310–326. ISSN: 0032-5910. DOI: 10.1016/S0032-5910(00)00314-4.
- [296] Caixia Chen and Liang-Shih Fan. “Discrete simulation of gas-liquid bubble columns and gas-liquid-solid fluidized beds”. In: *AIChE Journal* 50.2 (2004), pp. 288–301. ISSN: 1547-5905. DOI: 10.1002/aic.10027.
- [297] M. van Sint Annaland, N. G. Deen, and J.A.M. Kuipers. “Numerical simulation of gas bubbles behaviour using a three-dimensional volume of fluid method”. In: *17th International Symposium of Chemical Reaction Engineering (IS CRE 17)* 60.11 (2005), pp. 2999–3011. ISSN: 0009-2509. DOI: 10.1016/j.ces.2005.01.031.
- [298] Xinyu Zhang and Goodarz Ahmadi. “Eulerian-Lagrangian simulations of liquid-gas-solid flows in three-phase slurry reactors”. In: *17th International Symposium of Chemical Reaction Engineering (IS CRE 17)* 60.18 (2005), pp. 5089–5104. ISSN: 0009-2509. DOI: 10.1016/j.ces.2005.04.033.
- [299] Changqing Cao et al. “Experimental measurement and numerical simulation for liquid flow velocity and local phase hold-ups in the riser of a GLSCFB”. In: *Chemical Engineering and Processing: Process Intensification* 48.1 (2009), pp. 288–295. ISSN: 0255-2701. DOI: 10.1016/j.cep.2008.04.004.
- [300] E. W. Thiele. “Relation between Catalytic Activity and Size of Particle”. In: *Industrial & Engineering Chemistry* 31.7 (1939), pp. 916–920. ISSN: 0019-7866. DOI: 10.1021/ie50355a027.
- [301] David Schlereth and Olaf Hinrichsen. “A fixed-bed reactor modeling study on the methanation of CO₂”. In: *ECCE9 – 9th European Congress of Chemical Engineering* 92.4 (2014), pp. 702–712. ISSN: 0263-8762. DOI: 10.1016/j.cherd.2013.11.014.
- [302] Duo Sun and David S.A. Simakov. “Thermal management of a Sabatier reactor for CO₂ conversion into CH₄: Simulation-based analysis”. In: *Journal of CO₂ Utilization* 21.Supplement C (2017), pp. 368–382. ISSN: 2212-9820. DOI: 10.1016/j.jcou.2017.07.015.
- [303] Duo Sun, Faisal Mohamed Khan, and David S.A. Simakov. “Heat removal and catalyst deactivation in a Sabatier reactor for chemical fixation of CO₂: Simulation-based analysis”. In: *Catalytic Reaction and Reactor Engineering EuropaCat V Limerick, Sept 2-7 2001* 329.Supplement C (2017), pp. 165–177. ISSN: 1385-8947. DOI: 10.1016/j.cej.2017.06.160.

- [304] M. Götz et al. “Speicherung elektrischer Energie aus regenerativen Quellen im Erdgasnetz - Arbeitspaket 5: Betrachtungen des Gesamtsystems im Hinblick auf Dynamik und Prozessintegration”. In: *Energie-, Wasser-Praxis* 65.11 (2014), pp. 51–55. ISSN: 1436-6134.
- [305] Sasol GmbH. *MARLOTHERM SH Product Information*. 2014.
- [306] Anca Sauciuc et al. “Influence of operating conditions on the performance of biomass-based Fischer–Tropsch synthesis”. In: *Biomass Conversion and Biorefinery* 2.3 (2012), pp. 253–263. DOI: 10.1007/s13399-012-0060-4.
- [307] Holger Martin and Michael Nilles. “Radiale Wärmeleitung in durchströmten Schüttungsrohren”. In: *Chemie Ingenieur Technik* 65.12 (1993), pp. 1468–1477. ISSN: 1522-2640. DOI: 10.1002/cite.330651206.
- [308] Sabri Ergun. “Fluid flow through packed columns”. In: *Chem. Eng. Prog.* 48 (1952), pp. 89–94.
- [309] Eurostat. *Energy balance sheets — 2015 data — 2017 edition*. Luxembourg: Publications Office of the European Union, 2017. ISBN: 978-92-79-69844-6. DOI: 10.2785/032728.
- [310] Michael Kleiber and Ralph Joh. “D3 Stoffwerte von sonstigen reinen Fluiden”. In: *VDI-Wärmeatlas*. Berlin, Heidelberg: Springer Berlin Heidelberg, 2013, pp. 357–488. ISBN: 978-3-642-19981-3. DOI: 10.1007/978-3-642-19981-3_20.
- [311] Michael Kleiber and Ralph Joh. “Da1 Berechnungsmethoden für Stoffeigenschaften”. In: *VDI-Wärmeatlas*. Berlin, Heidelberg: Springer Berlin Heidelberg, 2006, pp. 103–132. ISBN: 978-3-540-32218-4. DOI: 10.1007/978-3-540-32218-4_10.
- [312] S. C. Saxena, N. S. Rao, and A. C. Saxena. “Heat-transfer and gas-holdup studies in a bubble column: Air-water-glass bead system”. In: *Chemical Engineering Communications* 96.1 (1990), pp. 31–55. ISSN: 0098-6445.
- [313] C. R. Wilke and Pin Chang. “Correlation of diffusion coefficients in dilute solutions”. In: *AIChE Journal* 1.2 (1955), pp. 264–270. ISSN: 1547-5905. DOI: 10.1002/aic.690010222.
- [314] Manfred Baerns, Hanns Hofmann, and Albert Renken. *Chemische Reaktionstechnik: Lehrbuch der Technischen Chemie*. 3rd ed. Stuttgart and , New York: Thieme, 1999. ISBN: 3-13-687503-6.
- [315] P. Sängler and W.-D. Deckwer. “Liquid–Solid Mass Transfer in Aerated Suspensions”. In: *The Chemical Engineering Journal* 22.3 (1981), pp. 179–186. ISSN: 0300-9467. DOI: 10.1016/0300-9467(81)80013-5.
- [316] Rosa Crovetto. “Evaluation of Solubility Data of the System CO₂–H₂O from 273 K to the Critical Point of Water”. In: *Journal of Physical and Chemical Reference Data* 20.3 (1991), p. 575. DOI: 10.1063/1.555905.
- [317] John J. Carroll, John D. Slupsky, and Alan E. Mather. “The Solubility of Carbon Dioxide in Water at Low Pressure”. In: *Journal of Physical and Chemical Reference Data* 20.6 (1991), pp. 1201–1209.

- [318] Roberto Fernández Prini and Rosa Crovetto. “Evaluation of Data on Solubility of Simple Apolar Gases in Light and Heavy Water at High Temperature”. In: *Journal of Physical and Chemical Reference Data* 18.3 (1989), pp. 1231–1243. DOI: 10.1063/1.555834.